Universidad del País Vasco
Euskal Herriko Unibertsitatea

Nonadiabatic effects in adsorbate-surface interactions from first principles

by

Dino Novko

Doctoral thesis submitted for the
Degree of Doctor in Physics

Thesis supervisor:
María Blanco Rey

2017

Contents

Acronyms

1BZ	**1**st **B**rillouin **Z**one
(AI)MD(EF)	(***A****b* ***I****nitio*) **M**olecular **D**ynamics (with **E**lectronic **F**riction)
ASM	**A**tomic **S**urface **M**odel
BOA	**B**orn-**O**ppenheimer **A**pproximation
CDD	**C**harge **D**ensity **D**ifference
DFPT	**D**ensity **F**uncitonal **P**erturbation **T**heory
DFT	**D**ensity **F**uncitonal **T**heory
e*-*h	***e***lectron-***h***ole
FEG	**F**ree **E**lectron **G**as
FSM	**F**rozen **S**urface **M**odel
GGA	**G**eneralized **G**radient **A**pproximation
HE	**H**igh **E**energy
HEG	**H**omogeneous **E**lectron **G**as
HM	**H**irshfeld **M**odel
HOMO, LUMO	**H**ighest **O**ccupied and **L**owest **U**noccupied **M**olecular **O**rbitals
IAA	**I**ndependent **A**tom **A**pproximation
IRAS	**I**nfra**R**ed **A**bsorption **S**pectroscopy
KS	**K**ohn-**S**ham
LDA	**L**ocal **D**ensity **A**pproximation
LDFA	**L**ocal **D**ensity **F**riction **A**pproximation
MP	**M**onkhorst-**P**ack
NAC	**N**on**a**diabatic **C**oupling
(N)FS(+EF)	(**N**on-)**F**rozen **S**urface (with **E**lectronic **F**riction)
(P)DOS	(**P**rojected) **D**ensity **O**f **S**tates

PCD	**P**artial **C**harge **D**ensity
PEC	**P**otential **E**nergy **C**urve
PES	**P**otential **E**nergy **S**urface
QE	**Q**UANTUM **E**SPRESSO
RTA	**R**elaxation **T**ime **A**pproximation
STM	**S**canning **T**unnelling **M**icroscopy
TS	**T**ransition **S**tate
vasp	**V**IENNA **A**B INITIO **S**IMULATION **P**ACKAGE
vdW	**v**an **d**er **W**aals

Chapter 1

Introduction

As the title openly announces, the main ambition of this Thesis is to discuss the fundamental aspects of the interaction between moving particles (atoms and molecules) and metallic surfaces, as well as to give our theoretical contribution to this problem. The efforts to understand the nature of the process underlying this interaction, namely the electron-ion coupling, gave birth to a vast number of outstanding theories and concepts. Even though this serious effort started over a century ago, with the dawn of quantum mechanics, our full understanding of the electron-ion interaction is still incomplete. One of the main reasons is certainly its many-body character, which forced scientists in the past to tailor their theories using perturbative treatments and many approximations. The fortunate advantage of contemporary scientists is an access to a huge computational power, which helps us to surmount the numerical hurdles (at least some of them) and carry on with the investigation of the matter. Experimentalists profit from a similar fortune as well, since the modern and highly advanced equipment gives them opportunity to analyze the physical phenomena with a great accuracy. To make our theoretical considerations more than just a "theory", we try as much as possible in this Thesis to follow and understand these experimental advances and use them as a benchmark to our findings.

Probably the most well known feature of the electron-ion interaction is its static contribution, namely when the electrons instantaneously follow the ion movements (adiabaticity) [1]. Since it requires a lower computational power than the dynamical contribution, it is favoured as a building block in many electronic structure investigations (see Chapter 2). Actually, in most of the cases this adiabatic contribution, along with an appropriate approximation of the electron-electron interaction, suffices to explain the ground state of a great number of systems. Nevertheless, many facets of the electron-ion interactions, such as the damping mechanisms of a moving ion, are omitted with the static approximation. To account them we need to incorporate

the dynamical contribution as well (i.e., the so-called nonadiabatic correction). It is precisely the latter contribution what constitutes the core of this Thesis and links all the chapters.

Historically speaking, the studies on the electron-ion interaction started with periodically extended systems, where the problem of electrons interacting with elastic waves of lattice distortions, i.e. phonons, was addressed [2–7]. In those seminal works on the electron-phonon interaction underlay the ambition to construct a general transport theory of electrons in a periodic potential of ions. In other words, the main concern was to describe the dynamical behaviour of electrons moving in metallic systems with some degree of probability to exchange energy and momentum with the intrinsic phonons. This lead to the development of some innovative ideas and theories that could explain some experimental findings, like phonon-mediated conventional superconductivity, temperature-dependent resistivity, optical adsorption, and so on [8]. All these phenomena and their corresponding theories emphasize the "electron" aspects of the electron-phonon interaction. However, the more appealing aspect for this Thesis is the remaining one, i.e., the influence of electron-phonon interaction on phonons. Fortunately, the perturbation theory developed in the context of electron transport [7, 9, 10] can be equally applied for studying the nonadiabatic effects of phonons [11, 12] and it successfully explains many experimental features obtained, for example, by helium atom scattering [13, 14] and by infrared or Raman spectroscopies [15, 16]. Another interesting example of electron-ion interaction theory was coined in order to explain the energy losses of single ions penetrating through metals [17, 18], for example when a hydrogen atom collides with the inner wall of a thermonuclear reactor [19]. The equations for stopping power adopted to explain these processes were developed initially from the linear, and then later from the nonlinear response theory for an atom impurity moving in the electron gas. Interestingly, these equations also share a similar form with the damping rates obtained in the transport theories of electrons[1].

To some degree, the methodologies presented in this Thesis import some ideas from these theories in order to explain some particular problems of atoms and molecules interacting with metallic surfaces. This is nowadays a highly active research field due to its prominent role in industrial processes. One such example is heterogeneous catalysis, where the presence of a surface may decrease reaction barriers and therefore promote chemical reactions. The decisive factor in some of these surface reactions is the energy exchange between moving adsorbates and surface electrons, i.e. the aforementioned dynamical part of the electron-ion interaction. The earliest experimental evidence of such energy exchange is found in the lifetime measurements of the

[1]This resemblance, along with the analogy between the damping rates for phonons and the ones obtained in transport theory of electrons is reminiscent of Newton's third law.

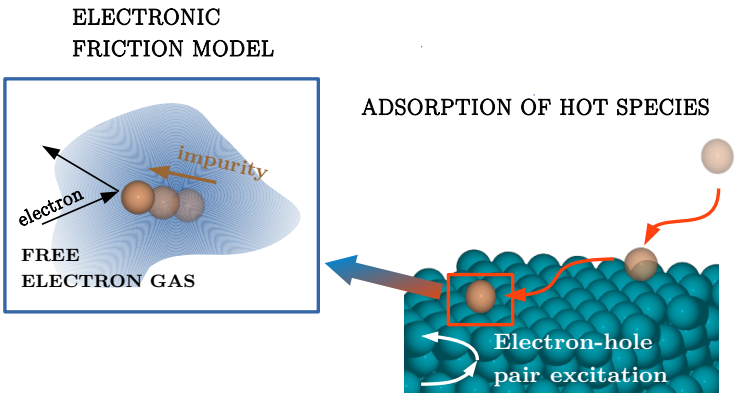

FIGURE 1.1: Schematic view of the electronic excitation model that we use for the relaxation dynamics of hot atomic and molecular species moving on metal surfaces. The moving atom scatters with electrons of the metal surface and therefore loses energy. The model treats this scattering as if the moving atom were an impurity embedded in a free electron gas. For further details see Chapter 3.

vibrationally excited molecules on metal surfaces, either by using infrared absorption spectroscopy (IRAS) or pump-probe techniques [16, 20–22]. These studies show that the lifetime of the high-frequency mode of a molecule adsorbed on a metal surface is considerably smaller than that of a molecule adsorbed on an insulating surface. Further evidences of these nonadiabatic phenomena in adsorbate-surface interactions are reported in many adsorption and scattering experiments [23–27]. The process in the aforesaid examples can also act in reverse, i.e., rather than damping the vibration of an adsorbate, the electron-ion interaction can help to induce it and even provoke an intramolecular bond breaking. This kind of manipulation of surface reactions can be achieved, for instance, with scanning tunnelling microscopy (STM) or with laser light [28–32]. Although a great effort was made to explain these dynamical aspects of the electron-ion interaction in adsorbate-surface systems with theoretical models, there still exist some gaps that we want to address and partially fill in this Thesis.

Our contribution to the topic of adsorbate-surface interaction starts with Chapter 3, where we study the adsorption dynamics of hot H, N, and N_2 on the Pd(100), Ag(111), and Fe(110) surfaces, respectively. Our particular interest is to investigate the two dominating mechanisms of energy loss during these events, namely surface motion and excitations of low-energy electron-hole (e-h) pairs (i.e., nonadiabatic effects). The main goal of this chapter is to understand the role of each of these two dissipation mechanisms in three qualitatively different adsorption scenarios and to support the related experimental findings. Specifically, our motivation comes from the results reported in Refs. [25, 26], where they measure the current intensity produced upon adsorption of different species on a metal surface (the so-called chemicurrents), which scales with the adsorption energies. In our study, we use *ab initio* molecular

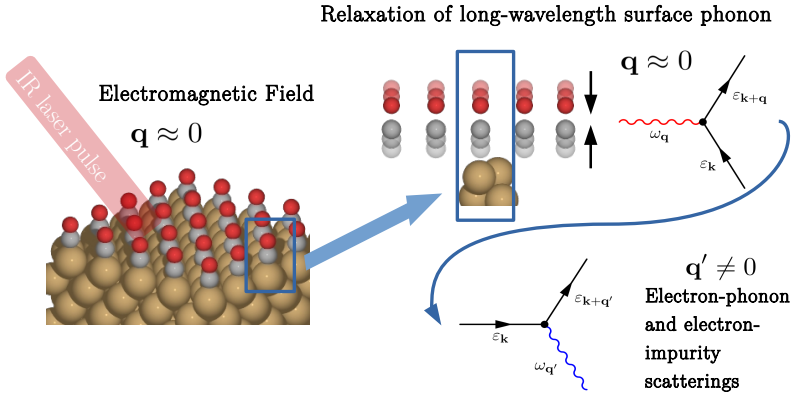

FIGURE 1.2: The panel on the left shows the c(2×2) monolayer of CO on Cu(100) excited by an infrared laser. The panel on the right depicts schematically the CO stretch mode relaxation process: the long-wavelength ($\mathbf{q} \approx 0$) phonon induces electron excitations (first-order process), which then scatter either on other phonons with $\mathbf{q}' \neq 0$ or on impurities (second-order process). The red wavy line in the diagram represents the studied long-wavelength phonon mode, while the blue wavy line represents other phonon modes in the system on which the excited electrons scatter. For further details see Chapter 4.

dynamics with electronic friction (AIMDEF) [33], in which the forces exerted on the atoms at each time step of the simulations are calculated *on-the-fly* using density functional theory (DFT), while the low-energy excitations induced by the moving adsorbate are accounted with an electronic friction force. The friction coefficient needed for the latter term is adopted from the expression of stopping power obtained in the nonlinear response theory for an impurity moving in a free electron gas (FEG) (see Fig. 1.1). The friction coefficient thus varies with the charge density of the FEG, while in the AIMDEF it is replaced with the position-dependent charge density obtained from the DFT calculations [34]. In the seminal work of AIMDEF, where a dominating role of the electronic excitations is reported for hot H-atom relaxation on Pd(100), the charge density is calculated for the rigid Pd(100) surface [33]. However, this approximation might bring some errors when heavier projectiles (like N and N_2) impinge the surface, since the large surface atomic displacements considerably distorts the charge density in these cases. Therefore, we propose and systematically explore different charge density models that account for the surface motion for the three case studies. With the most physically sound charge density model, which is based in the charge partitioning scheme by Hirshfeld [35], the AIMDEF becomes a powerful theoretical tool. It accounts for both energy loss channels on the same footing, and it can be used for studying the relaxation dynamics of a large variety of systems.

In Chapter 4 we explore the effects of electronic relaxation processes on the vibrating molecules on metal surfaces. As opposed to Chapter 3, where the damping

mechanism of a single adsorbate is investigated, here we study the collective motion of an extended and ordered molecular layer adsorbed on a metal surface. In other words, the general electron-ion interaction is manifested here as an electron-phonon interaction. In order to tackle the intricacies of the phonon damping mechanisms, we adopt the DFT-based many-body perturbation theory. Although the foundations for this theory were laid over a half century ago, it is only today that, with the help of predictive theories such as DFT, we can provide precise quantitative estimations. For our case we start by applying first-order perturbation theory, i.e., the corresponding damping rate formula is quadratic in the electron-phonon coupling function [36–40]. In this chapter we find it necessary to include higher-order effects (i.e., electronic relaxation processes), since it turns out that the first-order damping rate formula is not sufficient to explain the lifetime measurements of the high-frequency modes of molecular layers. Note that the early lifetime calculations of vibrating diatomic molecules on metallic surfaces report a good agreement with the experimental results, even though they apply the first-order damping rate formula [36, 37]. However, more accurate DFT-based simulations show a strong mismatch between the first-order calculations and the experiment, and therefore point to the fact that other contributions need to be included [40]. To incorporate the electronic relaxation processes into the phonon damping rate formula we first consider a phenomenological treatment, where a phenomenological parameter that accounts for these processes enters the damping rate expression. Apart from that, we explicitly calculate the second-order term [9, 11, 41], where the studied phonon (red wavy line in Fig. 1.2) excites electrons, which then inelastically scatter on other phonons (blue wavy line in Fig. 1.2) or impurities. The former scattering event describes the indirect phonon-phonon coupling mediated by the electronic excitations, which should be distinguished from the usual direct anharmonic effects. This indirect process includes temperature dependence in the damping rate formula, thus it could be important for explaining the experimentally observed temperature dependence of the vibrational lifetimes [42]. As Fig. 1.2 depicts, our particular system of interest is the stretch mode of CO on Cu(100), which we pick due to available extensive reports on its vibrational lifetimes [16, 20–22]. The general consent is that the value of the lifetime is around 2 ps, which is almost five times smaller than the one obtained in the DFT-based simulations [40]. One of the experiments even finds a small temperature dependence for this lifetime [22], which either could come from direct anharmonic coupling or indirect phonon-phonon coupling mediated by the electronic excitations. All these interesting attributes of the electron-phonon interaction in adsorbate-surface systems are further discussed in Chapter 4.

Last, but certainly not least, in Chapter 5 we study single-molecule manipulation at metal surfaces by means of STM-induced inelastic currents [30], which is another

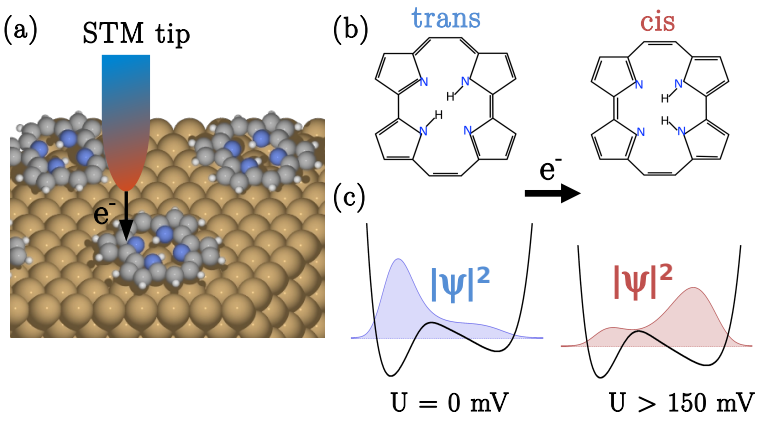

FIGURE 1.3: (a) Schematic representation of a STM tip injecting electrons in the porphycene/Cu(111) system. (b) Formula models for *trans* and *cis* porphycene configurations. (c) Potential energy curves along the H-transfer reaction paths and the corresponding probability densities for two applied bias voltages. The left and right potential wells correspond to the *trans* and *cis* configurations, respectively. At zero potential bias the *trans* configuration is thermodynamically stable. Above a threshold potential bias ($U \approx 150\,\text{mV}$) the *cis* configuration is favoured [43]. The underlying mechanism behind this transition is the nonadiabatic coupling between the STM-excited electrons of the substrate and the vibrational skeletal modes of the porphycene molecule. For further details see Chapter 5.

exciting manifestation of the dynamical electron-ion interaction. From the earliest experimental realizations of similar processes, where dissociation [28] and rotational motion [29] of single-molecules was achieved, there have been numerous attempts to trigger surface reactions in a similar manner. One such example that opens the door to technological applications is the tautomerization reaction [43–46], i.e., intramolecular transfer of a hydrogen atom. This single relocation can significantly alter the physical properties of the molecule, e.g. its conductivity, and thus it can be potentially employed in nanoscale electronics devices (i.e. the so-called "molecular switches") [47]. The particular example we chose to study is the recently achieved *trans* $\leftrightarrow$ *cis* tautomerization reaction of porphycene adsorbed on the Cu(111) surface [43] (see Fig. 1.3). It is believed that the driving mechanism for this reaction is the nonadiabatic coupling of inelastic hot electrons and the internal vibrational modes of the porphycene molecule. Furthermore, since the energy of the reaction coordinate mode, namely internal N-H stretch mode, almost doubles the threshold bias voltage, it is expected that the activation of the reaction occurs indirectly via excitation of the vibrational skeletal modes of the porphycene molecule. In other words, the inter-mode coupling must play a decisive role. On the one hand, most of the theoretical models present in the literature that deal with the electron-vibration coupling rely on the harmonic approximation [48, 49] and, therefore, cannot be applied for the tautomerization reaction, where large-amplitude atomic displacements are involved in the hydrogen transfer. On the other hand, the existing anharmonic theories are not

capable of tackling the prophycene problem in a simple fashion [50, 51], since many internal vibrational degrees of freedom have a role in this process. Therefore, our main goal in this chapter is to introduce a theoretical model that successfully overcomes these issues with a modest computational cost. In this model, the electron-vibration coupling and intermode energy flow are effectively incorporated via a deformation potential term along the one-dimensional reaction path describing the intramolecular hydrogen relocation. In that way the high-dimensional tautomerization reaction is effectively mapped onto a more simple one-dimensional problem. All the building blocks needed for our model, such as normal mode analysis, surface charge densities, and potential energy curves, are provided by the DFT calculations. Since the nature of the porphycene-surface interaction has a strong van der Waals (vdW) character, we need to carefully choose the functional to be used in the DFT calculation to account for the non-local correlations not included in the standard functionals [52]. We perform a systematic analysis of the porphycene adsorption energetics and electronic structure, and how these properties are influenced by the particular functional choice.

Chapter 2

Theoretical methods

2.1 The Born-Oppenheimer Hamiltonian

In a formal way, the dynamical properties of a many-body system composed of electrons and ions, such as a crystal or a molecule, are completely described by the time-dependent Schrödinger equation[1] [53],

$$i\frac{\partial\Psi\left(\{\mathcal{R}\},t\right)}{\partial t}=H\Psi\left(\{\mathcal{R}\},t\right), \tag{2.1}$$

where $\Psi\left(\{\mathcal{R}\},t\right)$ is the many-body time-dependent wavefunction, with $\{\mathcal{R}\}$ representing the set of space coordinates of all the particles in the system, namely n_e electrons and N_i ions. Providing that $\Psi\left(\{\mathcal{R}\},t\right)$ were known for the studied system, the static and dynamic properties of all the important physical observables would be available. The operator H in Eq. (2.1) stands for the Hamiltonian, consisting of a kinetic energy term and a potential energy term, which describes the interactions between all the particles in the electron-ion system. Additionally, when the system is exposed to some static or time-varying external field, the Hamiltonian H contains the corresponding external potential term. In the absence of external perturbations, the following Hamiltonian can be used to describe the Coulomb interactions in the system of electrons and ions

[1] In this Thesis atomic units ($m_e = e = \hbar = 1$) are used unless otherwise stated.

$$
\begin{aligned}
H &= T_e + V_{ee} + V_{ei} + T_i + V_{ii} \\
&= \sum_{\nu}^{n_e} \frac{\mathbf{p}_\nu^2}{2} + \frac{1}{2} \sum_{\nu \neq \nu'}^{n_e} \frac{1}{|\mathbf{r}_\nu - \mathbf{r}_{\nu'}|} - \sum_{\nu,\alpha}^{n_e,N_i} \frac{Z_\alpha}{|\mathbf{r}_\nu - \mathbf{R}_\alpha|} \\
&\quad + \sum_{\alpha}^{N_i} \frac{\mathbf{P}_\alpha^2}{2M_\alpha} + \frac{1}{2} \sum_{\alpha \neq \alpha'}^{N_i} \frac{Z_\alpha Z_{\alpha'}}{|\mathbf{R}_\alpha - \mathbf{R}_{\alpha'}|},
\end{aligned} \tag{2.2}
$$

where the indices ν and α run over electrons and ions, respectively, and M_α and Z_α are the mass and atomic number of each ion, respectively. The sets of momentum and position operators for ions and electrons are denoted with $(\mathbf{P}_\alpha, \mathbf{R}_\alpha)$ and $(\mathbf{p}_\nu, \mathbf{r}_\nu)$, respectively. The T and V operators in Eq. (2.2) describe the kinetic energy of electrons, electron-electron interaction, electron-ion interaction, kinetic energy of ions, and ion-ion interaction, respectively.

Since the defined electron-ion Hamiltonian does not depend on time, the wavefunction $\Psi(\{\mathcal{R}\}, t)$ and physical observables are stationary. Therefore the time-dependent Schrödinger equation Eq. (2.1) can be reduced to its time-independent (static) form

$$
H\Psi(\{\mathcal{R}\}) = E\Psi(\{\mathcal{R}\}). \tag{2.3}
$$

This equation is solved as an eigenvalue problem, where the solutions are the eigenfunctions $\Psi(\{\mathcal{R}\})$ with eigenenergies E. These energies could either account for discrete or continuous spectra. Although the above eigenvalue equation has a very compact form, in practical terms it is not useful for larger systems, considering it is daunting to obtain the analytical solution for systems bigger than the hydrogen atom. Actually, the problem with Eq. (2.3) is not only of mathematical but also of practical nature. It turns out that for large systems a numerical approach to solve Eq. (2.3) is more convenient. However the practical problem of storing the eigenfunctions $\Psi(\{\mathcal{R}\})$ appears in that case, since the memory requirement increase very rapidly with the increase in the number of spatial degrees of freedom $\{\mathcal{R}\}$.

One very successful step towards simplifying the above mentioned eigenvalue problem is to separate the electronic and ionic degrees of freedom in Eq. (2.3). This is known as the Born-Oppenheimer approximation (BOA) [1]. The idea behind the BOA is to write the full many-body wavefunction $\Psi(\{\mathcal{R}\})$ as follows:

$$
\Psi(\{\mathcal{R}\}) = \sum_m \chi_m(\{\mathbf{R}\}) \psi_m(\{\mathbf{r}\}, \{\mathbf{R}\}). \tag{2.4}
$$

Here we separate the notation $\{\mathcal{R}\}$ into electron $\{\mathbf{r}\}$ and ion $\{\mathbf{R}\}$ coordinates. The expansion functions $\chi_m(\{\mathbf{R}\})$ depend only on the ion subsystem, while $\psi_m(\{\mathbf{r}\},\{\mathbf{R}\})$ are the complete orthogonal set of electronic eigenfunctions of Eq. (2.2). In that way the ion positions $\{\mathbf{R}\}$ enter the function $\psi_m(\{\mathbf{r}\},\{\mathbf{R}\})$ only as parameters. When we include Eq. (2.4) into Eq. (2.3) we get two separated equations, one for the electron eigenfunction $\psi_n(\mathbf{r},\mathbf{R})$[2] [54–56]

$$[T_e + V_{ee}(\mathbf{r}) + V_{ei}(\mathbf{r},\mathbf{R}) + V_{ii}(\mathbf{R})]\,\psi_n(\mathbf{r},\mathbf{R}) = E_n(\mathbf{R})\psi_n(\mathbf{r},\mathbf{R}), \tag{2.5}$$

and another one for the ion eigenfunction $\chi_n(\mathbf{R})$

$$[T_i + E_n(\mathbf{R})]\,\chi_n(\mathbf{R}) + \sum_m (\mathcal{A}_{nm} + \mathcal{B}_{nm})\,\chi_m(\mathbf{R}) = E\chi_n(\mathbf{R}). \tag{2.6}$$

Here $\mathcal{A}_{nm}$ and $\mathcal{B}_{nm}$ are the nonadiabatic[3] terms describing the coupling of two electronic states (n and m) by the movement of ions. They are defined as [54, 55]

$$\mathcal{A}_{nm} = -\sum_\alpha \frac{1}{M_\alpha}\int d\mathbf{r}\psi_n^*(\mathbf{r},\mathbf{R})\,\nabla_\alpha\psi_m(\mathbf{r},\mathbf{R})\,\nabla_\alpha \tag{2.7}$$

$$\mathcal{B}_{nm} = -\sum_\alpha \frac{1}{2M_\alpha}\int d\mathbf{r}\psi_n^*(\mathbf{r},\mathbf{R})\,\nabla_\alpha^2\psi_m(\mathbf{r},\mathbf{R}), \tag{2.8}$$

where we introduce the definition of the ion momentum operator $\mathbf{P}_\alpha = -i\nabla_\alpha$. Considering that the nonadiabatic terms are not zero in general, the Eqs. (2.5) and (2.6) are fully separated only when we additionally require that $\mathcal{A}_{nm} + \mathcal{B}_{nm} = 0$. In that case the electrons adapt instantaneously to the movement of the ions. For this reason the BOA is often called the adiabatic approximation. In other words, we consider ions to have much greater mass than electrons, so the former ones move very slowly in the reference frame of the electrons. Since this Thesis deals in-depth with the nonadiabatic effects in the electron-ion systems, the nonadiabatic terms Eqs. (2.7) and (2.8) will be discussed further along the present work.

2.2 Density functional theory

When imposing the BOA for solving the eigenvalue problem of Eq. (2.3), the dimensionality of the eigenfunctions $\psi(\mathbf{r},\mathbf{R})$ is reduced from the total number of electrons

[2] starting from here we drop the $\{\dots\}$ curly brackets for simplicity
[3] The concept of adiabaticity will be explained later in this chapter.

and ions, $3n_e + 3N_i$, to only the electronic degrees of freedom, $3n_e$. However, since the number of electrons involved in the eigenvalue problem is still a large number, it is still very hard to tackle Eq. (2.3). The ingenious idea behind DFT is to overcome this issue by using the electron density instead of the electron wavefunction as the key quantity in the many-body problem [57, 58]. In this way the total number of degrees of freedom is reduced from $3n_e$ to only 3, since the electron density is defined as

$$n(\mathbf{r}) = \int d\mathbf{r}_2 \dots d\mathbf{r}_{n_e} \left|\psi(\mathbf{r}, \mathbf{r}_2, \dots, \mathbf{r}_{n_e})\right|^2, \tag{2.9}$$

where the parametric dependence of the electron density on the ionic positions is assumed, i.e. $n(\mathbf{r}) \equiv n(\mathbf{r}, \mathbf{R})$.

Before stating the principal theorems of DFT, we express the electronic Hamiltonian from Eq. (2.5), $H_e = T_e + V_{ee} + V_{ei}$,[4] in terms of the electron density $n(\mathbf{r})$, so that each contribution to the Hamiltonian becomes a functional of $n(\mathbf{r})$. In doing so, we approximate the electronic wavefunction $\psi_n(\mathbf{r})$ by the Slater determinant of single-particle wavefunctions $\phi_\nu(\mathbf{r}_\nu)$ as [59]

$$\psi(\mathbf{r}_1, \dots, \mathbf{r}_{n_e}) = \frac{1}{\sqrt{n_e!}} \begin{vmatrix} \phi_1(\mathbf{r}_1) & \cdots & \phi_1(\mathbf{r}_{n_e}) \\ \vdots & \ddots & \vdots \\ \phi_{n_e}(\mathbf{r}_1) & \cdots & \phi_{n_e}(\mathbf{r}_{n_e}) \end{vmatrix}, \tag{2.10}$$

which shows the fundamental properties of a fermionic system. Since the rows of the Slater determinant represent single-electron states, while the columns their corresponding positions, the exchange of two rows or columns equals the interchange of two particles. This makes the many-body wavefunction anti-symmetric with respect to particles exchange. Consequently, if two rows or columns are equal, meaning that two electrons occupy the same state, the wavefunction is identically zero. Whenever the studied system is composed of noninteracting electrons placed in the external field produced by the ions [i.e., if V_{ee} is set to zero in Eq. (2.5)], the Slater determinant Eq. (2.10) is an appropriate choice for the many-body wavefunction. Nevertheless, it turns out that the Slater representation is useful even for the case when electron-electron interactions are present.

We now express the electron density in terms of the single-electron wavefunctions $\phi_\nu(\mathbf{r}_\nu)$ using Eq. (2.10) as

[4] Here we exclude the pure nuclear term V_{ii} for the sake of simplicity and since in DFT formalism it does not depend on the electron density, it will only be a constant term. Thus, later in this section it is assumed that this constant term is added to the total energy.

$$n(\mathbf{r}) = \sum_{\nu}^{n_e} |\phi_\nu(\mathbf{r})|^2 , \tag{2.11}$$

in order to write the Hamiltonian as an electron density functional. With the use of Eqs. (2.9) and (2.11) the electron-ion interaction energy is

$$\begin{aligned} E_{ei}[n] = \langle\psi| V_{ei} |\psi\rangle &= -\sum_{\alpha}^{N_i} Z_\alpha \int d\mathbf{r} \frac{n(\mathbf{r})}{|\mathbf{r} - \mathbf{R}_\alpha|} \\ &\equiv \int d\mathbf{r} n(\mathbf{r}) v_{\text{ext}}(\mathbf{r}), \end{aligned} \tag{2.12}$$

where we define $v_{\text{ext}}(\mathbf{r})$ as the external potential of the ions. The electron-electron interaction energy is usually separated into two terms

$$\begin{aligned} E_{ee}[n] = \langle\psi| V_{ee} |\psi\rangle &= \frac{1}{2} \iint d\mathbf{r} d\mathbf{r}' \frac{n(\mathbf{r}) n(\mathbf{r}')}{|\mathbf{r} - \mathbf{r}'|} + E_{xc}[n] \\ &\equiv E_h[n] + E_{xc}[n], \end{aligned} \tag{2.13}$$

where the first term is the Hartree energy, coming from the electron density self-interaction, and the second term is the so-called exchange and correlation energy, which accounts for all the missing electron-electron interaction contributions not included in the first term. Namely, the contributions from the antisymmetric property of the many-body wavefunction (i.e., exchange) and interaction effects beyond the single-particle wavefunctions in $E_h[n]$ (i.e., correlation). Even though the exact form of the exchange and correlation energy $E_{xc}[n]$ is not known, we still consider it to be some functional of the electron density. The remaining term is the kinetic energy, which cannot be expressed as an electron density functional. However, it can be expressed in terms of single-electron wavefunctions as

$$E_{\text{kin}}[n] = \langle\psi| T_e |\psi\rangle = -\frac{1}{2} \sum_{\nu}^{n_e} \int d\mathbf{r} \phi_\nu^*(r) \nabla^2 \phi_\nu(r), \tag{2.14}$$

where the functional dependence on the electron density is formally retained in the notation. Finally, by collecting Eqs. (2.12)-(2.14), we write the total electron energy functional as

$$E_e[n] = E_{\text{kin}}[n] + E_h[n] + E_{xc}[n] + E_{ei}[n]. \tag{2.15}$$

The first three contributions are jointly called the universal functional, since they do

not depend explicitly on the specific electron-ion system, but only implicitly through the electron density n.

2.2.1 The Hohenberg-Kohn theorems

We now write the principal theorems, originally stated and proven by Hohenberg and Kohn in a simple and elegant way, the DFT is based on [57, 58]:

Theorem 2.1. *The external potential $v_{\text{ext}}(\mathbf{r})$ is a conversely unique functional of the electron density $n(\mathbf{r})$, apart from a trivial additive constant.*

Theorem 2.2. *The exact electron density $n(\mathbf{r})$ minimizes the electron energy functional $E_e[n]$.*

These two important theorems revived and theoretically improved the old idea by Thomas and Fermi of formulating the many-body problem using the electron density $n(\mathbf{r})$ instead of the many-body wavefunction $\psi(\mathbf{r}_1, \ldots, \mathbf{r}_{n_e})$ [60, 61]. The theorems show how in principle the ground state energy of the studied system could be uniquely determined by minimizing the electron energy functional $E_e[n]$ with respect to the electron density $n(\mathbf{r})$ by a variational method [58, 62]. However, the minimization of this energy functional is usually not feasible, since the exact functional dependence of the universal functional on $n(\mathbf{r})$ is not known. Specifically, the kinetic term $E_{\text{kin}}[n]$ cannot be expressed as a functional of $n(\mathbf{r})$ even in the Slater determinant representation [see Eq. (2.14)], while the exact analytical expression for the correlation part of the exchange and correlation term $E_{xc}[n]$ is out of reach even for the homogeneous electron gas (HEG).

2.2.2 The Kohn-Sham equations

To make the previously stated theorems more practical, it was proposed by Kohn and Sham to construct the exact electron density $n(\mathbf{r})$ using a set of the non-interacting electrons moving in the effective field of the electron-ion system [63] in order to minimize $E_e[n]$. In that case we can write

$$n(\mathbf{r}) = \int d\mathbf{r}_2 \ldots d\mathbf{r}_{n_e} \left|\psi(\mathbf{r}, \mathbf{r}_2, \ldots, \mathbf{r}_{n_e})\right|^2 = \sum_{\nu}^{n_e} \left|\phi_\nu^{\text{KS}}(\mathbf{r})\right|^2, \tag{2.16}$$

where $\phi_\nu^{\text{KS}}(\mathbf{r})$ are the Kohn-Sham (KS) non-interacting orbitals. Although these single-electron wavefunctions are in principle fictitious they are still very helpful in

replacing the actual wavefunction in a large amount of cases (e.g., when constructing the electron-phonon matrix elements as we will do in chapter 4).

Using this set of non-interacting orbitals, the kinetic energy functional can be expressed as in Eq. (2.14)

$$E_{\text{kin}}[n] = -\frac{1}{2}\sum_{\nu}^{n_e}\int d\mathbf{r}\left[\phi_{\nu}^{\text{KS}}(\mathbf{r})\right]^{*}\nabla^2\phi_{\nu}^{\text{KS}}(\mathbf{r}). \tag{2.17}$$

It can be shown that the minimization of the energy functional $E_e[n]$ [Eq. (2.15)] with respect to $\left[\phi_{\nu}^{\text{KS}}(\mathbf{r})\right]^{*}$, in a close analogy with the Hartree-Fock method, leads to the Schrödinger equations for the non-interacting electrons in a self-consistent effective potential

$$\left[-\frac{1}{2}\nabla^2 + v_{\text{eff}}(\mathbf{r})\right]\phi_{\nu}^{\text{KS}}(\mathbf{r}) = \varepsilon_{\nu}\phi_{\nu}^{\text{KS}}(\mathbf{r}), \tag{2.18}$$

which are usually referred to as the KS equations. The effective potential $v_{\text{eff}}(\mathbf{r})$ consists of the following terms

$$v_{\text{eff}}(\mathbf{r}) = v_{\text{ext}}(\mathbf{r}) + \int d\mathbf{r}'\frac{n(\mathbf{r}')}{|\mathbf{r}-\mathbf{r}'|} + \frac{\delta E_{xc}[n]}{\delta n(\mathbf{r})}, \tag{2.19}$$

where the first term is the external potential created by the ions, the second term is the Hartree potential $v_h(\mathbf{r})$ and the last term is the exchange and correlation potential $v_{xc}(\mathbf{r})$. When the functional dependence of the effective potential $v_{\text{eff}}(\mathbf{r})$ is known, the KS equations are solved self-consistently by repeating the following i-th step

$$n^i(\mathbf{r}) \longrightarrow v_{\text{eff}}^i(\mathbf{r}) \longrightarrow \text{KS equations} \longrightarrow \left[\phi_{\nu}^{\text{KS}}(\mathbf{r})\right]^{i+1} \longrightarrow n^{i+1}(\mathbf{r}),$$

until the desired convergence threshold is achieved. Note here that the total energy is not just the sum of the KS eigenvalues ε_{ν}, but rather

$$E_{\text{DFT}} = \sum_{\nu}^{n_e}\varepsilon_{\nu} - E_h[n] + E_{xc}[n] - \int d\mathbf{r}n(\mathbf{r})v_{xc}(n(\mathbf{r})). \tag{2.20}$$

By substituting the eigenvalue problem of Eq. (2.5), where the key role is played by the many-body wavefunction $\psi(\mathbf{r},\mathbf{R})$, by the set of the KS equations Eq. (2.18), the system of fully interacting electrons is replaced by the independent electrons moving in an effective field. We note here that no restrictions or approximations were made when going from the former to the latter methodology. Therefore, the electron

density and energy obtained from the KS equations are in principle as accurate as the ones obtained from the many-body eigenvalue problem Eq. (2.5) provided the actual functional dependence of the exchange and correlation term were known. However, this is not the case. We present in the following some of the successful approaches to approximate $v_{xc}(\mathbf{r})$.

2.2.3 Exchange and correlation functionals

The earliest and simplest approximation for the exchange and correlation density functional is the so-called local density approximation (LDA) [63]. Having in mind that the exchange and correlation energies are local functions of the electron density in the limit of the HEG, the first logical step towards finding an expression for $E_{xc}[n]$ would be to assume the same functional dependence for the actual system. In doing so, we can write

$$E_{xc}^{\mathrm{LDA}}[n] = \int d\mathbf{r} n(\mathbf{r}) v_{xc}^{\mathrm{HEG}}(n(\mathbf{r})). \tag{2.21}$$

Since the exchange and correlation potential in each point of the space $\mathbf{r}$ is assumed to have the same form as in the HEG we can linearly decompose $v_{xc}^{\mathrm{HEG}}(\mathbf{r})$ into the exchange and correlation terms

$$v_{xc}^{\mathrm{HEG}}(\mathbf{r}) = v_{x}^{\mathrm{HEG}}(\mathbf{r}) + v_{c}^{\mathrm{HEG}}(\mathbf{r}). \tag{2.22}$$

In that case the exchange term is well-known and reads [64]

$$v_{x}^{\mathrm{HEG}}(\mathbf{r}) = -\frac{0.4582}{r_s}, \tag{2.23}$$

where the Wigner-Seitz radius r_s is the radius of a sphere whose volume is equal to the mean volume per electron, i.e., $r_s = (3/4\pi n)^{1/3}$. To reach this result it is also assumed that electrons are independent and move in an external potential, as it happens to be the case for the electrons in the KS equations. As for the correlation term $v_{c}^{\mathrm{HEG}}(\mathbf{r})$, its values for different electron densities have been parametrized with quantum Monte-Carlo simulations [65]. That by Perdew and Zunger is one of the most often used parametrizations [66].

Regardless of being a crude approximation, the experience obtained from extensive numerical calculations shows how useful the LDA is. In particular, the geometries of many simple molecules and solids are adequately captured by the LDA [58]. Even

other physical properties are well described within the LDA when the electronic structure of the valence band is governed by the s-state electrons (e.g., as in the alkali and alkaline earth metals). As it is expected, the LDA can fail to produce accurate electronic properties when the variations in the electron density deviate considerably from a delocalised behaviour, like in the case of transition metals and highly inhomogeneous systems (e.g., molecules or surfaces), and for strongly correlated systems, where the effects of the electron-electron interactions are far beyond the HEG model.

The next step in approximating the exchange and correlation term is to introduce first-order density gradient contributions in the $E_{xc}[n]$ functional [58, 63, 67, 68]. This leads to the generalized gradient approximation (GGA) of the exchange and correlation functional, which has the following form

$$E_{xc}^{\mathrm{GGA}}[n] = \int d\mathbf{r} n(\mathbf{r}) v_{xc}(n(\mathbf{r}), \nabla n(\mathbf{r})), \tag{2.24}$$

where in practice $v_{xc}(n(\mathbf{r}), \nabla n(\mathbf{r}))$ must be parametrized. Since this approximation tries to correct the local character of the LDA, it is commonly referred to as the semi-local approximation. Taking into account these corrections, the description of some molecules and their adsorption on surfaces is greatly improved. Unfortunately, this is not the general case. Different GGA parametrizations need to be considered and compared for a particular system before choosing the appropriate one. One of the earliest GGA parametrizations was done by Perdew, Wang and other co-workers resulting in PW86 [69] and PW91 functionals [70]. In these approximations the LDA exchange term is corrected by a multiplicative factor $F_x(s)$ that depends on the density gradients (s is the generalized gradient defined as $s = |\nabla n|/2k_F n$, where k_F is the Fermi wavevector), while a density-dependent additive term corrects the LDA correlation part. Later, a simplification of these functionals was introduced by Perdew, Burke, and Ernzerhof (PBE) [71], where all the GGA parameters are fundamental physical constants. In order to choose the $F_x(s)$ parameters for the PBE functional it is required to preserve the good LDA description of the exchange-correlation energy in the linear response of the HEG (i.e., small s region) and to satisfy the Lieb-Oxford bound [72] in the large s region. Apart from the standard PBE formulation, the revisited versions of it are also widely used, like revPBE [73] and RPBE [74], which additionally improve the atomization and chemisorption energies of some small molecules.

The above mentioned approximations to the exchange and correlation term can already grasp most of the electronic structure properties of adsorbed atoms and small molecules on metal surfaces relevant for our study (and thus account for, e.g., adsorption energies and forces). However, when it comes to the molecule-surface

systems where the short-range, non-local interactions are important the semi-local approximations can fail. In that case, the weak, non-local interactions coming from the polarization fluctuations need to be included. Specifically, the correlation term needs to be corrected by non-local contributions, which account for these dispersion, also called vdW, interactions [52]. This can be written as [75–78]

$$E_{xc}[n] = E_x^{\mathrm{GGA}}[n] + E_c^{\mathrm{LDA}}[n] + E_c^{\mathrm{nl}}[n]. \tag{2.25}$$

The non-local energy can be expressed in its exact form as follows [76, 77]

$$E_c^{\mathrm{nl}} = \int_0^\infty \frac{du}{2\pi} \mathrm{Tr}\left[\ln(1 - V\chi) - \ln(\varepsilon(u, \mathbf{r}, \mathbf{r}'))\right], \tag{2.26}$$

where u is the imaginary frequency $-i\omega$ and $\varepsilon(\mathbf{r}, \mathbf{r}', u)$ is the dielectric function. The abbreviation $V\chi$ stands for $\int \mathbf{r}'' V(\mathbf{r} - \mathbf{r}'')\chi(\mathbf{r}'', \mathbf{r}', u)$, where $\chi(\mathbf{r}'', \mathbf{r}', u)$ is the charge response function and $V(\mathbf{r} - \mathbf{r}'')$ is the Coulomb potential. The trace integrates over diagonal elements. In the HEG the functions in Eq. (2.26) are diagonal in spatial coordinates, thus $\varepsilon = 1 - V\chi$ and the non-local corrections vanish. This ensures that there is no double counting and that for truly homogeneous systems we only have the LDA correlation. The vdW-DF functional proposed by Dion *et al.* is obtained by expanding Eq. (2.26) to second order in $1 - \varepsilon^{-1}$ and by expressing it in terms of the electron density and its gradient [76–78]. The computational cost of the original vdW-DF method was high, but the subsequent efficient implementation of Pérez and Soler reduced this cost [79]. It is also demonstrated that further improvements of the vdW-DF functional can be made by carefully choosing the GGA exchange term $E_x^{\mathrm{GGA}}[n]$ [80–84]. Specifically, the original revPBE exchange can be replaced by, for example, PBE [80], optPBE, or optB88 [81, 82] to achieve smaller deviations from the benchmark dimer data set S22 [85]. One such recent improvement of the vdW-DF functional is vdW-DF-cx, which uses the same exchange in the semi-local exchange and correlation (*outer*) term and in the calculation of the non-local (*inner*) term in order to satisfy the charge conservation rule in the low-to-moderate s regime [78, 83]. These variations of the vdW-DF functional will be used in the calculations of chapter 5.

Some semi-empirical dispersion corrections to semi-local functionals have been also proposed (e.g., DFT-D2 [86]), where a pairwise interatomic interaction $C_6 R^{-6}$ is added to the total energy [52, 86]

$$E_{\mathrm{tot}} = E_{\mathrm{DFT}} - \frac{1}{2} \sum_{A,B} f_{\mathrm{damp}}(R_{AB}, R_A^0, R_B^0) C_{6,AB} R_{AB}^{-6}. \tag{2.27}$$

In this expression the distance between two atoms, labelled A and B, is denoted with R_{AB}, the corresponding vdW radii are R_A^0 and R_B^0, while the damping function $f_{\text{damp}}(R_{AB}, R_A^0, R_B^0)$ eliminates the singularity in R_{AB}^{-6} for small interatomic distances. The coefficients C_6 are usually obtained by fitting to experimental or post-Hartree-Fock data. Since this prevents transferability of the DFT-D functional, some attempts have been made to obtain environment-dependent C_6 coefficients, for which the hybridization of an atom changes depending on the system. Some of the earliest methods, accounting for these effects, are proposed by Tkatchenko and Scheffler [87], as well as by Grimme (DFT-D3) [88], where the parameters in Eq. (2.27) are obtained by accounting for the effective volume of an atom in molecule. Some further refinements of these methods have also been made [89–91], like the vdW$^{\text{surf}}$ method, where the parameters in Eq. (2.27) for substrate atoms are renormalized due to the screening effects caused by the surface.

Here we restrict our theoretical considerations of the exchange and correlation functional mainly to the aforementioned approximations, since all the ground state electronic properties in this study are well captured by them. Further corrections and improvements could be made to account for the missing many-body effects (e.g., the exact exchange in hybrid functionals, the random phase approximation correlation, or the many-body dispersion correction [52, 90, 92–94]), at a high computational cost for gas-surface systems. Further discussion on the properties of the above mentioned exchange and correlation functionals is given in Sec. 5.

2.2.4 Crystal potential and plane-wave basis

For bulk systems and surfaces the crystal periodicity imposes periodic conditions upon the effective potential and the corresponding KS wavefunctions. The effective potential has then the following property

$$v_{\text{eff}}(\mathbf{r} + \mathbf{R}_l) = v_{\text{eff}}(\mathbf{r}), \tag{2.28}$$

where $\mathbf{R}_l$ is the crystal lattice vector. Correspondingly, the KS wavefunctions can be written with the help of Bloch's theorem [2] as

$$\phi_{\mu\mathbf{k}}^{\text{KS}}(\mathbf{r}) = u_{\mu\mathbf{k}}(\mathbf{r}) e^{i\mathbf{k}\cdot\mathbf{r}}, \tag{2.29}$$

where $u_{\mu\mathbf{k}}(\mathbf{r})$ is the periodic part of the KS wavefunction. In crystals the electronic quantum numbers are replaced with the electronic band numbers μ and electronic wavevectors $\mathbf{k}$ lying in the first Brillouin zone (1BZ) of the reciprocal space. Since

$u_{\mu\mathbf{k}}(\mathbf{r})$ satisfies the same periodicity condition as the effective potential, the KS wavefunctions can be further expanded using a plane-wave basis set as follows

$$\phi^{\mathrm{KS}}_{\mu\mathbf{k}}(\mathbf{r}) = \frac{1}{\sqrt{V}} \sum_{\mathbf{G}} C_{\mu\mathbf{k}}(\mathbf{G}) e^{i(\mathbf{k}+\mathbf{G})\cdot\mathbf{r}}, \tag{2.30}$$

where $C_{\mu\mathbf{k}}(\mathbf{G})$ are the plane-wave expansion coefficients, V is the total volume and $\mathbf{G}$ denotes the reciprocal lattice vectors. This basis set is not only the natural choice for most periodic systems, but it is also convenient to handle (e.g., when taking derivatives and integrating). By including the above expansion of the KS wavefunctions into the KS equations, a set of matrix equations for the expansion coefficients $C_{\mu\mathbf{k}}(\mathbf{G})$ is obtained that reads [95]

$$\sum_{\mathbf{G}'} \left[-\frac{1}{2} |\mathbf{k}+\mathbf{G}|^2 \delta_{\mathbf{G}\mathbf{G}'} + \langle \mathbf{k}+\mathbf{G}| \, v_{\mathrm{eff}}(\mathbf{r}) \, |\mathbf{k}+\mathbf{G}'\rangle \right] C_{\mu\mathbf{k}}(\mathbf{G}') = \varepsilon_{\mu\mathbf{k}} C_{\mu\mathbf{k}}(\mathbf{G}). \tag{2.31}$$

Here the matrix elements of the effective potential are defined as

$$\langle \mathbf{k}+\mathbf{G}| \, v_{\mathrm{eff}}(\mathbf{r}) \, |\mathbf{k}+\mathbf{G}'\rangle = \int d\mathbf{r} e^{-i(\mathbf{k}+\mathbf{G})\cdot\mathbf{r}} v_{\mathrm{eff}}(\mathbf{r}) e^{i(\mathbf{k}+\mathbf{G}')\cdot\mathbf{r}}. \tag{2.32}$$

In usual DFT simulations the effective potential $v_{\mathrm{eff}}(\mathbf{r})$ is actually not a functional of the total electron density, but rather of the valence electron density $n_v(\mathbf{r})$ only, i.e., $v_{\mathrm{eff}}(\mathbf{r}, n_v)$. In that way, the core and valence electrons are separated. The former electrons are static and treated as a part of the nuclei, while the latter appear in the KS equations. This convenient separation is reasonable, since the valence electrons are the ones responsible for the most of the physical properties solids (e.g., the formation of bonds). Furthermore, the oscillatory behaviour of the potential around the atomic nucleus requires extremely large numbers of plane waves. The so-called pseudopotential approximation overcomes this issue by replacing the strong ionic potential by a weaker pseudopotential, where the oscillatory core part of potential and the corresponding wavefunction are smoothed out, while the valence part remains essentially the same [95, 96]. Once the pseudopotentials of atoms are known for the studied system, the KS matrix equation for the valence electrons can be calculated self-consistently. Briefly, some of the key steps for obtaining the set of solutions $\{C_{\mu\mathbf{k}}(\mathbf{G}), \varepsilon_{\mu\mathbf{k}}\}$ of Eq. (2.31) are [95, 96]

- The KS equations for the total electron density are solved for the individual isolated atom (i.e., an all-electron calculation).

- Core and valence electrons are separated, and pseudowavefunctions are constructed by smoothing the oscillatory core part, for which a core radius needs to be defined. The energy and the valence electron density produced by this pseudowavefunction must be the same as the all-electron wavefunction. In the case of the norm-conserving pseudopotential [97, 98], the charge enclosed by a core radius in the all-electron wavefunction is preserved in pseudowavefunction. This means that the norm-conserving pseudopotentials are capable of describing the scattering due to the ion in a variety of atomic environments (i.e., they are transferable) [95]. For the ultrasoft pseudopotentials [99] and projector augmented wave (PAW) potentials [100] the latter condition is more flexible, which in general allows for a smoother core part of the wavefunction and requires less plane waves. To construct the pseudopotential from these smoothed wavefunctions, the KS matrix equation for a single atom is reversed.

- The pseudopotential accounts for the screening effects of all electrons in the atom. In order to use it efficiently in different environments it is necessary to subtract the screening effects of the valence electrons, i.e., to subtract $v_h(\mathbf{r}, n_v)$ and $v_{xc}(\mathbf{r}, n_v)$ from the pseudopotential. For the cases where overlap between core and valence electrons is small, a linear subtraction is sufficient [98], while otherwise non-linear corrections are made [101].

- When the effects of the valence electrons are removed, the crystal potential for a specific system can be constructed by summing the ionic pseudopotentials $\tilde{v}(\mathbf{r})$ centred at the crystal sites

$$v_{\mathrm{cr}}(\mathbf{r}) \equiv v_{\mathrm{ext}}(\mathbf{r}) = \sum_{\alpha,\mathbf{R}_0} \tilde{v}_\alpha(\mathbf{r} + \mathbf{R}_0 + \mathbf{R}_\alpha), \tag{2.33}$$

  where α runs over all nuclei, $\mathbf{R}_0$ represents the coordinates of each unit cell, and $\mathbf{R}_\alpha$ are positions of nuclei within the unit cell. The crystal potential serves now as the external potential produced by the nuclei and core electrons.

- Finally, the effective potential can be constructed as

$$v_{\mathrm{eff}}(\mathbf{r}, n_v) = v_{\mathrm{cr}}(\mathbf{r}) + v_h(\mathbf{r}, n_v) + v_{xc}(\mathbf{r}, n_v). \tag{2.34}$$

  Note that the screening effects of the valence electrons are recovered by the inclusion of Hartree and exchange and correlation potentials, which are contributed only by the valence density. Now, the KS matrix equation [Eq. (2.31)] can be solved self-consistently with this effective potential [Eq. (2.34)] until the desired convergence is reached.

In order to solve the KS equations numerically, the number of **G** vectors needs to be reduced to a finite number. The valence electrons are most probably not affected by large **G** contributions, thus it is safe to cut the plane wave expansion at a certain value of **G**. However, the cut-off needs to be sufficiently high to account for the physical properties (e.g., total energy) to be described and, at the same time, it must fit within our computational memory restrictions. This cut-off is usually imposed as the following condition

$$E_{\text{cut}-\text{off}} \leq \frac{1}{2} |\mathbf{k} + \mathbf{G}|^2 .$$

Another important parameter that needs to be chosen as finite is the number of electron wavevectors **k** [95]. By imposing the Born-Von Kármán boundary conditions the number of **k** points within the 1BZ equals the number of unit cells accounted for in the system [102]. Ideally, when the number of unit cells goes to infinity, **k** is a continuous quantity within the 1BZ. In the case of the valence electron density the **k** summation is as follows

$$n_v(\mathbf{r}) = \sum_{\mu, \mathbf{k} \in 1\text{BZ}} f_{\mu\mathbf{k}} \left| \phi^{\text{KS}}_{\mu\mathbf{k}}(\mathbf{r}) \right|^2 , \tag{2.35}$$

where $f_{\mu\mathbf{k}}$ is the temperature dependent Fermi-Dirac distribution function and the number of the electronic bands μ is restricted by the chosen energy cut-off. In the DFT simulations the number of **k** points in the 1BZ is usually given by the Monkhorst-Pack (MP) method [103]. Using this approximation the 1BZ is evenly sampled with a finite **k** point grid, with point rows running parallel to the **G** vectors. The **k** point summation in Eq. (2.35) is then simplified in the following way

$$\sum_{\mathbf{k} \in 1\text{BZ}} \approx \frac{V}{\Omega N_{\mathbf{k}}} \sum_{\mathbf{k} \in \text{MP}} \approx \frac{V}{\Omega N} \sum_{\mathbf{k} \in \text{IBZ}} w_{\mathbf{k}}.$$

In a first step the continuous 1BZ is approximated with the finite MP mesh. The unit cell volume is denoted with Ω, and the total number of MP **k** points is $N_{\mathbf{k}}$. In a second step the finite 1BZ is substituted with the irreducible wedge of the Brillouin zone (IBZ) by taking into account crystal symmetry operations. By doing so, each **k** point in the wedge contributes to the total sum with a particular weight $w_{\mathbf{k}}$ determined by its number of symmetry-equivalent points. Before choosing the final number of **k** points, the convergence of the electron density expressed in Eq. (2.35) needs to be tested, too.

One remaining problem important for our work needs to be addressed here. The Bloch theorem and plane-wave expansion only work in principle for truly three-dimensional crystals. Therefore, to use them efficiently for two- (e.g., surfaces, two-dimensional materials), one- (e.g., nanowires), or zero-dimensional (e.g., molecules) systems the supercell approach is usually considered. In the case of surfaces, this approach consists of replacing the semi-infinite crystal by a slab of a few atomic planes repeated along the surface normal direction. To avoid the interaction between the adjacent slabs, a sufficiently large vacuum region between them needs to be used.

The methodologies presented here are implemented in several widely employed DFT packages. The ones we have used to obtain the Thesis results are VIENNA AB INITIO SIMULATION PACKAGE (VASP) [104] and QUANTUM ESPRESSO (QE) [105].

2.3 Classical molecular dynamics

In principle, the motion of a multi-particle quantum mechanical system, for example atoms and molecules moving on surfaces, and its dissipative effects could be described fully through the time-dependent Schrödinger equation for nuclear wave-functions. However, as we discussed earlier, it is not feasible to solve computationally full quantum-dynamical equations for such large systems. Fortunately, the classical (Newtonian) molecular dynamics (MD) can be applicable in our case. In fact, when the mass of the nuclei is sufficiently large the corresponding wave packet is localized and, therefore, the classical MD is justified. This is the case for nuclei heavier than hydrogen. Nevertheless, numerous studies show that the properties of the adsorption dynamics of the hydrogen molecule are sufficiently well captured by classical MD simulations [106–108]. For example, when the kinetic energies of impinging hydrogen molecules are large, the dissociation probability provided by classical MD simulations is in a reasonable agreement with the quantum MD results [109]. The usual starting point for classical MD[5] is the following pair of equations of motion derived from Ehrenfest's theorem [110]

$$i\dot{\mathbf{R}}_\alpha = [H_i, \mathbf{R}_\alpha] = i\frac{\mathbf{P}_\alpha}{M_\alpha} \tag{2.36}$$

and

$$i\dot{\mathbf{P}}_\alpha = [H_i, \mathbf{P}_\alpha] = -i\nabla_{\mathbf{R}_\alpha} E(\mathbf{R}), \tag{2.37}$$

[5]For now on, we will refer to the classical molecular dynamics simply as "molecular dynamics", while for other cases we will explicitly write "quantum molecular dynamics".

where we write the ionic Hamiltonian as in Eq. (2.6), i.e., $H_i = T_i + E$, where T_i is the kinetic energy of ions and E is the ground-state energy of a system consisting of interacting electrons moving in the external field of ions. Another approach would be to use the Hellmann-Feynman theorem [111, 112], which states that the first derivative of the eigenvalue corresponding to the general Hamiltonian $H(\lambda)$ with respect to the parameter λ is given by

$$\nabla_\lambda E(\lambda) = \langle \Psi(\lambda)| \nabla_\lambda H(\lambda) |\Psi(\lambda)\rangle . \tag{2.38}$$

Since the ionic positions act as parameters in the electronic Hamiltonian within the BOA [Eq. (2.5)], we can apply the Hellmann-Feynman theorem with $\lambda = \mathbf{R}_\alpha$ to write the following

$$\nabla_{\mathbf{R}_\alpha} E(\mathbf{R}) = \langle \psi(\mathbf{r},\mathbf{R})| \nabla_{\mathbf{R}_\alpha} H_e |\psi(\mathbf{r},\mathbf{R})\rangle \equiv -\mathbf{F}_\alpha. \tag{2.39}$$

From this relation we express the force acting on the atom α as

$$\mathbf{F}_\alpha(t) = -\int d\mathbf{r} n(\mathbf{r},t) \nabla_{\mathbf{R}_\alpha} v_{\text{ext}}(\mathbf{r}). \tag{2.40}$$

Here the force is extended to a more general (dynamical) case, where it has an explicit time dependence. In this expression the external potential is defined as the sum of the electron-ion and ion-ion contributions, i.e., $v_{\text{ext}} = v_{ei} + v_{ii}$,[6] as in Eq. (2.2). The time-dependent electron density $n(\mathbf{r},t)$ can be divided into several contributions as

$$n(\mathbf{r},t) = n_0(\mathbf{r}) + \delta n_{\text{ad}}(\mathbf{r}) + \delta n_{\text{nonad}}(\mathbf{r},t) + \delta n_{\text{st}}(\mathbf{r},t), \tag{2.41}$$

where $n_0(\mathbf{r})$ is the unperturbed electron density, $\delta n_{\text{ad}}(\mathbf{r})$ is the static electron density (adiabatic) perturbed by the moving ion α, $\delta n_{\text{nonad}}(\mathbf{r},t)$ is dynamical (nonadiabatic) correction and $\delta n_{\text{st}}(\mathbf{r},t)$ is the stochastic part coming from charge fluctuations. Along this Thesis we will study some of these contributions (especially the nonadiabatic one) from different viewpoints and using different approaches.

2.3.1 Adiabatic equations

Keeping in mind the preceding considerations, the equations of motion for the ions can be expressed in the adiabatic approximation as

[6] Note that we reintroduced the ion-ion contribution to the external potential, which was not needed in the KS equations.

$$M_\alpha \ddot{\mathbf{R}}_\alpha = -\nabla_{\mathbf{R}_\alpha} E^{\mathrm{ad}}(\mathbf{R}). \tag{2.42}$$

In the context of molecular dynamics, $E^{\mathrm{ad}}(\mathbf{R})$ is commonly referred to as the potential energy surface (PES) or Born-Oppenheimer energy surface. Since only the adiabatic contributions to the force are considered here, $E^{\mathrm{ad}}(\mathbf{R})$ includes only the unperturbed $n_0(\mathbf{r})$ electron density and the adiabatic electron density $\delta n_{\mathrm{ad}}(\mathbf{r})$. In other words, there are no direct dynamical effects included in the forces acting on the ions, as it should be within the BOA. The system simulated by these equations corresponds to the microcanonical ensemble (NVE), where invariance with respect to changes in the number of particles, volume, and total energy is assumed.

In real experimental conditions, however, it is very unlikely that the total energy of the system will be conserved. Therefore, the canonical ensemble (NVT) would be more appropriate, since the temperature is usually easy to be kept constant in experimental set-ups. In this constant-temperature molecular dynamics the system exchanges energy with the thermostat. A NVT description of the system dynamics can be accomplished by retaining the nonadiabatic and stochastic terms in the dynamical force Eq. (2.40). The former introduces a dissipative (friction) term, while the latter a random stochastic force into Eq. (2.42). This formulation is known as the generalized Langevin dynamics [113, 114]. Another methodology for simulating the canonical ensemble was developed by Nosé and Hoover [115, 116], where the energy exchange between the system and the heat bath is modelled by a fictitious mass and a time-scaling parameter introduced in the molecular dynamics equations.

We note that Eq. (2.42) is the one used in the usual DFT molecular dynamics simulations when imposing the microcanonical ensemble [117]. We also refer to these as *ab initio* molecular dynamics (AIMD) simulations. Constant-temperature simulations are implemented in most of the DFT packages as well. However, in this Thesis we restrict ourselves to the NVE ensemble.

2.3.2 Friction coefficient: nonadiabatic correction

Up to this point, by considering Eq. (2.42), we have implied that molecular dynamics are non-dissipative since the electronic degrees of freedom are separated from the ionic ones. However, this approximation is not always valid and nonadiabatic corrections need to be taken into account whenever the energy threshold for electronic excitations is smaller than, or around the value of, the perturbation energy that is originated by the moving ions. It turns out that for metallic systems and in the dynamics of atoms and molecules that interact with metals this condition is essentially met. Therefore,

the nonadiabatic corrections for those systems should, in principle, play an important role.

Nonadiabatic corrections can be included into the equations of motion by an electronic friction term that accounts for the excitations of low-energy *e-h* pairs [18, 37, 118–121]. This term corresponds to the third dynamical contribution to the electron density in Eq. (2.41), which is included along with the first two statical contributions. In that way, the MD equations are contributed separately by the force terms originated from the adiabatic PES E^{ad} and the electronic friction $\mathcal{F}_\alpha$, respectively as

$$M_\alpha \ddot{\mathbf{R}}_\alpha = -\nabla_{\mathbf{R}_\alpha} E^{\mathrm{ad}}(\mathbf{R}) + \mathcal{F}_\alpha(t) \tag{2.43}$$

If the total induced electron density is written as $\delta n(\mathbf{r},t) = \delta n_{\mathrm{ad}}(\mathbf{r}) + \delta n_{\mathrm{nonad}}(\mathbf{r},t)$, then the electronic friction force is [118]

$$\mathcal{F}_\alpha(t) = -\int d\mathbf{r}\,[\delta n(\mathbf{r},t) - \delta n_{\mathrm{ad}}(\mathbf{r})]\,\nabla_{\mathbf{R}_\alpha} v_{\mathrm{ext}}(\mathbf{r}). \tag{2.44}$$

It is important to note here that the friction force expressed with Eq. (2.44) accounts for retardation effects, since generally the induced electron density at time t is related to all the preceding events (see the next section). When these events in the past are decoupled from the time t (i.e., the memory effects are disregarded) the friction force becomes linear in the velocity as $\mathcal{F}_\alpha(t) = -\eta\dot{\mathbf{R}}_\alpha$, where η is called the adiabatic friction coefficient. This friction coefficient accounts for the nonadiabatic effects due to the coupling of ion movements and electron gas calculated in the adiabatic limit. Due to the complexity of the induced electron density, Eq. (2.44) is not practical for MD simulations. Therefore, in the benefit of practical calculations the adiabatic friction coefficient is usually used instead. In the following, some of the existing models for obtaining explicit forms of the adiabatic friction coefficient are presented.

2.3.3 Linear response model for friction coefficients

The induced electron density due to the moving ion can be expressed within the linear response theory as follows [17, 118, 122–124]

$$\delta n(\mathbf{r},t) = \int d\mathbf{r}' \int_{-\infty}^{\infty} dt' \chi(\mathbf{r},\mathbf{r}';t-t') v_{\mathrm{ext}}\left[\mathbf{r}', \mathbf{R}(t')\right], \tag{2.45}$$

where an explicit time dependence of the ionic positions is introduced in the notation of the external potential. In that way the retardation effects can be clearly seen:

the induced electron density is correlated not only to the ion displacements in time t, but also in $t' < t$. This correlation is governed by the charge response function $\chi(\mathbf{r}, \mathbf{r}'; t - t')$. To express the friction force defined with Eq. (2.44), we also need the adiabatic induced electron density. The latter is obtained when no memory effects are included and only the displacement of the ion at the time t is considered as an external perturbation. Therefore, within the linear response theory we have

$$\begin{aligned} \delta n_{\mathrm{ad}}(\mathbf{r}, t) &= \int d\mathbf{r}' \int_{-\infty}^{\infty} dt' \chi(\mathbf{r}, \mathbf{r}'; t - t') v_{\mathrm{ext}}(\mathbf{r}', \mathbf{R}(t)) \\ &= \int d\mathbf{r}' \left[\int_{-\infty}^{\infty} \frac{d\omega}{2\pi} \chi(\mathbf{r}, \mathbf{r}', \omega) \delta(\omega) \right] v_{\mathrm{ext}} \left[\mathbf{r}', \mathbf{R}(t) \right]. \end{aligned} \tag{2.46}$$

Note that the adiabatic approximation corresponds to the static limit ($\omega = 0$) in the charge response function.

The friction force can be obtained now by introducing the total and adiabatic induced electron densities into Eq. (2.44), which results in

$$\mathcal{F}_{\alpha}(t) = - \iint d\mathbf{r} d\mathbf{r}' \nabla_{\mathbf{R}_{\alpha}} v_{\mathrm{ext}} \left[\mathbf{r}, \mathbf{R}(t) \right] \int_{-\infty}^{\infty} dt' \chi(\mathbf{r}, \mathbf{r}'; t - t') \left\{ v_{\mathrm{ext}} \left[\mathbf{r}', \mathbf{R}(t') \right] - v_{\mathrm{ext}} \left[\mathbf{r}', \mathbf{R}(t) \right] \right\} \tag{2.47}$$

This expression can be cast into a more convenient form by doing the partial time integration and defining a propagator $\Phi(\mathbf{r}, \mathbf{r}'; t - t')$ as

$$\chi(\mathbf{r}, \mathbf{r}'; t - t') \equiv \frac{\partial}{\partial t'} \Phi(\mathbf{r}, \mathbf{r}'; t - t'). \tag{2.48}$$

The friction force is then (in analogy to the friction term from the generalized Langevin equations [113, 125])

$$\mathcal{F}_{\alpha}(t) = - \int_{-\infty}^{\infty} dt' \eta(t - t') \dot{\mathbf{R}}_{\alpha}(t'), \tag{2.49}$$

where the fully nonadiabatic friction coefficient within linear response is defined as

$$\eta(t - t') \equiv - \iint d\mathbf{r} d\mathbf{r}' \nabla_{\mathbf{R}_{\alpha}} v_{\mathrm{ext}} \left[\mathbf{r}, \mathbf{R}(t) \right] \Phi(\mathbf{r}, \mathbf{r}'; t - t') \nabla_{\mathbf{R}_{\alpha}} v_{\mathrm{ext}} \left[\mathbf{r}', \mathbf{R}(t') \right]. \tag{2.50}$$

The adiabatic friction coefficient is obtained now by disregarding retardation effects in Eqs. (2.49) and (2.50). This makes the friction coefficient instantaneous (i.e.,

time-independent). Combining the Fourier transform and Eq. (2.48) the friction propagator $\Phi(\mathbf{r},\mathbf{r}';t-t')$ can be written as

$$\Phi(\mathbf{r},\mathbf{r}';t-t') = \int_{-\infty}^{\infty} \frac{d\omega}{2\pi} e^{-i\omega(t-t')} \left\{ \frac{i\chi(\mathbf{r},\mathbf{r}',\omega)}{\omega} \right\}. \tag{2.51}$$

Finally, the adiabatic friction coefficient can be expressed using the charge response function as[7]

$$\eta = -\iint d\mathbf{r}d\mathbf{r}' \left[\nabla_{\mathbf{R}_\alpha} v_{\text{ext}}(\mathbf{r})\right] \left[\nabla_{\mathbf{R}_\alpha} v_{\text{ext}}(\mathbf{r}')\right] \lim_{\omega\to 0} \left[\frac{\text{Im}\chi(\mathbf{r},\mathbf{r}',\omega)}{\omega}\right]. \tag{2.52}$$

We note here that $\chi(\mathbf{r},\mathbf{r}',\omega)$ is actually the fully screened charge response function, since it correlates the induced electron density with the external potential [126]. However, in order to stay within the linear response theory, the renormalization of $\chi(\mathbf{r},\mathbf{r}',\omega)$ must include only the higher orders of electron-electron and not of electron-ion interactions. The induced electron density can be obtained from the effective potential through the bare charge response function $\chi^0(\mathbf{r},\mathbf{r}';t-t')$ as

$$\delta n(\mathbf{r},t) = \int d\mathbf{r}' \int_{-\infty}^{\infty} dt' \chi^0(\mathbf{r},\mathbf{r}';t-t') v_{\text{eff}}\left[\mathbf{r}',\mathbf{R}(t')\right]. \tag{2.53}$$

In that case the adiabatic friction coefficient is [123]

$$\eta = -\iint d\mathbf{r}d\mathbf{r}' \left[\nabla_{\mathbf{R}_\alpha} v_{\text{ext}}(\mathbf{r})\right] \left[\nabla_{\mathbf{R}_\alpha} v_{\text{eff}}^{\text{ad}}(\mathbf{r}')\right] \lim_{\omega\to 0} \left[\frac{\text{Im}\chi^0(\mathbf{r},\mathbf{r}',\omega)}{\omega}\right], \tag{2.54}$$

where the adiabatic effective potential $v_{\text{eff}}^{\text{ad}}(\mathbf{r})$ does not have any explicit time or frequency dependence. This adiabatic potential is actually the usual screened potential obtained in DFT, i.e. Eq. (2.19). However, we emphasize here its adiabatic nature because in general it can also account for nonadiabatic effects through a frequency dependence [i.e., $v_{\text{eff}}^{\text{ad}}(\mathbf{r}) \to v_{\text{eff}}^{\text{nonad}}(\mathbf{r},\omega)$]. If the bare charge correlation function for a crystal system is expressed using single-electron wavefunctions [e.g., Eq. (2.30)] as

$$\chi^0(\mathbf{r},\mathbf{r}',\omega) = \sum_{\mu\mu',\mathbf{k}\mathbf{k}'} \phi^*_{\mu\mathbf{k}}(\mathbf{r})\phi_{\mu'\mathbf{k}'}(\mathbf{r})\phi_{\mu\mathbf{k}}(\mathbf{r}')\phi^*_{\mu'\mathbf{k}'}(\mathbf{r}') \frac{f_{\mu\mathbf{k}} - f_{\mu'\mathbf{k}'}}{\omega + \varepsilon_{\mu\mathbf{k}} - \varepsilon_{\mu'\mathbf{k}'} + i0^+}, \tag{2.55}$$

[7] We take here the imaginary part of $\chi(\mathbf{r},\mathbf{r}',\omega)$ since the friction coefficient is real. This can be obtained directly if the correlation function of the stochastic forces is evaluated and connected to the friction coefficient by using the fluctuation-dissipation theorem.

then the adiabatic friction coefficient becomes [118, 127]

$$\eta = \sum_{\mu\mu',\mathbf{k}\mathbf{k}'} \langle\phi_{\mu\mathbf{k}}|\nabla_{\mathbf{R}_\alpha} v_{\text{ext}}|\phi_{\mu'\mathbf{k}'}\rangle \langle\phi_{\mu'\mathbf{k}'}|\nabla_{\mathbf{R}_\alpha} v_{\text{eff}}^{\text{ad}}|\phi_{\mu\mathbf{k}}\rangle \left(-\frac{\partial f_{\mu\mathbf{k}}}{\partial \varepsilon_{\mu\mathbf{k}}}\right) \delta(\varepsilon_{\mu\mathbf{k}} - \varepsilon_{\mu'\mathbf{k}'}) \quad (2.56)$$

When only the crystal ions are considered within the molecular dynamics and friction coefficient calculations, then both the external and the effective potentials are periodic functions. Thus, the crystal periodicity can be applied on the $\mathbf{r}$ and $\mathbf{r}'$ integrals in Eq. (2.56). In that case, the wavevectors $\mathbf{k}$ and $\mathbf{k}'$ are related as $\mathbf{k}' - \mathbf{k} = \mathbf{q} + \mathbf{G}$, where $\mathbf{q}$ is the wavevector of the phonon mode produced by the periodic movement of the ions. The friction coefficient is then a function of this wavevector, i.e. $\eta(\mathbf{q})$, and it quantifies the electron-phonon coupling. For example, $\eta(\mathbf{q})/M$, where M is the reduced mass of the phonon mode, corresponds to the phonon linewidth, i.e., the rate at which the phonon mode is relaxed [128]. This case is analysed further in Secs. 2.4 and 4.2.

However, for the case of a single impurity moving in an otherwise periodic system, like a solid or surface, the situation is different [118, 127]. The external potential is then replaced with the impurity potential v_{imp} describing the interactions between the impurity and the electrons as well as with the other ions. Correspondingly, the adiabatic effective potential is then extended with this impurity potential. Clearly, with this inclusion of v_{imp} the periodicity in Eqs. (2.52) and (2.56) is broken, and thus the wavevectors $\mathbf{k}$ and $\mathbf{k}'$ are no longer related by $\mathbf{q}$.

Thus, when studying these two different problems using the usual DFT packages for treating periodic systems, the matrix elements in Eq. (2.56) need to be treated with great care, since the effective potential always contains the crystal periodicity because the impurity is periodically replicated by the need to use the supercell approach to account for it. In the next subsection we present a more convenient model to account for the low-energy electronic excitations induced by a mobile impurity within AIMD simulations.

2.3.4 Phase-shift model for friction coefficients

The linear response theory accounts only for the terms in the induced electron density which are linear in the external perturbation v_{ext} as in Eq. (2.45). This means that the charge response function χ does not include any v_{ext} contributions [17, 118, 122, 127] (i.e., the renormalization of χ is only due to electron-electron interactions). This result would be improved by considering also the higher order terms of v_{ext} in the

charge response function χ. Here we summarize the corresponding results for the case of a single impurity moving in a solid or on a surface [17, 122].

The electronic friction force acting on the single impurity is

$$\mathcal{F}_{\rm imp}(t) = -\int d\mathbf{r}\,[\delta n(\mathbf{r},t) - \delta n_{\rm ad}(\mathbf{r})]\,\nabla_{\mathbf{R}_{\rm imp}} v_{\rm imp}(\mathbf{r}), \tag{2.57}$$

where we write the explicit form of the impurity potential as $v_{\rm imp}(\mathbf{r}) = Z_{\rm imp}/\left|\mathbf{r}-\mathbf{R}_{\rm imp}\right|$, with $Z_{\rm imp}$ and $\mathbf{R}_{\rm imp}$ being the atomic number and the position of the impurity, respectively. The induced electron density can be written as an expansion in powers of the impurity potential $v_{\rm imp}$ [122]. The first term is linear in $v_{\rm imp}$ and corresponds to Eq. (2.45), where $v_{\rm ext}$ is replaced by $v_{\rm imp}$ and the screened charge response function χ is replaced with the bare one χ^0. In Fig. 2.1(a) this term is schematically represented with the first diagram if the electron and hole propagators are connected. After summation of all the diagrams up to infinity (i.e., beyond linear response) and in combination with Eq. (2.57), the following expression for the friction coefficient is obtained [129]

$$\eta = 2\pi \sum_{\mathbf{k}\mathbf{k}'} \delta(\varepsilon_{\mathbf{k}})\delta(\varepsilon_{\mathbf{k}'})\left|T_{\mathbf{k}\mathbf{k}'}\right|^2 (\mathbf{k}-\mathbf{k}')^2\,. \tag{2.58}$$

The T-matrix element for scattering of electrons from $\mathbf{k}$ to $\mathbf{k}'$ is defined as

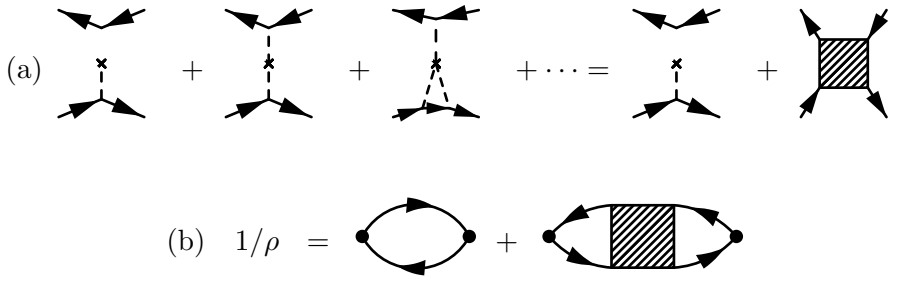

FIGURE 2.1: (a) Diagrammatic expansion representing the scattering of e-h pairs on a single impurity. Right- and left-pointing arrows represent electron and hole propagators (Green's functions), respectively. The impurity is denoted by a cross, while the interaction between the impurity and the electron (or hole), $v_{\rm imp}$, by a dashed line. The contributions that connect electron and hole propagators are called vertex corrections. (b) Diagrammatic representation of the inverse resistivity (conductivity) due to electron-impurity scattering. The dots represent the electron velocity matrix elements. In both figures the shaded rectangle is the abbreviation for all the relevant electron scattering events on the single impurity.

$$T_{\mathbf{k}\mathbf{k}'} = \int d\mathbf{r}\phi^*_{\mathbf{k}'}(\mathbf{r})v_{\rm imp}(\mathbf{r})\psi_{\mathbf{k}}(\mathbf{r}), \tag{2.59}$$

where the incoming single-electron wavefunctions $\phi_{\mathbf{k}'}(\mathbf{r})$ are approximated with plane waves, while the outgoing ones $\psi_{\mathbf{k}}(\mathbf{r})$ are perturbed by the impurity potential $v_{\rm imp}(\mathbf{r})$. We point here that an analogous formula can be obtained for the resistivity of electrons ρ due to impurity scattering in a FEG [129]. This calculation is equivalent to the summation of the diagrams of Fig. 2.1(b), which are related to the diagrams used for obtaining Eq. (2.58) [see Fig. 2.1(a)]. The final result in terms of the friction coefficient is $\rho = \eta/n_0^2$, where n_0 is the FEG electron density. This connection is reminiscent of Newton's third law: the intensity of the forces that slow down the impurity in the electron gas is equal and opposite to the forces that slow down the corresponding electron currents [118]. This result is very useful since it connects the problem of moving impurities in solids with the problem of electron transport. Therefore, the conclusions derived in the former formalism can be very easily transferred into the latter.

The T-matrix within the friction coefficient can be transformed into a phase-shift representation when the impurity potential has spherical symmetry. In that case, the final expression for the friction coefficient is [17, 37, 118, 121]

$$\eta = \frac{4\pi n_0}{k_F}\sum_{l=0}^{\infty}(l+1)\sin^2\left[\delta_l(k_F) - \delta_{l+1}(k_F)\right], \tag{2.60}$$

where $k_F = (3\pi^2 n_0)^{1/3}$ is the Fermi wavevector and $\delta_l(k_F)$ are the scattering phase shifts at the Fermi level of the lth partial wave. The same phase-shift formula for friction coefficient was also derived by Schönhammer in Refs. [130, 131], where the time-dependent Schrödinger equation is solved for the moving impurity in a HEG by using Galilean transformations. This formula has been proven to be very successful in describing the stopping power of atoms and ions in solids [18, 121, 132, 133].

In this Thesis we use the phase-shift model for the friction coefficient $\eta(\mathbf{r})$ in the context of molecular dynamics simulations of gas-surface interactions. The phase shifts are obtained from the scattering impurity potential calculated for an impurity embedded in the FEG using DFT [134]. Using the local density friction approximation (LDFA) the FEG electron density n_0 is replaced with the electron density $n(\mathbf{r})$ of the bare surface calculated within DFT, so that the impurity would be experiencing the same friction coefficient as if it were moving in a homogeneous FEG of density $n(\mathbf{r})$ [34]. This approximation is considered to be a good combination of accuracy and simplicity in investigation of the gas-surface dynamics. In Ref. [33] this methodology is extended to the case of AIMD and it is called AIMD with electronic friction

(AIMDEF). One major outcome of this Thesis deals with improvements in the latter methodology related to the electron density $n(\mathbf{r})$ of the bare surface. More details on AIMDEF and its further improvements are given in Secs. 3.3 and 3.3.1, respectively.

2.4 Electron-phonon interaction

We often deal with ordered layers of molecules adsorbed on metal surfaces. The nonadiabatic effects in this type of systems could be investigated by means of the molecular dynamics with electronic friction methodology addressed in the previous section. In this section we present another well established methodology that uses second quantization and treats atomic movements like phonons, taking advantage of the periodic nature of the atomic displacements in a crystal surface. Within this theory the electron-phonon coupling term is constructed and treated as a perturbation to obtain the phonon frequencies and the corresponding phonon linewidths [6, 8, 56, 135].

The usual starting point for obtaining the phonon properties within the DFT is the Hellmann-Feynman theorem [Eq. (2.40)]. Here we write more specifically the ionic position as

$$\mathbf{R}_\alpha = \mathbf{R}_l^0 + \boldsymbol{\tau}_s + \mathbf{u}_\alpha(t), \tag{2.61}$$

where $\mathbf{R}_l^0$ is the position of the lth unit cell, $\boldsymbol{\tau}_s$ is the equilibrium position of the sth ion in the unit cell, and $\mathbf{u}_\alpha(t)$ denotes the corresponding small time-dependent displacement from the equilibrium coordinates. The total position of the ion is labelled with $\alpha = \{l, s\}$. The second derivative of the energy, also called force-constant matrix element, is given by

$$C_{\alpha\beta}^{ij}(\mathbf{R}^0; t - t') = -\frac{\partial F_\alpha^i(t)}{\partial u_\beta^j(t')} = \frac{\partial^2 E}{\partial u_\alpha^i(t) \partial u_\beta^j(t')} \tag{2.62}$$

Here the other ion is labelled with $\beta = \{m, r\}$, indices i and j represent Cartesian coordinates, and $\mathbf{R}^0 \equiv \mathbf{R}_l^0 - \mathbf{R}_m^0$. The Fourier transform of Eq. (2.62) into the $(\mathbf{q}, \omega)$ space is

$$C_{\alpha\beta}^{ij}(\mathbf{q}, \omega) = \int dt \sum_{\mathbf{R}^0} e^{i(\omega t - \mathbf{q}\cdot\mathbf{R}^0)} C_{\alpha\beta}^{ij}(\mathbf{R}^0; t), \tag{2.63}$$

where $\mathbf{q}$ and ω are the phonon wavevector and frequency, respectively. Using the real and imaginary parts of this complex quantity, the phonon frequencies and linewidths, respectively can be obtained. For the former the self-consistent eigenvalue problem [135, 136]

$$\det \left| \frac{\mathrm{Re}\left\{C^{ij}_{\alpha\beta}(\mathbf{q},\omega_{\mathbf{q}\lambda})\right\}}{\sqrt{M_\alpha M_\beta}} - \omega^2_{\mathbf{q}\lambda} \right| = 0 \tag{2.64}$$

must be solved. The atomic masses of the α and β ions are denoted by $M_{\alpha,\beta}$. In addition to the frequencies $\omega_{\mathbf{q}\lambda}$ obtained for each phonon wavevector $\mathbf{q}$ and mode λ, this equation gives the phonon eigenvectors $\epsilon^{\alpha,i}_{\mathbf{q}\lambda}$. The phonon linewidth is then defined as [136]

$$\gamma_{\mathbf{q}\lambda} = 2 \sum_{\alpha\beta,ij} \epsilon^{\alpha,i}_{\mathbf{q}\lambda} \frac{\mathrm{Im}\left\{C^{ij}_{\alpha\beta}(\mathbf{q},\omega_{\mathbf{q}\lambda})\right\}}{\omega_{\mathbf{q}\lambda}\sqrt{M_\alpha M_\beta}} \epsilon^{\beta,j}_{\mathbf{q}\lambda}. \tag{2.65}$$

Note here that, if the force constant is calculated within the static limit [i.e., if $\omega = 0$ or if the time dependence is disregarded in Eq. (2.62)], then the obtained frequencies are adiabatic and the corresponding phonon linewidths are zero. Otherwise, the phonon frequencies are nonadiabatic and the linewidths can be finite.

2.4.1 Phonons from linear response theory

We rewrite the Hellmann-Feynman theorem in terms of small displacements $\mathbf{u}_\alpha$ and consider only the adiabatic contributions, since this restriction is present in the contemporary DFT simulation packages,

$$\mathbf{F}_\alpha = -\int d\mathbf{r} n(\mathbf{r}) \frac{\partial v_{\mathrm{ext}}(\mathbf{r})}{\partial \mathbf{u}_\alpha}. \tag{2.66}$$

The force-constant matrix elements are given by the following expression

$$\mathbf{C}_{\alpha\beta} = \int d\mathbf{r} \frac{\partial n(\mathbf{r})}{\partial \mathbf{u}_\beta} \frac{\partial v_{\mathrm{ext}}(\mathbf{r})}{\partial \mathbf{u}_\alpha} + \int d\mathbf{r} n(\mathbf{r}) \frac{\partial^2 v_{\mathrm{ext}}(\mathbf{r})}{\partial \mathbf{u}_\alpha \partial \mathbf{u}_\beta}. \tag{2.67}$$

We remind here that the external potential is the sum of the electron-ion and ion-ion potentials. Therefore, to make a clear distinction between the different contributions we can also write the force constant-matrix as

$$\mathbf{C}_{\alpha\beta} = \int d\mathbf{r} \frac{\partial n(\mathbf{r})}{\partial \mathbf{u}_\beta} \frac{\partial v_{\mathrm{ei}}(\mathbf{r})}{\partial \mathbf{u}_\alpha} + \int d\mathbf{r} n(\mathbf{r}) \frac{\partial^2 v_{\mathrm{ei}}(\mathbf{r})}{\partial \mathbf{u}_\alpha \partial \mathbf{u}_\beta} + \frac{\partial^2 v_{\mathrm{ii}}}{\partial \mathbf{u}_\alpha \partial \mathbf{u}_\beta}. \tag{2.68}$$

From the last equation it can be clearly seen that the phonon spectrum is governed by the electronic properties, namely, the electron density $n(\mathbf{r})$ and its first derivative with respect to small ion displacements $\frac{\partial n(\mathbf{r})}{\partial \mathbf{u}_\beta}$. The former can be easily obtained from DFT calculations, while for the latter the linear response approach can be adopted. The form of the induced adiabatic electron density[8] within the linear response was already discussed in the previous section [see Eq. (2.46)]. Its derivative with respect to the displacements is[9]

$$\frac{\partial n(\mathbf{r})}{\partial \mathbf{u}_\beta} = \int d\mathbf{r}' \chi(\mathbf{r}, \mathbf{r}', 0) \frac{\partial v_{\mathrm{ei}}(\mathbf{r}')}{\partial \mathbf{u}_\beta}. \tag{2.69}$$

Using Eq. (2.69) in Eq. (2.68) leads to the force-constant matrix within the linear response theory [137]. The final result is [135, 136, 138]

$$\mathbf{C}_{\alpha\beta} = \iint d\mathbf{r} d\mathbf{r}' \frac{\partial v_{\mathrm{ei}}(\mathbf{r}')}{\partial \mathbf{u}_\beta} \chi(\mathbf{r}, \mathbf{r}', 0) \frac{\partial v_{\mathrm{ei}}(\mathbf{r})}{\partial \mathbf{u}_\alpha} + \int d\mathbf{r} n(\mathbf{r}) \frac{\partial^2 v_{\mathrm{ei}}(\mathbf{r})}{\partial \mathbf{u}_\alpha \partial \mathbf{u}_\beta} + \frac{\partial^2 v_{\mathrm{ii}}}{\partial \mathbf{u}_\alpha \partial \mathbf{u}_\beta}, \tag{2.70}$$

where it is assumed that derivatives are taken at equilibrium positions. Although this methodology can produce very accurate adiabatic phonon properties, it has however some practical limitations [136]. The reason is that the Eq. (2.70) needs to be calculated self-consistently and the charge response function alone is already computationally demanding, since it includes a summation over unoccupied states. In the following we present a perturbation theory that overcomes this problem.

2.4.2 Density functional perturbation theory

The main advantage of the density functional perturbation theory (DFPT) over the linear response approach is that it allows to obtain the phonon spectrum entirely by expressing the induced electron density needed for the force-constant matrix through the occupied states only [135, 139]. The first step in the DFPT is to linearise (up to the first-order) the KS equations [Eq. (2.18)], the effective potential [Eq. (2.19)] and the electron density [Eq. (2.35)] using the following formula

[8] Note that the index "ad" from the induced adiabatic electron density notation is dropped here for simplicity.

[9] When the ω dependence is introduced in χ, a complex force-constant is obtained as in Eqs. (2.63)-(2.65).

$$\Delta K = \sum_{\beta} \frac{\partial K}{\partial \lambda_\beta} \Delta\lambda_\beta, \tag{2.71}$$

where K stands for any of the above mentioned physical quantities. To obtain the force-constant matrix these physical quantities need to be linearised with respect to the ionic displacements, i.e., $\lambda_\beta = \mathbf{u}_\beta$. The perturbed electron density can be written as

$$\Delta n(\mathbf{r}) = 2\mathrm{Re} \sum_{\mu,\mathbf{k}\in 1\mathrm{BZ}} f_{\mu\mathbf{k}} \phi^*_{\mu\mathbf{k}}(\mathbf{r}) \Delta\phi_{\mu\mathbf{k}}(\mathbf{r}). \tag{2.72}$$

Correspondingly, the first-order perturbation in KS wavefunctions results in

$$\left[-\frac{1}{2}\nabla^2 + v_{\mathrm{eff}}(\mathbf{r}) - \varepsilon_{\mu\mathbf{k}}\right] \Delta\phi_{\mu\mathbf{k}}(\mathbf{r}) = -\left[\Delta v_{\mathrm{eff}}(\mathbf{r}) - \Delta\varepsilon_{\mu\mathbf{k}}\right] \phi_{\mu\mathbf{k}}(\mathbf{r}), \tag{2.73}$$

where the first-order correction to the effective potential is

$$\Delta v_{\mathrm{eff}}(\mathbf{r}) = \Delta v_{\mathrm{ext}}(\mathbf{r}) + \int d\mathbf{r}' \frac{\Delta n(\mathbf{r}')}{|\mathbf{r} - \mathbf{r}'|} + \left.\frac{\delta v_{xc}[n]}{\delta n}\right|_{n=n(\mathbf{r})} \Delta n(\mathbf{r}), \tag{2.74}$$

and $\Delta\varepsilon_{\mu\mathbf{k}} = \langle\phi_{\mu\mathbf{k}}| \Delta v_{\mathrm{eff}} |\phi_{\mu\mathbf{k}}\rangle$. These form the self-consistent set of equations for the perturbed system analogous to the KS equations. They are also known as Sternheimer equations and could be used for calculating the atomic polarizabilities [140, 141]. Even though they evaluate perturbed quantities, the computational cost of the self-consistent procedure is of the same order as for the ground state KS equations, since Eq. (2.72) requires summations over occupied states only. Therefore, the DFPT is preferable to the linear response method when it comes to the computational cost and its reliability has been proved for a large number of systems [135].

In this Thesis we use the DFPT for calculating the vibrational spectra and to evaluate nonadiabatic effects of adsorbates on surfaces (see Sec. 4.3).

2.4.3 Beyond the adiabatic approximation

The adiabatic phonon spectra obtained from any of the two methods presented above should be interpreted under the assumption that the electron and phonon degrees of freedom are separated in a such way that there are no dynamical effects coming from the electron-phonon interaction. For some cases of semi-conductors and insulators, where the electronic energy gap is larger than the phonon frequencies, this assumption

is valid, but it cannot be true for metallic systems where the gap is zero [6, 12, 138, 142]. We have shown above several times that the adiabatic approximation corresponds to the static case, where no memory of the previous ionic movements is kept (i.e., the charge response function χ and the force-constant matrix $\mathbf{C}_{\alpha\beta}$ are evaluated for $\omega = 0$). It is obvious then that the nonadiabatic effects are dynamical and include retardation effects (i.e., χ and $\mathbf{C}_{\alpha\beta}$ are dependent on ω). In this and the following subsections we use these facts to separate the two mentioned contributions and to carefully evaluate nonadiabatic effects in an electron-phonon system. To reach this goal, the usual first step is to expand the effective potential in terms of small displacements up to the first order [8, 56, 135], in a similar manner as in Eqs. (2.71) and (2.74). Then we have

$$v_{\text{eff}}(\mathbf{r}) = v^0_{\text{eff}}(\mathbf{r}) + \sum_{l,s,i} \frac{\partial v_{\text{eff}}(\mathbf{r})}{\partial u^i_{l,s}} \Delta u^i_{l,s}. \tag{2.75}$$

By considering small displacements and introducing second quantization operators, the displacement $\Delta u^i_{l,s}$ can be written as an operator in terms of a linear combination of phonon creation $b^\dagger_{-\mathbf{q}\lambda}$ and annihilation $b_{\mathbf{q}\lambda}$ operators

$$\Delta u^i_{l,s} = \sum_{\lambda,\mathbf{q}\in 1\text{BZ}} \frac{\epsilon^i_{\mathbf{q}\lambda} e^{i\mathbf{q}\cdot\mathbf{R}_l}}{\sqrt{2M_s N\omega_{\mathbf{q}\lambda}}} \left(b_{\mathbf{q}\lambda} + b^\dagger_{-\mathbf{q}\lambda}\right), \tag{2.76}$$

where N is the number of unit cells. Using the standard prescription for obtaining the second quantization form of the Hamiltonian operator, we arrive at the following expression for the electron-phonon interaction Hamiltonian [56]

$$H_{ep} = \sum_{\mu\mu',\lambda} \sum_{\mathbf{k},\mathbf{q}\in 1\text{BZ}} g^{\mu\mu'}_\lambda(\mathbf{k},\mathbf{q}) c^\dagger_{\mu'\mathbf{k}+\mathbf{q}} c_{\mu\mathbf{k}} \left(b_{\mathbf{q}\lambda} + b^\dagger_{-\mathbf{q}\lambda}\right), \tag{2.77}$$

where $c^\dagger_{\mu'\mathbf{k}+\mathbf{q}}$ and $c_{\mu\mathbf{k}}$ are electron creation and annihilation operators, respectively, and the intensity of the electron-phonon coupling is given by the following matrix elements

$$g^{\mu\mu'}_\lambda(\mathbf{k},\mathbf{q}) = \sum_{l,s} \frac{e^{i\mathbf{q}\cdot\mathbf{R}_l}}{\sqrt{2M_s N\omega_{\mathbf{q}\lambda}}} \langle\phi_{\mu'\mathbf{k}+\mathbf{q}}| \sum_i \frac{\partial v_{\text{eff}}(\mathbf{r})}{\partial u^i_{l,s}} \epsilon^i_{\mathbf{q}\lambda} |\phi_{\mu\mathbf{k}}\rangle . \tag{2.78}$$

The Hamiltonian of Eq. (2.77) describes the creation (annihilation) of a phonon mode that at the same time annihilates (creates) an e-h pair. This is commonly known as the Fröhlich Hamiltonian and it is the usual starting point for calculating the electron-phonon properties of a many-body system (e.g., phonon frequencies and

linewidths, electron energy corrections due to electron-phonon coupling, corresponding temperature dependence, specific heats, etc. [8]).

There is another approach to obtain the electron-phonon Hamiltonian in which, instead of expanding the electronic Hamiltonian in Eq. (2.5) with respect to small displacements, the nonadiabatic operator $\mathcal{A}$ of Eq. (2.7) of the ionic Hamiltonian is considered [54, 55]. The operator $\mathcal{B}$ defined in Eq. (2.8) is not considered here because it does not contribute to the creation or annihilation of a phonon mode, since it is diagonal in the phonon representation. To reach the second quantization form of the operator $\mathcal{A}$ we need to use the off-diagonal Hellmann-Feynman theorem [143],

$$\langle \phi_{\mu\mathbf{k}} | \nabla^i_{l,s} | \phi_{\mu'\mathbf{k}'} \rangle = -\frac{\langle \phi_{\mu\mathbf{k}} | \frac{\partial v_{\text{eff}}(\mathbf{r})}{\partial u^i_{l,s}} | \phi_{\mu'\mathbf{k}'} \rangle}{\varepsilon_{\mu\mathbf{k}} - \varepsilon_{\mu'\mathbf{k}'}}, \tag{2.79}$$

as well as the relationship between the ion momentum operator, and the phonon creation and annihilation operators

$$\nabla^i_{l,s} = \sum_{\lambda,\mathbf{q}\in 1\text{BZ}} M_s \omega_{\mathbf{q}\lambda} \frac{\epsilon^i_{\mathbf{q}\lambda} e^{i\mathbf{q}\cdot\mathbf{R}_l}}{\sqrt{2M_s N \omega_{\mathbf{q}\lambda}}} \left(b_{-\mathbf{q}\lambda} - b^\dagger_{\mathbf{q}\lambda} \right). \tag{2.80}$$

Finally, by introducing Eqs. (2.79) and (2.80) into (2.7) we get

$$\widetilde{H}_{ep} = \sum_{\mu\mu',\lambda} \sum_{\mathbf{k},\mathbf{q}\in 1\text{BZ}} \frac{-\omega_{\mathbf{q}\lambda}}{\varepsilon_{\mu\mathbf{k}} - \varepsilon_{\mu'\mathbf{k}+\mathbf{q}}} g^{\mu'\mu}_\lambda(\mathbf{q},\mathbf{k}) c^\dagger_{\mu\mathbf{k}} c_{\mu'\mathbf{k}+\mathbf{q}} \left(b_{-\mathbf{q}\lambda} - b^\dagger_{\mathbf{q}\lambda} \right). \tag{2.81}$$

Many textbooks use the operator $\mathcal{A}$ to obtain the Fröhlich Hamiltonian H_{ep} [56]. To do so, one needs to consider that the annihilation and creation of the phonon mode conserve the energy as $\pm\omega_{\mathbf{q}\lambda} = \varepsilon_{\mu'\mathbf{k}+\mathbf{q}} - \varepsilon_{\mu\mathbf{k}}$. However, this is only true for real excitations and not in the case of virtual excitations, which are responsible for the phonon frequency renormalization. Another situation where this conservation law does not hold is when higher-order electron scattering processes are accounted (e.g., electron-electron, electron-impurity or electron-phonon scattering). Thus, in general we have that H_{ep} and $\widetilde{H}_{ep}$ are not equal. In fact, from the prefactor $\omega_{\mathbf{q}\lambda}/(\varepsilon_{\mu'\mathbf{k}+\mathbf{q}} - \varepsilon_{\mu\mathbf{k}})$ in Eq. (2.81) it is clear that $\widetilde{H}_{ep}$ accounts only for the pure nonadiabatic effects and that it is zero when the adiabatic approximation is included (i.e., if the phonon frequency is much smaller than the electron excitations, $\omega_{\mathbf{q}\lambda} \ll |\varepsilon_{\mu'\mathbf{k}+\mathbf{q}} - \varepsilon_{\mu\mathbf{k}}|$, then $\widetilde{H}_{ep} \to 0$). This is not the case when the perturbation theory is done with the Fröhlich Hamiltonian H_{ep}, where for $\omega = 0$ we get the adiabatic approximation, while for $\omega \neq 0$ we account for nonadiabatic effects.

In chapter 4 we consider both Hamiltonians for calculating the phonon linewidths and frequency renormalizations, and we discuss which one is better to be used within the DFPT approach.

2.4.4 Phonon and electron self-energies: Migdal's theory

In the above considerations we have seen to some extent how the coupling of electrons and ionic movements (or phonons) affects the phonon spectrum. However, to get a complete picture it is necessary to consider also the effects of the electron-phonon interaction on the electronic structure (i.e., shift and broadening of the electronic bands). In other words, the electron-phonon interaction affects both the lattice dynamics and the electronic structure, and these corrections in turn modify the electron-phonon interaction. Obviously, the problem should be treated self-consistently. In the many-body perturbation theory, this self-consistent problem is accounted for by the connected Dyson equations for the electron $G_\mu(\mathbf{k}, i\omega_n)$ and the phonon $D_\lambda(\mathbf{q}, i\nu_n)$ propagators as [3, 8, 129, 144]

$$G_\mu(\mathbf{k}, i\omega_n) = G^0_\mu(\mathbf{k}, i\omega_n) + G^0_\mu(\mathbf{k}, i\omega_n)\Sigma_\mu(\mathbf{k}, i\omega_n)G_\mu(\mathbf{k}, i\omega_n) \tag{2.82}$$

and

$$D_\lambda(\mathbf{q}, i\nu_n) = D^0_\lambda(\mathbf{q}, i\nu_n) + D^0_\lambda(\mathbf{q}, i\nu_n)\Pi_\lambda(\mathbf{q}, i\nu_n)D_\lambda(\mathbf{q}, i\nu_n). \tag{2.83}$$

Here the superscript "0" denotes the bare propagators, $\Sigma_\mu(\mathbf{k}, i\omega_n)$ is the electron self-energy, and $\Pi_\lambda(\mathbf{q}, i\nu_n)$ is the phonon self-energy. In systems where the harmonic approximation does not hold, phonon-phonon coupling effects (anharmonicity) should also be taken into account along with the electron-phonon effects, i.e., $\Pi_\lambda = \Pi^{\mathrm{el-ph}}_\lambda + \Pi^{\mathrm{ph-ph}}_\lambda$. However, in our present work we restrict ourselves to the electron-phonon coupling. These Dyson equations are written in the Matsubara notation, thus the imaginary fermion $i\omega_n$ and boson $i\nu_n$ frequencies need to be analytically continued to obtain the final expressions (i.e., $i\omega_n \to \varepsilon + i\eta$ and $i\nu_n \to \omega + i\eta$). The corresponding diagrammatic representation of the above equations is presented in Fig. 2.2. This figure shows how the phonon propagator $D_\lambda(\mathbf{q}, i\nu_n)$ depends on $G_\mu(\mathbf{k}, i\omega_n)$ and vice versa.

By using the definitions of the bare electron and phonon propagators,

$$G^0_\mu(\mathbf{k}, i\omega_n) = \frac{1}{i\omega_n - \varepsilon_{\mu\mathbf{k}}} \tag{2.84}$$

and

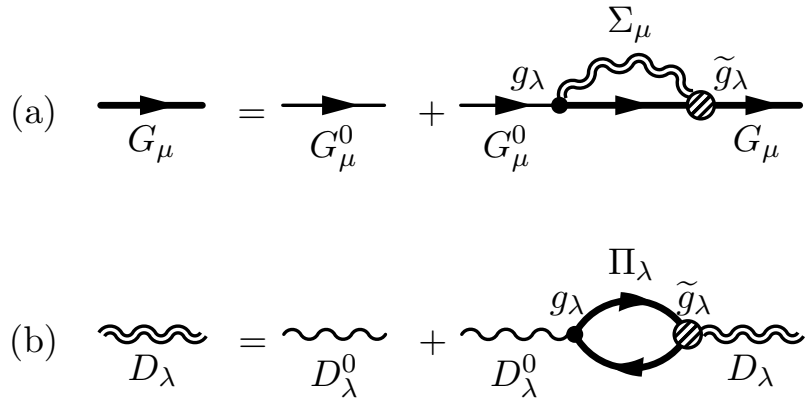

FIGURE 2.2: Diagrammatic representation of the Dyson equation for (a) the electron and the (b) phonon propagators. The thick straight (wavy) lines correspond to the exact electron G (phonon D) propagator, while the thin straight (wavy) lines to the bare G^0 (D^0). The bare and dressed electron-phonon vertex functions are labelled g_λ and $\widetilde{g}_\lambda$, respectively.

$$D^0_\lambda(\mathbf{q}, i\nu_n) = \frac{2\omega_{\mathbf{q}\lambda}}{(i\nu_n)^2 - \omega^2_{\mathbf{q}\lambda}}, \tag{2.85}$$

respectively, the above Dyson equations can be written as

$$G_\mu(\mathbf{k}, i\omega_n) = \frac{1}{i\omega_n - \varepsilon_{\mu\mathbf{k}} - \Sigma_\mu(\mathbf{k}, i\omega_n)} \tag{2.86}$$

and

$$D_\lambda(\mathbf{q}, i\nu_n) = \frac{2\omega_{\mathbf{q}\lambda}}{(i\nu_n)^2 - \omega^2_{\mathbf{q}\lambda} - 2\omega_{\mathbf{q}\lambda}\Pi_\lambda(\mathbf{q}, i\nu_n)}, \tag{2.87}$$

respectively. The physical meaning of $G_\mu(\mathbf{k}, i\omega_n)$ and $D_\lambda(\mathbf{q}, i\nu_n)$ is understood when their imaginary parts are considered. The imaginary part of $G_\mu(\mathbf{k}, i\omega_n)$ gives the spectrum of the electron excitations [measurable by, e.g., angle-resolved photoemision spectroscopy (ARPES) experiments], while the imaginary part of $D_\lambda(\mathbf{q}, i\nu_n)$ gives the phonon spectrum (measurable by, e.g., IRAS experiments). The key quantities for obtaining these spectra are the concomitant electron and phonon self-energies. By examining their diagrammatic representations in Fig. 2.2, the exact expressions can be written in a following formal way as[10] [8, 129]

[10]Note that in this formalism H_{ep} is used for the electron-phonon Hamiltonian, and not $\widetilde{H}_{ep}$.

$$\Sigma_\mu(\mathbf{k}, i\omega_n) = \sum_{\mu'\lambda\mathbf{q}} \frac{1}{\beta} \sum_{i\nu_n} \left[g_\lambda^{\mu\mu'}(\mathbf{k},\mathbf{q})\right]^* \widetilde{g}_\lambda^{\mu\mu'}(\mathbf{k},\mathbf{q},i\omega_n,i\nu_n) D_\lambda(\mathbf{q},i\nu_n) G_{\mu'}(\mathbf{k}+\mathbf{q}, i\omega_n+i\nu_n) \tag{2.88}$$

and

$$\Pi_\lambda(\mathbf{q}, i\nu_n) = \sum_{\mu\mu'\mathbf{k}\sigma} \frac{1}{\beta} \sum_{i\omega_n} \left[g_\lambda^{\mu\mu'}(\mathbf{k},\mathbf{q})\right]^* \widetilde{g}_\lambda^{\mu\mu'}(\mathbf{k},\mathbf{q},i\omega_n,i\nu_n) G_\mu(\mathbf{k}, i\omega_n) G_{\mu'}(\mathbf{k}+\mathbf{q}, i\omega_n+i\nu_n), \tag{2.89}$$

where the summation over σ accounts for the spin degrees of freedom, the inverse of the temperature is $\beta = 1/k_B T$, and $\widetilde{g}_\lambda^{\mu\mu'}(\mathbf{k},\mathbf{q},i\omega_n,i\nu_n)$ are the dressed (renormalized) electron-phonon matrix elements due to various electron scattering processes, i.e. with vertex corrections and single-particle self-energy contributions that come from electron-electron, electron-phonon or electron-impurity scatterings. It is clear now how the value of the electron self-energy Σ_μ influences the phonon self-energy Π_λ through the electron propagator G_μ, i.e., how the electron scattering processes influence the phonon self-energy. In a first approximation, we can decouple these expressions by disregarding the renormalizations in $\widetilde{g}_\lambda^{\mu\mu'}$ and writing the bare propagators instead of the exact ones. In that way, the electron and phonon self-energies are quadratic in the electron-phonon interaction (i.e., $|g_\lambda^{\mu\mu'}|^2$). After performing the Matsubara sums and the analytical continuation they read [8, 129]

$$\Sigma_\mu(\mathbf{k},\varepsilon) = \sum_{\mu'\lambda\mathbf{q}} \left|g_\lambda^{\mu\mu'}(\mathbf{k},\mathbf{q})\right|^2 \sum_{s=\pm1} \frac{n_b(\omega_{\mathbf{q}\lambda}) - f(s\varepsilon_{\mu'\mathbf{k}+\mathbf{q}})}{\varepsilon - \varepsilon_{\mu'\mathbf{k}+\mathbf{q}} + s\omega_{\mathbf{q}\lambda} + i\eta} \tag{2.90}$$

and

$$\Pi_\lambda(\mathbf{q},\omega) = \sum_{\mu\mu'\mathbf{k}} \left|g_\lambda^{\mu\mu'}(\mathbf{k},\mathbf{q})\right|^2 \frac{f(\varepsilon_{\mu\mathbf{k}}) - f(\varepsilon_{\mu'\mathbf{k}+\mathbf{q}})}{\omega + \varepsilon_{\mu\mathbf{k}} - \varepsilon_{\mu'\mathbf{k}+\mathbf{q}} + i\eta}, \tag{2.91}$$

where η is a positive infinitesimal number. The Fermi-Dirac and Bose-Einstein distribution functions are defined as $f(\varepsilon_{\mu\mathbf{k}}) = 1/(e^{\beta(\varepsilon_{\mu\mathbf{k}}-\varepsilon_F)}+1)$[11] and $n_b(\omega_{\mathbf{q}\lambda}) = 1/(e^{\beta\omega_{\mathbf{q}\lambda}}-1)$, respectively, where ε_F is the Fermi energy. The real and imaginary parts of the self-energies are associated to the renormalisation and linewidth, respectively, of the corresponding electron or phonon band. It is also convenient to express the electron self-energy in an integral form. In order to achieve this, we use the so-called Eliashberg function defined as [129]

$$\alpha^2 F_\mu(\mathbf{k},\Omega,\varepsilon') = \sum_{\mu'\lambda\mathbf{q}} \left|g_\lambda^{\mu\mu'}(\mathbf{k},\mathbf{q})\right|^2 B_\lambda^0(\mathbf{q},\Omega) A_{\mu'}^0(\mathbf{k}+\mathbf{q},\varepsilon'), \tag{2.92}$$

[11] Note that $f(-\varepsilon_{\mu\mathbf{k}}) = 1 - f(\varepsilon_{\mu\mathbf{k}})$

where the bare phonon and electron spectral functions are defined as $B^0_\lambda(\mathbf{q},\Omega) = \mathrm{Im}D^0_\lambda(\mathbf{q},\Omega)$ (for $\Omega > 0$) and $A^0_{\mu'}(\mathbf{k}+\mathbf{q},\varepsilon') = \mathrm{Im}G^0_{\mu'}(\mathbf{k}+\mathbf{q},\varepsilon')$, respectively. Introducing Eq. (2.92) in Eq. (2.90) we get

$$\Sigma_\mu(\mathbf{k},\varepsilon) = \int_{-\infty}^{\infty} d\varepsilon' \int_0^{\infty} d\Omega\ \alpha^2F_\mu(\mathbf{k},\Omega,\varepsilon') \sum_{s=\pm1} \frac{n_b(\Omega) - f(s\varepsilon')}{\varepsilon - \varepsilon' + s\Omega + i\eta}. \tag{2.93}$$

The Eliashberg function is usually used to investigate the superconducting states due to electron-phonon coupling [9, 129, 145]. Nevertheless, since it contains information on how the phonon spectrum is affected by the electron-phonon coupling, it can be also used to extract the electron damping functions (imaginary part of Σ_μ) due to electron-phonon scattering entering the higher order terms of Π_λ. In that way the phonon self-energy is additionally damped by higher-order electron-phonon scattering processes (i.e., apart from the $|g^{\mu\mu'}_\lambda|^2$ term, Π_λ contains $|g^{\mu\mu'}_\lambda|^4$ as well as even higher-order terms.). We discuss the influence of these processes on the phonon self-energy further in Secs. 4.2.2 and 4.2.5.

Finally, within this formalism, the adiabatic ($\omega = 0$) and nonadiabatic ($\omega \neq 0$) contributions to the phonon spectra can be separated in the following simple way [8]

$$\Pi_\lambda(\mathbf{q},\omega) = \Pi^{\mathrm{A}}_\lambda(\mathbf{q}) + \Pi^{\mathrm{NA}}_\lambda(\mathbf{q},\omega), \tag{2.94}$$

where $\Pi^{\mathrm{A}}_\lambda(\mathbf{q}) \equiv \Pi_\lambda(\mathbf{q},\omega=0)$. The corresponding phonon propagators are

$$D^{\mathrm{A}}_\lambda(\mathbf{q},\omega_{\mathrm{A}}) = \frac{2\omega^0_{\mathbf{q}\lambda}}{\omega^2_{\mathrm{A}} - \left[\omega^0_{\mathbf{q}\lambda}\right]^2 - 2\omega^0_{\mathbf{q}\lambda}\Pi^{\mathrm{A}}_\lambda(\mathbf{q})} \tag{2.95}$$

for the adiabatic case and

$$D^{\mathrm{NA}}_\lambda(\mathbf{q},\omega_{\mathrm{NA}}) = \frac{2\omega_{\mathrm{A}}}{\omega^2_{\mathrm{NA}} - \omega^2_{\mathrm{A}} - 2\omega_{\mathrm{A}}\Pi^{\mathrm{NA}}_\lambda(\mathbf{q},\omega_{\mathrm{NA}})}. \tag{2.96}$$

for the nonadiabatic case. Here $\omega^0_{\mathbf{q}\lambda}$ denotes the bare phonon frequency, ω_{A} the adiabatic, and ω_{NA} the nonadiabatic one. In the DFT calculations where the phonon frequencies are obtained by means of DFPT, they consequently already correspond to the adiabatic frequencies [135]. Thus, if the phonon self-energy is calculated using these adiabatic frequencies, the appropriate form to use should be the one in Eq. (2.96). This is further discussed throughout chapter 4.

2.5 Equations of motion for the density matrix

One very useful methodology for obtaining the dynamical properties of the low-dimensional quantum system is the density matrix theory [146–151]. Within this formalism the density matrix ϱ substitutes the many-body wavefunction Ψ as the fundamental quantity from which all the physical observables can be obtained. The equations of motion for ϱ, i.e. the Liouville-von Neumann equations, are then completely analogous to the Schrödinger equations. In fact, the former can be derived from the latter. Unfortunately, the latter equations are still infeasible for high-dimensional systems. Nevertheless, when the dynamics of the studied system can be reduced to several degrees of freedom without a significant lost of accuracy in the description of the relevant physical properties, the density matrix theory can be practical [152, 153]. For example, in gas-surface dynamics when the full dimensionality of the interaction is reduced to a few spatial coordinates [154–156]. In this section we derive the equations of motion within this formalism. Specifically, starting from the fundamental Liouville-von Neumann equation we obtain the equations of motion for the state population (i.e., diagonal elements of ϱ), which is the so-called Pauli master equation.

We start with the general Hamiltonian for the perturbed system [146, 147, 151],

$$H = H_0 + \lambda H', \tag{2.97}$$

where H_0 represents the unperturbed system Hamiltonian and $\lambda H'$ is some small perturbation. The parameter λ is a dimensionless measure of the perturbation strength. For example, in chapter 5 the eigenvalues corresponding to H_0 will be the adiabatic potential energies of molecule-surface system along the reaction path obtained by the DFT calculations and $\lambda H'$ will account for the nonadiabatic effects induced by the STM tip electron current pulse. We expand the single-particle wavefunctions $\widetilde{\phi}_i(\mathbf{r}, t)$ in a complete set of time-independent functions $\phi_n(\mathbf{r})$ as follows

$$\widetilde{\phi}_i(\mathbf{r}, t) = \sum_n c_n^i(t)\phi_n(\mathbf{r}), \tag{2.98}$$

where the time dependency is fully contained in the expansion coefficients $c_n^i(t)$. In that case, the density matrix can be defined as

$$\varrho(t) = \sum_i |\Psi_i\rangle \langle\Psi_i| = \sum_i \sum_{kl} c_k^i(t) c_l^{i*}(t) |\phi_k\rangle \langle\phi_l| , \tag{2.99}$$

or in the ϕ_n representation as

$$\varrho_{nm}(t) \equiv \langle \phi_n | \, \varrho(t) \, | \phi_m \rangle = \sum_i c_n^i(t) c_m^{i*}(t). \tag{2.100}$$

The diagonal elements of density matrix ϱ_{nn} represent the population of the state n, while the off-diagonal elements ϱ_{nm}, the so-called coherences, give information on the interference between n and m states. The relaxation of the coherence terms is called *dephasing*, while the terminology *energy relaxation* is usually reserved for the diagonal terms. The time evolution of the system in this formalism is given by the Liouville-von Neumann equation, i.e.,

$$\frac{\partial \varrho}{\partial t} = i \left[H, \varrho \right] + \left(\frac{\partial \varrho}{\partial t} \right)_{\text{bath}}, \tag{2.101}$$

where the second therm on the right comes from the interaction between the system and some external bath (i.e., reservoir that exchanges energy with the system). In what follows we restrict our considerations to a closed system where this second term is neglected.

2.5.1 Pauli master equation

Now we express the aforementioned density matrix equation [Eq. (2.101)] in terms of the perturbative transition rates, which describe energy relaxation and dephasing [146, 147, 151, 154]. In order to do so, we rewrite Eq. (2.101) as

$$\frac{\partial \varrho}{\partial t} = i \left[H, \varrho \right] - \frac{\varrho - \varrho_0}{\tau}. \tag{2.102}$$

The second term introduced here represents a weak perturbation coming from the contributions not considered in the first term. For example, if the nonadiabatic effects (i.e., electron-phonon coupling) accounted for in the first term are of the first-order, this second term phenomenologically represents the higher-order processes in the electron-phonon interaction. The time-scale at which this second term drives the density matrix towards its equilibrium value ϱ_0 is denoted as τ. Eventually, when the higher-order processes are disregarded, then $\tau \to 0$. If ε_n are the eigenvalues of the ground state Hamiltonian H_0, i.e., $H_0 \, |\phi_n\rangle = \varepsilon_n \, |\phi_n\rangle$, we can express Eq. (2.102) as

$$\frac{\partial \varrho_{nm}}{\partial t} = i\varrho_{nm}\left(\varepsilon_m - \varepsilon_n + i/\tau\right) + i\sum_{k(\neq n,m)}\left[\varrho_{nk}\left\langle\phi_k\right|\lambda H'\left|\phi_m\right\rangle - \left\langle\phi_n\right|\lambda H'\left|\phi_k\right\rangle\varrho_{km}\right] + i\left\langle\phi_n\right|\lambda H'\left|\phi_m\right\rangle\left(\varrho_{nn} - \varrho_{mm}\right), \tag{2.103}$$

where we exclude the constant term ϱ_0/τ and we renormalize the energies ε_n with the diagonal terms $\langle\phi_n|\,\lambda H'\,|\phi_n\rangle$, i.e., $\varepsilon_n + \langle\phi_n|\,\lambda H'\,|\phi_n\rangle \to \varepsilon_n$. The diagonal elements of Eq. (2.103) are

$$\frac{\partial \varrho_{nn}}{\partial t} = i\sum_{k\neq n}\left[\varrho_{nk}\left\langle\phi_k\right|\lambda H'\left|\phi_n\right\rangle - \left\langle\phi_n\right|\lambda H'\left|\phi_k\right\rangle\varrho_{kn}\right]. \tag{2.104}$$

To express the above equation in terms of transition rates (i.e., Fermi's golden rule rates) it is necessary to consider the diagonal and off-diagonal parts of the density matrix equation in the lowest order in λ. If we assume that the lowest order of $\partial\varrho/\partial t$ is λ^0, then it follows from Eq. (2.104) that the off-diagonal elements ϱ_{nk} are of order λ^{-1}. From this consideration and Eq. (2.103) we get the following relation

$$\varrho_{nm} = \frac{\left\langle\phi_n\right|\lambda H'\left|\phi_m\right\rangle}{\varepsilon_n - \varepsilon_m - i/\tau}\left(\varrho_{nn} - \varrho_{mm}\right). \tag{2.105}$$

By inserting Eq. (2.105) into Eq. (2.104) we obtain the equation of motion for the state population $P_n \equiv \varrho_{nn}$

$$\frac{\partial P_n}{\partial t} = i\sum_{m\neq n}\left|\left\langle\phi_n\right|\lambda H'\left|\phi_m\right\rangle\right|^2\left(P_n - P_m\right)\left[\frac{1}{\varepsilon_n - \varepsilon_m - i/\tau} - \frac{1}{\varepsilon_n - \varepsilon_m + i/\tau}\right]. \tag{2.106}$$

The state broadening parameter τ^{-1} accounts for the additional damping of the system coming from higher-order processes. More details about the meaning of a finite τ^{-1} parameter are given in chapter 4 in the context of the phonon-self energy. Here we neglect these processes and we write $\tau^{-1} = 0$ in Eq. (2.106), which leads to the Pauli master equation where the transition rates are expressed in terms of first-order Fermi's golden rule rates. This reads

$$\frac{\partial P_n}{\partial t} = \sum_{m\neq n}\left(\Gamma_{m\to n}P_m - \Gamma_{m\to n}P_n\right), \tag{2.107}$$

where $\Gamma_{n\to m} = 2\pi \left|\langle\phi_n| \lambda H' |\phi_m\rangle\right|^2 \delta(\varepsilon_n - \varepsilon_m)$ is the first-order Fermi's golden rule rate[12].

For the cases where the dephasing time is much smaller than the energy relaxation time-scales in Eq. (2.107), the dynamical processes associated to the off-diagonal elements ϱ_{nm} can be neglected and it is safe to work with the Pauli master equation. For the problem considered in chapter 5 this condition is met and we use Eq. (2.107) to investigate the dynamical behaviour of the STM-induced reaction.

2.5.2 Anharmonic transition rates

When the perturbation Hamiltonian H' is the electron-phonon coupling and we sum over all the electronic degrees of freedom the first-order Fermi's golden rule formula contained in Eq. (2.107) can be expressed as

$$\Gamma^{(\alpha)}_{i\to j} = 2\pi \sum_{ab} \left|\langle b, j|\hat{\mathcal{A}}_\alpha|a, i\rangle\right|^2 f_a\,(1 - f_b)\,\delta\left(\varepsilon_a - \varepsilon_b + \omega_{ij}\right), \tag{2.108}$$

where we generalize the single-particle state $|\phi_n\rangle$ to the state $|a, i\rangle$, which contains electronic and vibronic degrees of freedom denoted a and i, respectively. For a given mode α, the coupling between states $|a, i\rangle$ and $|b, j\rangle$ is mediated by the associated nonadiabatic energy operator $\hat{\mathcal{A}}_\alpha$. Note that the latter operator is analogous to the non-adiabatic operator defined by Eq. (2.7). The occupancy of the electronic states at a given temperature is taken into account via the Fermi distribution functions $f_{\{a,b\}}$.

In order to see how anharmonic effects enter Eq. (2.108) we explicitly write the matrix elements $\langle b, j|\hat{\mathcal{A}}_\alpha|a, i\rangle$ as

$$\langle b, j|\hat{\mathcal{A}}_\alpha|a, i\rangle = -\frac{1}{M_\alpha}\langle b|\nabla_\alpha|a\rangle\langle j|\nabla_\alpha|i\rangle. \tag{2.109}$$

In the harmonic approximation the momentum operator ∇_α in the term that describes the perturbation of the vibronic states $\langle j|\nabla_\alpha|i\rangle$ is quantized using Eq. (2.80). In that case, the only allowed vibrational excitations are either $|i\rangle \to |i+1\rangle$ or $|i\rangle \to |i-1\rangle$. It is worth mentioning that the first-order Fermi's golden rule formula [Eq. (2.108)] is then identical to the imaginary part of the phonon self-energy defined by Eqs. (2.91). If we go beyond the harmonic approximation, i.e., if we calculate the aforementioned

[12] We explicitly use the terminology "first-order" since in deriving Eq. (2.105) we consider only matrix elements $\langle\phi_k| \lambda H' |\phi_n\rangle$ of order λ^1. In chapter 4 we use the terminology "second-order Fermi's golden rule" when these matrix elements are of order λ^2 and when H' accounts for the electron-phonon coupling.

term explicitly, various $|i\rangle \rightarrow |j\rangle$ and $|j\rangle \rightarrow |i\rangle$ transitions are possible. In chapter 5 we adopt the model that goes beyond the harmonic approximation presented in Ref. [51] in order to calculate the transition rates for the STM-driven reaction.

Chapter 3

Electron-hole pair and phonon excitations upon adsorbate relaxation: H/Pd(100), N/Ag(111) and N_2/Fe(110)

3.1 Introduction

Many are the theoretical studies confirming that the fundamental properties in most elementary gas-surface processes are satisfactorily described by the BOA [157, 158]. Common to all these studies is the use of MD simulations with a DFT-based adiabatic PES that is at least parametrized for the degrees of freedom of the gas species involved in the event. Examples are the dissociative adsorption on different metal surfaces of H_2 [159–161], N_2 [162–164], O_2 [165–167], H_2O [168–170], CO_2 [171], CH_4 [172], recombination processes occurring on covered surfaces [173–177], H_2 diffraction [178–180], and the scattering of thermal/hyperthermal atoms and molecules [181–188].

Still, the challenge in present thermal and hyperthermal gas-surface simulations is to provide a reliable description of the two energy loss channels that may affect the dynamics and reactivity of gas-phase species on solid surfaces, namely, phonon[1] and *e-h* pair excitations [26, 33, 107, 119, 189–201]. In the end, these are the mechanisms that dictate the thermalization rate and the mean traveled length of the nascent adsorbates and, consequently, the probability to undergo a recombination reaction with another adsorbate [202–207]. Even more generally, these mechanisms

[1]Note that in this chapter we use the word "phonons" often for a more general concept of lattice movements, and not for quantized collective excitations as in chapter 4.

are expected to contribute actively in any gas-surface process that involves strong and long-lasting interactions between adsorbate and surface. One valuable evidence of the importance of the *e-h* pair damping channel in adsorption dynamics comes from chemicurrent experiments, where adsorption of various atomic and molecular species on metal surfaces induces electrical currents [26, 191]. The field of femtochemistry, where chemical reactions on femtosecond timescales are induced by laser pulses, is another good example of it [208–213]. There are various theoretical studies showing that phonons and *e-h* pairs are often important ingredients in understanding a reaction mechanism [196, 214–219].

In the past, the effect of energy exchange with the lattice in gas-surface dynamics has been reasonably described by using thermostats coupled to an adiabatic PES that neglects the degrees of freedom of the individual surface atoms [164, 174, 187, 188, 198, 207, 220–223]. A usual procedure to account for this energy exchange is to adopt the generalized Langevin oscillator (GLO) model that adds dissipation and thermal fluctuations to the lattice dynamics with the help of a three-dimensional ghost oscillator in agreement with the fluctuation-dissipation theorem [220, 224–226]. The GLO can become a serious limitation when large energy exchange and long interaction times are at work, since the corresponding distortions on the surface can modify the PES. In this respect, AIMD is nowadays the state-of-the-art methodology to account for the aforementioned phonon excitations effects, since it can individually treat the surface atom movements [200, 227–232]. This DFT-based methodology (see Sec. 2.3) is the main technique used in this chapter, and will be discussed in detail below. The QM/Me model developed by Meyer *et al.* [201] has been recently proposed as an improvement over the usual AIMD method because it avoids the spurious periodic distortions that may appear in AIMD in case of using too small surface unit cells. Notably, there are also theoretical studies that include a quantum treatment of the phonon excitations [233], but in those cases the gas-surface interaction is described through simplified model potentials [234, 235].

While searching for an accurate and joint description of the electronic and phononic energy dissipation channels, the recently developed AIMDEF method [33] that is based on the LDFA [34], constitutes a promising tool to meet this goal. The theoretical background of this methodology is presented in Sec. 2.3. It was shown by means of this method that *e-h* pair excitations are the dominant relaxation mechanism for hot H atoms on Pd(100) that originate from the dissociative adsorption of H_2 [33]. More particularly, this channel dissipates energy at a five times faster rate than the phonons channel [107]. The two main reasons behind this behavior are the long H-Pd interaction time, of hundreds of fs, and the low adsorbate-to-surface atom mass ratio, $\gamma = m_H/m_{Pd} = 0.0094$. The case of H on Pd(100) represents a limiting case. For heavier adsorbates, the relative weight of *e-h* pairs and phonons in the energy

loss is expected to vary. The energy transfer to the substrate will be determined not only by kinetic factors, such as the value of γ and the incidence conditions, but also by the topography of the multidimensional PES and the electronic structure details of the configurations probed along the relaxation trajectory. The electronic friction calculation of the original AIMDEF of Ref. [33] is based on the *rigid* surface electron density, which is a reasonable approximation for the cases of low γ values, where large surface atom displacements are not expected. However, such approximation may fail in the case of large surface atoms displacements that cause non-negligible changes in the surface electron density.

In this chapter, we propose and analyze three different methods to describe the electron density within the AIMDEF to successfully overcome this limitation. Apart from the previously used *rigid* surface electron density method, we introduce two schemes that account for the surface atom movements, which are therefore applicable for the case of high γ values. Having these powerful AIMDEF approaches, we apply them to investigate a central issue in gas-surface interactions: the adsorption and relaxation of hot gas species on metal surfaces. More precisely, we investigate three different adsorption scenarios that cover a representative range of adsorption energies E_{ads} and γ values. Specifically, we investigate dissociated H_2 on Pd(100), N on Ag(111), and N_2 on Fe(110) (see the top panel of Fig. 3.1). Our choice is also motivated by the results reported in the aforementioned chemicurrent experiments showing that the number of low-energy metal electrons excited during the adsorption of different gas species, i.e., the chemicurrent intensity, scales with E_{ads} [26, 191]. The wide range of E_{ads} values covered by the present case studies, between 0.2 and 2.3 eV, allows to elucidate the observed scaling law. In order to extract a more general conclusion on the role of these damping mechanisms in the gas-surface dynamics, we analyze and compare the kinetic and total energy loss in the aforementioned adsorption scenarios using the most reliable of the proposed surface density models. In addition, we study the influence of *e-h* pairs and phonons on the adsorbates trajectories. In particular, we calculate the mean traveled distance of the hot species on the surface, because, in principle, the in-plane distance between the initial and final positions of the adsorbate on the surface could be experimentally measured with STM [28, 236]. The connection of our theoretical predictions with experimental findings would shed more light on the importance of each of the two damping mechanisms in gas-surface reactions.

The outline of the chapter is as follows. The computational details are given in Sec. 3.2. Section 3.3 starts with the basics of the LDFA of Ref. [34] and continues with a detailed description of the surface electron density models we propose to use in AIMDEF simulations. The section ends by analyzing the performance of each

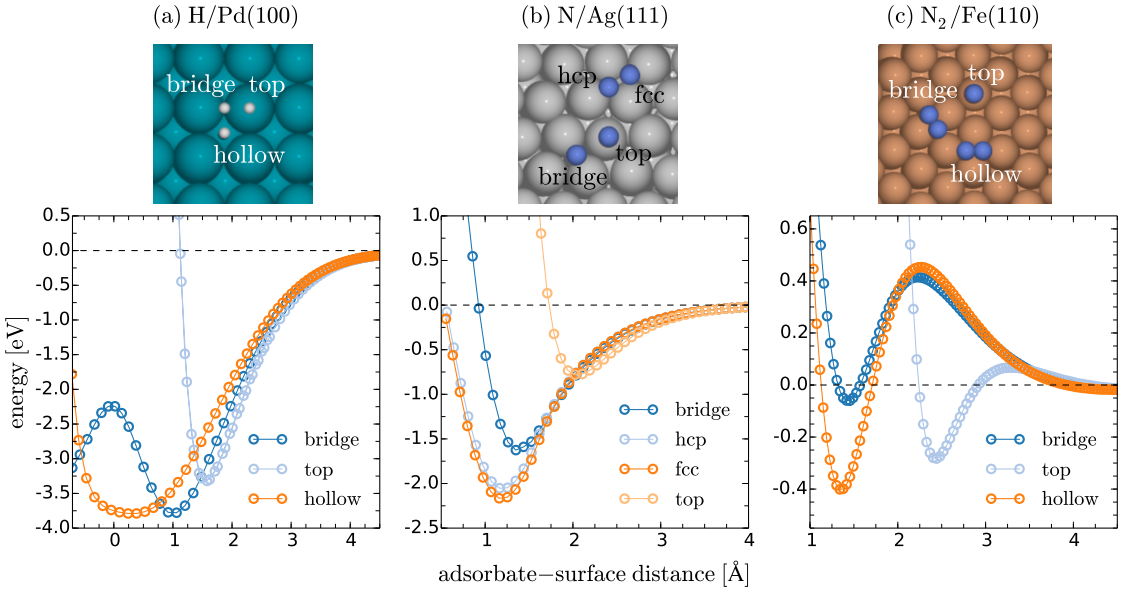

FIGURE 3.1: Top panel: Adsorption sites for each studied system. The orientation of N_2 on hollow and bridge sites is horizontal, while on the top it is vertical. Bottom panel: Relevant vertical cuts of the PES for each system. The orientations of N_2 along the curves are fixed as presented in the top panel.

density model under conditions of large surface atoms displacements as those occurring upon equilibration of the adsorbates at the adsorption wells. Their behaviour in representative AIMDEF simulations is discussed in Sec. 3.4. In particular, we analyze how the adsorption probabilities and energy dissipation into *e-h* pair and phonon excitations depend on the surface density description for the three above mentioned systems. In Sec. 3.5 we use the most accurate surface electron density model out of the ones analysed in the previous section to study the role of each damping mechanism in these adsorption scenarios. Specifically, we analyse the behaviour of the adsorbates energy and the lateral distance as a function of the propagation time for the cases where both or just one of the damping channels are active. The summary and conclusions are given in Sec 3.6.

3.2 Computational details

All the DFT calculations presented in this chapter are done with the VASP package, which uses a plane wave basis set. The core-electron interaction is approximated by PAW potentials [237]. Following previous works [33, 221, 222], a different GGA for the exchange and correlation functional is used in each of the studied systems, namely, the PW91 functional [70] for H/Pd(100) and N/Ag(111), and the RPBE functional [74] for N_2/Fe(110). The surfaces are modelled by five-layer (2×2) periodic slabs for

TABLE 3.1: Adsorption energies and geometries for each studied system and for each equilibrium configuration of the adsorbate. The vertical distance between the adsorbate height and the average height of the topmost layer of surface atoms, and intermolecular distance of N_2 are denoted with z_A and r_{mol}, respectively. The two topmost layers are allowed to move during the relaxation calculations.

	H/Pd(100)			N/Ag(111)				N_2/Fe(110)		
	top	hw	br	top	*hcp*	*fcc*	br	top-ver	hw-par	br-par
E_{ads} [eV]	-3.33	-3.81	-3.80	-0.83	-2.18	-2.30	-1.91	-0.31	-0.49	-0.22
z_A [Å]	1.57	0.32	1.00	2.06	1.08	1.09	1.13	2.51	1.36	1.36
r_{mol} [Å]								1.14	1.26	1.28

H/Pd(100) and N/Ag(111) and by a four-layer (3×3) periodic slab for N_2/Fe(110) in the supercell approach. The vacuum region heights are 25.74, 24.02, and 20.29 Å for H/Pd(100), N/Ag(111), and N_2/Fe(110), respectively. The Brillouin zone is sampled with $n \times n \times 1$ MP meshes [103], with $n = 6$ for H/Pd(100), $n = 5$ for N/Ag(111) and $n = 3$ for N_2/Fe(110). The energy cut-offs for the plane wave basis sets are 350 eV for H/Pd(100), and 400 eV for the other systems.

The AIMDEF results shown below for each system are statistical averages obtained from a suitable number of trajectories, in which the two outer layers of the surface are allowed to move (unless otherwise stated) and the initial conditions of the imping species are different for each trajectory. In the simulations, the Beeman predictor-corrector algorithm is used to integrate the classical equations of motion [Eq. (2.43) with Eq. (2.60)] [238], where 0.1, 0.5, and 0.7 fs are the time steps for H/Pd(100), N/Ag(111), and N_2/Fe(110), respectively. We note that the friction coefficient [Eq. (2.60)] is in all cases neglected when the hot species move in very-low-density regions. Specifically, $\eta = 0$ for surface densities smaller than 7.46×10^{-3} $e/\text{Å}^3$ ($r_s > 6$ a.u.).

For each density model, 50 hot H atom trajectories are simulated on Pd(100) that result from the dissociation of 25 H_2 molecules on the surface, where they impinge at normal incidence with initial kinetic energy $E_i = 0.5$ eV. As in the previous work of Ref. [33], the initial coordinates (x_i, y_i, z_i) and velocities of the individual H atoms are taken from adiabatic frozen surface MD simulations on a precalculated six-dimensional PES from the literature [33, 108, 230] that describes H_2 dissociation on Pd(100). When the H–H distance in those simulations reaches three times that of the H_2 equilibrium bond length in the gas-phase, we set the time $t = 0$ for the present AIMDEF simulations. From the relaxation calculations we find three different adsorption sites, as presented in Fig. 3.1(a), namely bridge, top, and hollow sites. The corresponding adsorption energies and relaxed geometries are shown in Table 3.1. In order to illustrate the potential energy landscape of this system, Fig. 3.1(a)

additionally shows one-dimensional PES cuts along the vertical direction for these adsorption sites.

The AIMDEF simulations with N atoms and N_2 molecules account, instead, for the complete adsorption process at normal incidence, where the used E_i values ensure large adsorption probabilities. For N atoms on Ag(111), 20 trajectories are simulated for each density model with $E_i = 0.1\,\text{eV}$, $z_i = 4\,\text{Å}$, and random (x_i, y_i) values. The open-shell character of N requires the use of spin-polarized DFT. However, since the spin is quenched upon N–Ag interaction, computational effort can be saved by doing non-spin-polarized calculations when N lies close to the surface (see Appendix A for a practical description of how this effect is considered in the AIMDEF simulations). The representative PES curves starting above the adsorption sites (i.e., bridge, hollow *hcp*, hollow *fcc*, and top) and the corresponding adsorption energies are shown in Fig. 3.1(b) and Table 3.1, respectively.

In the simulations of non-dissociative adsorption of N_2 on Fe(110), the molecules impinge normal to the surface with initial translational energy $E_i = 0.75\,\text{eV}$ and zero rotational and vibrational energies (i.e., the zero point energy is neglected). The initial coordinates of the N_2 center of mass are, as in the previous case, $z_i = 4\,\text{Å}$ and random (x_i, y_i). For each density model, 80 trajectories are calculated. As depicted in Fig. 3.1(c) and Table 3.1, N_2 can adsorb on the Fe(110) surface with upright orientation on top of the Fe atoms, and parallel to the surface with its center of mass over either the hollow or the bridge site. It is worth noting that the latter adsorption configuration only appears if the individual Fe atoms are allowed to relax around the molecule. The corresponding three representative PES curves show an incoming barrier. The heights of the barriers and the corresponding z values are 0.07 eV and 3.23 Å, 0.45 eV and 2.23 Å, and 0.41 eV and 2.23 Å for top, hollow, and bridge sites, respectively.

In order to disentangle the relevance of each energy dissipation channel, we perform AIMDEF simulations in the frozen surface (FS+EF) and the non-frozen surface (NFS+EF) approaches. In the former, the surface atoms are fixed at their equilibrium positions and in the latter we allow the atoms in the two topmost layers to move during the simulation run. Non-frozen surface AIMD simulations without electronic friction (NFS) are carried out as well.

3.3 Local density friction approximation for adsorbates on surfaces

As already pointed in Secs. 2.3.2, 2.3.3, and 2.3.3, nonadiabatic effects that come from the energy exchange between the nuclear and electronic degrees of freedom can be effectively included in the nuclei classical equations of motion in terms of a friction force [119]. The crucial point is to determine a realistic value of the friction coefficient $\eta(\mathbf{r}_i)$ acting on the gas-atom i at each point $\mathbf{r}_i$ along its trajectory. In this respect, different theoretical studies have been performed during the last years treating this issue [34, 124, 193]. The LDFA mentioned in Sec. 2.3.4 [34] is one of the formalisms that, in spite of its simplicity, captures the relevant physical aspects of the low energy e-h pair excitations [18, 121, 132, 133] as those created by slowly moving gas species. This is one of the reasons of being widely applied to study the effect of electronic excitations in the dynamics of atoms and molecules on metal surfaces [33, 34, 170, 184, 196, 198, 200, 219, 221, 239–245]. More recently, the LDFA has been shown to accurately describe the electronic energy loss in the scattering of H from Au(111) [246].

The LDFA assumes that $\eta(\mathbf{r}_i)$ is equal to the friction coefficient that the same atom i would have in case of being moving within a homogeneous FEG of density $n_0 = n_{\rm sur}(\mathbf{r}_i)$, where $n_{\rm sur}(\mathbf{r}_i)$ is the electron density of the bare metal surface at the atom position $\mathbf{r}_i$. We recall that the friction coefficient within the LDFA can be written as (see Sec. 2.3.4)

$$\eta = \frac{4\pi n_{\rm sur}(\mathbf{r}_i)}{k_F} \sum_{l=0}^{\infty} (l+1) \sin^2[\delta_l(k_F) - \delta_{l+1}(k_F)] \; , \tag{3.1}$$

where $k_F = [3\pi^2 n_{\rm sur}(\mathbf{r}_i)]^{1/3}$ and $\delta_l(k_F)$ are the scattering phase-shifts at the Fermi level that are calculated from the DFT scattering potential of an atom within the FEG. The latter turns out to be a crucial step to reproduce available experimental data on the stopping power of atoms and ions in metal solids and surfaces [18, 121, 132, 133]. For the case of a molecular projectile the original LDFA of Ref. [34] calculates the friction coefficient on each atom in the molecule as if they were non-interacting atoms (independent atom approximation, IAA). The latter has been shown to be a reasonable approximation for the translational degrees of freedom [247], but it may introduce errors when treating the coupling of the molecular vibrational movement with the metal electrons in situations of strong and long-time molecule-surface interactions. In this chapter we mostly tackle the former scenario. The electron-vibration coupling that affects the lifetime of the molecular vibration mode when adsorbed on metals is an example of undoubtedly extreme realization of

the aforementioned situations [248, 249]. Many aspects of this important problem will be addressed in chapter 4. In the recent study of Ref. [249], the authors use the Fermi golden rule formulation [37] and also analyze the anisotropies of the friction tensor in nonuniform systems that cannot be captured by the isotropic LDFA. We note, however, that a direct quantitative comparison between these results and those of the LDFA is not straightforward because in the calculation of the friction tensor only electronic transitions that conserves the crystal momentum is included (i.e. initial and final electronic wavevectors are equal, $\mathbf{k} = \mathbf{k}'$), whereas the calculation of the friction tensor for a single adsorbate requires the Fermi surface integration over transitions not conserving the crystal momentum (recall the discussion at the end of Sec. 2.3.3).

3.3.1 Surface density models

In the seminal study of Ref. [33], the bare surface electron density, which determines the friction coefficients $\eta(\mathbf{r}_i)$ within the LDFA, was approximated by the electron density of the bare frozen surface (FS) calculated self-consistently with DFT. This approach will be denoted as $n_{\mathrm{sur}}^{\mathrm{FS}}$ in the following. Although the use of $n_{\mathrm{sur}}^{\mathrm{FS}}$ is only justified in simulations where the surface atoms are fixed at the equilibrium positions, it is still a reasonable approximation in those cases where the surface atoms are barely moving [33, 241]. However, in most cases the surface atoms displacements are expected to cause appreciable changes in the bare surface electron density n_{sur}. Thus, the latter needs to be known at any instant t and it complicates the use of the LDFA in usual AIMDEF simulations because only the electron density of the whole system, i. e., gas species and surface atoms, is calculated self-consistently at each integration step.

Here, we introduce two methods that facilitate the applicability of the LDFA for moving surface atoms. In the first one, the surface electron density is calculated at each time step t as the superposition of the ground state electron densities of the isolated individual surface atoms n_j^{atom}, i.e.,

$$n_{\mathrm{sur}}^{\mathrm{AS}}(\mathbf{r}_i, t) = \sum_{j=1}^{N_{\mathrm{sur}}} n_j^{\mathrm{atom}}(\mathbf{r}_i, t), \tag{3.2}$$

where $\mathbf{r}_i$ is the position of adsorbate and the summation index j runs over all surface atoms N_{sur}. This method successfully accounts for the movement of the surface atoms at each time step, but it obviously misses the charge redistribution upon formation of bonds between the surface atoms.

The second method corrects this misbehavior by making use of the Hirshfeld partitioning scheme [35], which has been successfully applied to study the vibrational lifetimes of molecular adsorbates within the LDFA framework [248]. Here, we use it in order to subtract the contribution of the gas-phase atoms from the self-consistent density of the whole system $n^{\mathrm{SCF}}(\mathbf{r}_i, t)$. More precisely, the bare surface electron density is approximated at each t by

$$\begin{aligned} n^{\mathrm{H}}_{\mathrm{sur}}(\mathbf{r}_i, t) &= n^{\mathrm{SCF}}(\mathbf{r}_i, t) \left[1 - \sum_{n=1}^{N_{\mathrm{A}}} w_n(\mathbf{r}_i, t) \right], \\ w_n(\mathbf{r}_i, t) &= \frac{n_n^{\mathrm{atom}}(\mathbf{r}_i, t)}{\sum_{m=1}^{N} n_m^{\mathrm{atom}}(\mathbf{r}_i, t)}, \end{aligned} \tag{3.3}$$

where the indexes m and n run, respectively, over the total numbers of atoms in the system N and in the adsorbate N_{A}. In this equation, the Hirshfeld weighting factor $w_n(\mathbf{r}_i, t)$ represents the contribution of the n-th atom to the electron density of the whole system at $\mathbf{r}_{\mathrm{i}}$. Thus, the factor $\left[1 - \sum_{n=1}^{N_{\mathrm{A}}} w_n(\mathbf{r}_i, t)\right]$ defines the weight corresponding to the system without the contribution of the adsorbate.

The described electron density methods ($n^{\mathrm{FS}}_{\mathrm{sur}}$, $n^{\mathrm{AS}}_{\mathrm{sur}}$, and $n^{\mathrm{H}}_{\mathrm{sur}}$) have been implemented in VASP [117] to perform AIMDEF calculations [33, 243]. The three sets of AIMDEF simulations carried out using $n^{\mathrm{FS}}_{\mathrm{sur}}$, $n^{\mathrm{AS}}_{\mathrm{sur}}$, and $n^{\mathrm{H}}_{\mathrm{sur}}$ are correspondingly denoted as FSM, ASM, and HM in the following.

3.3.2 Performance of surface density models for static configurations

We start by examining the adequacy of $n^{\mathrm{FS}}_{\mathrm{sur}}$, $n^{\mathrm{AS}}_{\mathrm{sur}}$, and $n^{\mathrm{H}}_{\mathrm{sur}}$ in describing the self-consistent bare surface electron density n_{sur} once the adsorbates are fully relaxed and accommodated on the surface. In other words, these surface densities are extracted from a single point (static) DFT calculation of an already relaxed system. This case constitutes one of the possible real extreme conditions under which the surface density can be significantly altered as a consequence of the charge redistribution between the adsorbate and the surface. In fact, this redistribution even distorts locally the surface lattice.

In Fig. 3.2 we compare the spatial distributions of the three bare surface electron density models with n_{sur} for the case of a H atom adsorbed at the top, hollow and bridge sites of the Pd(100) surface. In each case, n_{sur} is calculated using the surface atom positions of the relaxed adsorbate-surface structure. For completeness, the self-consistent electron density of the whole system n^{SCF} is also shown. The curves display

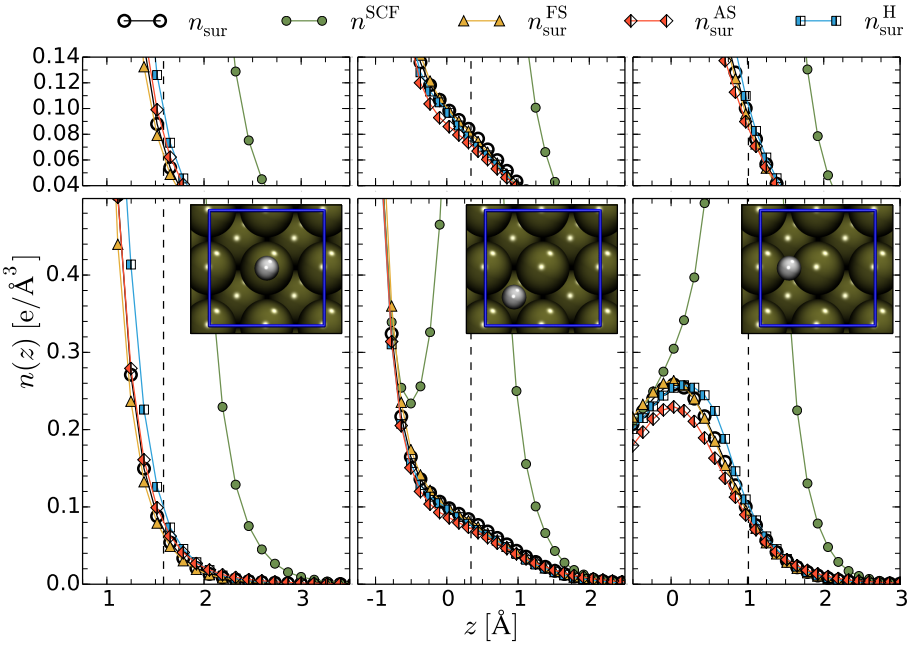

FIGURE 3.2: Electron density as a function of the distance from the surface z for a H atom adsorbed above the top, hollow and bridge sites of the Pd(100) surface. The n_{sur} (empty circles), n^{FS}_{sur} (yellow triangles), n^{AS}_{sur} (red-white diamonds), and n^{H}_{sur} (blue-white squares) are plotted along the line normal to the surface that contains the H atom, whose position is indicated by the dashed line. For completeness, the density of the whole system n^{SCF} is shown by the green circles. Inset: 2×2 unit cell (blue box) with H at the top, hollow and bridge sites.

the one dimensional (1D) cut of the electron densities along the line normal to the surface that contains the adsorbate. The n^{FS}_{sur} data practically coincide with n_{sur} due to the negligible displacements that the adsorbed H causes on the surrounding Pd (the displacements of the adsorbates nearest neighbors from their equilibrium positions in the clean surface d_{nn} are shown in Table 3.2). Obviously, dissimilarities appear in the region of large density gradients. The other two methods also reproduce well the values of n_{sur}. The agreement is particularly good at the position of the adsorbate z_A (dashed vertical line), which is the value of interest for applying the LDFA. It is also worthy to remark the goodness of the Hirshfeld partitioning scheme in removing the contribution of the adsorbate from the electron density of the whole system n^{SCF}. This becomes apparent when noticing how different n^{SCF} is from n_{sur}, but how finely the latter is reproduced by n^{H}_{sur}. Deviations of n^{H}_{sur} and n^{AS}_{sur} from the correct n_{sur} are more apparent at distances $z < z_A$, i.e., in the region where the adsorbate-surface bond and the surface metal bonds are formed, especially for the top and bridge sites. On the one hand, n^{H}_{sur} reproduces rather well the surface density for the bridge site (notably, around $z = 0$, where the metallic character of the bonds is manifest), but it overestimates it for the top case. On the other hand, n^{AS}_{sur} behaves well for the top site, but it underestimates n_{sur} around the topmost Pd layer ($z = 0$) in the bridge case. As argued below, these results are a consequence of the different charge

TABLE 3.2: Displacements d_{nn} of the surface atom(s) lying nearest to the adsorbate obtained for each system and each equilibrium position of the adsorbate. Values of the surface electron density n_{sur} at the position of the adsorbate calculated self-consistently and with the three different surface density models (see text). For N_2 adsorbed on the top-vertical well, the densities at the position of the most distant N are written in parenthesis.

	H/Pd(100)			N/Ag(111)				N_2/Fe(110)		
	top	hw	br	top	*hcp*	*fcc*	br	top-ver	hw-par	br-par
d_{nn}(Å)	0.030	0.024	0.030	0.027	0.081	0.073	0.18	0.047	0.06	0.12
n_{sur} (e/Å^3)	0.071	0.084	0.100	0.014	0.046	0.046	0.044	0.019(0.001)	0.054	0.056
n_{sur}^{FS} (e/Å^3)	0.064	0.082	0.095	0.015	0.055	0.056	0.066	0.017(0.001)	0.051	0.056
n_{sur}^{AS} (e/Å^3)	0.081	0.074	0.090	0.016	0.038	0.037	0.037	0.029(0.002)	0.040	0.045
n_{sur}^{H} (e/Å^3)	0.099	0.078	0.110	0.016	0.036	0.035	0.034	0.031(0.002)	0.048	0.052

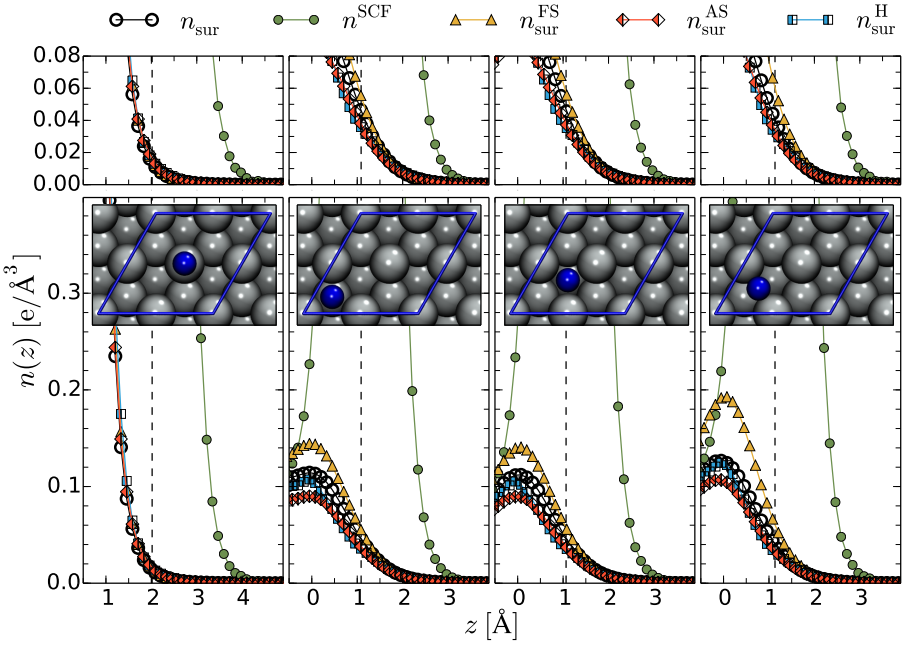

FIGURE 3.3: Same as Fig. 3.2 for N adsorbed above the top, hollow *hcp*, hollow *fcc* and bridge sites of Ag(111), as sketched in the insets. The (2×2) unit cell is indicated by a blue box in the insets.

redistribution occurring at each site.

The electron densities for N adsorbed at the top, *hcp* hollow, *fcc* hollow and bridge sites of the Ag(111) surface are compared in Fig. 3.3. As in the H/Pd(100) system, the three models are good in reproducing n_{sur} at the adsorbate position and above ($z \geq z_A$). The n_{sur}^{H} values are impressively good along the whole z-range, while both n_{sur}^{FS} and n_{sur}^{AS} deviate from n_{sur} in the region around the Ag topmost layer. In particular, n_{sur}^{FS} and n_{sur}^{AS} systematically overestimate and underestimate, respectively, the surface density. The somewhat large errors obtained with n_{sur}^{FS} when N is adsorbed on bridge are a consequence of the large displacements of about 0.18 Å

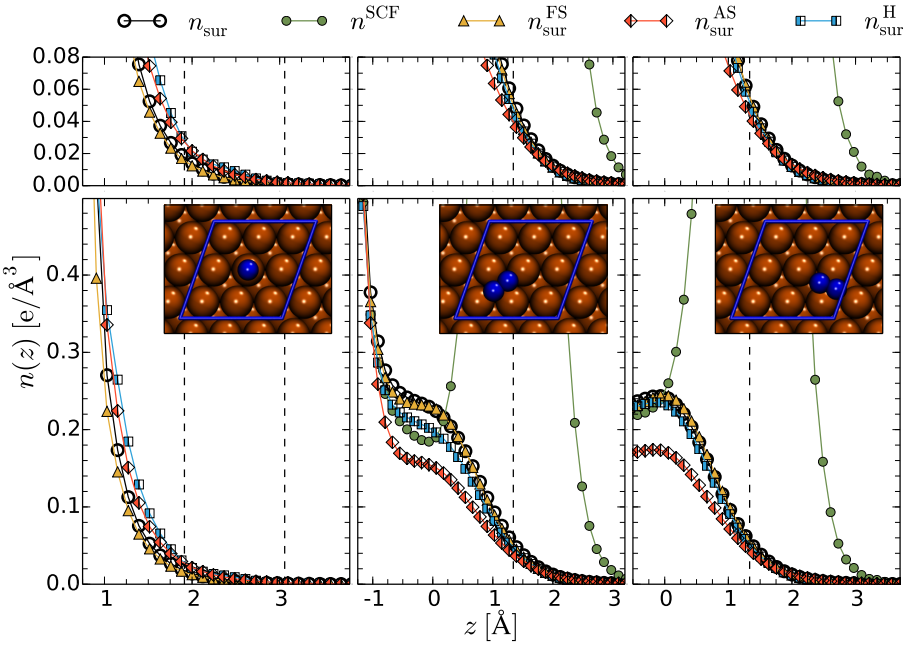

FIGURE 3.4: Same as Fig. 3.2 for N_2 adsorbed on the top, hollow, and bridge sites of the Fe(110) surface, as indicated by the insets in which the 3×3 unit cell is plotted with a blue box. Since the positions of the two N atoms are symmetrically equivalent for the bridge and hollow adsorption sites, only the densities along one N atom are plotted in these two cases.

that N is causing to the Ag atoms around it (see Table 3.2 for details on the other sites).

Figure 3.4 shows for the three N_2 adsorption sites that any of the proposed surface density models succeeds in reproducing n_{sur} at the position of each of the N atoms conforming the molecule. Regarding the performance of the three models along z, the smallest to the largest errors are obtained by n^{FS}_{sur}, n^{H}_{sur}, and n^{AS}_{sur}, following this order. As noted previously, the errors are expectably larger in the regions where the density changes rapidly with z.

All in all, the analysis of the different cases studied in Figs. 3.2, 3.3, and 3.4 allows us to extract the following conclusions. The three surface density models provide a good description of n_{sur} at distances from the surface close or larger than the equilibrium adsorption heights. In the bonding region between the adsorbate and the surface, the possible errors introduced by n^{H}_{sur} and n^{AS}_{sur} are reasonably small, while the adequacy of n^{FS}_{sur} depends strongly on the size of the lattice distortions, particularly, in those areas of large density gradients. By construction, n^{H}_{sur} is expected to overestimate (underestimate) the density whenever the adsorbate-surface interaction causes a negative (positive) induced density, i.e., a removal (piling up) of electrons, whereas n^{AS}_{sur} underestimates the electronic density in the interstitial region where the metal character of the surface atoms bonding is manifested.

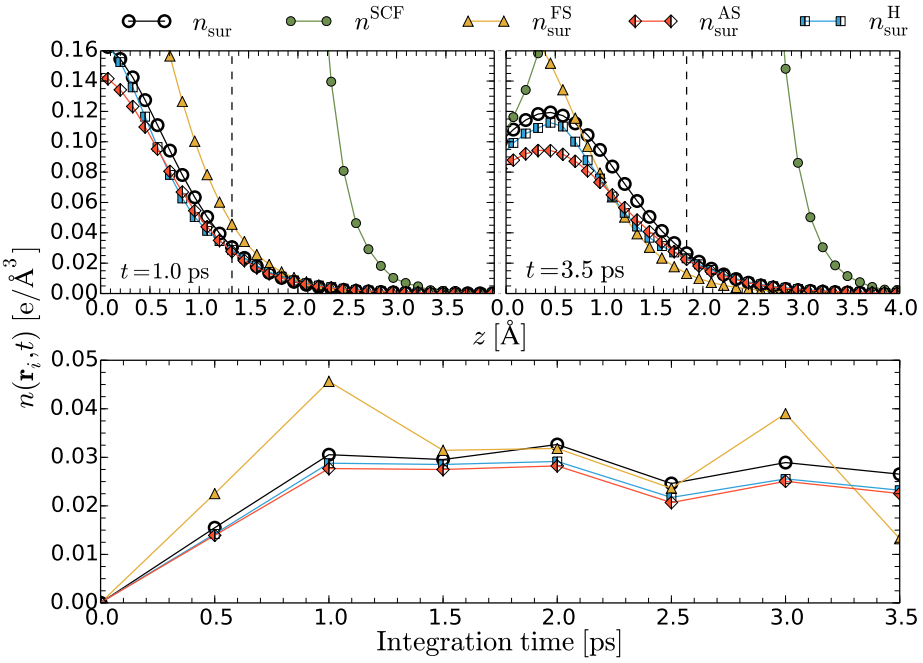

FIGURE 3.5: Bottom panel: Surface electron densities as a function of time for one N atom impinging on the Ag(111) surface with 0.1 eV of initial kinetic energy at normal incidence. Upper panels: 1D cuts of the electron densities calculated as those of Fig. 3.3, but using the positions of N and the Ag atoms at two different instants along the trajectory. Lines description as in Fig. 3.2.

As additional stringent tests, we have also compared the performance of the proposed density models for surface lattice distortions we encounter in real AIMD simulations as those presented in the next section. Figure 3.5 shows the results for one trajectory that is characterized by large lattice distortions, with averaged displacements of the surface atoms with respect to the equilibrium positions that vary between 0.2 Å and 0.4 Å in the topmost surface layer. This trajectory corresponds to the adsorption of the N atom on Ag(111). The self-consistent bare surface electron density n_{sur} and the model densities n^{FS}_{sur}, n^{AS}_{sur}, and n^{H}_{sur} are calculated using the surface atom positions at different instants along the trajectory. The bottom panel shows the values of the densities at the position where the N atom is located at each instant during the simulation. Clearly, both n^{H}_{sur} and n^{AS}_{sur} in this order are the best approximations to n_{sur}. In contrast, n^{FS}_{sur} while valid for small distortions, fails otherwise. The upper panels show a 1D cut of the surface densities along the same line used in Fig. 3.3 at two distinct instants. In both cases, n^{H}_{sur} is the model density that gives an overall better description of n_{sur}.

3.4 Surface density models in *ab initio* molecular dynamics with electronic friction simulations

In this section we study the performance of the three density models in a gas-surface dynamics problem, namely, the adsorption and relaxation of hot species on metal surfaces. Although we have shown that the differences in the densities are small, it is not clear that they will be manifested also as small differences in the dynamical magnitudes for, at least, three reasons: (i) the surface atom displacements vary in magnitude and are in persistent change along the trajectory, resulting in configurations where the different models can provide a fluctuactingly faithful description of the bare surface density (as shown in Fig. 3.5, where the density can be overestimated as well as underestimated); (ii) the friction coefficient η is not linearly dependent on n_{sur}; and (iii) since the friction force is also proportional to the projectile velocity, the electron density alone gives incomplete information about the *e-h* pairs excitation. Therefore, a detailed *dynamical* analysis is revealed as a necessary complement to the static one.

In this respect, H/Pd(100), N/Ag(111), and N_2/Fe(110) are well suited for the present analysis because they cover the limiting cases in which the energy exchange with the surface is dominated by either *e-h* pairs or phonons excitations [243]. For each system, we will examine how the differences in the densities originated by each density model affect: (i) the adsorption probability (Sec. 3.4.1), (ii) the surface atom displacements (Sec. 3.4.2) and the friction coefficients experienced by the hot species (Sec. 3.4.3), which are the factors determining the energy dissipation mechanisms, and, importantly, (iii) the kinetic energy loss of the hot species (Sec. 3.4.4), which is the central quantity of the problem.

3.4.1 Adsorption probabilities

Previous MD calculations performed on a precalculated (frozen surface) three-dimensional N/Ag(111) PES show that the initial adsorption probability for N impinging at off-normal incidence with $E_i = 0.1\,\mathrm{eV}$ is $S_0 \simeq 0.98$ for an ideal surface temperature $T_s = 0$ K [221]. In those simulations, the effect of *e-h* pair excitations is described through the LDFA, while energy exchange with the surface lattice (phonon excitations) is included by means of the GLO model [220, 224–226]. The same value was obtained in pure GLO calculations that only included phonons excitations, while the authors found a slightly smaller value $S_0 \simeq 0.87$ when only *e-h* pair excitations were considered.

In the present AIMDEF simulations, we obtain $S_0 = 1$ irrespective of the adopted surface density model (FSM, ASM, HM). Overall, our S_0 values are consistent with the previous MD results: on the one hand, NFS simulations yield $S_0 = 1$ and, on the other hand, FS+EF simulations yield a slightly lower $S_0 = 0.85$.

In the case of N_2/Fe(110), the global adsorption probability is $S_0 = 0.75$ and the site-specific adsorption probabilities are 0.31, 0.13, and 0.31 for top, hollow, and bridge configurations, respectively. Here, too, the latter values remain barely unchanged when using any of the proposed surface electron density models. Also in this system we have performed the two additional types of simulations described above. NFS simulations yield $S_0 = 0.71$, which is in good agreement with GLO simulations carried out with a six-dimensional N_2/Fe(110) PES for the same incidence conditions and low surface temperature T_s [222]. Interestingly, no adsorption event is observed with the FS+EF calculations that neglect energy exchange with the surface lattice.

In the following, we will focus on the adsorption process and restrict all the analysis to the results obtained from the adsorption trajectories exclusively.

3.4.2 Surface atoms displacements

The top and bottom panels of Fig. 3.6 show the mean displacements of the surface atoms within the first $\langle d_1 \rangle$ and second $\langle d_2 \rangle$ layers, respectively, as a function of time for each electron density model and for each system. The displacements are evaluated with respect to the equilibrium position for each trajectory and time step as,

$$d_l(t) = \frac{1}{N_l} \sum_{n=1}^{N_l} |\mathbf{r}_n(t) - \mathbf{r}_n(0)| \,, \tag{3.4}$$

where $l = 1, 2$ indicates the topmost and second layers, respectively, $\mathbf{r}_n$ are the surface atom positions, and the sum runs over the N_l atoms within the l-th layer of the unit cell. A common trend in the three systems is that $\langle d_1 \rangle > \langle d_2 \rangle$. This is a reasonable result, since the projectile exchanges energy and momentum directly with the top layer.

For H/Pd(100) and N_2/Fe(110) the differences between the displacements calculated with the three surface density models are almost negligible. For N/Ag(111) small differences appear after 1.3 ps. It is only after this time that the displacements of the HM model are visually lower than the ones of the FSM and ASM models.

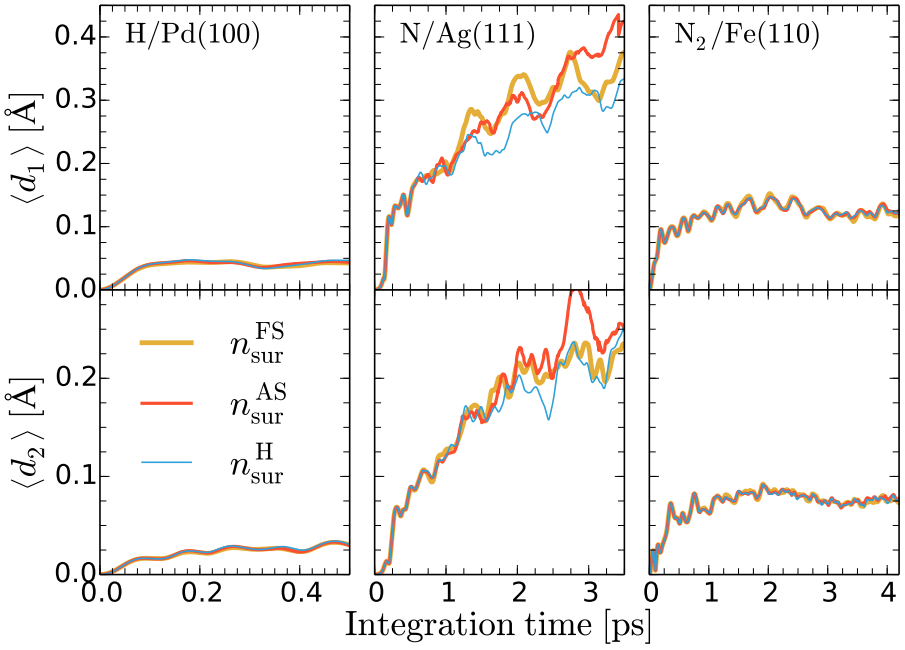

FIGURE 3.6: Average displacements from their equilibrium position of the surface atoms in the first (upper panels) and second (bottom panels) layers as a function of integration time. Left, middle, and right panels correspond to H/Pd(100), N/Ag(111), and N_2/Fe(110), respectively. Yellow, red, and blue lines are the results obtained with AIMDEF simulations, where the friction force is calculated with the FSM, ASM, and HM models, respectively.

Comparing the three systems, the Ag(111) displacements are much larger and increase faster with time than those of Pd(100) and Fe(110), which reach a plateau at earlier times. Notice that the values for Fe arrive close to their maximum less than 1 ps after the molecule-surface collision, while Ag movements continue to increase in amplitude even 3 ps after the collision. Interestingly, this different behaviour is not correlated with the different projectile-to-surface atom mass ratios γ we have for H/Pd(100) (γ=0.0095), N/Ag(111) (γ=0.13), and N_2/Fe(110) (γ=0.5). Within simple binary collision models [250, 251], this parameter relates (albeit not exclusively) to the projectile-to-surface momentum transfer in the successive collisions with the metal atoms. The low γ value of H/Pd(100) is in line with the small Pd displacements, but this argument alone cannot explain the N/Ag(111) and N_2/Fe(110) results of Fig. 3.6. These results are neither explained by the E_i value, which is smaller for N than for N_2. Instead, Fig. 3.6 is to be understood by considering the different PES topographies of these systems. As already illustrated in Fig. 3.1, the N_2/Fe(110) system has an entrance energy barrier above the surface, which diminishes the kinetic energy of the impinging molecules [222], whereas the N/Ag(111) PES is barrierless and strongly attractive at long range, which accelerates the N atoms [186].

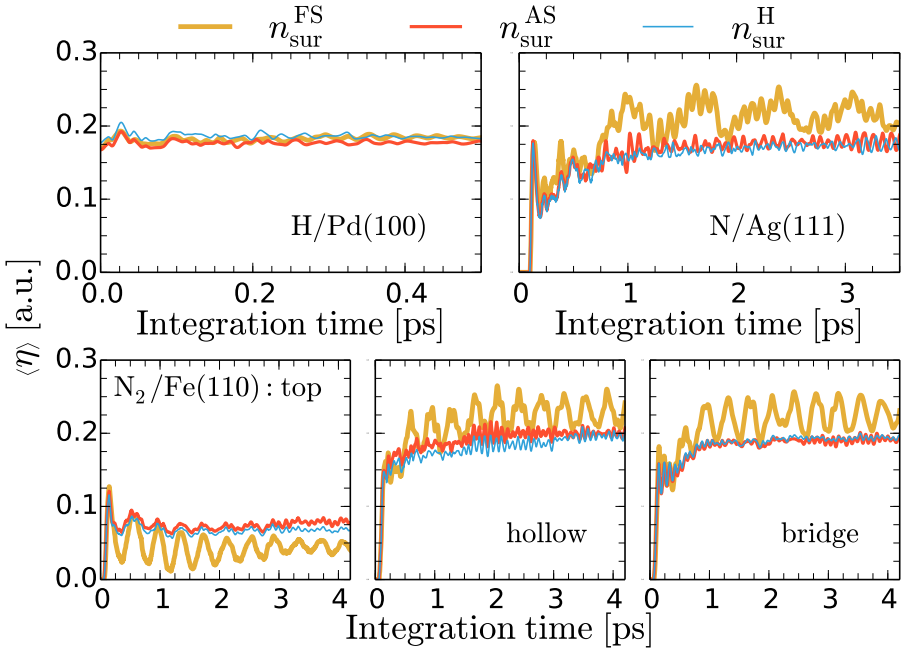

FIGURE 3.7: Average friction coefficient $\langle\eta\rangle$ as a function of time for H/Pd(100) and N/Ag(111) (upper panels), and for N_2 adsorbed at top, hollow, and bridge sites of Fe(110) (lower panels). Lines description as in Fig. 3.6.

3.4.3 Friction coefficients

In this subsection, we focus in the friction coefficients η experienced by the hot atoms during the simulations. Figure 3.7 compares their statistical averages $\langle\eta\rangle$ as a function of time for the three systems and for the different surface electron density models. In the case of N_2/Fe(110), we find meaningful to show the results for each of the adsorption configurations because the probed surface regions and hence the friction coefficients experienced by the molecules depend strongly on whether N_2 is adsorbed on the top-vertical or on the bridge- and hollow-parallel wells.

In accordance with the small surface atoms displacements occurring in H/Pd(100), the $\langle\eta\rangle$ values in the three density models are very similar. However, for N and N_2 adsorbed on any of the parallel configurations, Fig. 3.7 shows that FSM yields an overall overestimation of $\langle\eta\rangle$. This behaviour becomes very clear at times $t > 800$ fs in N/Ag(111) and $t > 500$ fs in N_2/Fe(110), namely when the energy lost into the phonons channel starts to saturate (see also Sec. 3.5.1). Comparing the time-averaged values of the friction coefficients $\langle\langle\eta\rangle\rangle_t$ computed for $t > 300$ fs, the relative differences between the FSM and HM simulations, calculated as $\Delta = (\langle\langle\eta\rangle\rangle_t^{FSM} - \langle\langle\eta\rangle\rangle_t^{HM})/\langle\langle\eta\rangle\rangle_t^{HM}$ amounts to 25% for N/Ag(111) and 16-20% for parallel N_2 on Fe(110). The FSM overestimation is a consequence of using the undistorted bare surface density n_{sur}^{FS} for moving surface atoms in cases in which the adsorption dynamics is dominated by on-surface ($z < 2$ Å) movements. Along

those trajectories, the large density regions existing within very short distances of the surface atoms are accordingly very repulsive and, hence, inaccessible for the typical hot species energies. However, if the surface atoms move from their equilibrium positions, the hot species may access those, otherwise, forbidden regions, where the $n_{\mathrm{sur}}^{\mathrm{FS}}$ values are large because they correspond to the undistorted surface. Since the electron density gradient increases rapidly as the distance to the surface atomic cores decreases, it is understandable that the time spent by the hot atoms nearby these regions, though short, will have more weight in the statistical average and thus result in the overall $\langle\eta\rangle$ overestimation observed in the FSM curves of Fig. 3.7. On the contrary, with the HM and ASM models, the probed densities, and consequently the friction coefficients that enter the average, are always similar to the actual distorted surface density values, as shown in Fig. 3.5.

The performance of the FSM model for N_2 adsorbed on the top-vertical configuration is completely different. Figure 3.7 shows that FSM largely underestimates $\langle\eta\rangle$ as compared to ASM and HM. The discrepancies start at $t > 250$ fs, while the relative difference in the time-averaged $\langle\eta\rangle$ between the FSM and HM simulations is around -37%. In this case, the molecule is mainly moving along the surface normal at 2–3 Å above the surface in a concerted N_2-Fe motion that brings the Fe atom inwards and also outwards the topmost layer. In contrast to the parallel-N_2 adsorption dynamics, the large density-gradients along the surface normal appear in the low-density regions of the undistorted surface that are probed by the top-vertical N_2 during the outwards motion. Therefore, the same large-density-gradient argument explains that during the concerted N_2-Fe movement $n_{\mathrm{sur}}^{\mathrm{FS}}$ is now predominantly underestimating the density.

When FSM is used, a modulation in $\langle\eta\rangle$ is clearly visible for N/Ag(111) and N_2/Fe(110), which consists in large-amplitude low-frequency oscillations with periods ~ 0.8 and ~ 0.3 ps, respectively. The trajectories that enter the statistical averages are not correlated and thus this modulation is to be interpreted as a mere statistical artifact. As a matter of fact, it is observed that the projectiles impact on different positions within the surface unit cell and that the paths followed by the hot species on the surface are very different. Nonetheless, there are cases in which an overlying low-frequency modulation that we tend to ascribe to the surface atoms movement seems to be also present and could explain the modulation in the FSM $\langle\eta\rangle$. A considerably much larger statistics would be needed to confirm that surface phonons and not statistical errors are at the origin of these FSM oscillations.

3.4.4 Kinetic energy loss

In the previous subsections we have demonstrated that the use of different models to evaluate the bare surface electron density during AIMDEF simulations of hot species on surfaces results in substantially different mean friction coefficients and, in some cases, also lattice distortions. These quantities determine the energy loss rate of the hot species, which after all, is the key quantity in the modeling of reactive processes on surfaces. The hot species kinetic energy is directly linked to several experimentally observable magnitudes, such as the maximum distance traveled on the surface, the relaxation process time-scale, and the amount of energy transferred to the substrate.

Since the friction force is also velocity-dependent, the variation of the relaxation rate with the density model cannot be predicted. Figures 3.8, 3.9 and 3.10 show, for the three systems and for the different density models, the kinetic energy of the hot species averaged over the adsorbed trajectories as a function of time, denoted $\langle E_K^A \rangle$ for both atomic and molecular adsorbates in the following. Importantly, the general observation is that this quantity is not sensitive to adopting FSM, HM or ASM to describe the electron densities (there may be subtle differences that are, nonetheless, of similar magnitude as the oscillations in the curves). Considering that for N/Ag(111) and N_2/Fe(110) the $\langle \eta \rangle$ values obtained with FSM deviate from those obtained with ASM and HM (see Fig. 3.7), it is unexpected to find hardly any difference between the corresponding $\langle E_K^A \rangle$ curves (see Figs. 3.9 and 3.10). This is indeed a remarkable observation, since it stresses that uncertainties in the friction coefficients do not necessarily translate into the final dynamics and the measurable magnitudes of interest.

The noise in the $\langle E_K^A \rangle$ curves originates from the PES corrugation. In the trajectories that enter in the averages, the hot species follow disparate routes on the surface, sampling thus PES regions of very different energies. Contrary to the rapidly oscillating behaviour of $\langle E_K^A \rangle$, the average energy dissipated into *e-h* pair excitations $\langle E_{\rm ehp}(t) \rangle$ shows a smooth time dependence (see upper panels of Figs. 3.8, 3.9, and 3.10). Therefore, the observation of $E_{\rm ehp}(t)$ allows a sound comparison of the performance of the three density models on the relaxation rates. For each individual trajectory, this energy is evaluated as

$$E_{\rm ehp}(t) = \sum_{n=1}^{N_A} \int_0^t dt' \eta(\mathbf{r}_n(t')) |\mathbf{v}_n(t')|^2, \tag{3.5}$$

where the summation runs over the atoms that constitute the hot species, and where $\mathbf{v}_n(t')$ is the atom instantaneous velocity. At the end of the simulation time, when the H atoms are close to being thermalised on Pd(100), they have lost 0.53 eV into *e-h* pair

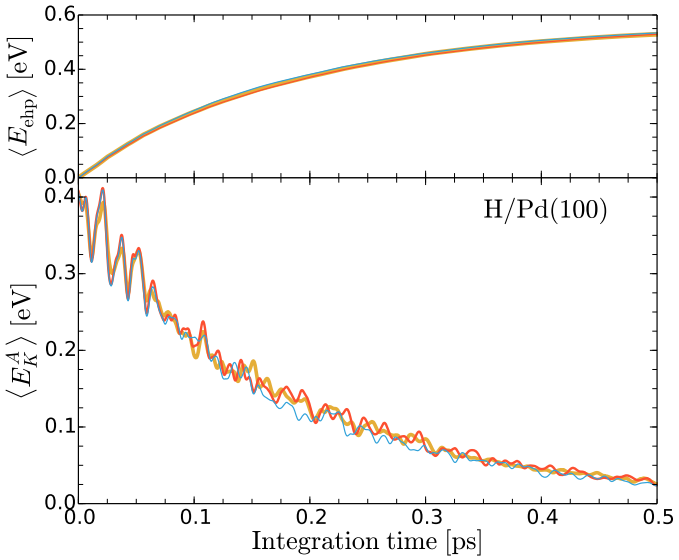

FIGURE 3.8: Energy loss due to *e-h* pairs excitation (upper panel) and average kinetic energy (lower panel) of the projectile as a function of time for H/Pd(100). The yellow, red and blue lines correspond to the results obtained with FSM, ASM and HM model, respectively.

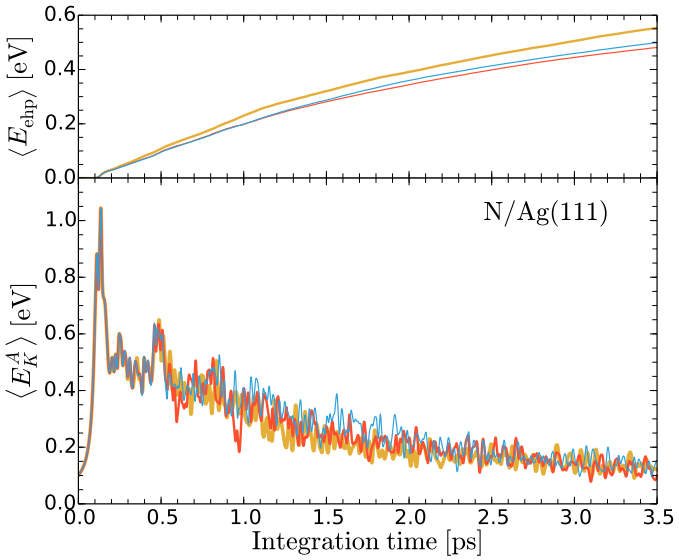

FIGURE 3.9: Same quantities and color code as described in Fig. 3.8 for N/Ag(111).

excitations and the energy differences between models are minimal, below 0.01 eV. For N_2/Fe(110), where we separately consider the energy loss for each adsorption site (see Fig. 3.10 upper panels), the differences between FSM and the other two models are more noticeable, and they are also in line with the underestimation or overestimation behaviors expected from the $\langle \eta \rangle$ values. Moreover, it must be taken into account that the molecule is far from being relaxed, and thus we can anticipate that the incipient deviations observed in Fig. 3.10 top panels will grow at longer times. This effect is manifested in N/Ag(111) too, where a very clear monotonously increasing deviation

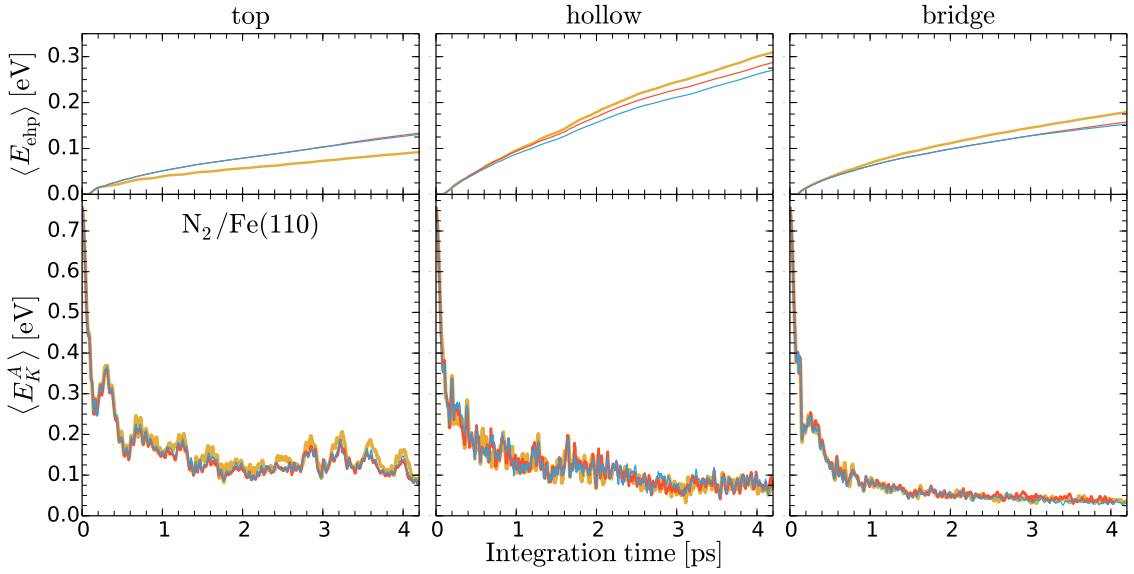

FIGURE 3.10: Same quantities and color code as described in Fig. 3.8 for N_2/Fe(110) specific for each adsorption configuration.

of FSM with respect to HM exists at the end of the simulation time. Here, the amount of energy used to excite *e-h* pairs is 0.499 eV with HM, and 0.054 (0.018) eV more (less) than that with FSM (ASM). Again, the larger $\langle E_{\rm ehp} \rangle$ values provided by FSM in the latter system are consistent with the $\langle \eta \rangle$ overestimation shown in Fig. 3.7.

The general conclusion we extract from the behaviors of $\langle E_K^A \rangle$ and $\langle E_{\rm ehp} \rangle$ is that the calculated energy loss rates and the relaxation times are, for practical purposes, density-model-independent. In other words, the three models under scrutiny are able to provide similar descriptions of the hot species adsorption dynamics of diversely behaving systems. Nevertheless, among the studied models, HM is the one that provides the best description of the bare surface electron density, and therefore its use should be recommended in simulations when there is no *a priori* knowledge of the dependence of the energy loss on the friction coefficient values and on the surface atoms motion. HM overcomes the limitations of FSM and ASM to describe, respectively, the instantaneous density when the surface atoms are free to move and the bonds between surface atoms.

3.5 Role of electron-hole pair excitations in gas-surface dynamics

So far we have been testing the performance of each type of surface electron density model in order to keep the accuracy of AIMDEF simulations also under the condition of large surface atom displacements. In this section we restrict ourselves to a

particular density model, namely HM, and we investigate the role of each dissipation channel in the three different adsorption scenarios (i.e., different adsorption energies E_{ads} and adsorbate-to-surface atom mass ratios γ). To reach the desired goal we analyse and compare the results from NFS+EF, FS+EF and NFS simulations. Since we are interested in the relaxation dynamics, the statistical averages of the following physical quantities are examined for each system: (i) kinetic energy of the adsorbate, (ii) energy loss due to phonons and *e-h* pairs, (iii) total energy of the adsorbate (Sec. 3.5.1), and (iv) lateral displacements of the adsorbate on surface (Sec. 3.5.2).

3.5.1 Energy loss due to phonon and electron-hole pair excitations

3.5.1.1 H/Pd(100)

Figure 3.11(a) shows the adsorbate kinetic energy $\langle E_K^A \rangle$ for the H/Pd(100) case and for each simulation type. From this figure we observe the two typical features of a system in which relaxation is dominated by *e-h* pair excitations: (i) $\langle E_K^A \rangle(t)$ decays more rapidly in the FS+EF than in the NFS simulations and, as a consequence, (ii) the NFS+EF results, which include both dissipation channels, lie close to the FS+EF curve, which only includes the dominant electronic channel.

Next, we analyze the amount of energy transferred from the adsorbate to *e-h* pairs and to the lattice. To evaluate the former energy transfer we use Eq. (3.5). The average value of this quantity over the available number of trajectories $\langle E_{\text{ehp}}(t) \rangle$ is shown in Fig. 3.11(b) for the FS+EF and NFS+EF simulations. In order to extract the energy transferred to the lattice atoms, we need both the instantaneous kinetic energy of the surface atoms and the instantaneous variation of the potential energy due to lattice distortions. The former is provided *on-the-fly* in the NFS+EF simulations and its statistical average over all the trajectories $\langle E_K^S(t) \rangle$ is also shown in Fig. 3.11(b). The energy stored as potential energy of the surface atoms $\langle E_P^S \rangle$ can be obtained from an analysis *a posteriori* of the simulated trajectories. For a few individual time steps $\{t_n\}$, we remove the adsorbate and consider only the surface atomic coordinates. In these distorted surface configurations, we evaluate the increase in the potential energy with respect to the equilibrium bare-surface configuration. This calculation is carried out for the available trajectories and then averaged to obtain estimates of $\langle E_P^S(t_n) \rangle$. The same procedure of extracting $\langle E_P^S \rangle$ is used as well for the other two systems in Secs. 3.5.1.2 and 3.5.1.3.

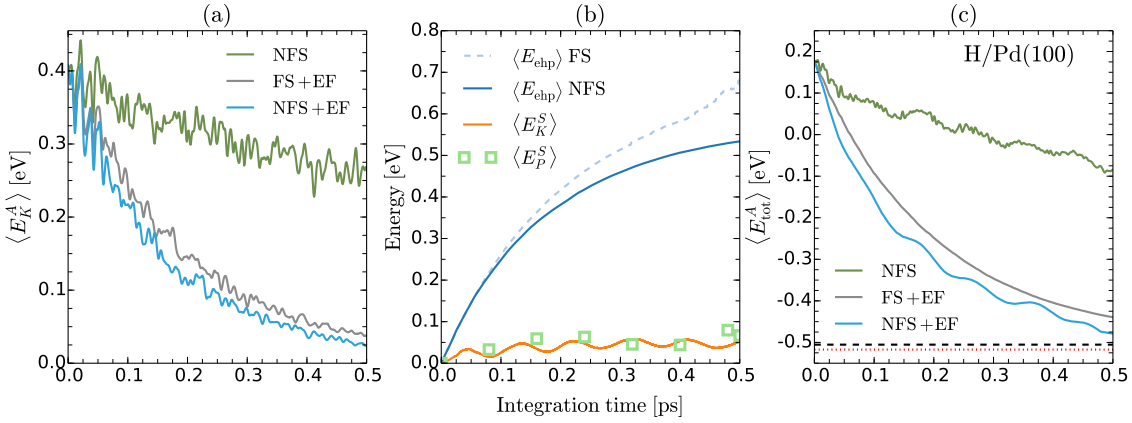

FIGURE 3.11: (a) Adsorbate kinetic energies averaged over AIMDEF-simulated trajectories of H on Pd(100). The grey (blue) lines correspond to FS+EF (NFS+EF) calculations, and the green lines correspond to NFS calculations. (b) Corresponding contributions to the energy transferred to the surface upon adsorption in NFS+EF simulations: energy lost into *e-h* pair excitations $\langle E_{\rm ehp} \rangle$ (dark blue), kinetic energy of surface atoms $\langle E_K^S \rangle$ (orange), and potential energy of the surface $\langle E_P^S \rangle$ (green squares). $\langle E_{\rm ehp} \rangle$ for FS+EF simulations is represented in light blue. (c) Average total energy of H on Pd(100), $\langle E_{\rm tot}^A \rangle$. Line colors description as in (a). The horizontal black dashed line indicates the energy needed for the H atom to jump between two adjacent hollow sites of the Pd(100) surface, this is, the potential energy of the H atom [see Eq. (3.6)] relaxed at the bridge site, $E_P^{\rm bri}$(H). The horizontal red dotted line indicates the potential energy at the adsorption hollow site $E_P^{\rm hol}$(H).

Figure 3.11(b) shows that $\langle E_P^S(t_n) \rangle$ and $\langle E_K^S(t) \rangle$ lie close to each other. This can be interpreted as a fingerprint of a harmonic oscillatory regime for the surface atoms. The average total energy transferred to the lattice, i.e., the phononic part of the energy loss, is $\langle E_{\rm ph} \rangle = \langle E_K^S \rangle + \langle E_P^S \rangle$. The overall comparison of these quantities in Fig. 3.11(b) shows that after just 0.5 ps the energy transferred to *e-h* pairs is around five times larger than the total energy transferred to the lattice ($\langle E_{\rm ph} \rangle \simeq 0.1\,$eV). We also observe that energy dissipation to each of the channels is not additive, since inclusion of phonon excitations reduces the amount of energy going to *e-h* pairs. The main reason is that the average $\mathbf{v}_n$ values entering Eq. (3.5) are lower in the NFS+EF than in the FS+EF simulations due to the additional energy release into the competing phononic channel.

Now we turn to analysis of the total energy of the H atom, from which we also extract the contribution of each of the damping mechanisms. In Fig. 3.11(a) we show the total energy of the H atom $\langle E_{\rm tot}^A \rangle$ as a function of integration time and averaged over the total number of trajectories. The total energy here is the sum of the kinetic and potential energies of the adsorbate, $E_{\rm tot}^A = E_K^A + E_P^A$. The zero of potential energy is defined as the potential energy of the adsorbate when it is located in vacuum and with accounting the spin polarization. In order to have the H atom in the H_2 molecule

located far from Pd(100) as the potential energy reference, we also subtract one half of the H_2 binding energy in the gas phase to that reference potential. The potential energy term of the adsorbate E_P^A can be obtained from the instantaneous variation of the potential energy due to lattice distortions $E_P^S(t_n)$ that we analysed above. To get the latter quantity at each time step of the simulation we linearly interpolate the $E_P^S(t_n)$ values from Fig. 3.11(b). Then, since we know the potential energy of the whole system $E_P^{A+S}(t)$ from the AIMDEF simulations, we can evaluate the potential energy of the adsorbate at each time step as,

$$E_P^A(t) = E_P^{A+S}(t) - E_P^S(t). \tag{3.6}$$

By looking at the total energy of the H atom moving on Pd(100) we observe a considerably larger decay rate when electronic friction is included in the calculation (FS+EF and NFS+EF) than when it is absent (NFS). The same dominant role of *e-h* pair excitations in this case was seen in the above analysis of the kinetic energy loss [33]. The horizontal black dashed line in Fig. 3.15(a) shows the potential energy of the H atom relaxed at the bridge site calculated with Eq. (3.6), $E_P^{\mathrm{bri}}(\mathrm{H})$. The latter represents the energy threshold for a H atom to jump from one hollow site to the adjacent one. In our simulations the H atom closely reaches this point at around 0.5 ps after dissociation, but only in the NFS+EF case. The red dotted line marks the H atom potential energy relaxed at the hollow site $E_P^{\mathrm{hol}}(\mathrm{H})$, i.e. the thermalised situation, which lies close to the H propagation threshold for this system.

3.5.1.2 N/Ag(111)

In contrast to the H/Pd(100) case, the N/Ag(111) results presented in Fig. 3.12(a) are those representative of a system in which relaxation is dominated by phonon excitations, i.e., they show a much faster decay of $\langle E_K^A(t)\rangle$ when surface atom movement is allowed. The obtained similarity of the $\langle E_K^A(t)\rangle$ curves for the cases when electronic friction is included (NFS+EF) and not (NFS) also reveals the dominance of the phonon loss channel. Regarding the details of the dynamics, at the beginning of the N/Ag(111) simulation ($t < 0.2$ ps), we observe a rapid kinetic energy gain, which is the result of the barrierless strong attraction felt by the N atom towards the Ag(111) surface [see Fig. 3.1(b)]. This increase is followed by a rapid decrease that is a consequence of N probing the repulsive part of the PES. In the NFS and NFS+EF cases there is an additional energy transfer to the surface atoms acting as soon as N approaches the surface, as we will discuss below. Therefore, after the first collision the N atom is left with about 0.5 eV of kinetic energy (0.8 eV in the FS+EF case) to be lost as a regular hot atom.

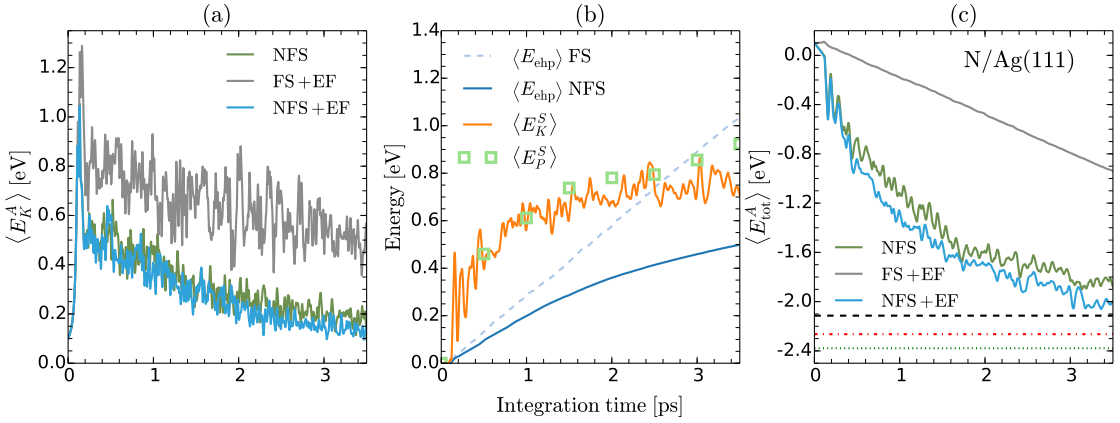

FIGURE 3.12: (a) Adsorbate kinetic energies averaged over AIMDEF-simulated trajectories of N on Ag(111). (b) Corresponding contributions to the energy transferred to the surface upon adsorption in NFS+EF simulations: energy lost into *e-h* pair excitations, $\langle E_{\rm ehp} \rangle$, kinetic energy of surface atoms, $\langle E_K^S \rangle$ and potential energy of the surface, $\langle E_P^S \rangle$. $\langle E_{\rm ehp} \rangle$ for FS+EF simulations is also shown. (c) Average total energy of N on Ag(111), $\langle E_{\rm tot}^A \rangle$. The horizontal black dashed line indicates the energy needed for a N atom to jump between two adjacent hollow sites of the Ag(111) surface, this is, the potential energy of N [see Eq. (3.6)] relaxed at the bridge site, $E_P^{\rm bri}$(N). The same quantity at the *fcc* and *hcp* adsorption sites is indicated by a green dotted and a red dashed-dotted line, respectively. Other line colors description as in Fig. 3.11.

Further quantitative analysis of the energy exchange between the adsorbate and the two damping mechanisms is given in Fig. 3.12(b). The non-additive character of the energy dissipation channels is even more pronounced in the N/Ag(111) system, where the energy transfer to *e-h* pair excitations is around a factor two larger in the FS+EF than in the NFS+EF simulations after 3.5 ps. The results for $\langle E_{\rm ph} \rangle$ show that a rapid energy transfer takes place from the N atom to the surface lattice at $t < 1.5$ ps. In fact, this fast energy transfer is the main cause of adsorption in this system. After this short period of time, while $\langle E_{\rm ph} \rangle$ reaches a plateau, $\langle E_{\rm ehp} \rangle$ increases monotonically. Interestingly, we observe that, despite the phononic channel dominates N relaxation [see Fig. 3.12(a)], the energy lost to *e-h* pairs is by no means negligible.

The importance of the *e-h* pair excitations in this system can be also seen from Fig. 3.12(c), where the decay in time of the total energy of adsorbate is shown. While the difference between the NFS and the NFS+EF simulations was not noticeable in the kinetic energy decay rate presented in Fig. 3.12(a), it is clear from Fig. 3.12(c) that the total energy of the adsorbate $\langle E_{\rm tot}^A \rangle$ goes through a faster decay when the electronic energy loss is included. Generally this means that *e-h* pair excitations are not only affecting the kinetic energy, but also the potential energy experienced by the adsorbate, because they modify the trajectory. Similar to the H/Pd(100) case, the energy threshold for the N atom to jump from one hollow site to the neighbouring

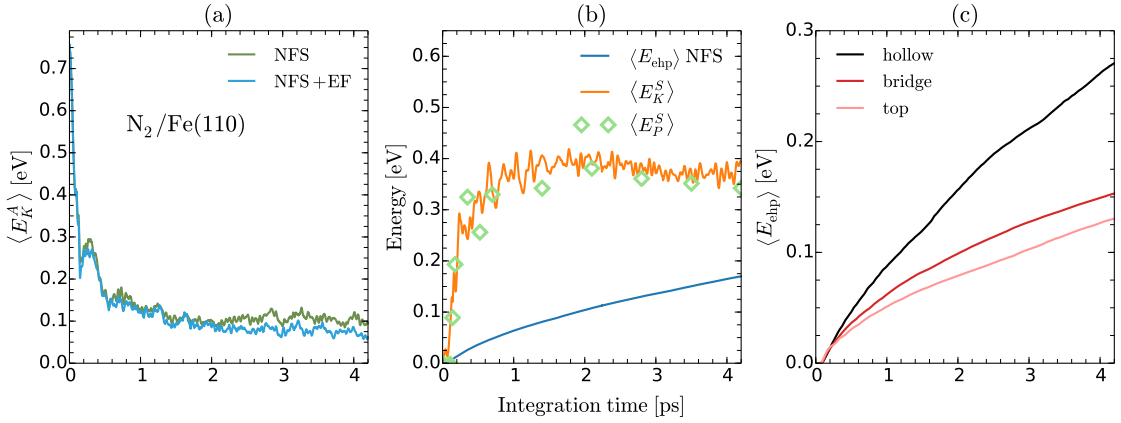

FIGURE 3.13: (a) Adsorbate kinetic energies averaged over AIMDEF-simulated trajectories of N_2 on Fe(110). (b) Corresponding contributions to the energy transferred to the surface upon adsorption in NFS+EF simulations: energy lost into *e-h* pair excitations $\langle E_{\text{ehp}} \rangle$, kinetic energy of surface atoms $\langle E_K^S \rangle$, and potential energy of the surface $\langle E_P^S \rangle$. Line colors description as in Fig. 3.11. (c) Energy lost to *e-h* pair excitation, $\langle E_{\text{ehp}} \rangle$, during NFS+EF simulations for N_2 trajectories ending up at each adsorption site on Fe(110).

one over the bridge site, $E_P^{\text{bri}}(\text{N})$, is almost reached for the NFS+EF simulations at the end of the simulation run [see the black dashed line in Fig. 3.12(c)]. Nevertheless, the relaxed N potential energies at the *fcc* and *hcp* sites [see the green dotted and red dashed-dotted lines in Fig. 3.12(c), respectively] indicate that the N atom still needs to lose a few hundred meV to be fully thermalised at either hollow site. As we will show in Sec. 3.5.2, the electronic excitations play an important role in the accommodation of the adsorbate in the adsorption well [221].

3.5.1.3 N_2/Fe(110)

The case of non-dissociative adsorption of N_2 on Fe(110) is more dramatic regarding the dominant role played by phonons over *e-h* pair excitations. In fact, there are no molecular adsorption events in the absence of surface atom movement (see also Sec. 3.4.1). Furthermore, the NFS and NFS+EF results in Fig. 3.13(a) are almost undistinguishable. In contrast to N/Ag(111), we do not observe the fast kinetic energy gain upon approach of the projectile to the surface. The reason is the presence of energy barriers at $z \sim 2.5$ Å that the molecules have to overcome before accessing the adsorption wells (see Fig. 3.1(c) and Refs. [164, 222]). As a result, we observe a drop of $\langle E_K^A \rangle$ starting at $t = 0$ that is the combined effect of an increase of the potential energy and of energy transfer to the surface lattice.

Similarly to the N/Ag(111) case, the $\langle E_{\text{ph}} \rangle$ values presented in Fig. 3.13(b) show a rapid energy transfer at $t < 0.5$ ps followed by a saturation. Around this

time period, the energy loss due to *e-h* pairs $\langle E_{\mathrm{ehp}} \rangle$ retains the monotonic increase. By comparing the $\langle E_{\mathrm{ehp}} \rangle$ curves in Figs. 3.12(b) and 3.13(b) it is clear that *e-h* pair excitation is much more important in N/Ag(111) than in N_2/Fe(110), though the initial kinetic energy of the projectile is larger in the latter. This is, in fact, related to the larger adsorption energies of N on Ag(111) than of N_2 on Fe(110) (see Table 3.1). The picture that emerges for these two systems is the following. At the first stages of the interaction the projectile transfers energy mainly to the lattice atoms in large momentum transfer collisions and gets trapped on the surface. Subsequently, it may travel as a hot species before being accommodated in the adsorption well by exciting, mainly, *e-h* pairs. The corresponding lateral movements of the adsorbates will be shown later in Sec. 3.5.2. Therefore, the amount of electronic excitation is closely related to the adsorption energy, i.e, to the energy that the adsorbate must dissipate to get fully relaxed. This is consistent with the reported scaling of the intensity of chemicurrents measured upon adsorption of different gas species with their adsorption energy [26].

The richness of the N_2/Fe(110) system regarding its adsorption properties allows us to characterize better this effect. More specifically, the existence of three adsorption wells permits to isolate the effect of E_{ads} on the *e-h* pair excitations from other factors. Figure 3.13(c) shows that the lowest $\langle E_{\mathrm{ehp}} \rangle$ occurs for adsorption on the top site, despite its E_{ads} is about 100 meV larger than on the bridge well. The reason is that the molecules adsorbed on top are farther away from the surface, where the electron density and, therefore, the probability to excite *e-h* pairs is considerably smaller [see Fig. 3.1(c) and Table 3.1]. The scaling of $\langle E_{\mathrm{ehp}} \rangle$ with E_{ads} is recovered when comparing the results for adsorption on the hollow and bridge wells, since in both cases the molecule is close to the surface in regions of relatively high and similar density.

The results of $\langle E^A_{\mathrm{tot}} \rangle$ as a function of time in Figs. 3.14(a)-(c) confirm that, independently of the adsorption site, N_2/Fe(110) is a system where the phonon energy loss channel dominates over the *e-h* pair excitations. It can be seen that the total energy of N_2 reaches the smallest value for the hollow site, while for the other two sites it remains slightly larger. This is mostly due to the different adsorption energies of N_2 (see Table 3.1). Interestingly, at the end of the simulation, the total energy of those molecules that end up on the top site [Fig. 3.14(a)] is still larger than for the ones that end up on the bridge site [Fig. 3.14(c)]. This result, which clearly contrasts with the values of E_{ads}, shows that thermalization at the top well is much slower than at the bridge one. This happens because both energy loss channels depend strongly on the adsorption configuration. As we already deduced from Fig. 3.13(c), the *e-h* pair excitations are less efficient at the top site since the molecule lies further from the surface where the electron density is lower. The comparison of the NFS curves in

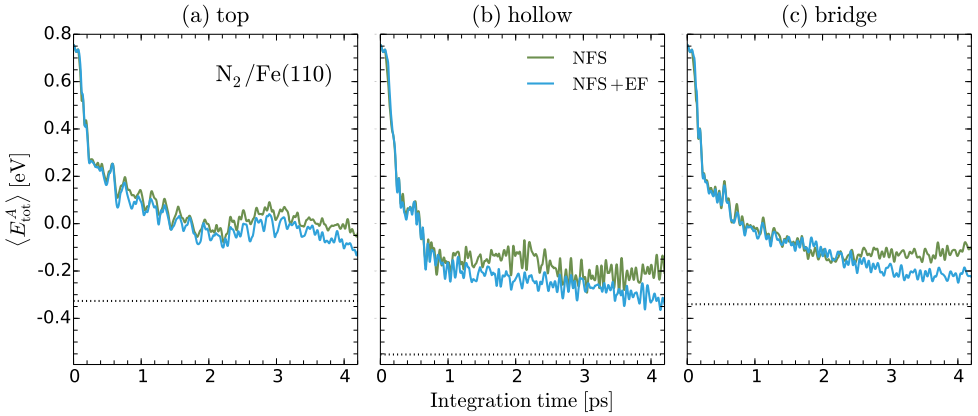

FIGURE 3.14: Average total energy of N_2 on Fe(110), $\langle E^A_{\text{tot}} \rangle$, as a function of the integration time for molecules that end up on (a) top, (b) hollow, and (c) bridge sites. The green (blue) lines correspond to NFS (NFS+EF) calculations. The horizontal dotted lines indicate the potential energy of the molecule at each adsorption site, which is calculated using Eq. (3.6).

Figs. 3.14(a) and (c) shows that the phonon excitation channel is also less efficient at the top site. However, the relationship between adsorption configuration and lattice excitations is less straightforward to understand here than in the electronic channel case. Finally, from the potential energies given by Eq. (3.6) for the molecule relaxed at each adsorption site, which are indicated by dotted lines in Figs. 3.14(a) and (c), we see that the molecules of the bridge site are the closest to thermalisation at the end of the simulation time.

3.5.1.4 Remarks on the *e-h* energy dissipation mechanism

All in all, Figs. 3.11, 3.12, 3.13, and 3.14 highlight that, under the usual conditions relevant for gas-surface reactions, *e-h* pair excitations will dominate energy dissipation only for light atoms ($\gamma \ll 1$). In principle, the kinetic energy of a free atom in a FEG decays at a rate $2\eta/m_A$, where m_A is the atom mass and its friction coefficient η depends non-trivially on the atomic number Z and the FEG density (Z-oscillations) [121]. Nevertheless, for the typical electron densities probed by hot atoms and molecules on metal surfaces, η varies slowly with Z [121, 133, 252] and thus the electronic decay rate is dominated by m_A. As a general trend, this causes the behavior observed in these figures, although the actual decay rates deviate from the free-atom values due to the PES topography of each system [33].

One of the remaining issues when accounting for the energy dissipation mechanisms is how to incorporate the *e-h* pair excitations created by the kinetically excited surface atoms. They can easily be incorporated with our present AIMDEF method. However, for the systems and incidence conditions considered here, we find that this

effect can be neglected within the time scale of the considered adsorption processes. We have made some estimations for the case of N/Ag(111), which is the system where the substrate atoms acquire the largest kinetic energies upon interaction with the impinging atom. The electron density for a surface Ag atom can be estimated by taking the electron density at a surface vacancy position. The corresponding mean electron radius would be $r_s \sim 5$ a.u., which results in a friction coefficient $\eta = 0.044$ a.u. for Ag. Using this value to estimate the energy relaxation rate for an ideal damped oscillator, we obtain $\eta/m(\mathrm{Ag}) = 0.009$ ps^{-1}. Interestingly, taking the value of the electron-phonon coupling factor for Ag at 300 K [2.5×10^{16} W/(m^{3}K)] [253] and dividing it by the specific heat of silver at the same temperature [2.52×10^6 J/(m^{3}K)], one obtains a similar relaxation rate of 0.010 ps^{-1}. Both estimations show that the rate at which the mobile Ag atoms dissipate energy to the electronic system is two orders of magnitude slower than the time scales of the hot atom relaxation processes studied in the present work.

3.5.2 Lateral displacements on the surface

Here we analyse the role of the *e-h* pair and phonon energy loss channels on the propagation of adsorbates on the surface for the three case studies. We calculate the averaged lateral distance $\langle l_\parallel \rangle$ traveled by the adsorbate from its initial in-plane coordinates (x_i, y_i) up to the end of the trajectories. In the case of the hot H and N atoms, for which the adsorption paths on the surface are more intricate and characterized by larger lateral displacements than for N_2 adsorption, we also calculate the averaged number of jumps between adjacent hollow sites $\langle N_{\mathrm{jumps}} \rangle$. These two quantities along with the knowledge of $\langle E^A_{\mathrm{tot}} \rangle$ allow a complete characterization of the hot species lateral movement on the surface, which is relevant for the reactivity properties. We show the results for each studied system next.

3.5.2.1 H/Pd(100)

Figs. 3.15(a) and 3.15(b) show the time evolution of $\langle N_{\mathrm{jumps}} \rangle$ and $\langle l_\parallel \rangle$, respectively, for H/Pd(100). We see that both quantities rapidly increase in the first 0.1 ps. It is during this time interval that the total energy of H is almost reduced by a half of the total energy lost at the end of simulation. The importance of *e-h* pair excitations in the relaxation process is also clearly visible in the trajectories. When the electronic energy loss channel is active, we observe a significant reduction in $\langle N_{\mathrm{jumps}} \rangle$ and $\langle l_\parallel \rangle$ by almost a factor of 2 and 1.5, respectively, at the final simulation time. Since the H atom in the NFS+EF simulations is close to the propagation threshold set by E_P^{bri}(H)

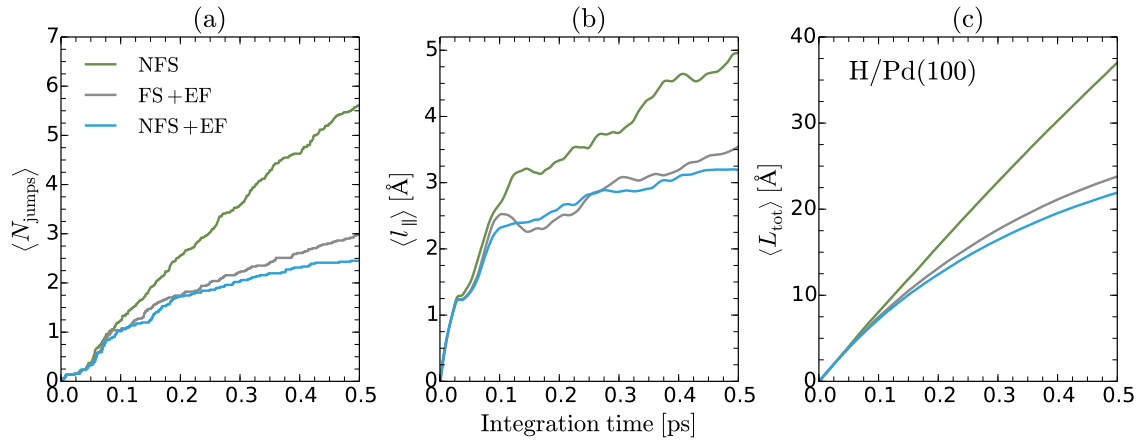

FIGURE 3.15: (a) Number of jumps between the hollow sites $\langle N_{\text{jump}} \rangle$, (b) lateral displacement from the initial position $\langle l_{\parallel} \rangle$, and (c) total traveled path length $\langle L_{\text{tot}} \rangle$, as a function of integration time for the H atom on Pd(100). Line colors description as in Fig. 3.11(a).

[see Fig. 3.11(c)], we can consider that the values of $\langle l_{\parallel} \rangle$ and $\langle N_{\text{jumps}} \rangle$ are basically close to saturation. With this information, we can establish that the final averaged number of jumps between neighbouring hollow sites will be between 2 and 3, while the lateral distance from the starting position will be around 3 Å [33]. Additionally, the averaged total traveled path length $\langle L_{\text{tot}} \rangle$ is shown in Fig. 3.15(c). The observed trend regarding the role of *e-h* pair excitations is similar to the cases of $\langle l_{\parallel} \rangle$ and $\langle N_{\text{jumps}} \rangle$.

3.5.2.2 N/Ag(111)

The dominant role of the phononic energy loss channel in the N/Ag(111) system, which was discussed in Sec. 3.5.1, is also apparent in Figs. 3.16(a)–(c) as a large difference in $\langle N_{\text{jumps}} \rangle$, $\langle l_{\parallel} \rangle$, and $\langle L_{\text{tot}} \rangle$ between the cases where the phonon energy loss channel is active (NFS and NFS+EF) and where it is not (FS+EF). We also observe that *e-h* pair excitations play a significant role in the difference between $\langle N_{\text{jumps}} \rangle$ obtained with the NFS and with the NFS+EF simulations, which amounts to $\Delta \langle N_{\text{jumps}} \rangle \approx 5$ in the final stage of the simulation. This difference is less noticeable for $\langle l_{\parallel} \rangle$ because the values in both cases are very similar and almost saturated after around 2 ps. However, the averaged traveled–path length $\langle L_{\text{tot}} \rangle$ at the end of the integration time is 4.5 Å longer in the NFS than in the NFS+EF simulations. First of all, the differences obtained in $\langle N_{\text{jumps}} \rangle$ and $\langle L_{\text{tot}} \rangle$ between both calculations show the importance of *e-h* pair excitations in the accommodation process of the N atom on the adsorption well [221]. And secondly, the saturation of $\langle l_{\parallel} \rangle$ reached after 2 ps in comparison to the still increasing behaviour of $\langle N_{\text{jumps}} \rangle$ (and also of $\langle L_{\text{tot}} \rangle$) tells us that N is hopping while conserving on average the in-plane distance to the initial

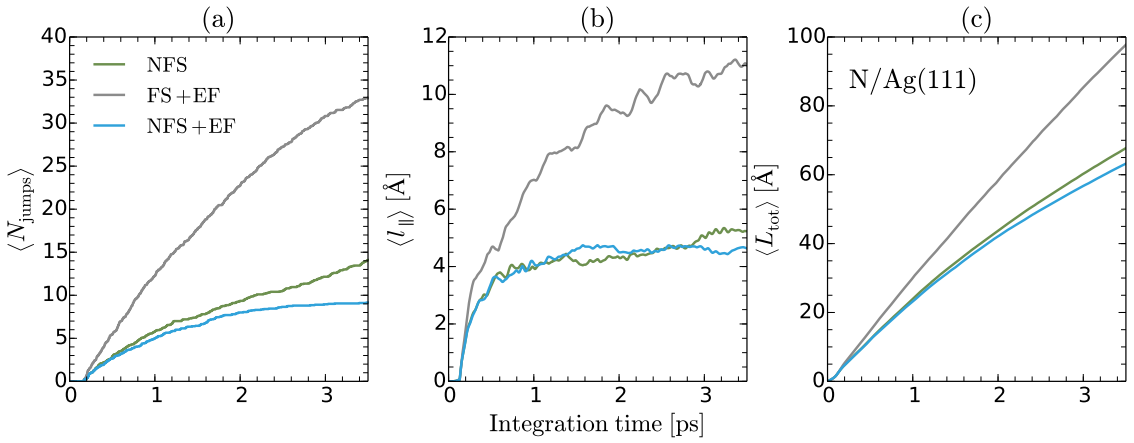

FIGURE 3.16: (a) Number of jumps between the hollow sites $\langle N_{\text{jump}} \rangle$, (b) lateral displacement from the initial position $\langle l_{\parallel} \rangle$, and (c) total traveled–path length $\langle L_{\text{tot}} \rangle$, as a function of integration time for the N atom on Ag(111). Line colors description as in Fig. 3.11(a).

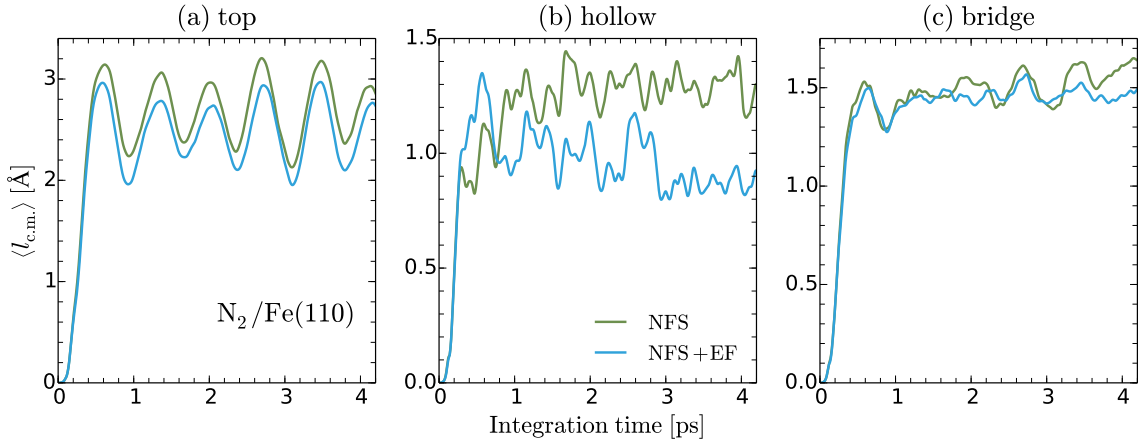

FIGURE 3.17: Lateral displacement of the N_2 molecules center of mass from the initial position $\langle l_{\text{c.m.}} \rangle$ as a function of the integration time for molecules that end up on (a) top, (b) hollow, and (c) bridge sites. Line colors description as in Fig. 3.14.

(x_i, y_i) coordinates. The fact that the $E_{\text{pot}}^{\text{bri}}(\text{N})$ threshold for N hopping is almost reached explains the saturation of $\langle N_{\text{jumps}} \rangle$ and $\langle l_{\parallel} \rangle$ by the end of the simulation run in the NFS+EF case, as discussed above. By comparing $\langle N_{\text{jumps}} \rangle$ and $\langle l_{\parallel} \rangle$ for this case with the H/Pd(100) case, it is clear that the N atom propagates longer distances than the H atom, which is primarily due to their different adsorption energies.

3.5.2.3 N_2/Fe(110)

Figures 3.17(a)–(c) show the time dependence of the statistically averaged lateral distance of the N_2 center of mass from its initial position (x_i, y_i), $\langle l_{\text{c.m.}} \rangle$, for the three adsorption sites. We have checked that the N_2 molecule barely makes jumps between adsorption sites and that it arrives quite fast at the maximum lateral distance. The

latter happens at around 0.5 ps for all the adsorption sites and it is due to the repulsive character of the PES for the approaching molecule [see Fig. 3.1(c) and Refs. [164, 222]], which strongly reduces the total energy in the first collision with the surface [see Figs 3.14(a)-(c)]. Afterwards, the molecules undergo small lateral displacements mostly due to movement at the adsorption site. For the molecules adsorbed at the top site this can be observed through oscillations of $\langle l_{\mathrm{c.m.}} \rangle$ for $t \gtrsim 0.5$ ps, which mostly come from the combination of frustrated translational modes and precession of the molecular center of mass on top of the Fe atom. We see that molecules ending up at the top sites reach the largest $\langle l_{\mathrm{c.m.}} \rangle$, while those ending up at hollow or bridge sites the smallest. This is due to the PES profile: at the top site N_2 lies upright and bound to one Fe atom, while it lies parallel and tightly bound to the surface at the other two sites due to the bonds that it forms with more than one Fe atom. As for the difference between the NFS and NFS+EF calculations, we observe that the excitation of *e-h* pairs causes in general a decrease in $\langle l_{\mathrm{c.m.}} \rangle$. The largest reduction of around 0.5 Å occurs for the hollow site, i.e., the configuration that, having the largest E_{ads} and being closest to the surface, where the electron density is high, better fulfills the conditions for an efficient excitation of *e-h* pairs.

3.6 Conclusions

3.6.1 On the surface density models

We have examined the performance of different models of the bare surface electron density n_{sur} in AIMDEF simulations of the adsorption dynamics of atoms and molecules on metals, using H, N, and N_2 on Pd(100), Ag(111), and Fe(110), respectively, as case studies. In the original formulation of AIMDEF the surface electron density n_{sur}, which is used to calculate the electronic friction force acting on the adsorbing species, was approximated by that of the frozen surface $n_{\mathrm{sur}}^{\mathrm{FS}}$ (FSM model). Here, we improve the methodology by using models that account for the n_{sur} changes brought by the displacements of the surface atoms during the simulations, which can reach considerably large values of up to ~ 0.4 Å in some of the studied surfaces. The proposed n_{sur} models are constructed *on-the-fly* at each simulation time step from either superposition of atomic electron densities (ASM model) or a Hirshfeld partitioning scheme (HM model) of the total self-consistent density.

From *static* analyses for a few fixed geometries, we deduce that all the models accurately reproduce n_{sur} at the hot atom positions, as required by the simulations,

and also that they provide good estimates at other positions. In a subsequent *dynamical* analysis, we find that the three of them yield similar energy loss rates, despite the limitations of FSM to model the distorted surface density as compared to ASM or HM. An in-depth examination of the trajectories reveals that FSM can produce significant deviations in the friction coefficients that depend closely on the surface density regions visited by the adsorbates.

Although the results presented in this work apply to a particular class of dynamical processes, they allow us to establish some guidelines for the applicability of each model in a broader context. First, we have shown that, when the dynamics involves large displacements of the surface atoms, $n_{\mathrm{sur}}^{\mathrm{FS}}$ clearly deviates from the average electron densities experienced by the hot species. Therefore, when modeling surface processes of similar characteristics, such as temperature effects in gas-surface interactions, ASM and HM will prove more reliable. Secondly, if the electronic structure of the surface under study is sensitive to changes in the interatomic distances, then HM is to be preferred over ASM, because it accounts more realistically for the charge distribution at the crystal bonds. This is particularly relevant in the description, for example, of surface penetration dynamics, where the projectile travels across both surface and bulk environments, of distinct electronic structure. Such penetration processes are more likely to occur, for instance, for faster impinging atoms. In practical terms, the evaluation of the Hirshfeld partitioning of charge in HM simulations does not imply a major computational cost increase with respect to the other methods. For all the reasons stated here, we can conclude that the use of a surface electron density model based in a Hirshfeld partitioning scheme can be considered a highly accurate and efficient strategy to describe *e-h* pair excitations in AIMDEF simulations. Finally, note that our new AIMDEF methodology is also well-suited to incorporate, when necessary, the effect of the *e-h* pair excitations created by the moving surface atoms.

3.6.2 On the role of electron-hole pair excitations

We have used the adapted AIMDEF methodology described above with the surface electron density based in Hirshfeld partitioning scheme to study the role of *e-h* pair and phonon excitations during the thermalization of hot species on the aforementioned systems. The use of different representative systems allow us to extract general conclusions for reactions on surfaces. Thermalization of light hot reactants and intermediate products on the surface, e.g. H, will happen at a faster rate than for heavier species that involve C, N, O, because *e-h* pairs are more efficiently excited by the lighter atoms. For heavier atoms, we find that dissipation is dominated by lattice

vibrations mainly at the initial stages of the hot species interaction with the surface, along with a substantial excitation of *e-h* pairs that is active during long timescales. The inspection of the corresponding lateral displacements of the adsorbates shows how this persistent *e-h* pairs excitations play a decisive role for the final accommodation in the adsorption well. We find that more energy is diverted into the *e-h* pair channel for higher adsorption energies, in consistency with the experimental observations on chemicurrents, although deviations from that behavior can be induced by the particular details of the surface electron density distribution. These conclusions can only be drawn within the theory level used here. Ultimately, the weight of each channel in the energy loss is the result of the non-trivial interplay of atomic masses, PES topography and surface electronic structure.

Chapter 4

Vibrational linewidths of adsorbed molecules on metal surfaces under the influence of electronic damping processes

4.1 Introduction

In the previous chapter, the breakdown of the BOA was triggered by a hot atom or molecule moving on a metallic surface during the adsorption process. In that case, the equations of motion for the adsorbate acquire an additional dissipative term, namely the electronic friction force, which describes the energy exchange between the adsorbate in motion and the substrate electronic degrees of freedom. In the adiabatic limit and when the excited electrons are treated as non-interacting (i.e., the adsorbate motion is the only perturbation for the electrons) the friction coefficient is described by Eqs. (2.58) and (2.60). However, under real experimental conditions, the excited electrons in the metallic substrate undergo various scattering processes and the effects beyond the non-interacting picture can be important. The goal of this chapter is to extend our previous analysis of the breakdown of the BOA by investigating the subtle details of the electronic scattering processes and their impact on the adsorbate movement. More specifically, on its vibrational damping rates. Instead of looking at the nonadiabatic effects of a single adsorbate, here we concentrate on the ordered molecular layer adsorbed on metallic surface. In other words, the nonadiabatic effects studied here have their origin at the coupling between the collective motion of the molecular layer, i.e., the phonons, and the electrons of the substrate.

As discussed throughout chapter 2, the BOA is fundamentally valid only for systems where the energies of the electronic excitations are much larger than the vibrational energies (adiabaticity) [138], e.g. insulators and semiconductors. However, it turns out that the BOA gives a very good description of the phonon dispersions even in metallic systems [135], where the adiabatic condition is not met. Nevertheless, the early theoretical studies on the electron-phonon interaction in metallic systems [6, 11, 12, 142] demonstrated that nonadiabaticity manifests not only through the renormalization of the phonon spectrum, but also as the appearance of the corresponding phonon linewidth (i.e., rate of phonon relaxation).

In the context of the dynamical effects of adsorbed atomic and molecular species on metallic surfaces, the experimentally observed finite vibrational linewidths of the adsorbates high-frequency modes reflects the importance of nonadiabatic corrections (see Ref. [16] and references therein). Namely, the experiments show how the lifetime of vibrationally excited dipolar molecules is substantially reduced from the millisecond regime in the gas phase to the picosecond regime on various metallic surfaces. For example, the lifetime of the CO stretch mode in the gas phase is 33 ms [254], while it reduces to around 2 ps when adsorbed on Cu(100) [21] and Pt(111) [255]. As pointed out in the introduction of chapter 3, further evidences of nonadiabaticity are found in the chemicurrent experiments [25, 26, 191]. Similarly, excited electrons are observed when highly vibrationally excited molecules collide with a metal surface [24, 27]. Great theoretical efforts have also been made in order to explain these effects, either by using isotropic friction coefficients in molecular dynamics simulations, i.e. the methodology described in Secs. 2.3.4 and 3.3 [33, 34, 198, 219, 241, 242, 248], or by calculating the vibrational damping rate with Fermi's golden rule formula [36–40, 49, 51, 154, 249, 256–258].

In the aforementioned cases the key physical quantity for understanding nonadiabatic effects on the vibrational spectra is the phonon self-energy due to electron-phonon coupling $\Pi_\lambda(\mathbf{q},\omega)$ defined by Eq. 2.89 (here $\mathbf{q}$ and ω are the momentum and frequency of the excitation and λ denotes the phonon mode). The static part of this phonon self-energy $\Pi_\lambda(\mathbf{q},0)$ (i.e., in the $\omega \ll |\varepsilon_\alpha - \varepsilon_\beta|$ limit, where $\varepsilon_{\alpha,\beta}$ are the eigenvalues of the electronic states α and β involved in the coupling) is relevant for obtaining the adiabatic phonon frequencies [259], while the dynamic part $\Pi_\lambda(\mathbf{q},\omega \neq 0)$ gives information on the nonadiabatic effects (see Sec. 2.4). More specifically, the imaginary part of the latter is related to the phonon linewidth, while the real part renormalizes the phonon frequency. In usual vibrational spectroscopy experiments (e.g., infrared and Raman spectroscopies) an electromagnetic field is used as the external perturbation. Therefore, the relevant phonon self-energy for describing these experimental results is the long-wavelength part of this self-energy,

$\Pi_\lambda(\mathbf{q} \approx 0, \omega)$ [260]. It has been shown, both experimentally [261–264] and theoretically [11, 12, 42, 265–267], that this $\mathbf{q} \approx 0$ part is considerably affected by the relaxation processes of the electronic system (e.g., electron scattering on phonons, impurities or other electrons), in a close analogy with the $\mathbf{q} \approx 0$ part of the Kubo conductivity formula [9, 10, 41, 129, 268–270] and the electronic Raman correlation function [271–275]. In particular, the intraband part, which includes transitions only within the same electronic band, goes to zero in the clean (i.e., impurity-free) non-interacting limit, while it takes a finite value when electron relaxation processes are considered. In fact, for high vibrational frequencies, $\omega_{\mathbf{q}\lambda} \gg |\varepsilon_\alpha - \varepsilon_\beta|$, it is proportional to $(\omega\tau_{\mathrm{tr}})^{-1}$ [11, 275, 276], where τ_{tr} is the electron transport relaxation time. These scattering processes affect the interband part, which includes transitions between two different electronic bands, in a similar manner as well [277].

In this chapter we analyze the DFT-based phonon self-energy due to the electron-phonon coupling with emphasis on the mentioned electronic relaxation processes. As opposed to chapter 3, where energy exchange mechanisms of single adsorbates on metallic surfaces are investigated with a time resolution, here we focus on dynamical effects of ordered monolayers of adsorbates on metallic surfaces in the $(\mathbf{q}, \omega)$ space. To account for relaxation processes we use the relaxation time approximation (RTA), where the frequency- and momentum-dependent damping function, the so-called *e-h* self-energy [41], is replaced by the variable parameter Γ. This way of treating the phonon self-energy can be useful for those numerical calculations where the broadening parameter, used for summation over the momentum space, has a finite value [38, 39, 49, 154, 249, 257].

Apart from the phenomenological RTA approach, we derive and calculate from first principles the *e-h* self-energy due to the electron-phonon scattering processes, which quantifies the additional damping of the $(\mathbf{q} \approx \mathbf{0}, \lambda)$ mode due to all other $(\mathbf{q}', \lambda')$ modes in the system. Accordingly, this *e-h* self-energy is then temperature- and frequency-dependent [9, 11, 12, 41, 42, 129, 272, 278]. This higher-order process can be described as the *indirect* phonon-phonon coupling mediated by the *e-h* excitations [50, 279]. For the specific situation, where the quasi-elastic *e-h* excitations relax the studied $(\mathbf{q} \approx \mathbf{0}, \lambda)$ mode into other $\mathbf{q}'$ modes within the same λ phonon band, this *e-h* self-energy accounts for *e-h* pair dephasing (i.e., decay of the phase memory of the phonon excitation)[1] [280]. These contributions, coming from electron-phonon scattering, are considered to be important for understanding the relaxation processes of phonon modes where *e-h* pairs are the main excitation channel. The present

[1] In Sec. 2.5 we defined the dephasing time within the density matrix theory very generally, namely as the time at which the interference between two quantum states decays. Here we have the specific situation where these two states are the ground and excited states of the $(\mathbf{q} \approx \mathbf{0}, \lambda)$ mode, and the quasi-elastic *e-h* excitations break down the correlation between these two states (i.e., dephasing).

approach to accounting for the electronic relaxation processes is more general and can be formally applied to the problems of long-wavelength conductivity [41, 270] and electronic Raman scattering[2] [275, 276, 281].

When all the contributions to the total phonon self-energy are summed up, the obtained value needs to be compared with the experimental results. However, to make a meaningful comparison, it is necessary to understand the corresponding technique for measuring the vibrational linewidth. Two of the most widely used methods for extracting the vibrational spectra of ordered molecular layers adsorbed on surfaces are IRAS and pump-probe laser spectroscopy [16]. In the former technique the sample interacts with the incident infrared light and the corresponding reflected beam is used to analyse the absorption. When the frequency of the incident light coincides with the infrared-active[3] vibrational mode of molecule, the resonant peak with the Lorentzian-like shape appears in the absorption spectrum. In this technique the linewidth of the resonant peak, i.e., the so-called full width at half maximum FWHM, contains at least two contributions [16, 20, 282]: the energy relaxation rate, which measures the decay of the excited state population, and the vibrational phase relaxation rate (i.e., the aforementioned dephasing) [282–284]. Unlike the former contribution, the latter contribution to the linewidth is energy-conserving, i.e., it includes elastic scattering processes. Another important contribution comes from disorder and impurities (i.e., inhomogeneities), which can be either static or vibrating [285]. Distinguishing these contributions to the linewidth is very difficult in IRAS, but fortunately pump-probe spectroscopy is at least sensitive to the energy relaxation rate. In this technique the first step is to saturate the population of the studied mode with a resonant infrared pump laser. After some delay time the probe, consisting of weak infrared and visible lights, creates a non-linear polarization effect, which contains information on a population difference between the excited and the ground states (i.e., energy-non-conserving processes), and on dephasing and inhomogeneities. If the probe is just a weak visible light, the corresponding polarization gives only the energy-conserving linewidth. In this chapter we use this knowledge of the different contributions to the linewidths obtained in IRAS and pump-probe spectroscopy experiments to understand and benchmark our theoretical phonon linewidths obtained from phonon self-energy calculations.

As case study we select the stretch mode of an ordered CO molecular layer adsorbed on the Cu(100) surface, which was one of the first examples that revealed the

[2]This is due to the two-particle propagator form of the phonon self-energy, which is the essential part of the general correlation function. Extending this formalism to other physical problems is equivalent to changing the electron-phonon vertex by the corresponding vertex (e.g., Raman vertex in the case of electronic Raman scattering).

[3]The vibrational mode is infrared-active when the dipole moment of the molecule perpendicular to the metal surface changes with the motion.

importance of nonadiabatic corrections for the vibrational lifetimes of adsorbates on metal surfaces. The earliest experiments done on this system with IRAS reported vibrational lifetimes in the range $\tau = 1.2 - 1.4$ ps, or the corresponding linewidths $\gamma = 110 - 140$ GHz [20, 22]. The slight change of the linewidth with surface temperature observed in Ref. [22] ($\delta\gamma \approx 11$ GHz within the range $T = 100 - 160$ K) was attributed to pure anharmonic dephasing. The latter process describes the anharmonic relaxation of the high-frequency CO stretch mode via the quasi-elastic scattering with the low-frequency intramolecular modes. This coupling is analogous to the aforementioned *e-h* pair dephasing, where the role of low-frequency phonon modes is played by *e-h* pairs. Nevertheless, this anharmonic effect on the linewidth is relatively small and the excitation of *e-h* pairs is still considered to be the relevant damping channel [282]. Later pump-probe laser spectroscopy experiments reported lifetimes of the same order of magnitude, $\tau = 2 \pm 1$ ps ($\gamma = 80 \pm 40$ GHz) [21]. These experimental results were modelled by many theoretical calculations [36–40, 49, 248]. However, none of these studies made a clear distinction between the $\mathbf{q} \approx 0$ intraband and interband contributions, neither they considered the case where the phonon relaxation rate due to electron-phonon coupling is additionally triggered by other electronic scattering processes (such as electron-electron, electron-impurity, and higher-orders of electron-phonon scatterings)[4]. The use of large values of numerical broadening intended to fit experiments could mask the subtle physical mechanisms responsible for the phonon linewidth. Therefore, in this chapter we emphasize the importance of the correct interpretation of the broadening parameter: whenever a finite Γ is used, one should be aware that electronic damping processes are being included in the phonon self-energy (or in any other correlation function). Therefore, in doing so, physically meaningful values of Γ need to be used.

This chapter is organized as follows. In Sec. 4.2 we present the general theory for obtaining nonadiabatic effects in the electron-phonon system and we define the corresponding phonon self-energy. Using this general formulation as the starting point, in Sec. 4.2.1 we derive the bare phonon self-energy valid in the clean noninteracting regime. In Sec. 4.2.2 we introduce the electronic damping rate in a phenomenological way (RTA). A discussion on the effects of long-range screening on the bare phonon self-energy is given in Sec. 4.2.3. In Sec. 4.2.5 we derive the high-energy intraband phonon self-energy relevant for the large (optical) phonon frequencies and in the presence of impurities (dirty regime) and other phonons. The validity of the widely used so-called quasi-static approximation of the phonon self-energy, which consists in taking the limit of small phonon frequencies, in evaluating the linewidth

[4] Although it was not studied to a great extent, the problem of finite broadening of the electronic states has been addressed earlier in the context of nonadiabatic effects in the adsorbate-surface dynamics [256]. However, the broadening is considered there to be only due to the interaction between the adsorbate and metal states, i.e., due to electron-electron interaction.

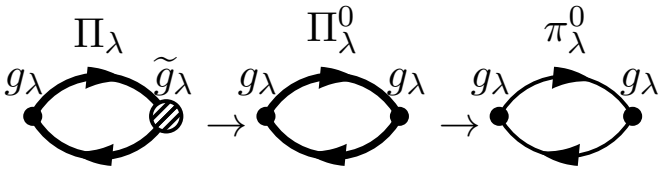

FIGURE 4.1: Diagrammatic representation of the reduction of the exact phonon self-energy Π_λ to the bare one π^0_λ. The thick lines correspond to the exact Green's function G, while the thin lines to the bare G^0. The bare and dressed electron-phonon vertex functions are labelled g_λ and $\widetilde{g}_\lambda$, respectively.

of high-frequency vibrational modes is discussed in Sec. 4.2.4. In Sec. 4.3 we put the theory presented in Sec. 4.2 into practice using CO adsorbed on Cu(100) as a case study. We give the computational details, geometric and electronic structure, interband and intraband phonon linewidths, total phonon linewidth, and renormalized phonon frequencies for the CO stretch mode on Cu(100) in Secs. 4.3.1, 4.3.2, 4.3.3, 4.3.4, 4.3.5, and 4.3.6, respectively. Finally, we present the concluding remarks in Sec. 4.4.

4.2 Phonon self-energy with electronic damping effects

In Secs. 2.4.3 and 2.4.4 we laid down the foundations for understanding electron-phonon interaction and how to incorporate electronic relaxation processes into the phonon self-energy due to electron-phonon coupling. Here we recall that nonadiabatic effects are actually dynamic effects, which means that the corresponding phonon self-energy needs to be obtained for $\omega \neq 0$. In addition, the damping effects coming from the electronic degrees of freedom enter the phonon self-energy through the electron propagator (i.e., electron Green's functions) defined by Eq. (2.86). In order to see this more clearly we use the Dyson equation for the electron Green's function $G_\mu(\mathbf{k}, i\omega_n)$ defined by Eq. (2.82) to express $\Pi_\lambda(\mathbf{q}, i\nu_n)$ in a slightly different form to that of Eq. (2.89)

$$\begin{aligned}\Pi_\lambda(\mathbf{q}, i\nu_n) &= \sum_{\mu\mu'\mathbf{k}\sigma} \frac{1}{\beta} \sum_{i\omega_n} \left[g^{\mu\mu'}_\lambda(\mathbf{k}, \mathbf{q}) \right]^* \widetilde{g}^{\mu\mu'}_\lambda(\mathbf{k}, \mathbf{q}, i\omega_n, i\nu_n) \\ &\quad \times \frac{G_\mu(\mathbf{k}, i\omega_n) - G_{\mu'}(\mathbf{k}+\mathbf{q}, i\omega_n + i\nu_n)}{i\nu_n + \varepsilon_{\mu\mathbf{k}} - \varepsilon_{\mu'\mathbf{k}+\mathbf{q}} + \Delta\Sigma_{\mu\mu'}(\mathbf{k}, \mathbf{q}, i\omega_n, i\nu_n)},\end{aligned} \tag{4.1}$$

where we define the bare *e-h* self-energy as the difference between two single-electron self-energies, i.e., $\Delta\Sigma_{\mu\mu'}(\mathbf{k},\mathbf{q},i\omega_n,i\nu_n) \equiv \Sigma_\mu(\mathbf{k},i\omega_n) - \Sigma_{\mu'}(\mathbf{k}+\mathbf{q},i\omega_n+i\nu_n)$ [41]. This exact phonon self-energy due to electron-phonon coupling is represented by the first bubble diagram in Fig. 4.1 [6, 8, 259]. From the above expression we can see what the role of the *e-h* self-energy is: its real part renormalizes the electronic structure (i.e., the electron energy levels $\varepsilon_{\mu\mathbf{k}}$), while its imaginary part gives additional damping to the phonon spectrum. Another source of the electronic damping in this phonon self-energy is that from the electron self-energies that enter the Green's functions in the numerator giving a finite smearing to the electron occupation functions. This is discussed further in Sec. 4.2.2.

The analytical continuation of the phonon propagator $D_\lambda(\mathbf{q},i\nu_n)$, defined in terms of $\Pi_\lambda(\mathbf{q},i\nu_n)$ [see Eq. (2.87)], is of great interest, because its imaginary part gives the spectral function of the phonon excitations, which is measured experimentally by, for example, IRAS. The phonon linewidth and the renormalized phonon frequency are then respectively given by[5]

$$\gamma_{\mathbf{q}\lambda} = -2\mathrm{Im}\Pi_\lambda(\mathbf{q},\omega_{\mathbf{q}\lambda}) \tag{4.2}$$

and

$$\omega^2 = \omega_{\mathbf{q}\lambda}^2 + 2\omega_{\mathbf{q}\lambda}\mathrm{Re}\Pi_\lambda(\mathbf{q},\omega), \tag{4.3}$$

where Eq. (4.3) needs to be calculated self-consistently. Our main goal is to analyse these quantities and, in particular, to study the impact of the electronic scattering processes on the phonon linewidth $\gamma_{\mathbf{q}\lambda}$.

4.2.1 Bare phonon self-energy

The first step of our analysis consists in examining the general properties of the bare phonon self-energy defined by Eq. (2.91). We recall that the bare phonon self-energy is defined as in the third bubble diagram of Fig. 4.1, i.e. without vertex corrections and with the exact Green's function $G_\mu(\mathbf{k},i\omega_n)$ [Eq. (2.86)] replaced by the bare one $G_\mu^0(\mathbf{k},i\omega_n)$ [Eq. (2.84)]. By doing this, the phonon self-energy is reduced to a form that describes the ideal electron-phonon system, where the impurities, the electron-electron interactions and higher orders of electron-phonon interactions are neglected.

[5] If one is interested in the electronic excitations (e.g., single-electron excitations or plasmons), it is useful to know that the spectral function of the phonon excitations shares close resemblance with the energy loss function, $\mathrm{Im}\,\varepsilon^{-1}(\mathbf{q},\omega)$, but then $\omega_{\mathbf{q}\lambda}$ and Π_λ would have to be replaced by the bare plasmon energy and the appropriate current-current correlation function, respectively [270, 286, 287]. In that case Eq. (4.2) would give the plasmon linewidth, while Eq. (4.3) the renormalization of its energy.

For systems in which these scattering processes do not play an important role, the bare phonon self-energy serves as a good approximation for obtaining the phonon spectra. The form of the bare phonon self-energy is as follows (see Sec. 2.4.4 and Refs. [142, 267])

$$\pi_\lambda^0(\mathbf{q},\omega) = \sum_{\mu\mu'\mathbf{k}\sigma} \left| g_\lambda^{\mu\mu'}(\mathbf{k},\mathbf{q}) \right|^2 \frac{f_{\mu\mathbf{k}} - f_{\mu'\mathbf{k}+\mathbf{q}}}{\omega + \varepsilon_{\mu\mathbf{k}} - \varepsilon_{\mu'\mathbf{k}+\mathbf{q}} + i\eta}, \tag{4.4}$$

where $\eta \to 0^+$, $f_{\mu\mathbf{k}} = (1/\beta)\sum_{i\omega_n} G_\mu^0(\mathbf{k}, i\omega_n)$ is the temperature-dependent Fermi-Dirac distribution function, and $\beta = 1/k_B T$.

To get a closer insight into the bare phonon self-energy and to understand what kind of electronic excitations are involved in it, we decompose it in its intraband ($\mu = \mu'$) and interband ($\mu \neq \mu'$) contributions, i.e.

$$\pi_\lambda^0(\mathbf{q},\omega) = \pi_\lambda^{\text{intra},0}(\mathbf{q},\omega) + \pi_\lambda^{\text{inter},0}(\mathbf{q},\omega). \tag{4.5}$$

Due to the long-wavelength nature of the electromagnetic field in infrared spectroscopy experiments, our main concern are the $\mathbf{q} \approx 0$ phonons. In that case we can expand the intraband part of expression (4.4) into powers of small $\mathbf{q}$ and write the first non-zero term as

$$\pi_\lambda^{\text{intra},0}(\omega) = \sum_{\mu\mathbf{k}\sigma,\alpha\beta} \frac{\left| g_\lambda^{\mu\mu}(\mathbf{k},0) \right|^2}{(\omega + i\eta)^2} f_{\mu\mathbf{k}} \frac{\partial^2 \varepsilon_{\mu\mathbf{k}}}{\partial k_\alpha \partial k_\beta} q_\alpha q_\beta, \tag{4.6}$$

where we write $\pi_\lambda^{\text{intra},0}(\mathbf{q} \approx 0, \omega) \equiv \pi_\lambda^{\text{intra},0}(\omega)$ to simplify the notation. This expression allows us to extract already some important conclusions about the nature of the bare $\mathbf{q} \approx 0$ intraband phonon self-energy: (i) the terms of order q^0 and q^1 are zero, so when $q \to 0$ then $\pi_\lambda^{\text{intra},0} \to 0$ as q^2, (ii) the dependence q^2/ω^2 resembles the Lindhard-like form of the charge-charge correlation function if $\left| g_\lambda^{\mu\mu}(\mathbf{k},0) \right|^2$ is replaced with the bare charge vertex $\left| \rho^{\mu\mu}(\mathbf{k}, \mathbf{q} \approx 0) \right|^2 = \left| \langle \psi_{\mu\mathbf{k}+\mathbf{q}} | \, e^{-i\mathbf{q}\cdot\mathbf{r}} \, | \psi_{\mu\mathbf{k}} \rangle \right|^2 \approx 1$ [126], (iii) the imaginary part is proportional to $\delta(\omega)/\omega$, where $\delta(\omega)$ is the Dirac-delta function, thus only the acoustic phonons are damped.

The interband part for $\mathbf{q} \approx 0$ is

$$\pi_\lambda^{\text{inter},0}(\omega) = \sum_{\mu\neq\mu',\mathbf{k}\sigma} \left| g_\lambda^{\mu\mu'}(\mathbf{k},0) \right|^2 \frac{f_{\mu\mathbf{k}} - f_{\mu'\mathbf{k}}}{\omega + \varepsilon_{\mu\mathbf{k}} - \varepsilon_{\mu'\mathbf{k}} + i\eta}. \tag{4.7}$$

Here $f_{\mu\mathbf{k}} \neq f_{\mu'\mathbf{k}}$, which in principle makes the $\mathbf{q} \approx 0$ interband self-energy finite for all phonon (acoustic and optical) modes. We write the imaginary and real parts of

the latter contribution as

$$\mathrm{Im}\pi_{\lambda}^{\mathrm{inter},0}(\omega) = -\pi \sum_{\mu\neq\mu',\mathbf{k}\sigma} \left|g_{\lambda}^{\mu\mu'}(\mathbf{k},0)\right|^2 (f_{\mu\mathbf{k}} - f_{\mu'\mathbf{k}})\,\delta(\omega + \varepsilon_{\mu\mathbf{k}} - \varepsilon_{\mu'\mathbf{k}}) \tag{4.8}$$

and

$$\mathrm{Re}\pi_{\lambda}^{\mathrm{inter},0}(\omega) = \sum_{\mu\neq\mu',\mathbf{k}\sigma} \left|g_{\lambda}^{\mu\mu'}(\mathbf{k},0)\right|^2 \mathcal{P}\frac{f_{\mu\mathbf{k}} - f_{\mu'\mathbf{k}}}{\omega + \varepsilon_{\mu\mathbf{k}} - \varepsilon_{\mu'\mathbf{k}}}, \tag{4.9}$$

where $\mathcal{P}$ stands for the principal value. Expressions (4.2) and (4.8) show that the linewidth of the $\mathbf{q} \approx 0$ phonon mode is finite due to interband transitions only if the condition $\omega_{\mathbf{q}\lambda} = \varepsilon_{\mu'\mathbf{k}} - \varepsilon_{\mu\mathbf{k}}$ is strictly met. Since we are mainly interested in the optical phonon modes, we can safely use the interband part as the total $\mathbf{q} \approx 0$ bare phonon self-energy, i.e.

$$\pi_{\lambda}^{0}(\omega) \approx \pi_{\lambda}^{\mathrm{inter},0}(\omega). \tag{4.10}$$

This result is analogous to the first-order Fermi's golden rule formula for the phonon damping rate due to the electron-phonon interaction [56].

The bare phonon frequency $\omega_{\mathbf{q}\lambda}$ that enters the phonon propagator of Eq. (2.87) is usually calculated within the adiabatic approximation (see Secs. 2.4.3 and 2.4.4). Therefore, to avoid the erroneous phonon renormalization by counting the adiabatic contribution twice, the bare phonon self-energy value at $\omega = 0$ (adiabatic part) should be subtracted in Eq. (4.4) as follows [8, 54, 55, 136, 142, 288, 289]

$$\begin{aligned} \widehat{\pi}_{\lambda}^{0}(\mathbf{q},\omega) &= \pi_{\lambda}^{0}(\mathbf{q},\omega) - \pi_{\lambda}^{0}(\mathbf{q},0) \\ &= \sum_{\mu\mu'\mathbf{k}\sigma} \frac{-\omega \left|g_{\lambda}^{\mu\mu'}(\mathbf{k},\mathbf{q})\right|^2}{\varepsilon_{\mu\mathbf{k}} - \varepsilon_{\mu'\mathbf{k}+\mathbf{q}}} \frac{f_{\mu\mathbf{k}} - f_{\mu'\mathbf{k}+\mathbf{q}}}{\omega + \varepsilon_{\mu\mathbf{k}} - \varepsilon_{\mu'\mathbf{k}+\mathbf{q}} + i\eta}. \end{aligned} \tag{4.11}$$

It can be seen from Eq. (4.11) that this correction can also be done informally by replacing one of the vertex functions $g_{\lambda}^{\mu\mu'}(\mathbf{k},\mathbf{q})$ with $-\omega g_{\lambda}^{\mu\mu'}(\mathbf{k},\mathbf{q})/(\varepsilon_{\mu\mathbf{k}} - \varepsilon_{\mu'\mathbf{k}+\mathbf{q}})$ in Eq. (4.4) [54]. Since the parameter η is infinitesimal in the bare phonon self-energy, this subtraction only affects the real part of the phonon self-energy (renormalization of the phonon frequency), while the imaginary part stays the same. We will see in Sec. 4.2.2 that this is not the case in the RTA regime, due to the spurious effects that appear when including damping mechanisms in the system by hand.

For the intraband part of the $\mathbf{q} \approx 0$ bare phonon self-energy $\widehat{\pi}_{\lambda}^{0}(\mathbf{q},\omega)$ already the

q^0 order term is not zero. Thus, to renormalise the phonon spectrum with $\widehat{\pi}^0_\lambda(\mathbf{q},\omega)$ both the intraband and interband parts should be included,

$$\mathrm{Re}\widehat{\pi}^0_\lambda(\omega) = \mathrm{Re}\widehat{\pi}^{\mathrm{intra},0}_\lambda(\omega) + \mathrm{Re}\widehat{\pi}^{\mathrm{inter},0}_\lambda(\omega). \tag{4.12}$$

The first term can be expressed as [265, 290]

$$\mathrm{Re}\widehat{\pi}^{\mathrm{intra},0}_\lambda(\omega) = \lim_{\eta\to 0^+}\left(\frac{\omega^2}{\omega^2+\eta^2}\right)\sum_{\mu\mathbf{k}}\left|g^{\mu\mu}_\lambda(\mathbf{k},0)\right|^2\left(-\frac{\partial f_{\mu\mathbf{k}}}{\partial\varepsilon_{\mu\mathbf{k}}}\right) \tag{4.13}$$

with

$$-\frac{\partial f_{\mu\mathbf{k}}}{\partial\varepsilon_{\mu\mathbf{k}}} = \frac{1}{2k_BT}\frac{1}{1+\cosh(\frac{\varepsilon_{\mu\mathbf{k}}-\varepsilon_F}{k_BT})}, \tag{4.14}$$

while the second term is

$$\mathrm{Re}\widehat{\pi}^{\mathrm{inter},0}_\lambda(\omega) = \sum_{\mu\neq\mu',\mathbf{k}\sigma}\frac{-\omega\left|g^{\mu\mu'}_\lambda(\mathbf{k},0)\right|^2}{\varepsilon_{\mu\mathbf{k}}-\varepsilon_{\mu'\mathbf{k}}}\mathcal{P}\frac{f_{\mu\mathbf{k}}-f_{\mu'\mathbf{k}}}{\omega+\varepsilon_{\mu\mathbf{k}}-\varepsilon_{\mu'\mathbf{k}}}. \tag{4.15}$$

In Eq. (4.13) we deliberately leave the infinitesimal parameter η to show what the actual dependence on ω is. In the case of optical phonons, the limit in this expression is one. When doing the static limit, $\omega\to 0$, of this expression, the ordering of limits should be reversed, i.e. take first $\omega\to 0$, and then $\eta\to 0$, in order to satisfy the condition $\widehat{\pi}^0_\lambda(0)=0$.

4.2.2 Phonon self-energy within the relaxation time approximation

The simplest case of the RTA for the phonon self-energy, in which η is replaced by a phenomenological damping energy $\Gamma > 0$, corresponds to the approximation of Eq. (4.1) in which (i) the vertex renormalization is neglected, (ii) the exact Matsubara Green's functions in the numerator are replaced with the bare ones, and (iii) only the imaginary part of the bare *e-h* self-energy is kept, but without their energy and momentum dependence, i.e., $\Delta\Sigma_{\mu\mu'}(\mathbf{k},\mathbf{q},i\omega_n,i\nu_n) \approx i\mathrm{Im}\Delta\Sigma_{\mu\mu'} \equiv i\Gamma_{\mu\mu'}$. Without this specific structure of the *e-h* self-energy, information on which electrons and phonon modes are responsible for the damping and the breakdown of the momentum conservation law is lost [9, 41, 129]. Nevertheless, as we are interested in

the phonon linewidth for the specific $(\mathbf{q},\lambda)$ mode and not in its functional dependence of ω, in Sec. 4.3.3 we use a physically meaningful range of $\Gamma_{\mu\mu'}$ and discuss the corresponding linewidths. Following previous works [270, 275], it is convenient to distinguish different damping energies for intraband, $\mathrm{Im}\Delta\Sigma_{\mu=\mu'} \equiv \Gamma_{\mathrm{intra}}$, and interband, $\mathrm{Im}\Delta\Sigma_{\mu\neq\mu'} \equiv \Gamma_{\mathrm{inter}}$, transitions. The effects of the electron processes (i.e., electron-electron, electron-phonon and electron-impurity scattering) on the renormalization of the electronic band structure are neglected within the RTA, i.e. $\mathrm{Re}\Delta\Sigma_{\mu\mu'} = 0$. This is a reasonable approximation for weak scattering processes [275, 276]. Under these assumptions the $\mathbf{q} \approx 0$ phonon self-energy from Eq. (4.10) becomes

$$\pi^0_\lambda(\omega) = \sum_{\mu\neq\mu',\mathbf{k}\sigma} \left|g^{\mu\mu'}_\lambda(\mathbf{k},0)\right|^2 \frac{f_{\mu\mathbf{k}} - f_{\mu'\mathbf{k}}}{\omega + \varepsilon_{\mu\mathbf{k}} - \varepsilon_{\mu'\mathbf{k}} + i\Gamma_{\mathrm{inter}}}. \tag{4.16}$$

This expression shows how the strict condition imposed by the Dirac-delta function in $\mathrm{Im}\pi^0_\lambda(\omega)$ for interband transitions [Eq. (4.8)] is now loosened, and it reads $|\omega + \varepsilon_{\mu\mathbf{k}} - \varepsilon_{\mu'\mathbf{k}}| \lesssim \Gamma_{\mathrm{inter}}/2$. Similarly, if we apply the same RTA to the phonon self-energy of Eq. (4.11) (replacing η by $\Gamma_{\mu\mu'}$), we get for $\mathbf{q} \approx 0$

$$\widehat{\pi}^0_\lambda(\omega) = \sum_{\mu\mu'\mathbf{k}\sigma} \frac{-\omega \left|g^{\mu\mu'}_\lambda(\mathbf{k},0)\right|^2}{\varepsilon_{\mu\mathbf{k}} - \varepsilon_{\mu'\mathbf{k}}} \frac{f_{\mu\mathbf{k}} - f_{\mu'\mathbf{k}}}{\omega + \varepsilon_{\mu\mathbf{k}} - \varepsilon_{\mu'\mathbf{k}} + i\Gamma_{\mu\mu'}}. \tag{4.17}$$

Comparing Eqs. (4.16) and (4.17), it is clear that the imaginary parts of the phonon self-energies π^0_λ and $\widehat{\pi}^0_\lambda$ within the RTA differ considerably, because now the factor $\omega/(\varepsilon_{\mu\mathbf{k}} - \varepsilon_{\mu'\mathbf{k}})$ of Eq. (4.17) is not cancelled out, since $\omega \neq \varepsilon_{\mu'\mathbf{k}} - \varepsilon_{\mu\mathbf{k}}$ when $\Gamma_{\mu\mu'} > 0$ (see also Appendix B for differences between π^0_λ and $\widehat{\pi}^0_\lambda$). This implies that the interband parts of these two self-energies are different and, furthermore, that the imaginary part of the phonon self-energy $\widehat{\pi}^0_\lambda$ has both interband and intraband parts, while the imaginary part of π^0_λ has only the interband contribution for $\mathbf{q} \approx 0$. At this point, it is important to remark that the different behaviour of $\widehat{\pi}^0_\lambda$ with respect to π^0_λ in the RTA is due to the *ad hoc* inclusion of the relaxation processes in Eq. (4.11), which in fact turns out to be non-physical. More precisely, in the case of π^0_λ the higher order diagrammatic expansion of the scattering processes leads naturally to the appearance of a damping energy, i.e. an *e-h* self-energy. However, in the case of $\widehat{\pi}^0_\lambda$ to our knowledge there is no corresponding perturbation expansion of the Hamiltonian associated with this bare phonon self-energy present in the literature (see Secs. 2.4.3 and 2.4.4 and Ref. [138]). Thus, it is not completely clear how the RTA form of $\widehat{\pi}^0_\lambda$ should look like. In Appendix C we propose a possible expression of $\widehat{\pi}^0_\lambda$ in RTA.

Next, we consider the damping effects in π^0_λ a step further than in Eq. (4.16).

Instead of neglecting the dressed single-electron self-energies in the Green's functions appearing in the numerator of Eq. (4.1), we account for them phenomenologically. Such a phonon self-energy corresponds to the second bubble diagram in Fig. 4.1, where $\Delta\Sigma_{\mu\mu'}(\mathbf{k},\mathbf{q},i\omega_n,i\nu_n) \to i\Gamma_{\mu\mu'}$, and reads

$$\Pi^0_\lambda(\omega) = \sum_{\mu\neq\mu',\mathbf{k}\sigma} \left|g^{\mu\mu'}_\lambda(\mathbf{k},0)\right|^2 \frac{n_\mu(\mathbf{k}) - n_{\mu'}(\mathbf{k})}{\omega + \varepsilon_{\mu\mathbf{k}} - \varepsilon_{\mu'\mathbf{k}} + i\Gamma_{\text{inter}}}. \tag{4.18}$$

In this expression the momentum distribution functions $n_\mu(\mathbf{k})$ appear instead of the usual Fermi-Dirac distribution functions. Approximating $n_\mu(\mathbf{k})$ by $f_{\mu\mathbf{k}}$, as done in Eq. (4.16), is equivalent to substituting the interacting electron distribution by the thermal equilibrium value for the noninteracting electrons. The exact definition of the momentum distribution function is

$$\begin{aligned} n_\mu(\mathbf{k}) &= \frac{1}{\beta}\sum_{i\omega_n} G_\mu(\mathbf{k},i\omega_n) \\ &= \int_{-\infty}^{\infty} \frac{d\varepsilon}{2\pi} A_\mu(\mathbf{k},\varepsilon) f(\varepsilon), \end{aligned} \tag{4.19}$$

where $f(\varepsilon)$ is the Fermi-Dirac distribution function and $A_\mu(\mathbf{k},\varepsilon)$ is the exact single-electron spectral function

$$A_\mu(\mathbf{k},\varepsilon) = \frac{-2\text{Im}\Sigma_\mu(\mathbf{k},\varepsilon)}{\left[\varepsilon - \varepsilon_{\mu\mathbf{k}} - \text{Re}\Sigma_\mu(\mathbf{k},\varepsilon)\right]^2 + \left[\text{Im}\Sigma_\mu(\mathbf{k},\varepsilon)\right]^2}. \tag{4.20}$$

In our phenomenological approximation, we neglect the real part of the single-electron self-energy, $\text{Re}\Sigma_\mu(\mathbf{k},\varepsilon) = 0$, and use a constant damping parameter Γ_μ instead of $-2\text{Im}\Sigma_\mu(\mathbf{k},\varepsilon)$. One further simplification is to use the same damping parameter for all the electronic bands μ, i.e., $\Gamma_\mu \equiv \Gamma^A$. This approximation is reasonable in a phenomenological treatment of the intraband relaxation processes of electrons scattering on impurities, where the damping of the single-electron spectral function is $-\text{Im}\Sigma_\mu(\mathbf{k},\varepsilon) \approx 1/2\tau_{\text{tr}}$, while the damping of the two-particle propagator (e.g., phonon self-energy or Kubo conductivity formula) is $\text{Im}\Delta\Sigma_{\mu\mu'}(\mathbf{k},\mathbf{q},\omega) \approx 1/\tau_{\text{tr}}$. However, for the interband channel this is no longer the case and this simplification serves just as a coarse estimation. Although the mentioned approximations make the integration in Eq. (4.19) simpler, it is still a difficult task to perform it analytically for a finite temperature T. As we are only interested in the effects of the damping parameter Γ^A on the phonon self-energy $\Pi^0_\lambda(\omega)$, we do the explicit integration of expression (4.19) for $T \to 0\text{K}$,

$$n_\mu(\mathbf{k}) \approx \frac{1}{2} - \frac{1}{\pi}\tan^{-1}\left[\frac{2(\varepsilon_{\mu\mathbf{k}} - \varepsilon_F)}{\Gamma^A}\right]. \tag{4.21}$$

In this expression we see that when the temperature is very low, but we are still considering electron relaxation processes (e.g., scattering on impurities), the electronic states distribution is still broadened and governed by the intensity of such processes [291].

4.2.3 Long-range screening of the phonon self-energy

In this section we analyze how the long-range Coulomb interaction affects the bare phonon self-energy and, in particular, whether it can eliminate the q^2 dependence in the intraband part. When the phonon excitations produce charge fluctuations in the electron gas, the long-range screening should, in principle, influence the phonon linewidth and the frequency renormalization. Inclusion of the long-range screening into the bare phonon self-energy π^0_λ can be done as in Fig. 4.2 [142, 275],

$$\widetilde{\pi}^0_\lambda(\mathbf{q},\omega) = \pi^0_\lambda(\mathbf{q},\omega) + \pi^0_{\lambda 0}(\mathbf{q},\omega)V_q\frac{\pi^0_{0\lambda}(\mathbf{q},\omega)}{\epsilon(\mathbf{q},\omega)}, \tag{4.22}$$

where we have defined a more general form of the correlation function as

$$\pi^0_{\alpha\beta}(\mathbf{q},\omega) = \sum_{\mu\mu'\mathbf{k}\sigma}\left[F^{\mu\mu'}_\alpha(\mathbf{k},\mathbf{q})\right]^* F^{\mu\mu'}_\beta(\mathbf{k},\mathbf{q})\frac{f_{\mu\mathbf{k}} - f_{\mu'\mathbf{k}+\mathbf{q}}}{\omega + \varepsilon_{\mu\mathbf{k}} - \varepsilon_{\mu'\mathbf{k}+\mathbf{q}} + i\eta}, \tag{4.23}$$

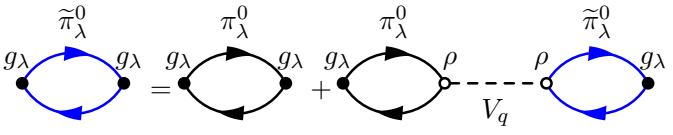

FIGURE 4.2: Diagrammatic representation of the long-range screening of the phonon self-energy π^0_λ. The electron-phonon vertex function is represented by filled circle and denoted as g_λ, the charge vertex function by empty circles and denoted as ρ, and the bare Coulomb interaction by dashed line and denoted as V_q. Blue and black lines represent the screened and bare Green's functions, respectively.

$$F_{\alpha}^{\mu\mu'}(\mathbf{k},\mathbf{q}) = \begin{cases} g_{\lambda}^{\mu\mu'}(\mathbf{k},\mathbf{q}), & \text{for } \alpha = \lambda \\ \rho^{\mu\mu'}(\mathbf{k},\mathbf{q}), & \text{for } \alpha = 0. \end{cases} \tag{4.24}$$

Here we have introduced the charge vertex function $\rho^{\mu\mu'}(\mathbf{k},\mathbf{q}) = \langle\psi_{\mu\mathbf{k}}|\, e^{-i\mathbf{q}\cdot\mathbf{r}}\, |\psi_{\mu'\mathbf{k}+\mathbf{q}}\rangle$, the bare Coulomb interaction V_q, and the dielectric screening function

$$\epsilon(\mathbf{q},\omega) = 1 - V_q\chi(\mathbf{q},\omega). \tag{4.25}$$

The function $\chi(\mathbf{q},\omega)$ is the charge-charge correlation function given by $\pi_{00}^{0}(\mathbf{q},\omega)$, and the function $\pi_{\lambda 0}^{0}(\mathbf{q},\omega)$ represents the electron-mediated coupling of the phonon mode λ to the external scalar field. We can look now separately into the screening of the long-wavelength intraband and interband phonon self-energies.

In the long-wavelength limit, $\mathbf{q} \approx 0$, Eq. (4.22) has the following form

$$\widetilde{\pi}_{\lambda}^{0}(\omega) = \pi_{\lambda}^{0}(\omega) - \frac{\pi_{\lambda 0}^{0}(\omega)\pi_{0\lambda}^{0}(\omega)}{\chi(\omega)}, \tag{4.26}$$

where the essential difference between the intraband and interband contributions is in the corresponding vertex functions,

$$\rho^{\mu\mu'}(\mathbf{k},\mathbf{q}\approx 0) = \begin{cases} 1, & \text{for } \mu = \mu' \\ \frac{-\mathbf{q}\cdot\mathbf{J}^{\mu\mu'}(\mathbf{k},\mathbf{q}\approx 0)}{\varepsilon_{\mu\mathbf{k}} - \varepsilon_{\mu'\mathbf{k}}}, & \text{for } \mu \neq \mu'. \end{cases} \tag{4.27}$$

The relationship between the charge $\rho^{\mu\mu'}(\mathbf{k},\mathbf{q}\approx 0)$ and the current $\mathbf{J}^{\mu\mu'}(\mathbf{k},\mathbf{q}\approx 0)$ vertex functions is derived using the charge continuity equation for the operators [126]. Now, the symmetry of the vertex function product in the $\pi_{\lambda 0}^{0}(\omega)$ function governs the degree of phonon self-energy screening, i.e. when the product $\left[g_{\lambda}^{\mu\mu'}(\mathbf{k},0)\right]^{*}\rho^{\mu\mu'}(\mathbf{k},0)$ is an odd function of $\mathbf{k}$, the function $\pi_{\lambda 0}^{0}(\omega)$ vanishes and when it is even, it does not. For example, the vibrational modes of the vertical CO molecule adsorbed on the c(2×2) unit cell of Cu(100) belong to the C_{4v} point group symmetry, where the CO stretch mode corresponds to the A_1 irreducible representation. In that case $g_{\lambda=A_1}^{\mu\mu'}(\mathbf{k},0)$ is an even function, thus $\pi_{A_1 0}^{\mathrm{intra},0}(\omega)$ will be finite, while $\pi_{A_1 0}^{\mathrm{inter},0}(\omega)$ will vanish due to the odd character of $\mathbf{J}^{\mu\mu'}(\mathbf{k},0)$. Therefore, when Eqs. (4.26) and (4.27) are combined, it can be seen that the long-range screening does not affect the interband channel, while the intraband contribution is modified, i.e.,

$$\widetilde{\pi}_{\lambda}^{\mathrm{inter},0}(\omega) \approx \pi_{\lambda}^{\mathrm{inter},0}(\omega) \tag{4.28}$$

and

$$\widetilde{\pi}_{\lambda}^{\mathrm{intra},0}(\omega) \approx \pi_{\lambda}^{\mathrm{intra},0}(\omega) - \frac{\pi_{\lambda 0}^{\mathrm{intra},0}(\omega)\pi_{0\lambda}^{\mathrm{intra},0}(\omega)}{\chi^{\mathrm{intra}}(\omega)}. \tag{4.29}$$

Since the long-wavelength intraband part of the correlation function $\pi^0_{\alpha\beta}(\mathbf{q},\omega)$ has the same dependence on q as Eq. (4.6), we can observe from the last expression that the screened intraband part is still proportional to q^2 [142], and thus that it is still negligible for the $\mathbf{q} \approx 0$ case.

In contemporary *ab initio* calculations the screening effects of the phonon self-energy are implemented in a different but closely related way. In principle, the inner bubble diagrams connected with the Coulomb interactions should be all gathered within one of the electron-phonon vertex functions, while the remaining vertex should be bare (e.g., as in Ref. [56]). This new screened electron-phonon vertex function is then frequency dependent. However, in DFT calculations both vertex functions are screened and usually treated within the adiabatic (static) approximation for practical reasons [8].

4.2.4 Quasi-static approximations

A common practice when studying the linewidth of low-energy phonons and also of vibrationally excited adsorbates is the use of the quasi-static limit ($\omega_{0\lambda} \ll |\varepsilon_{\mu\mathbf{k}} - \varepsilon_{\mu'\mathbf{k}}|$) in Eqs. (4.4) and (4.11). In this respect, we consider it meaningful to examine step by step the implications of using this limit in calculations of the $\mathbf{q} \approx 0$ phonon self-energy. First of all, if the $\omega \to 0$ limit is taken directly in Eq. (4.4), the following expression is obtained

$$\pi_{\lambda}^{0}(0) = \sum_{\mu\mu'\mathbf{k}\sigma} \frac{\left|d_{\lambda}^{\mu\mu'}(\mathbf{k},0)\right|^2}{2M_{\lambda}\omega_{0\lambda}} \frac{f_{\mu\mathbf{k}} - f_{\mu'\mathbf{k}}}{\varepsilon_{\mu\mathbf{k}} - \varepsilon_{\mu'\mathbf{k}}}, \tag{4.30}$$

where $d_{\lambda}^{\mu\mu'}(\mathbf{k},0) = g_{\lambda}^{\mu\mu'}(\mathbf{k},0)\sqrt{2M_{\lambda}\omega_{0\lambda}}$ is the deformation potential and M_{λ} is the effective mass of the mode λ. This expression is purely real, which is actually required by the definition of the bare phonon self-energy given in Eq. (4.4). However, a practical formula for the phonon linewidth can still be obtained by taking carefully the quasi-static limit. In what follows we use η as a finite parameter, since this is usually done in the phonon linewidth calculations within DFT to ensure numerical convergence. When applying the RTA as done above, a finite η is used, too, that has a physical meaning (i.e., $\eta = \Gamma_{\mu\mu'}$). We write the imaginary part of Eq. (4.4) for $\omega = \omega_{0\lambda}$ as

$$-\operatorname{Im}\pi^0_\lambda(\omega_{0\lambda}) = \pi \sum_{\mu\mu'\mathbf{k}\sigma} \frac{\left|d^{\mu\mu'}_\lambda(\mathbf{k},0)\right|^2}{2M_\lambda} \frac{f_{\mu\mathbf{k}} - f_{\mu'\mathbf{k}}}{\omega_{0\lambda}} \mathcal{L}_\eta(\omega_{0\lambda} + \varepsilon_{\mu\mathbf{k}} - \varepsilon_{\mu'\mathbf{k}}) \tag{4.31}$$

where $\mathcal{L}_\eta(x)$ stands for the Lorentzian function $\eta/\pi(x^2+\eta^2)$ (see Appendix B for a summary of the used Lorentzian functions). To obtain the quasi-static limit that is always positive-definite we need to take the $\omega_{0\lambda} \to 0$ limit both in the Lorentzian function and in $(f_{\mu\mathbf{k}} - f_{\mu'\mathbf{k}})/\omega_{0\lambda}$. The latter limit is the derivative of the Fermi-Dirac distribution function, $-\partial f_{\mu\mathbf{k}}/\partial\varepsilon_{\mu\mathbf{k}}$. Otherwise, if we only took the limit of the Lorentzian function, the imaginary part could give negative, non-physical values because it could happen that $f_{\mu\mathbf{k}} - f_{\mu'\mathbf{k}} < 0$ when summation over the Fermi surface is performed. Therefore, by taking both limits the following expression for the quasi-static phonon self-energy is obtained

$$-\operatorname{Im}\pi^0_\lambda(0) \approx \pi \sum_{\mu\mu'\mathbf{k}\sigma} \frac{\left|d^{\mu\mu'}_\lambda(\mathbf{k},0)\right|^2}{2M_\lambda} \left(-\frac{\partial f_{\mu\mathbf{k}}}{\partial\varepsilon_{\mu\mathbf{k}}}\right) \mathcal{L}_\eta(\varepsilon_{\mu\mathbf{k}} - \varepsilon_{\mu'\mathbf{k}}). \tag{4.32}$$

In the low-temperature limit $T \to 0$, the derivative of the Fermi-Dirac distribution function $-\partial f_{\mu\mathbf{k}}/\partial\varepsilon_{\mu\mathbf{k}}$ goes to $\delta(\varepsilon_{\mu\mathbf{k}} - \varepsilon_F)$, where ε_F denotes the Fermi level. This expression is also known as Allen's formula for the phonon linewidth [292]. The same formula can be obtained by taking the quasi-static limit in Eq. (4.11). In that case, the imaginary part for $\omega = \omega_{0\lambda}$ is

$$-\operatorname{Im}\widehat{\pi}^0_\lambda(\omega_{0\lambda}) = -\pi \sum_{\mu\mu'\mathbf{k}\sigma} \frac{\left|d^{\mu\mu'}_\lambda(\mathbf{k},0)\right|^2}{2M_\lambda} \frac{f_{\mu\mathbf{k}} - f_{\mu'\mathbf{k}}}{\varepsilon_{\mu\mathbf{k}} - \varepsilon_{\mu'\mathbf{k}}} \mathcal{L}_\eta(\omega_{0\lambda} + \varepsilon_{\mu\mathbf{k}} - \varepsilon_{\mu'\mathbf{k}}). \tag{4.33}$$

Since $-(f_{\mu\mathbf{k}} - f_{\mu'\mathbf{k}})/(\varepsilon_{\mu\mathbf{k}} - \varepsilon_{\mu'\mathbf{k}})$ is always positive, the $\omega_{0\lambda} \to 0$ limit in the Lorentzian function can be safely performed, which leads to the following quasi-static expression

$$-\operatorname{Im}\widehat{\pi}^0_\lambda(0) \approx -\pi \sum_{\mu\mu'\mathbf{k}\sigma} \frac{\left|d^{\mu\mu'}_\lambda(\mathbf{k},0)\right|^2}{2M_\lambda} \frac{f_{\mu\mathbf{k}} - f_{\mu'\mathbf{k}}}{\varepsilon_{\mu\mathbf{k}} - \varepsilon_{\mu'\mathbf{k}}} \mathcal{L}_\eta(\varepsilon_{\mu\mathbf{k}} - \varepsilon_{\mu'\mathbf{k}}). \tag{4.34}$$

When we additionally require that $\varepsilon_{\mu\mathbf{k}} \to \varepsilon_{\mu'\mathbf{k}}$ this expression also leads to Allen's formula [Eq. (4.32)]. Since the intraband part of Allen's formula diverges [267], only the interband part is usually considered for calculating linewidths. To avoid this divergent form, the derivative $\partial/\partial\varepsilon_{\mu\mathbf{k}}$ can be applied to the Lorentzian $\mathcal{L}_\eta(x)$ instead of applying it to the Fermi-Dirac distribution function $f_{\mu\mathbf{k}}$ [257],

$$-\operatorname{Im}^{\partial}\pi^{0}_{\lambda}(0) \equiv -\pi \sum_{\mu\mu'\mathbf{k}\sigma} \frac{\left|d^{\mu\mu'}_{\lambda}(\mathbf{k},0)\right|^{2}}{2M_{\lambda}}(f_{\mu\mathbf{k}} - f_{\mu'\mathbf{k}})\frac{\partial\mathcal{L}_{\eta}(\varepsilon_{\mu\mathbf{k}} - \varepsilon_{\mu'\mathbf{k}})}{\partial\varepsilon_{\mu\mathbf{k}}}. \tag{4.35}$$

Although this trick disregards the divergent intraband part, it actually changes the interband part as well, as we will show in the results section for a particular case of the CO stretch mode on Cu(100).

All in all, the expressions for the quasi-static $\mathbf{q} \approx 0$ phonon self-energies [Eqs. (4.32), (4.34), and (4.35)] should be taken with care when the phonon linewidth of high-frequency mode is calculated for, at least, three reasons: (i) the imaginary part of the static phonon self-energy should vanish by definition (adiabaticity) in the clean noninteracting limit $\eta \to 0^{+}$, as Eq. (4.30) shows, (ii) the intraband part of Eqs. (4.32) and (4.34) diverges[6], and (iii) the interband parts of Eqs. (4.32), (4.34), and (4.35) can give different values of the phonon linewidth for the physically meaningful range of Γ when compared to the dynamic results, as we show in Sec. 4.3.3. A similar precaution should be taken when studying the quasi-static limit for high-frequency $\mathbf{q} \neq 0$ modes (e.g., adiabatic electronic friction coefficient) [37–39, 49]. Nevertheless, Allen's formula should be more reliable in that case, since the intraband part is not divergent for finite $\mathbf{q}$ [267].

4.2.5 High-energy expansion of the intraband phonon self-energy

In the preceding analysis of the intraband part of the phonon self-energy we were only considering direct transitions, i.e., those where an electron with momentum $\mathbf{k}$ is directly scattered to the state $\mathbf{k}+\mathbf{q}$ by absorbing the energy of a phonon with momentum $\mathbf{q}$ [first term in Eq. (D.7)]. As we already saw in Sec. 4.2.1, this process is proportional to q^2, and thus negligible for the $\mathbf{q} \approx 0$ phonons. However, this result does not completely exclude the existence of intraband transitions contributing to the phonon self-energy. In addition to the mentioned direct intraband transitions, there are also indirect ones, in which the electron is scattered from $\mathbf{k}$ to $\mathbf{k}'$, but now these

[6] This result is in close analogy to the behavior of the direct current conductivity formula $\sigma(\omega = 0)$, that fulfills $\mathrm{Re}\sigma(\omega = 0) \to +\infty$ in the $\eta \to 0^{+}$ limit, where η is a broadening parameter as in Eq. (4.4). In both cases, the divergence comes from the fact that both $\mathrm{Re}\sigma(\omega = 0)$ and $\mathrm{Im}\pi^{0}_{\lambda}(\omega_{0\lambda} = 0)$ are proportional to η^{-1} [129]. Physically, this would mean that the system has an ideal direct current conductivity in the clean noninteracting limit and that any external perturbation could excite an infinite number of e-h pairs. Thus, an external perturbation to the electron gas, such as $\omega_{0\lambda} \approx 0$ phonons, would have an infinite damping, which is clearly non-physical.

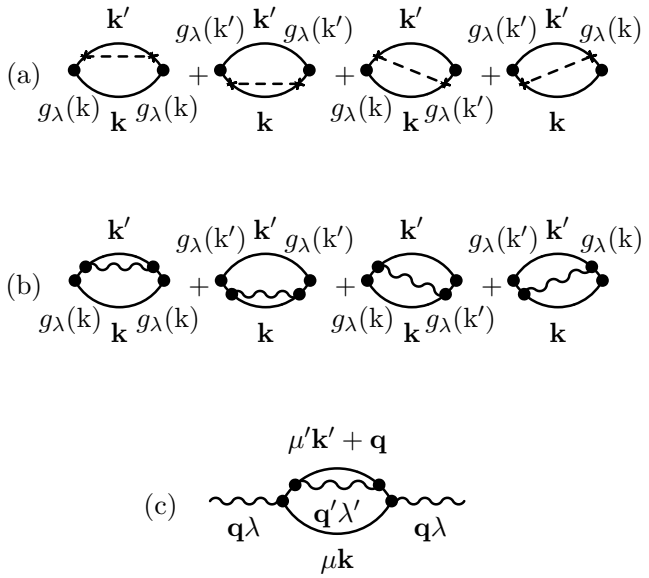

FIGURE 4.3: (a), (b) Diagrammatic representation of the leading terms in the high-energy expansion of the indirect contribution to the intraband phonon self-energy π^0_λ. The diagrams in (a) show the electron-impurity scattering and the ones in (b) show the electron-phonon scattering. The impurity potential v_{imp} is labelled by crosses and the electron-phonon matrix elements g with full circles. (c) Electron self-energy correction to the phonon propagator (in our case $\mathbf{q} \approx 0$). This term is an example of how the $(\mathbf{q}, \lambda)$ phonon mode couples to the $(\mathbf{q}', \lambda')$ modes via the e-h pairs.

two states are not correlated directly by the phonon momentum $\mathbf{q}$ [9, 12, 266, 273–276] [second term in Eq. (D.7)]. This correlation is destroyed by the scattering of the electron on impurities, other phonons in the system, or other electrons. In other words, the momentum conservation law is broken. In our case, we only consider the indirect transitions due to impurity and phonon scattering. We sum the leading terms of these processes. These impurity and phonon terms are represented in Figs. 4.3(a) and 4.3(b), respectively, where the first two bubbles are the self-energy contributions, while the other two are the vertex corrections. This type of expansion is called "high-energy" (HE) because it is valid for $\omega \gg |\varepsilon_{\mu\mathbf{k}} - \varepsilon_{\mu\mathbf{k}+\mathbf{q}}|$ and $\omega \gg \Gamma_{\mathrm{intra}}$ [276]. Therefore, when $\mathbf{q} \approx 0$ the indirect contribution to the intraband phonon self-energy in the HE limit $\pi^{\mathrm{intra,HE}}_\lambda(\omega)$ together with the interband phonon self-energy $\pi^{\mathrm{inter},0}_\lambda(\omega)$ are of particular importance for describing the phonon linewidth of the high-frequency mode.

Before performing the explicit summation of the diagrams in Figs. 4.3(a) and 4.3(b) we write the total phonon self-energy as the sum of direct and indirect terms

$$\begin{aligned}\Pi_\lambda(\omega) &= \Pi_\lambda^{\mathrm{d}}(\omega) + \Pi_\lambda^{\mathrm{id}}(\omega) \\ &\approx \pi_\lambda^{\mathrm{inter,0}}(\omega) + \pi_\lambda^{\mathrm{intra,HE}}(\omega) \end{aligned} \tag{4.36}$$

As for the interband transitions, we keep the leading direct contributions as in Eq. (4.16). The summation of the leading terms in the $\pi_\lambda^{\mathrm{intra,HE}}$ can be performed using the force-force correlation function approach for the phonon self-energy [10, 129, 276]. In Appendix D we derive the corresponding force-force correlation function from the equations of motion for the two-particle propagators. Here we only give the final result which reads in Matsubara notation[7],

$$\pi_\lambda^{\mathrm{HE}}(i\nu_n) = -\frac{1}{(i\nu_n)^2}\left[\phi_{\lambda\lambda}(i\nu_n) - \phi_{\lambda\lambda}(0)\right]. \tag{4.37}$$

In the following we evaluate $\pi_\lambda^{\mathrm{HE}}$ for the electron-impurity and electron-phonon scatterings.

4.2.5.1 Electron-impurity scattering contribution to the intraband phonon self-energy

In the case of impurity scattering, the summation of the diagrams in Fig. 4.3(a) leads to the following form of the force-force correlation function

$$\begin{aligned}\phi_{\lambda\lambda}^{\mathrm{imp}}(i\nu_n) &= \sum_{\mu\mathbf{k}\mathbf{k}'\sigma} \left|g_\lambda^{\mu\mu}(\mathbf{k},0) + g_\lambda^{\mu\mu}(\mathbf{k}',0)\right|^2 \\ &\quad \times \frac{1}{\beta}\sum_{i\omega_n} \left\langle \left|v_{\mathrm{imp}}\left(\mathbf{k}-\mathbf{k}'\right)\right|^2 \right\rangle G_\mu^0(\mathbf{k}, i\omega_n) G_\mu^0(\mathbf{k}', i\omega_n + i\nu_n), \end{aligned} \tag{4.38}$$

where $\left\langle \left|v_{\mathrm{imp}}\left(\mathbf{k}-\mathbf{k}'\right)\right|^2 \right\rangle$ is the impurity potential averaged over the impurity sites [129]. After performing the Matsubara summation and analytical continuation we arrive at the final expression for the force-force correlation function

$$\phi_{\lambda\lambda}^{\mathrm{imp}}(\omega) = \sum_{\mu\mathbf{k}\mathbf{k}'\sigma} \left\langle \left|v_{\mathrm{imp}}\left(\mathbf{k}-\mathbf{k}'\right)\right|^2 \right\rangle \left|g_\lambda^{\mu\mu}(\mathbf{k},0) + g_\lambda^{\mu\mu}(\mathbf{k}',0)\right|^2 \frac{f_{\mu\mathbf{k}} - f_{\mu\mathbf{k}'}}{\omega + \varepsilon_{\mu\mathbf{k}} - \varepsilon_{\mu\mathbf{k}'} + i\eta}, \tag{4.39}$$

[7] Starting from here we drop the "intra" superscript from $\pi_\lambda^{\mathrm{intra,HE}}$ for simplicity. Therefore, whenever "HE" appears, "intra" is implicit.

By combining Eqs. (4.37) and (4.38) we get the result for the high-energy expansion of the indirect contribution to the intraband phonon self-energy activated by electron-impurity scattering

$$\pi_{\lambda}^{\mathrm{HE,imp}}(\omega) = \sum_{\mu\mathbf{k}\sigma} |g_{\lambda}^{\mu\mu}(\mathbf{k},0)|^2 \frac{\partial f_{\mu\mathbf{k}}}{\partial \varepsilon_{\mu\mathbf{k}}} \frac{\Delta\Sigma_{\mu\mu}^{\lambda}(\mathbf{k},\omega)}{\omega}. \tag{4.40}$$

In doing so, we approximate the term $(f_{\mu\mathbf{k}} - f_{\mu\mathbf{k}'}) / (\varepsilon_{\mu\mathbf{k}} - \varepsilon_{\mu\mathbf{k}'})$ with the derivative $\partial f_{\mu\mathbf{k}}/\partial\varepsilon_{\mu\mathbf{k}}$ to separate the $\mathbf{k}$ and $\mathbf{k}'$ summations. In Eq. (4.40) we have defined the e-h self-energy due to electron scattering on impurities as

$$\Delta\Sigma_{\mu\mu}^{\lambda,\mathrm{imp}}(\mathbf{k},\omega) = -\sum_{\mathbf{k}'} \left\langle |v_{\mathrm{imp}}(\mathbf{k}-\mathbf{k}')|^2 \right\rangle \left(1 - \frac{g_{\lambda}^{\mu\mu}(\mathbf{k}',0)}{g_{\lambda}^{\mu\mu}(\mathbf{k},0)}\right) \frac{2\omega}{(\omega+i\eta)^2 - (\varepsilon_{\mu\mathbf{k}} - \varepsilon_{\mu\mathbf{k}'})^2}. \tag{4.41}$$

Here we approximate the e-h self-energy $\Delta\Sigma_{\mu\mu}^{\lambda,\mathrm{imp}}(\mathbf{k},\omega)$ by the phenomenological parameter $i\Gamma_{\mathrm{imp}}$,

$$\pi_{\lambda}^{\mathrm{HE,imp}}(\omega) \approx i \sum_{\mu\mathbf{k}\sigma} |g_{\lambda}^{\mu\mu}(\mathbf{k},0)|^2 \frac{\partial f_{\mu\mathbf{k}}}{\partial \varepsilon_{\mu\mathbf{k}}} \frac{\Gamma_{\mathrm{imp}}}{\omega}. \tag{4.42}$$

From the structure of expressions (4.40) - (4.42) we can deduce that Γ_{imp} is actually the inverse of the transport relaxation time $\tau_{\mathrm{tr}}^{\mathrm{imp}}$ due to electron-impurity scattering obtained in the Boltzmann equations, i.e. $\Gamma_{\mathrm{imp}} = 1/\tau_{\mathrm{tr}}^{\mathrm{imp}}$ [129]. We note that the phenomenological damping energy $\Gamma_{\mu\mu'}$ should, in principle, account for all the relevant scattering processes in the system, while Γ_{imp} accounts just for the specific case of electron-impurity scattering. An equivalent expression for the indirect intraband phonon self-energy [Eq. (4.42)] can be derived for the case of electron-phonon scattering [11, 12, 42, 129, 272, 278].

4.2.5.2 Electron-phonon scattering contribution to the intraband phonon self-energy

By including the indirect electron-phonon scattering[8] processes in the intraband phonon self-energy, we account for contributions such as e-h pair dephasing [280] and indirect phonon-phonon coupling mediated by electron excitations [50, 279], which are also important to describe the experimental phonon linewidth of a vibrating ordered

[8]Note that the expression "electron-phonon scattering" refers throughout this chapter to the higher-order electron-phonon contributions to the phonon self-energy [in particular, to the ones presented in Fig. 4.3(b)].

layer of molecules on a metallic surface. To include these indirect electron-phonon scattering processes we perform the diagrammatic summation of Fig. 4.3(b), which gives

$$\phi^{\rm ph}_{\lambda\lambda}(i\nu_n) = \sum_{\mu\mu'\mathbf{k}\lambda'\mathbf{k}'\sigma} \left|g^{\mu\mu}_{\lambda}(\mathbf{k},0)+g^{\mu\mu}_{\lambda}(\mathbf{k}',0)\right|^2 \frac{1}{\beta^2}\sum_{i\omega_n}\sum_{i\nu_m}\left|g^{\mu\mu'}_{\lambda'}(\mathbf{k},\mathbf{q}')\right|^2 \times G^0_{\mu}(\mathbf{k},i\omega_n)G^0_{\mu}(\mathbf{k}',i\omega_n+i\nu_m+i\nu_n)D^0_{\lambda'}(\mathbf{q}',i\nu_m), \tag{4.43}$$

where $\mathbf{q}' = \mathbf{k}' - \mathbf{k}$. Analogously to the impurity scattering case, the Matsubara summation leads to the following expression

$$\pi^{\rm HE,ph}_{\lambda}(\omega) = -\sum_{\mu\mu'\mathbf{k}\lambda'\mathbf{k}'\sigma}\left|g^{\mu\mu}_{\lambda}(\mathbf{k},0)\right|^2\left[1-\frac{g^{\mu\mu}_{\lambda}(\mathbf{k}',0)}{g^{\mu\mu}_{\lambda}(\mathbf{k},0)}\right]\left|g^{\mu\mu'}_{\lambda'}(\mathbf{k},\mathbf{q}')\right|^2 \times \sum_{s,s'=\pm1}\frac{s\left[n_b(s\omega_{\mathbf{q}'\lambda'})+f(s'\varepsilon_{\mu'\mathbf{k}'})\right]\left[f(\varepsilon_{\mu\mathbf{k}})-f(\varepsilon_{\mu'\mathbf{k}'}-s's\omega_{\mathbf{q}'\lambda'})\right]}{\omega\left[\omega+i\eta+s'(\varepsilon_{\mu\mathbf{k}}-\varepsilon_{\mu'\mathbf{k}'})+s\omega_{\mathbf{q}'\lambda'}\right]\left[\varepsilon_{\mu\mathbf{k}}-(\varepsilon_{\mu'\mathbf{k}'}-s's\omega_{\mathbf{q}'\lambda'})\right]}, \tag{4.44}$$

where $n_b(\omega_{\mathbf{q}\lambda}) = 1/(e^{\beta\omega_{\mathbf{q}\lambda}}-1)$ and $f(\varepsilon_{\mu\mathbf{k}}) = 1/(e^{\beta(\varepsilon_{\mu\mathbf{k}}-\varepsilon_F)}+1)$[9]. This expression contains all the information on the damping and renormalization effects of the high frequency phonons when the excited electrons scatter on the other phonons in the system. However, it is not easy to handle, since it includes a large number of momentum and band summation terms. Therefore, we have to impose a few simplifications to make this phonon self-energy numerically accessible. In order to achieve this, we make use of the so-called transport Eliashberg spectral function, $\alpha^2_{\rm tr}F_{\mu}$, for electron-phonon scattering [9]

$$\alpha^2_{\rm tr}F_{\mu}(\mathbf{k},\Omega,\varepsilon') = \sum_{\mu'\lambda'\mathbf{k}'}\left|g^{\mu\mu'}_{\lambda'}(\mathbf{k},\mathbf{q}')\right|^2\left[1-\frac{g^{\mu\mu}_{\lambda}(\mathbf{k}',0)}{g^{\mu\mu}_{\lambda}(\mathbf{k},0)}\right]B^0_{\lambda'}(\mathbf{q}',\Omega)A^0_{\mu'}(\mathbf{k}',\varepsilon'), \tag{4.45}$$

where the factor in square brackets, which weights the large angle scattering terms, does not appear in the usual Eliashberg spectral function α^2F_{μ} [see Eq. 2.92], since it is a direct consequence of the vertex corrections[10]. Now we write Eq. (4.44) in terms of this transport Eliashberg function as

[9] Note that $n_b(-\omega_{\mathbf{q}\lambda}) = -1 - n_b(\omega_{\mathbf{q}\lambda})$ and $f(-\varepsilon_{\mu\mathbf{k}}) = 1 - f(\varepsilon_{\mu\mathbf{k}})$

[10] Note that the $\alpha^2_{\rm tr}F_{\mu}$ function appearing in the generalized Drude conductivity formula is weighted with the current vertex functions instead of the electron-phonon ones [9, 41].

$$\pi_{\lambda}^{\mathrm{HE,ph}}(\omega) = -\sum_{\mu\mathbf{k}\sigma} |g_{\lambda}^{\mu\mu}(\mathbf{k},0)|^2 \int_0^{\infty} d\Omega \int_{-\infty}^{\infty} d\varepsilon \int_{-\infty}^{\infty} d\varepsilon' \frac{A_{\mu'}^0(\mathbf{k},\varepsilon)}{\omega}$$
$$\times \alpha_{\mathrm{tr}}^2 F_{\mu}(\mathbf{k},\Omega,\varepsilon') \sum_{s'=\pm 1} \frac{f(\varepsilon) - f(\varepsilon' - s'\Omega)}{\varepsilon - (\varepsilon' - s'\Omega)} \frac{n_b(\Omega) + f(s'\varepsilon')}{\omega + i\eta + s'(\varepsilon - \varepsilon') + \Omega}. \quad (4.46)$$

A typical approximation that simplifies the above expression is to neglect the energy variations in $A_{\mu'}^0(\mathbf{k},\varepsilon)$ and $\alpha_{\mathrm{tr}}^2 F_{\mu}(\mathbf{k},\Omega,\varepsilon')$ by writing $\varepsilon = \varepsilon' = \varepsilon_F$ [129] [$\alpha_{\mathrm{tr}}^2 F_{\mu}(\mathbf{k},\Omega,0) \equiv \alpha_{\mathrm{tr}}^2 F_{\mu}(\mathbf{k},\Omega)$]. Then we can write the imaginary part of $\pi_{\lambda}^{\mathrm{HE,ph}}(\omega)$ as[11]

$$-\mathrm{Im}\pi_{\lambda}^{\mathrm{HE,ph}}(\omega) \approx -\sum_{\mu\mathbf{k}\sigma} |g_{\lambda}^{\mu\mu}(\mathbf{k},0)|^2 \, \delta(\varepsilon_{\mu\mathbf{k}} - \varepsilon_F) \frac{\mathrm{Im}\Delta\Sigma_{\mu\mu}^{\lambda,\mathrm{ph}}(\mathbf{k},\omega)}{\omega}, \quad (4.47)$$

where the imaginary part of the *e-h* self-energy for the electron-phonon coupling is defined as

$$\mathrm{Im}\Delta\Sigma_{\mu\mu}^{\lambda,\mathrm{ph}}(\mathbf{k},\omega) = \int d\varepsilon \frac{f(\varepsilon) - f(\varepsilon+\omega)}{\omega} \int d\Omega \pi \alpha_{\mathrm{tr}}^2 F_{\mu}(\mathbf{k},\Omega)$$
$$\times [4n_b(\Omega) + f(\Omega + \varepsilon + \omega) + f(\Omega - \varepsilon - \omega) + f(\Omega + \varepsilon) + f(\Omega - \varepsilon)]. \quad (4.48)$$

Two further approximations can be made by neglecting the vertex corrections and $\mathbf{k}$ anisotropy of $\mathrm{Im}\Delta\Sigma_{\mu\mu}^{\lambda,\mathrm{ph}}(\mathbf{k},\omega)$ [269]. With the first approximation we replace $\alpha_{\mathrm{tr}}^2 F_{\mu}(\mathbf{k},\Omega)$ with $\alpha^2 F_{\mu}(\mathbf{k},\Omega)$[12]. In that case, the comparison of the above *e-h* self-energy with the electron self-energy expressed in Eq. (2.93) leads to the following expression [145]

$$\mathrm{Im}\Delta\Sigma_{\mu\mu}^{\lambda,\mathrm{ph}}(\mathbf{k},\omega) = \int d\varepsilon \frac{f(\varepsilon) - f(\varepsilon+\omega)}{\omega} \left[\mathrm{Im}\Sigma_{\mu}(\mathbf{k},\varepsilon) + \mathrm{Im}\Sigma_{\mu}(\mathbf{k},\varepsilon+\omega)\right]. \quad (4.49)$$

From this we get the direct relation between the damping functions of the collective modes (i.e., the imaginary part of the *e-h* self-energy) and the single-electron states (i.e., the imaginary part of the single-electron self-energy), already discussed formally in the beginning of Sec. 4.2 and in Sec. 4.2.2.

[11] We keep in mind that the real part can be obtained with the use of Kramers-Kronig relations.
[12] For consequences of this replacement see Ref. [293].

For the second approximation, i.e., neglecting the **k**-dependence, we substitute $\mathrm{Im}\Delta\Sigma^{\lambda,\mathrm{ph}}_{\mu\mu}(\mathbf{k},\omega)$ by its average around the Fermi energy

$$\Gamma_{\mathrm{ph}}(\omega) \equiv \frac{1}{N(\varepsilon_F)} \sum_{\mu\mathbf{k}\sigma} \delta(\varepsilon_{\mu\mathbf{k}} - \varepsilon_F) \mathrm{Im}\Delta\Sigma^{\lambda,\mathrm{ph}}_{\mu\mu}(\mathbf{k},\omega), \tag{4.50}$$

where $N(\varepsilon_F) = \sum_{\mu\mathbf{k}\sigma} \delta(\varepsilon_{\mu\mathbf{k}} - \varepsilon_F)$. Now we have a convenient expression for $\pi^{\mathrm{HE,ph}}_{\lambda}(\omega)$ where the electronic damping function $\Gamma_{\mathrm{ph}}(\omega)$ is separated from the **k** summation in the phonon self-energy. To understand the damping processes contained in $-\mathrm{Im}\pi^{\mathrm{HE,ph}}_{\lambda}(\omega)$ in depth it is useful to relate it with the Allen's phonon linewidth [292]. In Sec. 4.2.4 we derive this formula for the $\mathbf{q} \approx 0$ case [Eq. (4.32)] and here we write it for any **q** and in the $T \to 0$ limit as

$$\gamma^{\mathrm{allen}}_{\mathbf{q}\lambda} = 2\pi\omega_{\mathbf{q}\lambda} \sum_{\mu\mu'\mathbf{k}\sigma} \left| g^{\mu\mu'}_{\lambda}(\mathbf{k},\mathbf{q}) \right|^2 \delta(\varepsilon_{\mu\mathbf{k}} - \varepsilon_F) \delta(\varepsilon_{\mu'\mathbf{k}+\mathbf{q}} - \varepsilon_F). \tag{4.51}$$

In the same low-temperature limit ($kT \ll \omega_{0\lambda}$) Eq. (4.50) reads [145]

$$\Gamma_{\mathrm{ph}}(\omega) \approx \frac{2\pi}{\omega} \int_0^{\omega} d\Omega (\omega - \Omega) \alpha^2 F(\Omega), \tag{4.52}$$

where $\alpha^2 F(\Omega) \equiv \sum_{\mu\mathbf{k}\sigma} \delta(\varepsilon_{\mu\mathbf{k}} - \varepsilon_F) \alpha^2 F_{\mu}(\mathbf{k},\Omega)/N(\varepsilon_F)$. In order to see the connection between $\gamma^{\mathrm{allen}}_{\mathbf{q}\lambda}$ and $-\mathrm{Im}\pi^{\mathrm{HE,ph}}_{\lambda}(\omega)$ we explicitly write the expression for the averaged Eliashberg function $\alpha^2 F(\Omega)$ as

$$\alpha^2 F(\Omega) = \frac{1}{N(\varepsilon_F)} \sum_{\mathbf{q}'\lambda'} \sum_{\mu\mu'\mathbf{k}\sigma} \left| g^{\mu\mu'}_{\lambda'}(\mathbf{k},\mathbf{q}') \right|^2 \delta(\varepsilon_{\mu\mathbf{k}} - \varepsilon_F) \delta(\varepsilon_{\mu'\mathbf{k}+\mathbf{q}'} - \varepsilon_F) \delta(\Omega - \omega_{\mathbf{q}'\lambda'}). \tag{4.53}$$

Finally, by combining the last three equations with Eqs. (4.47) and (4.2) we get the following expression for the low-temperature limit of the HE phonon linewidth for the electron-phonon scattering

$$\gamma^{\mathrm{HE}}_{0\lambda} = \frac{2\langle g_{0\lambda} \rangle_{\varepsilon_F}}{\omega^2_{0\lambda} N(\varepsilon_F)} \sum_{\mathbf{q}'\lambda'} \frac{\gamma^{\mathrm{allen}}_{\mathbf{q}'\lambda'}}{\omega_{\mathbf{q}'\lambda'}} \int_0^{\omega_{0\lambda}} d\Omega (\omega_{0\lambda} - \Omega) \delta(\Omega - \omega_{\mathbf{q}'\lambda'}), \tag{4.54}$$

where $\langle g_{0\lambda} \rangle_{\varepsilon_F} \equiv \sum_{\mu\mathbf{k}\sigma} |g^{\mu\mu}_{\lambda}(\mathbf{k},0)|^2 \delta(\varepsilon_{\mu\mathbf{k}} - \varepsilon_F)$. We stop now to analyse the two phonon linewidth formulas: the widely used Allen's formula $\gamma^{\mathrm{allen}}_{\mathbf{q}\lambda}$ and the HE phonon linewidth activated by the higher-order electron-phonon scattering $\gamma^{\mathrm{HE}}_{0\lambda}$. From Eq. (4.51) we can see that $\gamma^{\mathrm{allen}}_{\mathbf{q}\lambda}$ accounts only for the quasi-elastic transitions that conserve the **q** momentum. As for the HE phonon linewidth, Eq. (4.54) shows how

the studied mode [in our case the $(\mathbf{q} \approx 0, \lambda)$ mode] is coupled to all other $(\mathbf{q}', \lambda')$ modes in the system via $\gamma^{\text{allen}}_{\mathbf{q}'\lambda'}$, with smaller frequency than that of the studied mode, i.e. $\omega_{\mathbf{q}'\lambda'} < \omega_{0\lambda}$ [279] [see Fig. 4.3(c)]. However, note that this coupling is not the direct phonon-phonon coupling (i.e., what is usually understood as anharmonicity), but the coupling of the particular phonon to the electronic damping effects coming from the other phonon modes in the system, i.e., *indirect* phonon-phonon coupling mediated by the electronic excitations. It is worth mentioning that an expression similar to Eq. (4.54) is derived in Ref. [50]. The second-order Fermi's golden rule formula is used there to describe transfer of energy in adsorbates on metallic surfaces from the molecular high-frequency internal vibration to a low-frequency translational or rotational degree of freedom via *e-h* pair excitation. This methodology successfully describes lateral hopping of molecules on metal surfaces induced by inelastic tunnelling electrons from the STM tip [294].

4.2.5.3 Total contribution to the HE intraband phonon self-energy

We can write now the imaginary part of the total HE intraband phonon self-energy damped by the electron-impurity and the electron-phonon scattering processes in a final form, which we will use later in the results section, as

$$\begin{aligned} -\text{Im}\pi^{\text{HE}}_{\lambda}(\omega) &\equiv -\text{Im}\pi^{\text{HE,imp}}_{\lambda}(\omega) - \text{Im}\pi^{\text{HE,ph}}_{\lambda}(\omega) \\ &\approx \frac{\Gamma_{\text{imp}} + \Gamma_{\text{ph}}(\omega)}{\omega} \sum_{\mu\mathbf{k}\sigma} |g^{\mu\mu}_{\lambda}(\mathbf{k}, 0)|^2 \, \delta(\varepsilon_{\mu\mathbf{k}} - \varepsilon_F). \end{aligned} \tag{4.55}$$

Interestingly, this type of high-energy expansion of the intraband phonon self-energy has a form analogous to that of the high-energy expansion of the conductivity formula obtained within the memory-function model [10, 41], the second-order Fermi's golden rule formula [9] and Holstein's theory [7, 9]. In these closely related transport theories, the damping functions Γ_{imp} and $\Gamma_{\text{ph}}(\omega)$, along with their real parts, are usually referred to as "memory functions" or "optical self-energies", and they are considered to be important for explaining experimental conductivity measurements in normal metals and superconductors [295]. In Sec. 4.3.4 we will use Eq. (4.55) together with the RTA interband contribution defined by Eq. (4.16) to estimate the phonon linewidth of the CO stretch mode on the Cu(100) surface. For the electron-impurity scattering contribution we use the RTA with physically meaningful values of the broadening Γ_{imp}. To obtain the damping function $\Gamma_{\text{ph}}(\omega)$ for the CO stretch mode, we first calculate the corresponding Eliashberg function $\alpha^2F(\Omega)$ and then we use it to evaluate Eqs. (4.50) and (4.52). The Eliashberg function is very useful in this

context, since it directly illustrates which of the phonon modes is coupled to the studied mode via the *e-h* pairs, and what is the relative intensity of this coupling.

One final comment on the RTA form of the imaginary part of Eq. (4.17) is in order. Apart from the interband contribution, the RTA form of $\widehat{\pi}^0_\lambda(\omega)$ has an intraband contribution as well. The imaginary part of the former can be expressed as

$$-\operatorname{Im}\widehat{\pi}^{\text{intra},0}_\lambda(\omega) \approx \frac{\omega\Gamma_{\text{intra}}}{\omega^2+\Gamma^2_{\text{intra}}} \sum_{\mu\mathbf{k}\sigma} |g^{\mu\mu}_\lambda(\mathbf{k},0)|^2\, \delta(\varepsilon_{\mu\mathbf{k}}-\varepsilon_F). \tag{4.56}$$

In the high-energy limit ($\omega \gg \Gamma_{\text{intra}}$) this expression is equivalent to the high-energy expansion of the intraband phonon self-energy $\pi^{\text{HE}}_\lambda(\omega)$ [Eq. (4.55)] that we obtained by summation of the leading indirect terms in the electron-impurity and electron-phonon scattering processes. However, there is no equivalent physical justification for the $\mathbf{q} \approx 0$ intraband transitions in Eq. (4.17) (see Sec. 4.2.2 and Appendix C). Thus, this expression should be taken with caution if electron scattering processes are neglected and a finite Γ_{intra} is used as a broadening parameter to simulate the clean noninteracting limit.

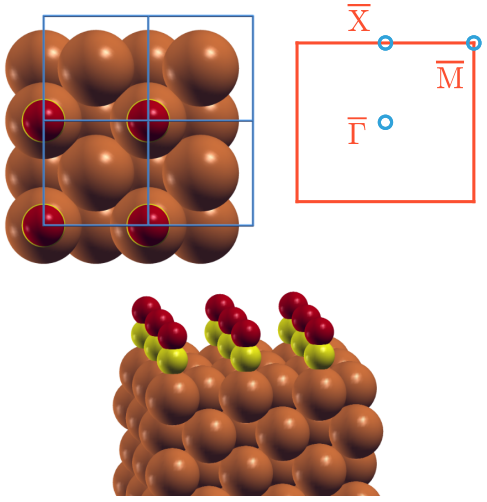

FIGURE 4.4: Unit cell of the c(2 × 2) structure of CO molecules adsorbed on the top site of the Cu(100) surface and the corresponding Brillouin zone with high-symmetry points. Red balls represent oxygen, yellow ones carbon, and brown ones copper atoms.

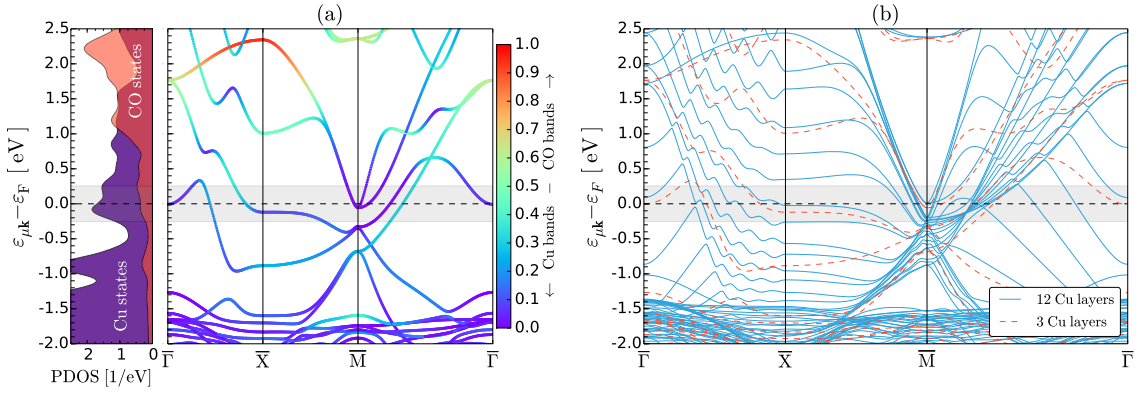

FIGURE 4.5: (a) Electronic band structure for the CO molecule on the Cu(100) three-layer surface. Red (purple) bands correspond to contributions from the CO molecule (Cu atoms). Inset: the projected density of states is shown for CO (red) and Cu (purple) states. (b) Comparison between the electronic band structure of CO adsorbed on 12 (blue lines) and three (red dashed lines) layers of the Cu(100) surface. The shaded areas in the electronic band plots represent the energy window $\varepsilon_F \pm \omega_{0\lambda}$, where $\omega_{0\lambda}$ is the energy of the CO stretch mode.

4.3 Results for CO stretch mode on the Cu(100) surface

4.3.1 Computational details

All calculations are done using the plane-wave DFT-based QE package [105] with a plane-wave cut-off energy of 50 Ry. The core-electron interaction is approximated with ultrasoft pseudopotentials, and the exchange and correlation functional with the revPBE version [73] of the GGA[13]. The adiabatic vibrational frequencies $\omega_{0\lambda}$ and harmonic electron-phonon matrix elements $g_\lambda^{\mu\mu'}(\mathbf{k}, 0)$ defined in Eq. (2.78) are calculated on a $(8 \times 8 \times 1)$ MP $\mathbf{k}$ point grid [103] using DFPT [135]. In that case, $\psi_{\mu\mathbf{k}}$ are the KS electronic wavefunctions, while V_{ei} is replaced with the self-consistent KS potential V^{SCF} in electron-phonon matrix elements. Generally, the KS potential is frequency dependent. However, for practical reasons it is approximated with its static value $V^{SCF} \approx V^{SCF}(\omega = 0)$ in usual DFT calculations [8, 136]. In order to properly reproduce the continuous momentum space for the different phonon self-energies discussed in Sec. 4.2 we use denser $\mathbf{k}$ point grids ranging from $(16 \times 16 \times 1)$ to $(160 \times 160 \times 1)$. In doing so, the electron-phonon matrix elements $g_\lambda^{\mu\mu'}(\mathbf{k}, 0)$ obtained on the coarser grid are interpolated on these denser grids following the QE implementation. The calculation of the Eliashberg function $\alpha^2F(\omega)$ [Eq. (4.53)]

[13]We have checked that different exchange and correlation functionals do not change significantly the value of phonon linewidth using the following functionals: revPBE, PBE [71], LDA [66] and WC [296].

needed for the damping function $\Gamma_{\mathrm{ph}}(\omega)$ [Eq. (4.50)] is performed on a $(8 \times 8 \times 1)$ $\mathbf{q}$ point grid and including the two uppermost layers of Cu(100) in the DFPT calculations.

4.3.2 Geometry and electronic structure

All the analyses presented here are performed for the adsorption structure and coverage reported from IRAS and pump-probe laser spectroscopy experiments in Refs. [20, 21], respectively: one CO molecule in the c(2×2) unit cell of Cu(100) adsorbed vertically on the top site [Fig. 4.4]. Using the aforementioned parameters, the adsorption geometry is optimized until forces are smaller than 0.01 eV/Å, where only the bottom surface layer is not allowed to move. The obtained Cu-C and C-O bond lengths are 1.875 and 1.154 Å, respectively, which are in good agreement with the experimental data [297] and previous theoretical works [298]. In our study we vary the number of Cu layers, going from three to 18 layers. Although the relevant geometrical parameters (Cu-C and C-O bond lengths) do not depend much on the number of layers included in the calculation, we will show how it significantly affects the electronic structure and, hence, the calculated phonon linewidth.

The states with mixed electron contributions by CO and Cu, when affected by the CO stretch mode, are the ones that will show finite non-negligible values of $g_{\lambda}^{\mu\mu'}(\mathbf{k}, 0)$. The projected density of states (PDOS)[14] on the individual atoms and the electronic band structure along the the high-symmetry points of the 1BZ allow us to identify the states contributing to the finite phonon linewidth. The results for the CO/Cu(100) system with three layers are shown in Fig. 4.5(a). The color scale in the band structure represents states contributed by either the CO molecule (red color) or Cu atoms (purple color). This identification is made by defining the coefficient $\mathcal{C}_{\mu\mathbf{k}}$ for each state as

$$\mathcal{C}_{\mu\mathbf{k}} = \frac{\iint dxdy \int_{z_0-a}^{z_0+a} dz \, |\psi_{\mu\mathbf{k}}(\mathbf{r})|^2}{\int_V d\mathbf{r} \, |\psi_{\mu\mathbf{k}}(\mathbf{r})|^2}, \tag{4.57}$$

where a is the distance between the midpoint of CO and the midpoint of the Cu-C bond, z_0 is the z coordinate of the midpoint of CO, and V is the total volume of the unit cell.

In agreement with Refs. [49, 298], the PDOS shows that there is a significant hybridization between the CO states with p-symmetry (π^*) and the Cu states around

[14] The PDOS is calculated by projecting on s- and p-states centered at the selected atoms, using the implementation of QE.

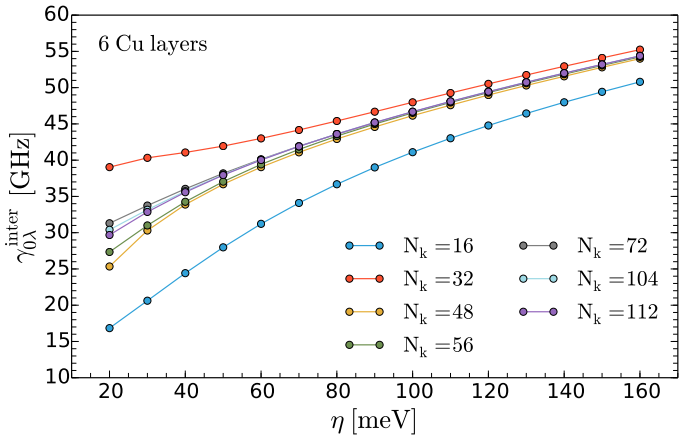

FIGURE 4.6: Interband part of the $\mathbf{q} \approx 0$ phonon linewidth $\gamma_{0\lambda}^{\mathrm{inter}}$ of the CO stretch mode as a function of η calculated with Eq. (4.4). The Cu(100) surface is approximated by six layers. The number $\mathrm{N_k}$ defines the $\mathbf{k}$ point grid with $(\mathrm{N_k} \times \mathrm{N_k} \times 1)$. The temperature is $T = 200$ K.

the Fermi level. In addition, the colored band structure provides precise information on what states can contribute to the interband transition with $\mathbf{q} \approx 0$. Note that only the electronic transitions within the shaded grey area around the Fermi energy can be induced by the CO stretch mode ($\omega_{0\lambda}^{\mathrm{exp}} = 0.259$ eV [16]). Clearly, this region is poorly described by the three-layer surface. However, as we increase the number of Cu layers, the number of bands in this area increases significantly [Fig. 4.5(b)]. Therefore, it is reasonable to expect the imaginary part of any of the above phonon self-energy expressions to change with the increase of the number of electronic bands, since more electronic transitions fulfilling the energy conservation condition $\delta(\omega_{0\lambda} + \varepsilon_{\mu\mathbf{k}} - \varepsilon_{\mu'\mathbf{k}})$ may contribute $g_{\lambda}^{\mu\mu'}$ defined by Eq. (2.78). As dictated by the causality principle, the real part of the phonon self-energy can be obtained by using the imaginary part and the Kramers-Kronig relations, so the mentioned changes will affect the real part as well. All these observations indicate that a proper description of the Cu surface is needed to assure an accurate calculation of the phonon self-energy.

4.3.3 Interband part of the long-wavelength phonon linewidth

4.3.3.1 Convergence analysis of the linewidths

Before analysing the role of electronic relaxation processes in the stretch-mode linewidth of CO adsorbed on Cu(100), it is necessary to assure first that the value of the noninteracting phonon linewidth is well converged with respect to those parameters controlling the quality of the CO/Cu(100) electronic states, namely, the

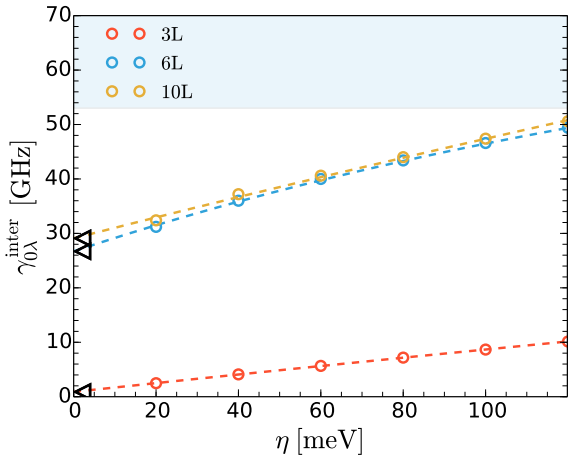

FIGURE 4.7: Interband part of the $\mathbf{q} \approx 0$ phonon linewidth $\gamma_{0\lambda}^{\text{inter}}$ of the CO stretch mode on the Cu(100) surface for three, six and 10 Cu layers (red, blue, and yellow colors, respectively). The results are obtained with Eq. (4.4) and extrapolating the finite η values to $\eta = 0$, we get the result of the bare phonon linewidth (black triangles). The number of $\mathbf{k}$ points used here is $(160 \times 160 \times 1)$ for three layers, and $(72 \times 72 \times 1)$ for six and 10 layers. The temperature is $T = 200$ K. The blue shaded area represents the area from the lowest measured experimental linewidth (~ 50 GHz) to the highest (~ 140 GHz) one (including experimental error bars).

number of $\mathbf{k}$ points and the number of Cu layers. In doing this selection, one should be aware that the Dirac-delta function appearing in the imaginary part of Eq. (4.4) (bare phonon self-energy) is numerically approximated by a Lorentzian function of half-width-at-half-maximum η. Therefore, the calculated values of the bare phonon linewidth should be well converged for reasonably small η values as we check next.

In an ideal situation, the summation appearing in the expressions of the correlation functions (e.g., phonon self-energy) would be a continuous integral over the $\mathbf{k}$ space. Thus, in order to obtain accurate numerical results, we need to achieve convergence with respect to the discrete number of $\mathbf{k}$ points used to simulate the continuum. To clarify this issue we plot in Fig. 4.6 the results for the CO stretch mode phonon linewidth $\gamma_{0\lambda}^{\text{inter}}$ obtained with Eqs. (4.2) and (4.4) as a function of η and for different $\mathbf{k}$ point grids, where all the calculations were performed for a slab of six Cu layers. We observe that for $\eta \geq 60$ meV the convergence is achieved with the $(48 \times 48 \times 1)$ grid, while for smaller values of η we need at least the $(72 \times 72 \times 1)$ grid. Therefore, this latter grid will be used in the rest of this section unless otherwise stated.

The convergence of the bare phonon self-energy as a function of the number of Cu layers used in the slab is shown in Fig. 4.7. For each slab, the phonon linewidth in the clean noninteracting limit $\eta \to 0^+$ (black triangles) is obtained by extrapolating the corresponding $\gamma_{0\lambda}^{\text{inter}}(\eta)$ curve. The results of Fig. 4.7 show that the bare $\gamma_{0\lambda}^{\text{inter}}$ obtained with six Cu layers is already converged. Importantly, the obtained values

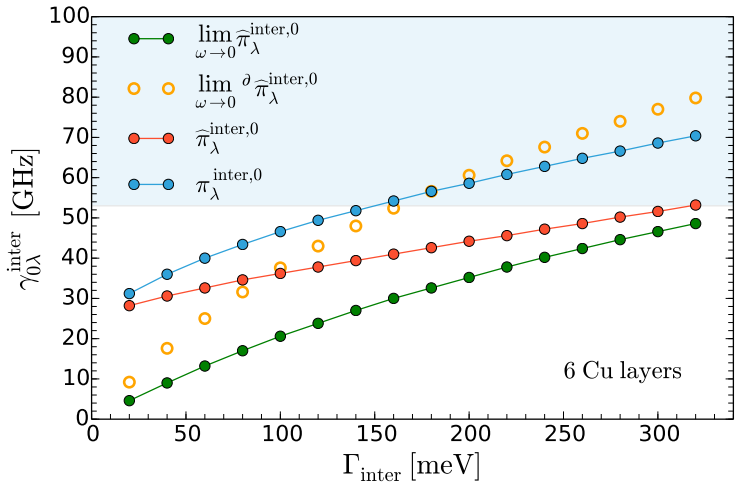

FIGURE 4.8: Interband part of the $\mathbf{q} \approx 0$ phonon linewidth $\gamma^{\mathrm{inter}}_{0\lambda}$ of the CO stretch mode as a function of Γ_{inter} for six Cu layers calculated with Eqs. (4.16) (blue circles), (4.17) (red circles), (4.34) (green circles), and (4.35) (yellow circles), using the $(72 \times 72 \times 1)$ $\mathbf{k}$ point grid. Blue shaded area as in Fig. 4.7. The temperature is $T = 200$ K.

for six and 10 layers are 26.7 and 29.1 GHz, respectively, which are far below the lowest reported experimental values [16, 20–22]. In principle, a theoretical linewidth smaller than the experimental one is not that surprising, because further electron scattering effects that exist under real experimental conditions are not captured by an ideal theoretical model. For this reason we analyze next how these results change when electron relaxation processes are included at the RTA level ($\eta \to \Gamma_{\mathrm{inter}}$), i.e., by giving a physical meaning to the broadening.

4.3.3.2 RTA results

The results in Fig. 4.8 show the values of $\gamma^{\mathrm{inter}}_{0\lambda}$ for six Cu layers as a function of the damping energy Γ_{inter} calculated with the RTA phonon self-energy $\pi^{\mathrm{inter},0}_{\lambda}(\omega_{0\lambda})$ [see Eq. (4.16)]. We observe how the phonon linewidth increases with the damping energy, i.e. with the intensity of the electronic scattering processes. Consequently, including a finite electron damping energy improves the bare phonon linewidth result by bringing it closer to the experimental values. Figure 4.8 also shows that the results obtained with $\pi^{\mathrm{inter},0}_{\lambda}(\omega_{0\lambda})$ [Eq. (4.16)] (blue circles) and $\widehat{\pi}^{\mathrm{inter},0}_{\lambda}(\omega_{0\lambda})$ [Eq. (4.17)] (red circles) are different for finite Γ_{inter}, while they tend to the same values when $\Gamma_{\mathrm{inter}} \to 0^{+}$. Note that, as discussed in Sec. 4.2 (see also Appendix B), Eq. (4.16) is the correct phonon self-energy within the RTA. This shows that Eq. (4.17), which corresponds to introducing a finite damping into the phonon self-energy expression obtained after removing the adiabatic contribution [Eq. (4.11)], is only correct in the strict $\Gamma_{\mathrm{inter}} \to 0$ limit, but not in the general RTA approximation with finite Γ_{inter}.

As we mentioned earlier, the calculated phonon linewidth depends on the number of Cu layers used to describe the surface. In Fig. 4.9 we show the RTA phonon linewidth $\gamma_{0\lambda}^{\text{inter}}$ obtained with Eqs. (4.16) (open blue circles) and (4.17) (blue circles) as a function of the number of Cu layers. As we already anticipated from the electronic structure analysis in Sec. 4.3.2, the RTA linewidths are closer to the experimental values as the slab thickness increases from three to 16 layers. Here we see that six layers provide a reasonably good approximation for the surface and, even though the linewidth further increases with the number of layers, the change is not drastic. Also, the RTA phonon linewidths obtained with $\pi_{\lambda}^{\text{inter},0}(\omega_{0\lambda})$ are always higher than the ones obtained with $\widehat{\pi}_{\lambda}^{\text{inter},0}(\omega_{0\lambda})$. The presented results are calculated with $\Gamma_{\text{inter}} = 150$ meV, so they should be interpreted as an upper limit for the given number of Cu layers.

4.3.3.3 Analysis of the quasi-static limit

In order to get insight in the limitations of the quasi-static limit for high-frequency vibrational modes or for optical phonons, we also show in Fig. 4.8 the quasi-static forms of the interband phonon linewidths obtained with Allen's formula [Eq. (4.32)] (black circles), $\widehat{\pi}_{\lambda}^{\text{inter},0}(0)$ [Eq. (4.34)] (green circles), and ${}^{\partial}\pi_{\lambda}^{\text{inter},0}(0)$ [Eq. (4.35)] (yellow circles). We recall here that Eq. (4.34) is obtained by taking the quasi-static limit in Eq. (4.17) (as described in Sec. 4.2.4) when $\eta \to \Gamma_{\text{inter}}$. Allen's formula is obtained after taking $\omega_{0\lambda} \to 0$ and $\varepsilon_{\mu\mathbf{k}} \to \varepsilon_{\mu'\mathbf{k}}$ in Eqs. (4.31) and (4.34), respectively. Additionally, Eq. (4.35) has been used in the literature to avoid the divergence in the intraband part of the phonon self-energy in the quasi-static limit [257]. As

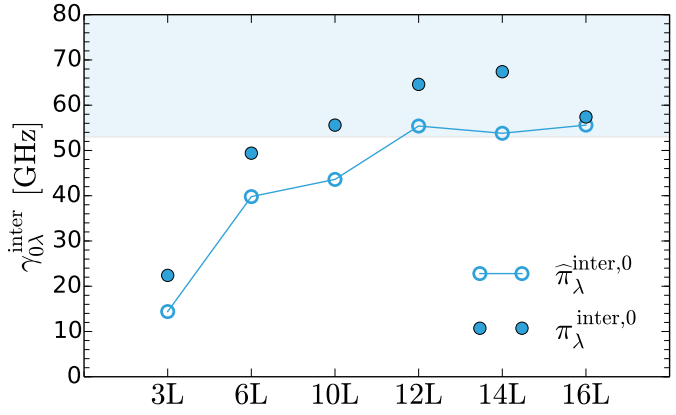

FIGURE 4.9: $\gamma_{0\lambda}^{\text{inter}}$ of the CO stretch mode calculated with Eqs. (4.16) (blue circles) as a function of the number of Cu layers. The damping energy is $\Gamma_{\text{inter}} = 150$ meV and the numbers of $\mathbf{k}$ points are $\text{N}_{\text{k}} = 160, 72, 72, 56, 56, 32$ for the number of layers $\text{N}_{\text{layer}} = 3, 6, 10, 12, 14, 16$, respectively. The blue shaded area represents the same as in Fig. 4.7. The temperature is $T = 200$ K.

$\Gamma_{\text{inter}} \to 0^+$ the three quasi-static curves go to zero, as required by definition of adiabaticity. For large values of Γ_{inter} the phonon linewidth obtained with $\widehat{\pi}_\lambda^{\text{inter},0}(0)$ approaches the result obtained with $\widehat{\pi}_\lambda^{\text{inter},0}(\omega_{0\lambda})$, which means that the Lorentzian loses resolution when Γ_{inter} becomes larger than $\omega_{0\lambda}$. From the perspective of the quasi-static expression $\widehat{\pi}_\lambda^{\text{inter},0}(0)$ this implies that Γ_{inter} is so large that it actually introduces dynamic ($\omega \neq 0$) instead of static contributions, which are the only ones that should strictly appear in the quasi-static limit. Similarly, the large broadening parameter ($\eta = 0.6$ eV) used in Ref. [249] forces the quasi-static phonon linewidth and also the adiabatic friction coefficients that are calculated from an expression analogous to $\widehat{\pi}_\lambda^{\text{inter},0}(0)$ to fall into the dynamical regime. In a realistic situation the case $\Gamma_{\text{inter}} \gtrsim \omega_{0\lambda}$ is unlikely to happen, because the energy of the CO stretch mode is 0.26 eV, and a value $\Gamma_{\text{inter}} \gtrsim 0.26$ eV would correspond to a very dirty system characterized by various and highly-probable scattering processes. In fact, the realistic values of Γ_{inter} should be within the same order of magnitude as Γ_{intra} [270, 299], where the usual values range from ~ 1 meV up to around 100 meV [102]. Therefore the values of $\gamma_{0\lambda}^{\text{inter}}$ at $\Gamma_{\text{inter}} \approx 100 - 150$ meV should be taken as the uppermost limit. The results obtained from the interband part of Allen's formula (black circles) exhibit a dependence on Γ_{inter} very similar to that of the interband phonon linewidth obtained from Eq. (4.34). Regarding the results of the phonon linewidth obtained with ${}^{\partial}\pi_\lambda^{\text{inter},0}(0)$, note that even if they match the $\pi_\lambda^{\text{inter},0}(\omega_{0\lambda})$ results for some values of Γ_{inter}, this quasi-static limit faces the same inconsistencies as $\widehat{\pi}_\lambda^{\text{inter},0}(0)$ for $\Gamma_{\text{inter}} \lesssim 150$ meV.

Having the above discussion in mind, we can summarize the problems of the quasi-static approximations when applied to high-frequency modes in the following two points: (i) if the clean noninteracting limit ($\Gamma_{\text{inter}} \to 0^+$) is simulated, then the interband expressions in the quasi-static limit are zero, leaving only the intraband term of $\widehat{\pi}_\lambda^{0}(0)$ finite (as discussed in Sec. 4.2.4). (ii) If the interacting case ($\Gamma_{\text{inter}} > 0$) is regarded relevant in the studied system, then realistic values of Γ_{inter} should be taken into account, since the phonon linewidth is not constant with respect to different Γ_{inter} values. However, even in that case the quasi-static approximations may give inconsistent results, being therefore more meaningful to use the frequency dependent phonon self-energy $\pi_\lambda^{\text{inter},0}(\omega_{0\lambda})$.

4.3.3.4 Temperature and momentum distribution function effects

As for the temperature effects that enter the Fermi-Dirac distribution functions $f_{\mu\mathbf{k}}$, we observe only minor changes in the phonon linewidth. Specifically, $\gamma_{0\lambda}^{\text{inter}}$ changes less than 1 GHz for electronic temperatures within the range $T = 40 - 300$ K. In general, this does not mean that the phonon linewidth due to electron-phonon

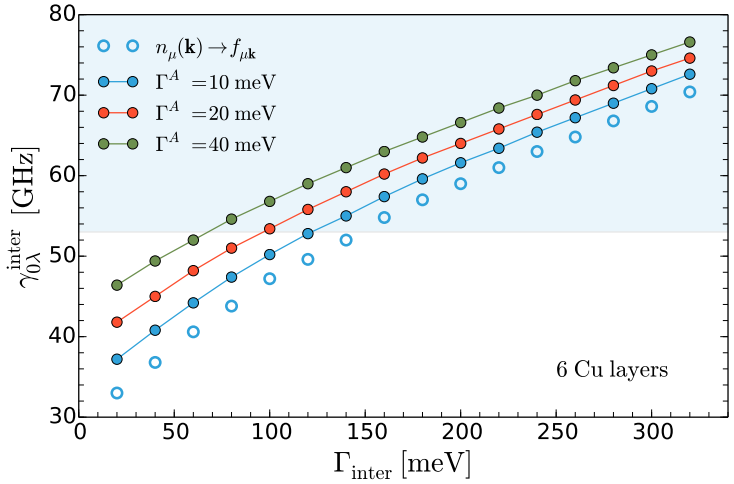

FIGURE 4.10: $\gamma_{0\lambda}^{\text{inter}}$ as a function of Γ_{inter} of the CO stretch mode obtained with Eq. (4.18), where the low temperature ($T = 10$ K) Fermi-Dirac distribution functions $f_{\mu\mathbf{k}}$ (open circles) are replaced with the momentum distribution functions $n_\mu(\mathbf{k})$ obtained with Eq. (4.21) (closed circles). The results are shown also for different damping energies of the single-particle spectral function Γ^A. The number of $\mathbf{k}$ points used here is $(72 \times 72 \times 1)$. The blue shaded area represents the same as in Fig. 4.7.

coupling is independent of temperature. Well on the contrary, the *e-h* self-energy is a complex function of temperature, and thus the damping energy Γ_{inter} should also change when the temperature changes (in a similar way as Γ_{intra} changes in Sec. 4.3.4 and in Refs. [11, 12, 42, 272]).

Next we analyze the effect of including electronic relaxation processes in the electron momentum distribution functions, i.e. of replacing $f_{\mu\mathbf{k}}$ by $n_\mu(\mathbf{k})$ as defined in Eq. (4.21). The results for this replacement are shown in Fig. 4.10 for three different values of Γ^A. For each Γ_{inter}, the interband phonon linewidth increases when including relaxation processes in the distribution function. As a result we get better agreement with the experimental values. Still, it is not possible to establish a correct quantitative estimation of the theoretical $\gamma_{0\lambda}^{\text{inter}}$ since the exact value of Γ^A is unknown, except for the fact that it should be within the usual values of the electron self-energy ($\sim 1-100$ meV). Thus these results show qualitatively how accounting for relaxation processes in the single-electron spectral function (quasi-particle linewidth) influences the phonon linewidth through the momentum distribution function.

4.3.4 Intraband part of the long-wavelength phonon linewidth

Now, we turn our attention to the intraband transitions, which give contribution proportional to q^2 and thus negligible for the $\mathbf{q} \approx 0$ optical phonons (see Eq. (4.6)), i.e. the CO stretch mode in our particular case. If we take into account higher order electron scattering processes (e.g., electron-impurity and electron-phonon scattering), the indirect intraband channel is open, as discussed in Sec. 4.2.5. For the CO stretch mode excited by infrared light ($\mathbf{q} \approx 0$), the condition $\omega \gg |\varepsilon_{\mu\mathbf{k}} - \varepsilon_{\mu\mathbf{k}+\mathbf{q}}|$ is met. Thus we can apply the high-energy expansion of the indirect intraband phonon self-energy provided by Eq. (4.55). Along with the interband contribution analysed in the previous section, this indirect intraband phonon self-energy is considered to be important for understanding the experimental $\mathbf{q} \approx \mathbf{0}$ phonon linewidths. In the following we study electron-impurity and electron-phonon scattering separately.

4.3.4.1 Electron-impurity scattering

First we consider the electron-impurity scattering within the RTA where the corresponding values of $-\mathrm{Im}\pi_\lambda^{\mathrm{HE,imp}}(\omega_{0\lambda})$ are shown in Fig. 4.11 as a function of Γ_{imp}. As the intraband damping energies (i.e. transport relaxation times, τ_{tr}) can be extracted very easily from optical conductivity measurements by fitting the results to the Drude model, the values for usual bulk systems are well known. The reported

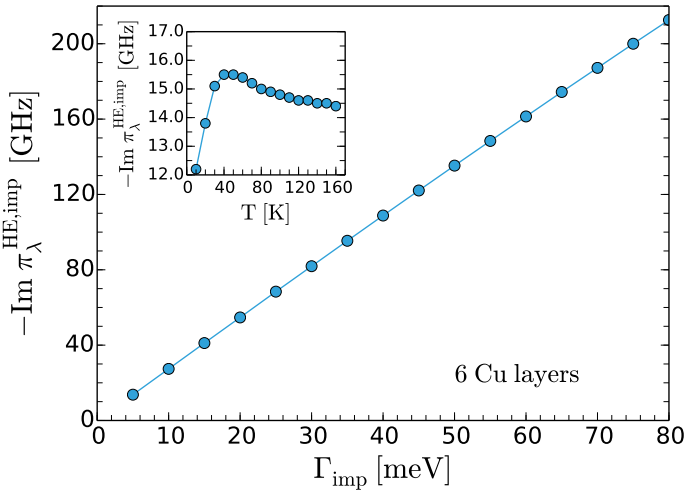

FIGURE 4.11: High-energy expansion of the indirect contribution to the intraband phonon self-energy activated by electron-impurity scattering [Eq. (4.42)] of the CO stretch mode as a function of Γ_{imp} with $T = 200$ K and as a function of the temperature with $\Gamma_{\mathrm{imp}} = 5$ meV (inset) for six Cu layers. The number of $\mathbf{k}$ points used here is $(80 \times 80 \times 1)$.

values for bulk Cu in the range $T = 60 - 150$ K are $\Gamma_{\rm imp} = 1/\tau_{\rm tr} = 2 - 11$ meV [102]. From these values we take the one corresponding to the lowest temperature, since the electron damping processes due to electron-phonon scattering are considered to be suppressed then, while electron-impurity processes prevail. For this range of $\Gamma_{\rm imp}$ values in our system we get $-{\rm Im}\pi_\lambda^{\rm HE,imp}(\omega_{0\lambda}) \approx 10$ GHz [see Fig. 4.11]. Note however that this value should be taken as a coarse estimation, since the intraband electron scattering processes in bulk Cu could be different from the ones in CO/Cu(100). Moreover, $1/\tau_{\rm tr}$ in the low temperature limit includes also the electron-electron scattering processes in the system ($1/\tau_{\rm tr} = 1/\tau_{\rm tr}^{\rm imp} + 1/\tau_{\rm tr}^{\rm el}$, where $\tau_{\rm tr}^{\rm imp}$ and $\tau_{\rm tr}^{\rm el}$ are relaxation times for the impurity and electron scattering, respectively) and not just the impurity scattering ($1/\tau_{\rm tr}^{\rm imp}$). In the inset of Fig. 4.11 we also show the temperature dependence of $-{\rm Im}\pi_\lambda^{\rm HE,imp}(\omega_{0\lambda})$ obtained through the $\partial f_{\mu\mathbf{k}}/\partial\varepsilon_{\mu\mathbf{k}}$ factor. In the range $T = 100 - 160$ K relevant for the experiment [22], no significant temperature effects are observed.

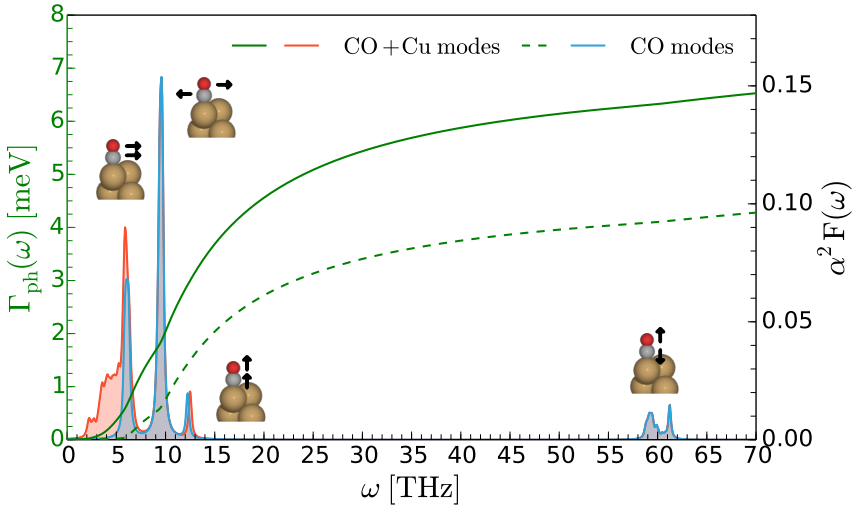

FIGURE 4.12: Damping function $\Gamma_{\rm ph}(\omega)$ in the low temperature limit, $T \approx 0$K, calculated with Eq. (4.52) (left axis) and Eliashberg function $\alpha^2F(\omega)$ calculated with Eq. (4.53) (right axis) as a function of ω for the cases when only the CO molecule is allowed to move (blue area and dashed green line, respectively) and when both CO and the Cu(100) atoms are allowed to move (red area and full green line, respectively). The cartoon models in the insets show the movements of the CO molecules for each phonon mode. From left to right they show frustrated translation, frustrated rotation, CO - Cu stretch mode, and C - O stretch mode, respectively. The number of $\mathbf{k}$ and $\mathbf{q}$ points used here are $(80 \times 80 \times 1)$ and $(8 \times 8 \times 1)$, respectively. The number of Cu layers is six.

TABLE 4.1: Column labels: C - O denotes the internal stretch mode, CO - Cu denotes substrate-molecule stretch mode, FR means frustrated rotation mode, FT frustrated translation, and CO/Cu the phonon modes coming from the joint motion of CO and Cu(100). First row: vibrational frequencies of the CO molecule and Cu(100) within the 1BZ (bands of the Eliashberg function). Second row: the same frequencies as in the first row, but only for $\mathbf{q} \approx 0$. Third Row: experimental frequencies of the modes corresponding to the second row. Here we compare the frequencies of the CO/Cu modes with the experimental frequencies of the bare Cu(100) surface [300] since this low-frequency band mostly comes from the pure Cu(100) modes. Fourth row: contributions of each λ' mode of the CO/Cu(100) system to the electron damping function $\Gamma_{\mathrm{ph}}(\omega_{0\lambda})$ [Eq. (4.52)]. Fifth row: the $\mathbf{q} \approx 0$ HE phonon linewidth of the CO stretch mode $\gamma_{0\lambda}^{\mathrm{HE}}$ obtained by introducing the values of $\Gamma_{\mathrm{ph}}(\omega_{0\lambda})$ from the previous row into Eq. (4.55) (with $\Gamma_{\mathrm{imp}} = 0$).

	λ' mode (λ = C - O)				
	C - O	CO - Cu	FR	FT	CO/Cu
α^2F bands	58.70 - 61.37	12.11 - 12.33	9.14 - 9.78	5.79 - 6.33	< 7 [THz]
$\omega_{0\lambda'}$	61.37	12.33	9.78	6.05	< 7 [THz]
Exp. $\omega_{0\lambda'}$	62.54 [20]	10.34 [301]	8.54 [301]	0.96 [302]	$\lesssim 7$ [300] [THz]
$\Gamma_{\mathrm{ph}}(\omega_{0\lambda})$	0.01	0.22	2.54	1.34	2.23 [meV]
$\gamma_{0\lambda}^{\mathrm{HE}}$	0.07	1.18	13.95	7.37	12.23 [GHz]

4.3.4.2 Electron-phonon scattering

To account for the electron-phonon scattering contributions[15] to the intraband phonon linewidth, we consider the corresponding electronic damping function Γ_{ph} beyond the RTA by doing the explicit calculations. In particular, to get Γ_{ph} in the low-temperature limit ($T \approx 0$K) we evaluate Eq. (4.52) and for finite T we calculate Eqs. (4.48) and (4.50). The Eliashberg function is always calculated with the use of Eq. (4.53). In Fig. 4.12 the Eliashberg function $\alpha^2F(\omega)$ and $\Gamma_{\mathrm{ph}}(\omega)$ for $T \approx 0$K are shown for the CO molecule on Cu(100). The Eliashberg function $\alpha^2F(\omega)$ calculated allowing only the C and O to move shows peaks that can be assigned to three low-frequency modes besides the CO stretch mode, which correspond to the frustrated translation (FT), the frustrated rotation (FR), and the CO-Cu stretch mode [see cartoons of these modes in the insets of Fig. 4.12]. By allowing the two uppermost layers of Cu(100) also to move, an additional low-frequency phonon band below 7 THz appears in the Eliashberg function, which includes combined motions of the bare Cu(100) surface and the CO molecule. The main CO molecule phonon modes (i.e., FT, FR, and the CO-Cu and CO stretch modes) are not altered significantly by inclusion of Cu atoms movement. The calculated frequencies of these modes are presented in Table 4.1, along with the corresponding experimental values [20, 300–302]. The relative intensities (peak heights) of $\alpha^2F(\omega)$ for each phonon mode allow us to quantify their contribution to $\Gamma_{\mathrm{ph}}(\omega_{0\lambda})$ and consequently to the phonon linewidth

[15] We recall that the term "electron-phonon scattering" actually refers to the higher-order terms. The lowest-order electron-phonon term is Eq. (4.6).

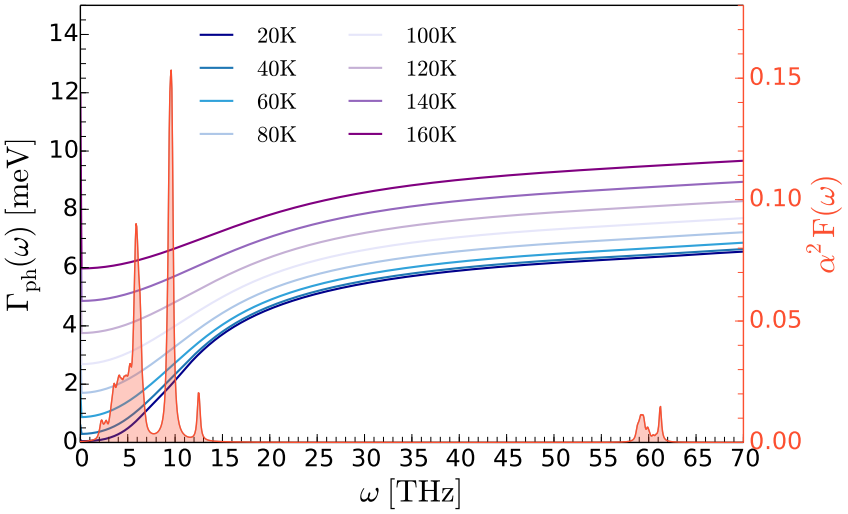

FIGURE 4.13: Damping function $\Gamma_{\rm ph}(\omega)$ (left axis) as a function of ω for different temperatures calculated with the use of Eqs. (4.48) and (4.50) (various blue and purple curves). Eliashberg function $\alpha^2F(\omega)$ [Eq. (4.53)] (right axis) calculated allowing both CO and Cu to move is shown in red. The numbers of $\mathbf{k}$ and $\mathbf{q}$ points used here are $(80 \times 80 \times 1)$ and $(8 \times 8 \times 1)$, respectively. The number of Cu layers is six.

$\gamma_{0\lambda}^{\rm HE}$ if $\omega < \omega_{0\lambda}$ [see Eq. (4.54)]. The values of each contribution are summarized in Table 4.1. From this we see that the largest damping of the CO stretch mode is caused by the electron damping effects coming from the FR modes within the molecular overlayer, while the smallest contribution comes from the CO-Cu and the CO[16] stretch modes. Apart from the internal FR and FT modes, we find that the phonon modes coming from the joint motion of CO and the Cu(100) atoms also play an important role in the damping mechanism of the CO stretch mode [compare solid and dashed lines in Fig. 4.12, and the $\gamma_{0\lambda}^{\rm HE}$ values for the FR and the CO/Cu modes in Table 4.1].

Next we analyse the temperature effects coming from these higher-order effects. Since the CO stretch mode is coupled to the rest of the phonon modes in the system through the *e*-*h* pairs, the temperature enters the intraband phonon self-energy through the Bose-Einstein distribution function $n_b(\omega_{\mathbf{q}'\lambda'})$ [see Eq. (4.44)]. The temperature-dependent $\Gamma_{\rm ph}(\omega)$ calculated with the use of Eqs. (4.48) and (4.50) is shown in Fig. 4.13, where an increase is observed as the temperature increases. This result is expected for this kind of processes [11, 12, 42, 295], considering that the temperature enhances the population of excited phonons [through $n_b(\omega_{\mathbf{q}'\lambda'})$], thus increasing the probability of electron-phonon scattering events. In Fig. 4.14 we show the HE intraband phonon linewidth $\gamma_{0\lambda}^{\rm HE}$ calculated with Eq. (4.55) and $\Gamma_{\rm imp} = 0$

[16]This "self" contribution to $\Gamma_{\rm ph}(\omega_{0\lambda})$ comes from all the CO stretch modes with $\mathbf{q}'$ in the 1BZ that satisfy the condition $\omega_{\mathbf{q}'\lambda} < \omega_{0\lambda}$. In other words, this accounts for the coupling of the studied CO stretch mode at $\mathbf{q} \approx 0$ with all other $\mathbf{q}'$ modes within the same phonon band.

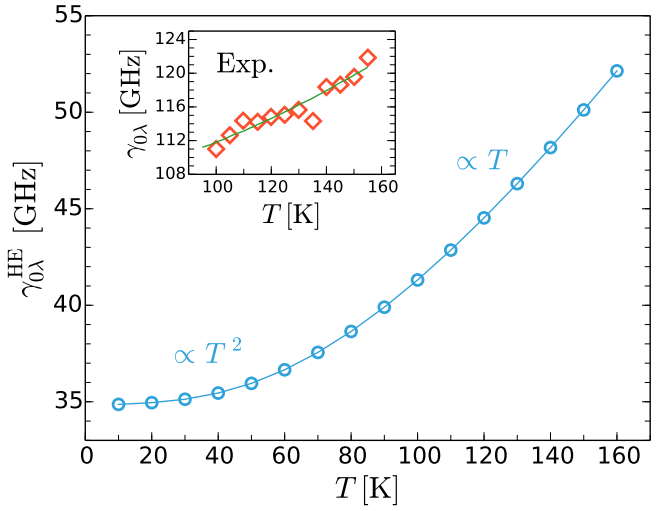

FIGURE 4.14: The HE intraband phonon linewidth $\gamma_{0\lambda}^{\mathrm{HE}}$ calculated with Eq. (4.55) (when $\Gamma_{\mathrm{imp}} = 0$) as a function of temperature (blue circles). The numbers of $\mathbf{k}$ and $\mathbf{q}$ points used here are $(80 \times 80 \times 1)$ and $(8 \times 8 \times 1)$, respectively. The number of Cu layers is six. The inset shows the experimental total phonon linewidth (red diamonds) obtained in Ref. [22]. The green line represents the corresponding fitting curve also taken from Ref. [22].

(i.e., pure electron-phonon scattering contributions) as a function of temperature. In the range between 0K and 160K the phonon linewidth increases by $\sim$ 20 GHz due to the electron-phonon scattering. In Ref. [22] the temperature dependence of the CO stretch mode linewidth is measured between 100K and 160K using IRAS. They obtain a linear increase in this range of $\sim$ 10 GHz (see the inset of Fig. 4.14). The temperature increase shown in Fig. 4.14 is in qualitative good agreement with those experimental findings (i.e., the linear increase in the aforementioned temperature range is also around 10 GHz). Usually the temperature dependence of the adsorbates high-frequency modes is considered to be the footprint of an underlying pure dephasing mechanism, either coming from elastic scattering with low-frequency modes (direct elastic anharmonic effect) [16, 22, 303] or with *e-h* pairs [280]. In Ref. [22] the temperature dependence is assigned to the former process and the theoretical modelling of this mechanism is made by fitting the model parameters to the experimental results (green line in the inset of Fig. 4.14). Here we give an alternative mechanism for explaining the temperature dependence, namely *indirect* phonon-phonon coupling mediated by the *e-h* pairs. This mechanism also includes the aforementioned *e-h* pair dephasing when the studied $(\mathbf{q} \approx 0, \lambda)$ mode is coupled to the different $\mathbf{q}'$ modes within the same λ phonon band.

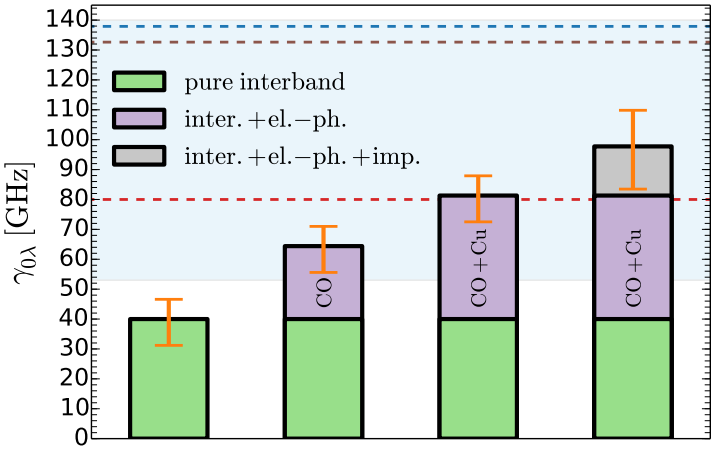

FIGURE 4.15: First column: $\gamma_{0\lambda}^{\text{inter}}$ value obtained when only the interband transitions are included [calculated with Eq. (4.16) for $\Gamma_{\text{inter}} = 60$ meV]. Second column: to the previous $\gamma_{0\lambda}^{\text{inter}}$ value we add the HE intraband indirect contribution coming from the electron-phonon coupling calculated allowing only C and O to move [Eq. (4.55) with $T = 140$ K and without the impurity effects]. Third column: to the first column we add the HE intraband phonon linewidth that includes the electron-phonon coupling calculated allowing both CO and Cu to move. Fourth column: to the third column we add the HE intraband phonon linewidth that includes electron-impurity scattering [Eq. (4.42) with $\Gamma_{\text{imp}} = 3$ meV]. The orange error bars in the first three columns represent the range of results obtained with $\Gamma_{\text{inter}} = 60 \pm 40$ meV. The error bar in the fourth column additionally includes the range of results obtained with $\Gamma_{\text{imp}} = 3 \pm 2$ meV. The blue shaded area has the same meaning as in Fig. 4.7. The horizontal dashed lines represent a few specific experimental results: the linewidth coming from energy relaxation obtained in Ref. [21] (red), the corresponding total linewidth, which also includes energy-conserving processes (brown) [21], and the total linewidth obtained in Ref. [20] (blue).

4.3.5 Total phonon linewidth

Finally, we summarize in Fig. 4.15 all the calculated contributions to the phonon linewidth and compare them to the experimental findings. The horizontal dashed lines represents the experimental linewidths obtained in Refs. [20, 21]. All the other literature results and the experimental error values are shown as a blue shaded area as in previous figures. The total phonon linewidth obtained in IRAS [20] is represented as a blue dashed line. Here we recall all possible processes that can affect in general the IRAS phonon linewidth [16, 20, 282]:

- *Inelastic processes* responsible for the decay of the vibrational state population. This includes inelastic scattering of the studied phonon mode with *e-h* pairs and other phonons in the system (direct phonon-phonon coupling).

- *Elastic processes* responsible for the vibrational phase decay (i.e., dephasing). In this case the studied phonon modes scatter elastically either with *e-h* pairs or other phonons.

- *Effects of inhomogeneities* (i.e., impurities or disorders), which can be either elastic (e.g., static impurities) or inelastic (e.g., vibrating impurities).

It is shown in Ref. [282] that for the high-frequency mode, like the CO stretch mode, the direct anharmonic processes, i.e., the anharmonic energy relaxation and anharmonic dephasing, are negligible. Therefore, we consider that the blue dashed line in Fig. 4.15 is at least the sum of the energy relaxation rate due to *e-h* pairs, the corresponding dephasing rate, and the rate due inhomogeneities. The result obtained with infrared pump-probe spectroscopy that is analogous to IRAS result is shown as a brown dashed line [21]. As described in the introduction of this chapter, this experimental technique can distinguish the energy relaxation contribution (i.e., inelastic processes) to the linewidth from all other contributions [16]. The phonon linewidth that includes only energy relaxation processes is shown with the red dashed line [21]. The remaining elastic processes contributions are contained in the difference between the brown and red lines.

The first column shows the interband phonon linewidth obtained with Eq. (4.16) using $\Gamma_{\text{inter}} = 60 \pm 40$ meV, and it is clear that this contribution is far below the usual experimental values[17]. The results presented in the second and third columns show how, along with the interband contribution, the higher-order intraband contributions coming from electron-phonon scattering play an important role in explaining the experimental findings. In fact, the latter effect contributes with the same order of magnitude to the phonon linewidth as the interband term. Additionally, impurity effects need to be considered that help improve the agreement. In our theoretical framework, the interband phonon linewidth and the energy-non-conserving intraband contribution coming from electron-phonon scattering correspond to inelastic processes, while the energy-conserving intraband contributions coming from electron-phonon and electron-impurity scatterings correspond to elastic processes (i.e., dephasing and static inhomogeneities, respectively). However, note that we do not separately consider energy-conserving and energy-non-conserving processes within the electron-phonon scattering contribution, but instead we account for them together. Also, in our theory we do not include vibrating impurities [285]. This contribution could be important in the cases of partially disordered molecular layers, where the molecules that deviate from the periodicity of the ordered layer act as excitable impurities. Although Fig. 4.15 shows an overall good agreement with

[17] Note that the lower edge of the blue shaded area in Fig. 4.15 includes the large error bars from the result obtained in Ref. [21].

the experimental results, further work is desirable since we do not know the actual values of the RTA damping parameters (i.e., Γ_{inter}, Γ^A, and Γ_{imp}). Even more, the improvement of semi-local DFT functionals should contribute to the final accuracy of the phonon linewidth.

To get a more precise estimation of the RTA phonon linewidths and the corresponding phenomenological damping energies, one should either calculate the damping energies $\text{Im}\Sigma_\mu(\mathbf{k}, \varepsilon)$ and $\text{Im}\Delta\Sigma_{\mu\mu'}(\mathbf{k}, \mathbf{q}, \omega)$ explicitly as we did for the electron-phonon scattering, or extract these values from experiments, for example ARPES for the former and optical conductivity measurements for the latter [304]. These calculations are rather difficult to be done *ab initio*, and according to our knowledge, this has not been done yet systematically for both intraband and interband phonon self-energies. As for the corresponding experiments, they are not available for our studied system. Thus, we are restricted to using phenomenological parameters in our calculations, where we give the results for a range of meaningful damping energies Γ.

4.3.6 Long-wavelength renormalization of the phonon frequency

Thus far we have been analysing different contributions to the phonon linewidth of the CO stretch mode by looking at the imaginary parts of the corresponding phonon self-energies. We finish the chapter results by analysing the real part of the phonon self-energy, i.e., the renormalization of the CO stretch mode due to the nonadiabatic effects.

If the change from the adiabatic to the nonadiabatic phonon frequency is relatively small, the renormalization of the $\mathbf{q} \approx 0$ phonon frequencies given by Eq. (4.3) can be approximated as

$$\omega^{\text{NA}} \approx \omega_{0\lambda} + \text{Re}\pi^0_\lambda(\omega_{0\lambda}), \tag{4.58}$$

TABLE 4.2: Renormalization of the CO stretch mode frequency on the Cu(100) surface ($\omega_{0\lambda} = 61.37$ THz) due to the nonadiabatic electron-phonon coupling. The number of Cu layers is six and the $\mathbf{k}$ point grid is $(80 \times 80 \times 1)$. The units are THz.

	$\mathbf{q} \approx 0$					
	intraband		interband		total	
	π^0_λ	$\widehat{\pi}^0_\lambda$	π^0_λ	$\widehat{\pi}^0_\lambda$	π^0_λ	$\widehat{\pi}^0_\lambda$
$\text{Re}\pi^0_\lambda$	0.0	0.69	−4.97	−0.019	−4.97	0.671
$\omega_{0\lambda} + \text{Re}\pi^0_\lambda$	61.37	62.06	56.4	61.35	56.4	62.04
$\omega^{\text{exp}}_{0\lambda}$ [16]					62.51	

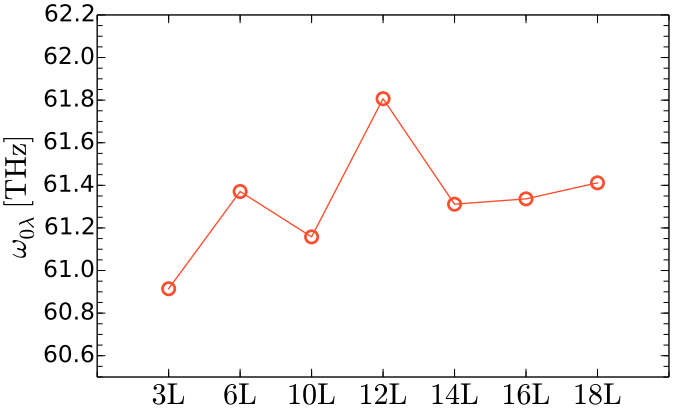

FIGURE 4.16: Long-wavelength adiabatic frequency of the CO stretch mode $\omega_{0\lambda}$ as a function of the number of Cu layers.

where change the exact form of the phonon self-energy by the bare one, and $\omega_{0\lambda}$ is the phonon frequency obtained within the adiabatic DFT calculations (see Secs. 2.4.2 and 2.4.4 for an explanation on how to obtain adiabatic frequency from the DFT calculations and what is the difference between adiabatic and nonadiabatic frequency, respectively). For the CO stretch mode we get $\omega_{0\lambda} \simeq 61.4$ THz as the converged value (see Fig. 4.16), which is already in good agreement with the reported experimental value $\omega_{0\lambda}^{\text{exp}} = 62.51$ THz [16]. This means that nonadiabatic effects should indeed be small, as we demonstrate next.

Table 4.2 shows the results for the real parts of $\widehat{\pi}_{\lambda}^{0}(\omega_{0\lambda})$ [Eqs. (4.13) and (4.15)] calculated with six Cu layers, as well as the corresponding nonadiabatic phonon frequencies ω^{NA}. For completeness, we have also calculated the interband part of $\text{Re}\pi_{\lambda}^{0}(\omega_{0\lambda})$ [Eq. (4.9)], although it cannot be taken as a correction to the DFT adiabatic frequency (see Sec. 4.2.1). Note that it actually would reduce the value of $\omega_{0\lambda}$, and therefore further increase the difference between calculated and experimental frequencies. On the contrary, the phonon self-energy $\widehat{\pi}_{\lambda}^{0}(\omega_{0\lambda})$, which directly gives the difference between the adiabatic and nonadiabatic frequencies [54, 142, 265] (see Sec. 4.2.1), shifts the phonon frequency closer to the experimental one.

The next point we investigate is how sensitive this value is to the number of Cu layers used in the calculation. Figure 4.17 shows the intraband and interband contributions to $\text{Re}\widehat{\pi}_{\lambda}^{0}(\omega_{0\lambda})$ as a function of the number of Cu layers. The interband contribution is in all cases very small, thus it does not affect the phonon frequency. However, the value of the intraband part considered as converged is between 2 and 2.5 THz. With this interval the nonadiabatic frequency overestimates the experimental value by around 1 THz. Although the accuracy could be improved by choosing a finite η as in the inset of Fig. 4.17 (electronic damping effects as in Ref. [265]) or possibly by the long-range screening effects discussed in Sec. 4.2.3, we leave the results as they

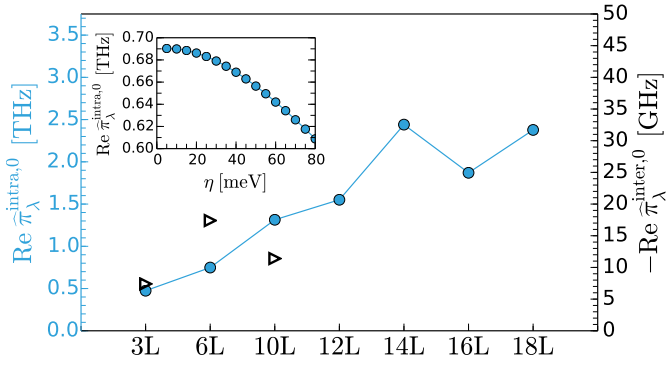

FIGURE 4.17: Real part of the intraband (blue circles) [Eq. (4.13)] and interband (black triangles) [Eq. (4.15)] contributions to the phonon self-energy $\widehat{\pi}_\lambda^0(\omega_{0\lambda})$ of the CO stretch mode as a function of the number of Cu layers. The number of $\mathbf{k}$ points used are $\mathrm{N_k} = 160, 80$ for $\mathrm{N_{layer}} = 3, 6$ and $\mathrm{N_k} = 64$ for the rest. The inset shows the intraband contribution Eq. (4.13) for six Cu layers as a function of η, where the $\eta \to 0^+$ limit corresponds to the results presented in the main panel.

are for at least three reasons: (i) all the above nonadiabatic corrections to the phonon frequencies are relatively small, (ii) the adiabatic phonon frequency $\omega_{0\lambda}$ could depend on the choice of the DFT functional [18], and (iii) there is no way, to our knowledge, to use $\widehat{\pi}_\lambda^0(\omega)$ in a diagrammatic perturbation expansion to obtain the electronic damping effects. One possibility to overcome the issue (iii) would be not to use $\widehat{\pi}_\lambda^0(\omega)$ directly, but to gather all the irreducible diagram terms in a random phase approximation fashion for $\pi_\lambda^0(\omega)$, and then subtract the static part in the clean noninteracting limit from the dynamic one, $\Pi_\lambda(\omega) - \pi_\lambda^0(0)$ (this is in fact explored in Appendix C). For the indirect intraband channel this summation of diagrams would include all possible scattering processes beyond the leading terms presented in Figs. 4.3(a) and 4.3(b), which would lead to a phonon self-energy not just valid for $\omega \gg |\varepsilon_{\mu\mathbf{k}} - \varepsilon_{\mu\mathbf{k}+\mathbf{q}}|$, but for any ω value [276]. This is left as future work.

4.4 Conclusions

In this chapter, we have analyzed the dynamical (nonadiabatic) phonon self-energy in the long-wavelength limit, both for the cases where the electronic scattering processes are disregarded and where they are included, either in a phenomenological way (relaxation-time approximation) or by explicit calculation of the damping energy

[18] The adiabatic frequency for the CO stretch mode on Cu(100) approximated with 6 layers obtained with the PBE functional is $\omega_{0\lambda}^{\mathrm{PBE}} = 61.66$ THz, while with the included non-local vdW-DF(revPBE) [76, 305], vdW-DF(PBE) [80], and rVV10 [306] corrections is $\omega_{0\lambda}^{\mathrm{vdW-DF(revPBE)}} = 60.56$ THz, $\omega_{0\lambda}^{\mathrm{rVV10}} = 60.58$ THz, and $\omega_{0\lambda}^{\mathrm{vdW-DF(PBE)}} = 60.89$ THz, respectively. These results are slightly higher and lower than the revPBE result, $\omega_{0\lambda}^{\mathrm{revPBE}} = 61.37$ THz.

coming from the electron-phonon scattering in the intraband channel. This general formulation was then used to calculate the long-wavelength phonon linewidth and frequency shift due to the electron-phonon coupling for the CO stretch mode on the Cu(100) surface.

The results for the phonon linewidth show that the phonon self-energy in the clean noninteracting limit, corresponding to the first-order Fermi's golden rule formula, is not enough to explain the experimental results of the CO stretch mode obtained from infrared spectroscopy. To get a better agreement it is necessary to account for electronic scattering processes (i.e., electron scattering on phonons, impurities or other electrons). We do so by including a finite electron self-energy into the Green's functions and use them together with the Dyson equation to construct the phonon self-energy. This procedure naturally includes electron damping processes into the phonon self-energy through the difference of electron and hole self-energies, as well as through the single-electron spectral function that enters the momentum distribution functions. Using a phenomenological treatment we show that the interband part of this phonon self-energy is then considerably affected by the mentioned scattering processes, that is, by the corresponding damping energies. For the electron-impurity and electron-phonon scattering processes we have summed the four leading terms in the high-energy expansion of the indirect contribution to the intraband phonon self-energy. The result is an expression for the intraband phonon self-energy analogous to the high-energy form of the intraband Kubo conductivity formula, where the explicit expression for the *e-h* self-energy, which resembles the inverse of the transport relaxation time, is obtained. Since inhomogeneities and contamination with impurities are unavoidable in the experimental set-ups, the indirect phonon self-energy term from electron-impurity scattering is necessary to explain the experimental phonon linewidths.

Along with this impurity and the RTA interband contributions, we also show the importance of accounting for the higher order terms of electron-phonon scattering in the intraband phonon self-energy for explaining the experimental findings. The formulation of this contribution, which is closely related to the *e-h* pair dephasing theory [280], describes the indirect phonon-phonon coupling mediated by electron excitations [12, 42, 50, 279]. Therefore, by using this we are able to detect which other phonon modes contribute to the phonon linewidth of the studied mode through electron excitations (i.e., which phonon modes are responsible for the breakdown of the momentum conservation law). We find that the modes that contribute mainly to the CO stretch mode damping are the frustrated rotation, the frustrated translation, and the modes consisting of the joint motion of substrate atoms and CO.

We have examined, in addition, the reliability of the quasi-static approximation

for the phonon linewidth of the CO stretch mode. Considerably different results with respect to the dynamical phonon linewidth are found, especially for damping energies that are much smaller than the phonon frequency of the CO stretch mode (0.26 eV). Importantly, we show that the interband part of the $\mathbf{q} = 0$ quasi-static phonon self-energy is exactly zero in the limit of zero damping energy. For this reason, the quantity that is calculated using this approach with finite damping values [249] cannot be connected to the adiabatic friction coefficient of atoms/molecules interacting with metal surfaces because it already includes dynamical effects that should be absent of it. Quasi-static expressions are expected to show the same flaws for similar high-frequency modes in other systems when $\mathbf{q} = 0$. Therefore, Allen's formula (both its intraband and interband parts) is not applicable when calculating the phonon linewidth of high-frequency modes obtained in infrared or Raman spectroscopies [267]. Nevertheless, we expect it to be suitable for low-frequency modes and for $\mathbf{q} \neq 0$.

We also find that the temperature dependence of the phonon linewidth that comes from the Fermi-Dirac distribution function is negligible. However, electronic scattering processes, such as electron-phonon scattering, are temperature-dependent, thus the overall temperature dependence of the phonon self-energy is not excluded by this. In fact, we show how the phonon linewidth of the CO stretch mode increases with the temperature due to electron-mediated coupling with the other phonons in the system. This increase is in a qualitative good agreement with the experimental results.

Regarding the renormalization of the CO stretch mode, we show the necessity of subtracting the static (adiabatic) phonon self-energy from the dynamic (nonadiabatic) one. The result so obtained is more reasonable, since adiabaticity is already included into the phonon frequency obtained from DFT-based calculations. In addition, we find that the phonon linewidth is very sensitive to the parameters used. Good convergence is only achieved after a careful consideration of the numbers of $\mathbf{k}$ points and surface layers.

All in all, we would like to emphasize that the presented approach to study nonadiabatic effects is a general one, which can be applied to any well-defined high-frequency optical phonon mode. When the studied mode of vibrating atoms or molecules adsorbed on metal surfaces has a frequency sufficiently larger than other modes in the system, the dominant damping mechanism comes from e-h pairs excitations. For this situation we show that the important electronic transitions are the direct interband and the indirect intraband excitations. Even though the latter dissipation channel comes from the higher order terms than the former, its contribution to the phonon linewidth can be of the same order of magnitude as that of the

former channel. Our studied example of CO on Cu(100) shows that anharmonicity effects can also be described by our theory in this type of systems, though taking into account that the phonon-phonon coupling is then mediated by electron excitations. Finally, this higher-order intraband process is temperature-dependent and could be important for explaining the temperature dependence of the phonon linewidth in other cases [20, 303, 307].

Chapter 5

Nonadiabatic coupling as the underlying mechanism for STM-induced tautomerization of porphycene on Cu(111)

5.1 Introduction

Thus far we have studied dynamical effects of single adsorbates (chapter 3) and ordered molecular monolayers (chapter 4) propagating and vibrating, respectively, on metallic surfaces, and therefore dissipating part of their energy into the surface in the form of low-energy *e-h* excitations and surface phonons. The former process, i.e. nonadiabatic coupling (NAC), plays the leading role in this chapter, where it serves as the driving mechanism for promoting a reaction within an adsorbed molecule. More specifically, hot charge carriers (electrons or holes) flowing in the substrate couple inelastically to molecular vibrational modes, which then enables the reaction. The latter process is considered to be one of the most important mechanisms for manipulating the chemical reactivity of single molecules adsorbed on surfaces [30–32, 218]. Many techniques emerged in order to achieve an efficient control over these inelastic effects. Two such techniques that stand out are STM [28–30, 308, 309] and manipulation with laser light [31, 32, 218]. In the former the use of different current intensities, voltages and tip-substrate heights provides us with the information necessary to construct a model for the reaction dynamics. For example, the reaction rate as a function of current intensity may tell us how many inelastic electrons are needed for the reaction to occur [28]. As for the light techniques, a high resolution of the

laser source prevents interferences from other processes and thus allows for a highly accurate manipulation [31]. Some of the processes experimentally accomplished on single molecular adsorbates in the literature by means of these two techniques are rotational motion of molecules [29], desorption [218, 308], dissociation [28, 31], lateral hopping [294], and single bond-breaking [310] or switching[1] [32, 311–313] within a molecule.

Most theoretical models that describe the aforementioned NAC processes rely on the harmonic approximation for the atomic displacements [48, 49, 314, 315], in a close analogy with some of the models discussed in chapter 4. However, the reactions involving large amplitude motions (e.g. diffusion of adsorbates, conformational changes, bond breaking and formation, etc.) depart strongly from this picture. A few anharmonic theories have been proposed to circumvent this limitation. For example, by introducing coupling terms between specific soft modes in the rates calculations [50, 316–319]. In this model the second-order perturbation theory is used to describe the STM-induced process in which a molecular stretch mode is coupled to a frustrated translational mode and *e*-*h* pairs [50]. In Sec. 4.2.5 we propose an alternative mechanism for this anharmonic effect, namely the indirect phonon-phonon coupling mediated by *e*-*h* pairs. Another example that goes beyond the harmonic approximation is one that uses the fully anharmonic rates along the reaction path via a position-dependent NAC term [51, 154, 155]. Although promising, these methods remain only tractable in a low-dimensional space, where only a few relevant degrees of freedom are included in the model.

Here we focus on a specific class of the aforementioned indirect molecular transformations by inelastic electron currents, namely, on tautomerization reactions, which are defined as an intramolecular transfer of a hydrogen between two sites of an organic molecule [320]. The isomers[2] convertible by this reaction type are known as tautomers. These reactions are particularly attractive, since large changes in conductivity and chemical reactivity are associated with a simple intramolecular hydrogen transfer [47, 320]. In recent years, much effort has been devoted to harness their potential as molecular switches [313, 321–329], for which porphycene on Cu surfaces appears as a promising candidate [43–46]. In particular, the unidirectional *trans*→*cis* tautomerization, depicted schematically in Fig. 5.1, of porphycene on Cu(111) has been experimentally accomplished using laser excitations [330], by application of a chemical force [46], and by injection of tunnelling electrons via STM [43]. In the latter case, the process was observed to take place only above a specific threshold

[1] In the present context the word "switching" refers to a reversible or irreversible change of the molecular structure and potentially its physical properties (e.g., conductivity or electronic absorption spectrum) induced by the two mentioned manipulation techniques.

[2] This term refers to molecules with the same chemical formula, but with a different structure.

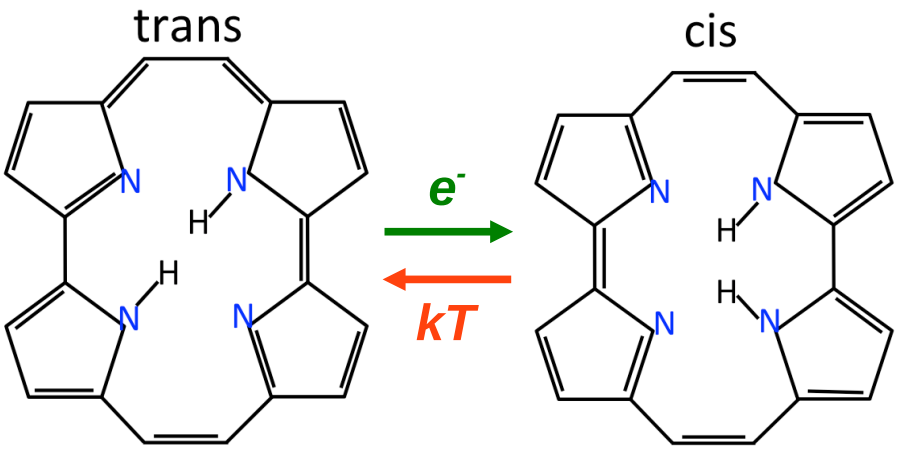

FIGURE 5.1: Chemical formula representation of the *trans*→*cis* porphycene reaction induced by the STM injected inelastic electrons. The backward *cis*→*trans* reaction can be induced only by heating the surface [43].

voltage, about half of the resonant frequency of the N-H stretch mode and in the vibrational band of the skeletal modes. Further, it was found that the backward *cis*→*trans* tautomerization can be induced only by heating the surface (thermal activation), and that the process can take place in molecules up to tens of nanometers away from the STM tip position by hot carriers traveling along the surface. Kumagai and co-workers [43] have accumulated evidence suggesting that the surface state should play a role in the latter phenomenon.

The aim of this chapter is to comprehend the NAC mechanism responsible for the porphycene tautomerization reaction. The positions within the molecular central cavity of the H-saturated and hydrogenated N atoms, which we will refer to as amine and imine N in the following, respectively, define the *trans* and *cis* tautomers. In analogy to the examples mentioned in the beginning of this introduction, it is believed that H-transfer is mediated by NAC between the STM-induced low-energy excited electrons or holes in the metal and the vibrational degrees of freedom associated with the =N-H bonds breaking and formation at the amine and imine groups. However, the direct coupling of tunnelling inelastic electrons and the N-H stretch mode does not trigger the reaction, since the energy threshold is far below the vibrational frequency of the latter mode. This implies that, in addition to a single H-transfer coordinate, many of the porphycene $\sim$ 100 internal vibrational modes have to be involved in the reaction [44, 331]. Therefore, a successful model for describing this process must certainly add other subtle details to the NAC mechanism, such as anharmonicity, intermolecular vibrational energy redistribution, and the importance of tunnelling for the H atom [332, 333]. In this chapter we put forward a microscopic dynamical model that allows to circumvent the need for high-dimensional quantum dynamics

and rationalizes the experimental details of the STM-induced *trans*→*cis* tautomerization reaction in porphycene/Cu(111) in simple physical terms. In order to do so, we make use of a perturbative treatment of the NAC to model the deformation of the potential energy curve (PEC) coming from the intermode coupling between the reaction coordinate mode and all other relevant vibrational modes in the molecule excited by the substrate hot carriers.

As a foundation for the mentioned dynamical mechanism we need a faithful description of the energy landscape associated with the cavity deformation, and in particular with the motion of the H atom. The importance of the latter ingredient is illustrated in the STM-induced manipulation of hydrogen on Pd(111) [334, 335], where the potential energy topography is decisive in the dynamics description. It was shown in that system that a quasi-thermal mechanism promoted by NAC suffices to explain the H-transfer behaviour under a wide range of external parameters (tunneling bias and current intensity) [156]. Therefore, the first task in this chapter is to calculate, by means of DFT, the PEC along a one-dimensional adiabatic reaction path to describe the *trans*↔*cis* tautomerization of isolated porphycene molecules adsorbed on Cu(111). That, in conjunction with the electronic structure analysis for both tautomers in their equilibrium configurations, serves the double purpose of (i) extracting information from the STM images (e.g. tautomer recognition, molecule buckling, and other geometrical parameters) and (ii) addressing the degree of importance of the vdW interactions in the system. The latter is a fundamental aspect of the DFT study of organic and organo-metallic molecule adsorption on metal surfaces that, despite the latest major vdW functional developments [52], still demands benchmarking and refinement. One challenge faced in this theoretical area is functional transferability, in the sense that a functional should be valid to describe a wide range of system classes (e.g. molecular and layered crystals [336–338], or molecule-metal surface interactions [339–342]) or long and short length scales, (e.g. in gas-surface interactions in a dynamical environment [343, 344]), simultaneously.

The chapter is organised as follows. The methodology is given in Sec. 5.2, where the details for obtaining the deformation potential are described. The computational details are given in Sec. 5.3, namely, the parameters for the DFT calculations and details on the vdW functionals. In Sec. 5.4 we discuss the results on the gas-phase and adsorbed porphycene energetics (5.4.1 and 5.4.2) and electronic structure (5.4.3 and 5.4.3.1) in terms of the functionals used. In Sec. 5.4.4 we give final remarks on the chosen vdW functional. In Sec. 5.5 we study the dynamical effects of the STM-induced tautomerization in terms of the deformation potential. The informations on the vibrational properties and NAC along the tautomerization path are analysed in Sec. 5.5.1. In Sec. 5.5.2 we discuss the results on the STM-induced potential

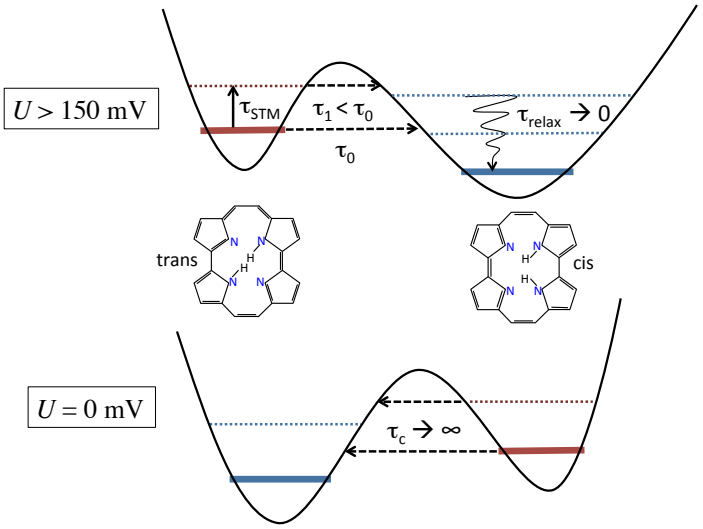

FIGURE 5.2: Schematic representation of the STM-induced tautomerization of porphycene on Cu(111). After switching on the bias voltage, the molecule is found in the *trans* configuration (upper curve, thick red line). The molecule tunnels to the *cis* conformation within a time τ_0 and relaxes almost instantaneously ($\tau_{\text{relax}} \to 0$) to the local ground state (thick blue line). At a bias above the resonance, the *trans* molecule becomes partially excited to a state with shorter tunneling time $\tau_1 < \tau_0$, accelerating the tautomerization dynamics. After switching off the bias voltage (lower curve), the molecule remains trapped in the *cis* conformation, $\tau_c \to \infty$.

deformation and the corresponding vibrational states, and we use them to perform dynamical simulations. Finally, conclusions are presented in Sec. 5.6.

5.2 STM-induced potential deformation model

In order to describe the underlying process of the STM-induced tautomerization of porphycene/Cu(111) system we propose a mechanism in which the STM creates hot electrons in the metal that are propagated as an S-wave through the substrate to reach the adsorbate [345]. This first accounts for the observed non-locality of the STM-driven tautomerization, i.e. the fact that it can be triggered in molecules up to tens of nanometers away from the injection point of the tunnelling electrons. The excitation of internal molecular vibrations indirectly distorts the potential non-uniformly along the reaction path, thereby reversing the thermodynamical stability of the *trans* and *cis* configurations (see the cartoon in Fig. 5.2). The H atom slowly tunnels through the tautomerization barrier (with time $\tau_0 \gg \tau_{\text{relax}}$) and relaxes rapidly ($\tau_{\text{relax}} \to 0$) through *e-h* pair excitation in the substrate to the thermodynamically more stable *cis* configuration. At higher bias votages, the resonant excitation of the tautomerization

mode increases the tunnelling rate ($\tau_1 < \tau_0$) along with the global reaction rate, including all tunnelling and above-threshold channels.

The foundation of our model is to treat the intermode coupling, or intramolecular vibrational energy redistribution, as a deformation of the vibrationally adiabatic PEC along the H-transfer coordinate q, i.e.

$$V(q;U,I) = V_0(q) + \Delta V(q;U,I). \tag{5.1}$$

A large part of the intermode coupling is included in the zeroth-order potential $V_0(q)$ by adiabatic relaxation of the atomic positions along the constrained reaction path [346]. The potential deformation $\Delta V(q;U,I)$, where (U,I) are respectively the STM bias voltage and current intensity, originates from the excitation of all modes orthogonal to the reaction path q (i.e. to the mode associated with the N-H stretch) via NAC to hot electrons in the metal. Note that a field-induced potential distortion could also in principle arise from the proximity of the STM tip [312, 347–350]. In the case of porphycene/Cu(111), this mechanism can be ruled out since tautomerization could be triggered non-locally, as mentioned above [43]. Further, the reaction was found to be insensitive to the sign of the bias voltage, ruling out dipole-field interactions.

In formal terms, the deformation potential is modelled as the following sum of energy contributions:

$$\Delta V(q;U,I) = \sum_{\alpha} \left[\frac{\Gamma^{(\alpha)}_{0\to1}}{\Gamma^{(\alpha)}_{1\to0}} \right] \omega^{(\alpha)}_{01}(q). \tag{5.2}$$

Intramolecular vibrational energy redistribution is a dynamical effect, and it is included in the reduced-dimensional dynamics as a "mean field" potential deformation via the associated vibrational frequencies $\omega^{(\alpha)}_{01}(q)$. These are evaluated in the harmonic approximation at each point along the reaction path, and their variation accounts for intermode coupling to the tautomerization coordinate. The term in brackets describes the probability of excitation of the locally harmonic mode α, as the ratio of upward $\left[\Gamma^{(\alpha)}_{0\to1}\right]$ to downward $\left[\Gamma^{(\alpha)}_{1\to0}\right]$ NAC rates. As demonstrated below, these rates are also a function of the STM parameters (U,I), which determine the importance and energy range of the electronic excitations. The degree of potential deformation thus depends non-linearly on the temperature, the specific STM parameters, and the intermode coupling via the variation of the internal mode frequencies along the tautomerization path.

The rates required in Eq. (5.2) originate from the creation of *e-h* pairs in the metal and they can be computed perturbatively using Fermi's golden rule formula

with anhamronic NAC matrix elements defined by Eq. (2.108). In recent work, it was shown how this anharmonic coupling rates for pairwise transitions $i \to j$ can be modelled using the following expression [51]

$$\Gamma_{i\to j}^{(\alpha)} = \begin{cases} \left[n_b(|\omega_{ij}|) + w_\alpha(U,I) \left(\frac{e|U|-|\omega_{ij}|}{|\omega_{ij}|} \right) \theta(e|U| - |\omega_{ij}|) \right] \gamma_{ij}^{(\alpha)} & \text{if } \varepsilon_j > \varepsilon_i, \\ \left[1 + n_b(|\omega_{ij}|) + w_\alpha(U,I) \left(\frac{e|U|-|\omega_{ij}|}{|\omega_{ij}|} \right) \theta(e|U| - |\omega_{ij}|) \right] \gamma_{ij}^{(\alpha)} & \text{otherwise.} \end{cases} \tag{5.3}$$

These equations are written here in a form also valid in the low-bias limit [319, 351]. The Bose-Einstein distribution $n_b(|\omega_{ij}|)$ ensures that the zero-bias NAC rates obey the detailed balance. The last term in the brackets describes the efficiency of the STM perturbation, where the step function θ ensures that only vibrational states at energies below $e|U|$ can be excited. The STM enhancement factor, $w_\alpha(U,I) = \frac{I\tau_\alpha}{e\rho_0(U)}$, accounts for the current dependence and the residence time τ_α of an electron on a particular mode α [156, 345]. The quantity $\rho_0(U) = |\rho(eU) - \rho(\varepsilon_F)|$ describes the number of one-electron states per atom up to a given bias, which can be estimated, for example, using the PDOS on the Cu atoms obtained from first principles calculations.

The zero-bias NAC rate between vibrational states $|i\rangle$ and $|j\rangle$ for the mode α can be shown to take the following form [51]

$$\gamma_{ij}^{(\alpha)} = \frac{\gamma_\alpha^*}{|\omega_{ij}|} \left| \langle i | n^{1/3} \frac{\partial}{\partial u_\alpha} | j \rangle \right|^2, \tag{5.4}$$

where u_α is the displacement along the mode α. A similar equation can be obtained for the reaction coordinate q. The density $n^{1/3}$ describes the bare surface electron density at the position of the transferred H atom, which is related to the phase shift of one-electron wave functions upon scattering in a jellium via the LDFA (see Secs. 2.3.4 and 3.3). It effectively modulates the strength of the NAC elements along the coordinate u_α. As such, it accounts for part of the anharmonic effects on the relaxation rates, and the numerical resolution of the gradient operator accounts for the remaining contributions. Since the electron-phonon coupling constant γ_α^* is state- and position-independent, it can be determined from first principles by taking the harmonic limit of Eq. (5.4) at the equilibrium geometry, $\Gamma_{1\to 0}^{(\alpha)} = \gamma_\alpha^* \frac{n_{eq}^{2/3} M_\alpha}{2}$. A unique expression is then obtained by relating these fundamental harmonic relaxation rates to the friction tensor $\underline{\underline{\eta}}$ as [37, 51, 154]

$$\Gamma_{1\to 0}^{(\alpha)} = \frac{1}{M_\alpha} \hat{e}_\alpha \cdot \underline{\underline{\eta}} \cdot \hat{e}_\alpha \tag{5.5}$$

The unit vectors and the mass associated with the normal mode α are denoted with $\hat{e}_\alpha$ and M_α, respectively. In the following we make use of the IAA as in Sec. 3.3, in

which the friction tensor is diagonal.

At this point we have all the ingredients for constructing the deformation potential $\Delta V(q; U, I)$: surface electron density n needed for the relaxation rates defined by Eqs. (5.3) and (5.5) and harmonic vibrational properties [i.e., $\hat{e}_\alpha$, M_α and $\omega_{01}^{(\alpha)}(q)$]. To obtain the vibrational states $|i\rangle$ for each of the PECs we diagonalize the corresponding one-dimensional reaction path Hamiltonians (see Appendix E).

5.2.1 Pauli master equation

Finally, the eigenvalues ω_{ij} and the eigenfunctions $|i\rangle$ of the above mentioned reaction path Hamiltonians are used for studying the dynamical behaviour of the system. Since the STM pulses are applied at the millisecond time-scale in Ref. [43] and the relaxation processes in a given potential well are in the picosecond regime (see Sec. 5.5.1 for typical relaxation times), we can safely neglect the coherences between states localized within one well [i.e., pure dephasing effects as described in Secs. 2.5 and 4.1 for the CO molecule on Cu(100)]. In that case, the dynamical behavior of the system is studied using the Pauli master equation

$$\frac{dP_i(t)}{dt} = \sum_j \left(\Gamma_{j\to i}^{(q)} P_j(t) - \Gamma_{i\to j}^{(q)} P_i(t) \right) \tag{5.6}$$

where $P_i(t)$ is the population of state $|i\rangle$ (see Sec. 2.5 for the derivation of this equation). It is important to recognize that only the coherence between localized states can be neglected, and not that of the delocalized states sustained by the reaction path Hamiltonian. The latter states are defined by an effective potential given by Eq. (5.1) between the *trans* and *cis* conformers. As such, the potential is adiabatic in the sense that it supposes that the whole molecule reacts instantaneously to the motion of the H atom [346]. This leads to the significant distortions of molecular structure along the adiabatic reaction path (see Fig. 5.6) and it gives the largest estimate of the tunnelling probability through the barrier, i.e. the eigenfunctions $|i\rangle$ are too delocalized, as we will see in Sec. 5.5.2. To account for the molecular frame reorganization during the reaction, the vibrational eigenfunctions used to calculate the NAC rates contained in Eq. (5.6) are localized prior to the dynamics using a formalism similar to the one used in other STM simulations [352]. More details can be found in Appendix E.

5.3 Computational details

In the present DFT calculations we use the periodic supercell approach to represent an infinite Cu(111) surface. The calculations are carried out with the VASP code [104]. In the analysis of the porphycene-Cu vdW interaction, the performance of various exchange and correlation functionals presented in Sec. 2.2.3 is examined. We have used a few representatives of the non-local DF [76, 82, 353] and *opt* [81, 82] families of DFT-vdW functionals, which are self-consistently [305] implemented in VASP by means of an efficient algorithm to compute the dispersion corrections [82, 354]. The functionals of the *opt* family are based on the DF non-local correlation. They are made more attractive by parametrization of the exchange functionals [81, 82] to obtain smaller deviations from the benchmark dimer data set S22 [85]. As will be shown below, the attractive or repulsive character of the exchange functional employed is key to explain the relative stabilities and barrier heights of the porphycene-copper system. The literature describes how the use of alternative exchanges to those featured in the original vdW functional formulations improves the binding properties of several system classes [80, 83, 84]. Therefore, we studied the role of exchange in the molecule-surface binding using vdW-DF with PBE in the semilocal exchange and correlation (*outer*) term [80] and vdW-DF-cx, which uses the same exchange in the *outer* term and in the calculation of the non-local (*inner*) term [78, 83]. We have also applied other methodologies, namely Grimme's semiempirical dispersion corrections to the energy at the D3 level [88] and the density-based model of Tkatchenko-Sheffler (TkS) in its original form [87], as well as in the reparametrized version vdW$^{\text{surf}}$ [89] which accounts for the many-body screening of the substrate electrons, and the many-body dispersion approach MBD [90, 355]. Note that in the latter a screened polarizability in the metal substrate atoms needs to be considered [93].

Finite slabs with four Cu layers and a (6×6) lateral periodicity suffice for the lateral vdW interactions between molecules to be negligible. We keep the Cu lattice constant fixed to its experimental value, $a_0 = 3.61\,\text{Å}$, and we also fix the two bottom Cu layers, while allowing for relaxation of all other atomic coordinates. The vacuum space between slabs is equivalent to $7d_0$, where d_0 is the bare surface interlayer spacing. Note that vdW-DF2 largely overestimates lattice constants [82]. In fact, here we observe an overestimation of about 4% in the interlayer distance at the topmost layer. In this particular case, only the molecular degrees of freedom are optimized to avoid unphysical expansion of the surface. Ion cores are treated in the calculations through PAW potentials [237]. The energy cutoff for the basis set is 400 eV and the MP mesh for the 1BZ k-point sampling [103] is $3 \times 3 \times 1$. To extract properties of the gas-phase molecule, a larger hexagonal supercell of $14 \times 14 \times 10$ Å^3 and a $1 \times 1 \times 1$ k-point mesh were used. The convergence criteria for the total

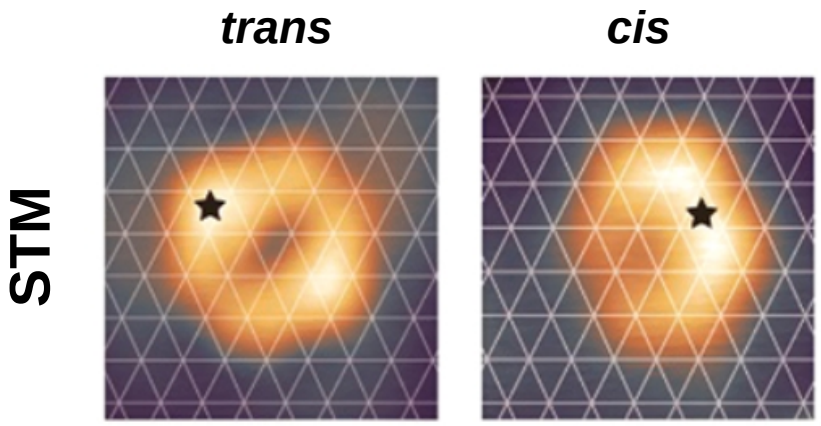

FIGURE 5.3: Experimental STM images for the *trans* and *cis*-porphycene isomers at 5 K. The current intensity is 100 pA and the bias voltage is −100 mV. The white grid shows the surface lattice of Cu(111) with the nearest-neighbour distance of 2.55 Å. This figure is reproduced from Ref. [43].

energies in the self-consistent loop is 10^{-5} eV. In the geometry optimizations, the atomic coordinates are considered converged when energy differences are $< 10^{-5}$ eV and forces $< 0.02\,\mathrm{eV\AA^{-1}}$.

We use constrained minimization to obtain the zeroth-order adiabatic potential $V_0(q)$. The corresponding reaction coordinate q is determined by following the potential energy landscape along the N-H distance of the hopping H atom. At each point along the calculated path this distance is kept fixed (i.e. it is a nonlinear constraint) and the remaining molecular degrees of freedom are allowed to relax and follow the H migration adiabatically. All the structures along the reaction path were optimised with the ASE package [356] using the FIRE algorithm [357]. To obtain initial guesses for the intermediate structures, the cartesian coordinates of the *trans* and *cis* equilibrium configurations are linearly interpolated. The harmonic relaxation rates $\Gamma^{(\alpha)}_{1\to0}$ and the quantities associated to the normal mode α [i.e., $\hat{e}_\alpha$, M_α and $\omega^{(\alpha)}_{01}(q)$] are evaluated along the 8 points of this linearly interpolated reaction path using the vdW-DF(PBE) functional. The latter quantities along with the adiabatic potential $V_0(q)$ are used to construct the total PEC defined by Eq. (5.1), which is then fitted using the two Morse potentials with the wells centred at the *trans* and *cis* coordinates for each potential bias U. For further details of this procedure see Appendix E.

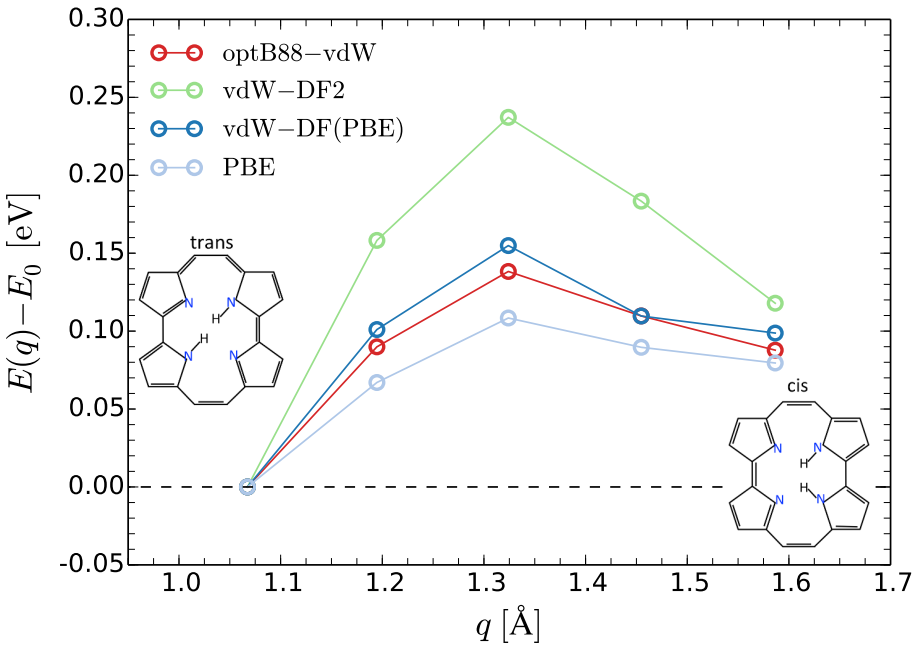

FIGURE 5.4: One-dimensional energy barrier of the *trans*→*cis*-porphycene (shown in the insets) process in the gas phase for various functionals, referred to the potential energy E_0 of the *trans* tautomer, as a function of the N-H stretched bond length q.

5.4 Porphycene-copper interaction along the tautomerization path

The accuracy of the PEC relies in a correct description of the vdW interactions and in order to choose appropriate vdW functional, it should, at least qualitatively, capture the following experimental results [43]: (i) *trans* is the thermodynamically stable isomer on Cu(111), (ii) the value of the *cis*→*trans* reaction energy barrier height (a small value of 42.3 meV), and (iii) STM images of both isomers (see Fig. 5.3). Having these requirements in mind, we analyse the energetics (adsorption energies, energy barrier, etc.) and electronic structure (porphycene-copper charge transfer, STM images, etc.) obtained by means of different DFT functionals in the following.

5.4.1 *trans* → *cis* energy barrier of porphycene in the gas phase

Table 5.1 shows the potential energy difference E_{c-t} between the *cis* and *trans* configurations in the gas phase (a positive E_{c-t} indicates that *trans* is more stable than *cis*) and the energy at the *trans*→*cis* transition state (TS) for various functionals, compared with B3LYP [358, 359] and MP2 [360, 361] literature values [362, 363]. Fig. 5.4

TABLE 5.1: Relative energies of gas-phase *trans* and *cis* porphycence and *trans*→*cis* barrier heights (E_{TS}) from VASP calculations (in eV) for various functionals. Literature values calculated with TZ2P and 6-31G(d,p) gaussian basis sets at the B3LYP and MP2 levels are shown, too.

	E_{c-t}	E_{TS}
optB86b-vdW [45]	0.077	
optB88-vdW	0.088	0.138
vdW-DF2	0.118	0.237
PBE	0.080	0.108
vdW-DF(PBE)	0.099	0.155
B3LYP (TZ2P [362])	0.1036	0.2125
B3LYP (6-31G(d,p) [363])	0.09974	0.2029
MP2 [363]	0.1149	0.1626

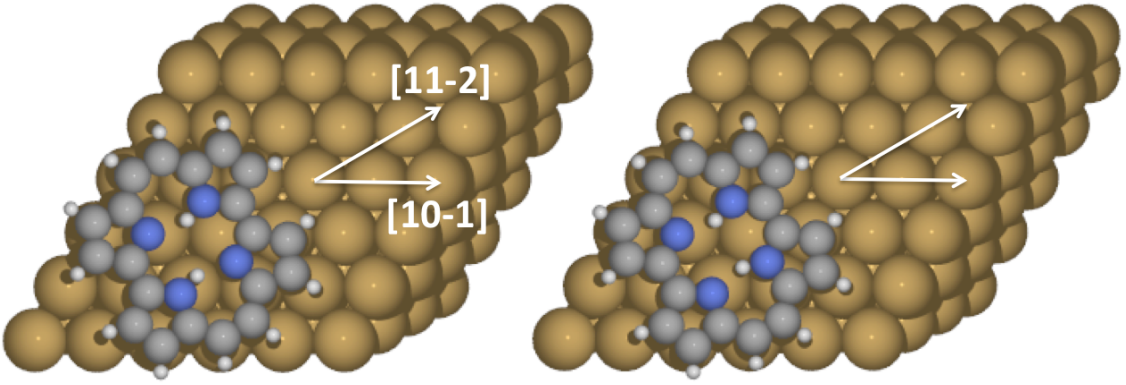

FIGURE 5.5: Models of *trans* and *cis*-porphycene adsorption on Cu(111).

shows the one-dimensional potential energy barrier calculated with constrained minimization. The vdW-DF2 functional results in much larger E_{c-t} and barrier values than the other studied functionals, which lie closer to the MP2 data that we consider a reliable reference. The best agreement is found for vdW-DF with PBE exchange. We recall that the original vdW-DF is constructed with revPBE exchange. Note that the results labelled as PBE are obtained with PBE semilocal correlation, while the vdW-DF(PBE) ones are obtained with the LDA plus non-local correlation. Therefore, the differences in the energies obtained from these two levels of approximation might be attributed to the two intramolecular hydrogen bonds N-H$\cdots$N, as main supplementary sources of dispersion interactions. This seems to be a minor effect, though, as differences of only ~ 20 meV are found (see Fig. 5.4).

5.4.2 Energetics of the adsorbed configurations

We calculate next the energy minima corresponding to the adsorbed *trans* and *cis* configurations. Since the STM experiments (see Fig. 5.3) show that the molecules lie oriented along the $[11\bar{2}]$ surface crystallographic direction or their symmetry equivalents (in total they can adopt six equivalent orientations and both chiralities of the isomers), in the present work we consider the configurations shown in Fig. 5.5, which guarantee that both unsaturated N atoms of the *cis* isomer are in registry with neighbouring Cu atoms. This configuration is supported by the fact that experiments show a rigid shift of the molecule of $\sim 1.4\,\text{Å}$ along $[\bar{1}10]$ (symmetry equivalent to $[10\bar{1}]$) during the *cis*↔*cis* tautomerization [43]. Although no evident conformation that pairs up unsaturated N and Cu atoms of the Cu(111) substrate exists for the *trans* isomer, no significant shift or rotation of the molecule is observed upon *trans*→*cis* transformation. This supports the structures shown in Fig. 5.5 where the molecule lies at a hollow site as being the most stable ones, which is confirmed by most density functionals. Experimentally, it is difficult to distinguish *fcc* from *hcp* hollows or to determine the adsorption height of the molecules.

Table 5.2 summarizes the E_{c-t} energies and adsorption heights, given as the average height $\tilde{z}$ of the four pyrrole centres, obtained with several functionals for the Fig. 5.5 geometries. According to the experiment, all the molecules adsorb only in the *trans* conformation. The thermodynamical stability of the *trans* molecules proves univocally that values $E_{c-t} > 0$ should be obtained. Theoretically, we observe that

TABLE 5.2: For various DFT functionals, adsorption energy difference between *cis* and *trans* configurations on Cu(111), and molecule heights measured as the average height $\tilde{z}$ of the centres of mass of the four pyrroles in each molecule.

Functional	E_{c-t} (eV)	$\tilde{z}_{trans}$ (Å)	$\tilde{z}_{cis}$ (Å)
optB86b-vdW	-0.130	2.50	2.65
optB88-vdW	-0.167	2.69	2.72
DFT-D3(PBE)	-0.115	2.59	2.54
DFT-D3(revPBE)	-0.034	2.63	2.57
DFT-D3(RPBE)	-0.011	2.61	2.60
TkS	-0.159	2.59	2.62
vdW^{surf}	-0.081	2.52	2.53
MBD	-0.093	2.49	2.55
vdW-DF(PBE)	0.085	3.29	2.96
vdW-DF-cx	0.049	3.29	2.87
vdW-DF2	0.106	3.55	3.54
vdW-DF2(PBE)	0.094	3.42	3.43

optB86b-vdW, optB88-vdW, and TkS (with PBE exchange) fail to reproduce this qualitative trend, yielding a *cis* configuration that is $\sim 0.15\,\text{eV}$ more stable than the *trans* one. The many-body corrections to the latter functional vdW$^{\text{surf}}$ and MBD do not modify this conclusion, although they significantly reduce the energy difference between both configurations. The Grimme vdW-D3 functional also predicts the wrong ordering and about the same stability when PBE exchange is used. However, the *cis* stability is largely reduced for other exchange choices: revPBE and RPBE result in nearly equally stable *trans* and *cis*, with absolute values of E_{c-t} 0.034 and 0.011 eV, respectively. We observe two typical adsorption heights for both tautomers across the table: $\tilde{z} \simeq 2.5\,\text{Å}$ for the functionals that yield energies $E_{c-t} \simeq -0.15\,\text{eV}$ or $E_{c-t} \simeq 0$, in disagreement with the experimental observations, and $\tilde{z} \simeq 3.5\,\text{Å}$ for the ones resulting in values $E_{c-t} \simeq 0.1\,\text{eV}$. The vdW-DF(PBE) and vdW-DF2 functionals provide similar $E_{c-t} \simeq 0.1\,\text{eV}$, consistent with the experimental result regardless of the choice of exchange functional. The behaviour of vdW-DF-cx is similar to vdW-DF(PBE), with a slightly more strongly bound *cis*. They differ significantly, though, in the height and shape of the tautomerization barrier, as shown in Fig. 5.6 top panel, as well as in the distance $\tilde{z}$ of *cis*-porphycene to the surface. The original vdW-DF2 functional, which uses rPW86 exchange, overestimates the experimental *cis*→*trans* barrier of $42.3 \pm 2.7\,\text{meV}$, while vdW-DF(PBE) is in good agreement with the experiment (the functional vdW-DF-cx also overestimates the barrier, mainly because the *cis* conformation is more stable). In this figure and in the analysis hereafter we mostly focus on the three functionals that are representative of the different DFT-vdW functionals and molecule-substrate interaction strength scenarios: the strongly attractive optB88-vdW, the weakly attractive vdW-DF2, and the vdW-DF(PBE) as an intermediate case. The medium strength of the latter functional is also revealed in the adsorption heights $\tilde{z}_{trans} = 3.29$ and $\tilde{z}_{cis} = 2.96\,\text{Å}$, which are intermediate between the two typical heights mentioned above (see Table 5.2). The binding strength provided by each of these functionals is reflected in the variation of the molecular structure as the H is being transferred from one N atom to the other. This is shown in the bottom panels of Fig. 5.6, where the adsorption heights and molecule bucklings are given as averages of the heights of the four N atoms (z) and of the pyrrole centres ($\tilde{z}$) above Cu(111). These two ways of accounting for the geometrical details provide very similar information, with differences of less than 0.1 Å. These could be attributed to the distortion of the polyaromatic ring along the reaction path, which is barely observable. The overbinding character of optB88-vdW is reflected in the small adsorption heights and larger buckling of the molecule. The opposite behaviour is obtained for the weakly binding vdW-DF2. In the intermediate vdW-DF(PBE) case we observe a progressive decrease in height and an increase in buckling along the reaction path.

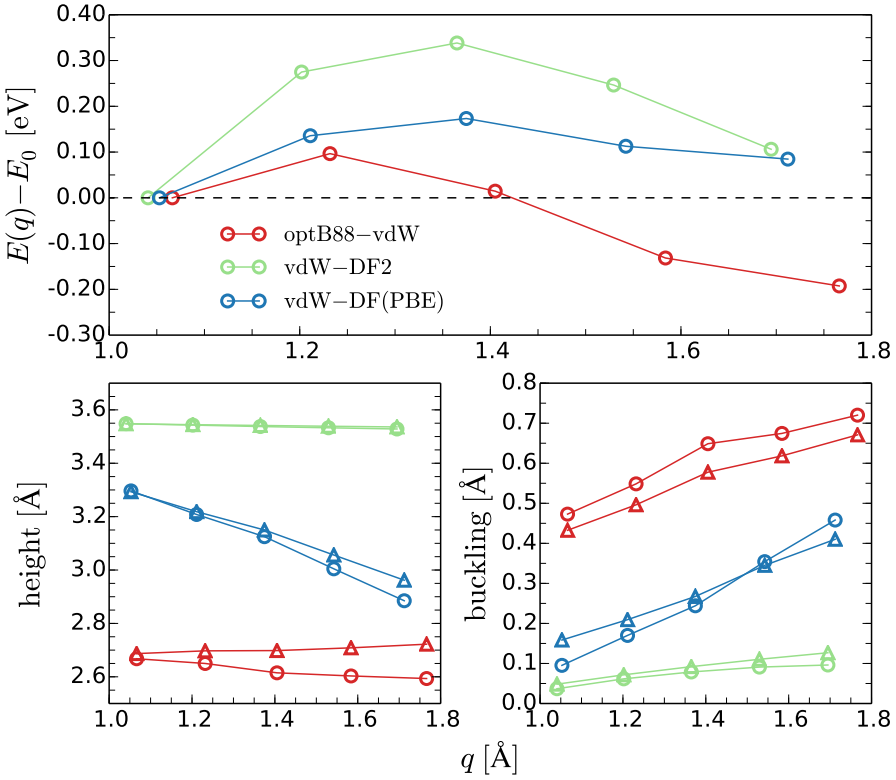

FIGURE 5.6: Top panel: *trans*→*cis* one-dimensional barriers for porphycene adsorbed on Cu(111) for several functionals, referred to the potential energy E_0 of the *trans* tautomer, as a function of the N-H stretched bond length q. Bottom left and right panels: change in the average heights above the topmost Cu layer and bucklings, respectively, of the molecules during H-transfer. Circles and triangles show the quantities as average values of the four N atoms or the four pyrrole centres, respectively.

The molecule adsorption energies E_{ads} with respect to the gas-phase and the attraction range exerted by five of the studied functionals are depicted in the molecule-surface potential energy as a function of the molecule height, $V(z)$, in Fig. 5.7. The curves are calculated by shifting the rigid molecule upward and downward from the potential energy minima configurations, i.e. the atomic positions are not relaxed. No barrier for the molecule approach from the gas phase is observed, at least with these constraints. The energy zero in each curve is taken at the potential energy of the molecule lying far from the clean surface in its relaxed configuration, i.e. the energy value at the minimum is E_{ads}. Because of the constraints adopted here, some of the potential curves at high z values tend to ~ 0.7 eV due to the strong buckling caused by adsorption near the surface. We observe E_{ads} differences of the order of 1 eV depending on the functional and wider adsorption wells for the least binding ones.

The original vdW-DF2 formulation, with rPW86 exchange contribution [69, 364], correctly predicts the thermodynamical stability of the *trans* isomer upon adsorption

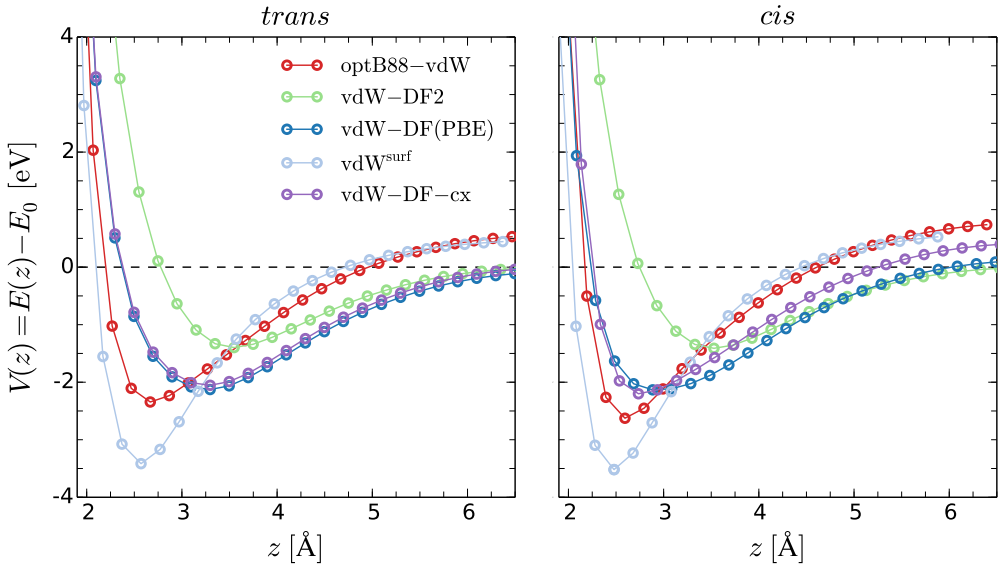

FIGURE 5.7: One-dimensional adsorption potential for porphycene approaching the Cu(111) surface. The minimum corresponds to the *cis* and *trans* minima shown in Fig. 5.6. The z values represent the molecule height (measured as the average height of the N atoms) for equispaced rigid shifts of the unrelaxed molecule. The energy zero each potential curve indicates the adsorption energy E_0 with respect to the relaxed gas-phase molecular geometry.

on Cu(111) (as it will be discussed below, despite correctly predicting the sign of E_{c-t}, vdW-DF2 does not correctly describe the porphycene/Cu(111) interaction), unlike optB86b-vdW and optB88-vdW, which yield a much more stable *cis* configuration by nearly 0.15 eV. The latter two functionals use optimised exchange contributions, formulated as the gradient-modified Becke86 [365] and Becke88 [68], respectively, but with a reparameterisation of the exchange enhancement factor $F_x(s)$ (where $s \propto |\nabla n| n^{-4/3}$ is the reduced density gradient and n the point electron density) optimised to better match the S22 benchmark dataset [85]. PBE and revPBE also use an alternative parametrization of the Becke expression for the exchange enhancement factor [366]. Figures 2 of Ref. [364], 2 of Ref. [82], 3a of Ref. [74], and 11 of Ref. [78] nicely summarize the $F_x(s)$ values of a number of exchange functionals in the literature. The rationale behind those formulations is that $F_x(s)$ must increase steeply enough with s to avoid the overbinding brought by the LDA, in some cases while attempting also to satisfy the Lieb-Oxford bound [72] at large s. This typically causes a stronger binding behaviour for PBE than for revPBE, since the latter takes larger $F_x(s)$ values. In order to improve in the S22 benchmarkings, RPBE, rPW86, optB86b, and optB88 are generally made to adopt intermediate values between revPBE and PBE with the following exceptions: (i) optB86b and optB88 are smaller than PBE at around $s < 3$ and increase above revPBE rapidly at around $s > 4.5$, (ii) rPW86 is higher than revPBE at low $s < 1.8$, and (iii) RPBE and revPBE take very similar values at $s < 2.5$. The overall quality of the physical

description is highly dependent on the different s-values spanned by the electron density in each particular system. In fact, Fig. 5.7 shows that both tautomers are most strongly bound by optB88-vdW and least by vdW-DF2 with rPW86, while vdW-DF(PBE) shows an intermediate strength, which is reflected both in the energy and the adsorption heights. This suggests that the porphycene-Cu(111) interaction is mainly influenced by low-s regions. This is further supported by the result of vdW-DF-cx. This functional has a $F_x(s)$ similar to rPW86 at large s values. Note that it is not directly comparable to the other studied methods of the DF family because the same exchange enters also in the nonlocal correlation term. As for the *trans* vs. *cis* difference, it is not straightforward to anticipate the effect of each functional on the relative binding energy E_{c-t} and height. The results of Table 5.2 for optB88-vdW and optB86b-vdW ($E_{c-t} \simeq -0.15\,\text{eV}$, in disagreement with the experiment) show that the *cis* tautomer is more overbound than the *trans* one. This makes sense if we assume that the general effect produced by these functionals is to create a strong bond at each molecule-surface anchoring points, since *cis* has two of these imine N-Cu bonds and *trans* just one (see Fig. 5.9 below). In contrast, the two vdW-DF2 results with rPW86 and PBE exchanges [and also vdW-DF(PBE)], favour the *trans* tautomer by $E_{c-t} \simeq 0.1\,\text{eV}$ and adsorb the molecules $\sim 1\,\text{Å}$ farther from the surface.

The trend predicted by the low-s enhancement factors is also observed with the semiempirical vdW-D3 functional, where PBE yields an overbound *cis* (same for TkS with PBE). This is in contrast with RPBE and revPBE, which yield similarly small E_{c-t} values, well within the uncertainty of DFT. Note that the use of PBE exchange in the vdW-DFT functionals does not result in overbinding. This proves that, despite the exchange being a relevant factor in the adsorption strength, the correlation formulation is by no means less relevant to describe the dispersion interactions accurately. From these results we infer that the above described exchange effects affect mostly the binding through the imine N atoms (i.e. the region of the interface below the molecule), while the outer polyaromatic ring of the molecule weakly binds to the surface. The latter is dominated by attractive dispersion forces, which tend to bind the molecule at higher z values. These forces may counteract an eventually overestimated imine N-Cu bond strength, causing an overall upward shift of the molecule, as we discuss in the next subsection.

5.4.3 Electronic structure of adsorbed porphycene

Fig. 5.8 shows the sum of PDOSs on the atomic orbitals of N, C, and H, which provide a simple tool to univocally identify the binding energies of the highest occupied and lowest unoccupied molecular orbitals (HOMO and LUMO, respectively) in particular

for weak hybridization with the surface. This is clearly the case for vdW-DF2 and for *trans*-porphycene with vdW-DF(PBE), where the HOMO and LUMO peaks are localized. In the other cases peaks are less clear as a consequence of significant hybridization between the molecular orbitals and the Cu(111) substrate. To confirm this interpretation, we have also inspected the KS states located at the relevant peaks or energy ranges in the PDOS curves and compared them with the KS states calculated in the gas-phase that correspond to the HOMO and LUMO (see the charge density associated to the gas-phase molecular orbitals in Fig. 5.10). For the optB88-vdW and vdW-DF(PBE) functionals the *cis*-porphycene hybridization with the Cu substrate is strong enough to shift the LUMO downward in energy around the Fermi level. Only for the most attractive functional does the *trans* LUMO hybridize close to the Fermi level. The HOMO lies well below, at about -1 eV.

The HOMO-LUMO gap of both isomers in the gas phase takes an approximate value of 1.6 eV for the investigated functionals (the experimental gas-phase value is 2.2 eV [367]). Fig. 5.8 shows that the gap is not significantly altered upon adsorption, but marginal changes due to screening effects might be present. Although we cannot expect accurate gap values at this level of theory, we can infer charge transfer differences because of the functional-dependent gap alignment with respect to the Fermi level. The use of hybrid functionals, which include exact exchange, in combination with a nonlocal correlation correction could reduce self-interaction errors and thus improve the quantitative description of the HOMO and LUMO binding energies, as well as of the charge transfer [92]. These calculations currently come at a prohibitive computational cost for a system like the present one.

The charge density alterations at the interface are studied in further detail with a so-called charge density difference (CDD) map, i.e. the difference between the actual electron density in the adsorbed configuration and the sum of the bare surface and the isolated molecule densities, both calculated with the atomic positions frozen

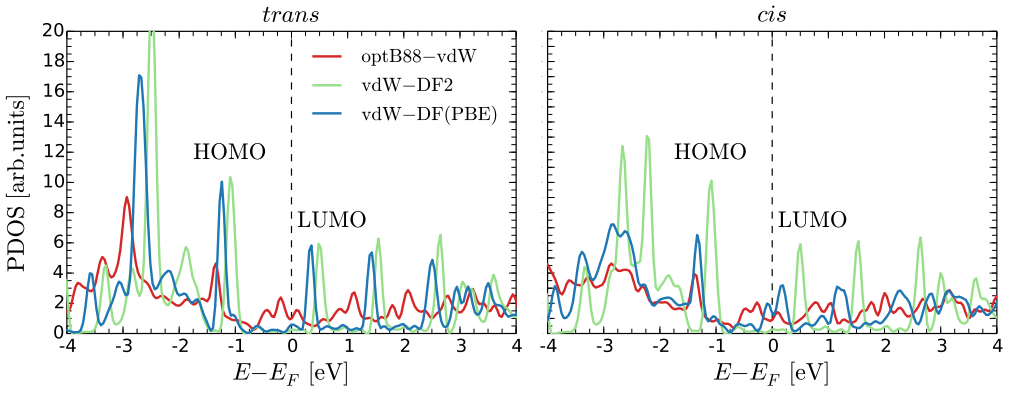

FIGURE 5.8: PDOS of *cis* and *trans*-porphycene near the Fermi level for various functionals.

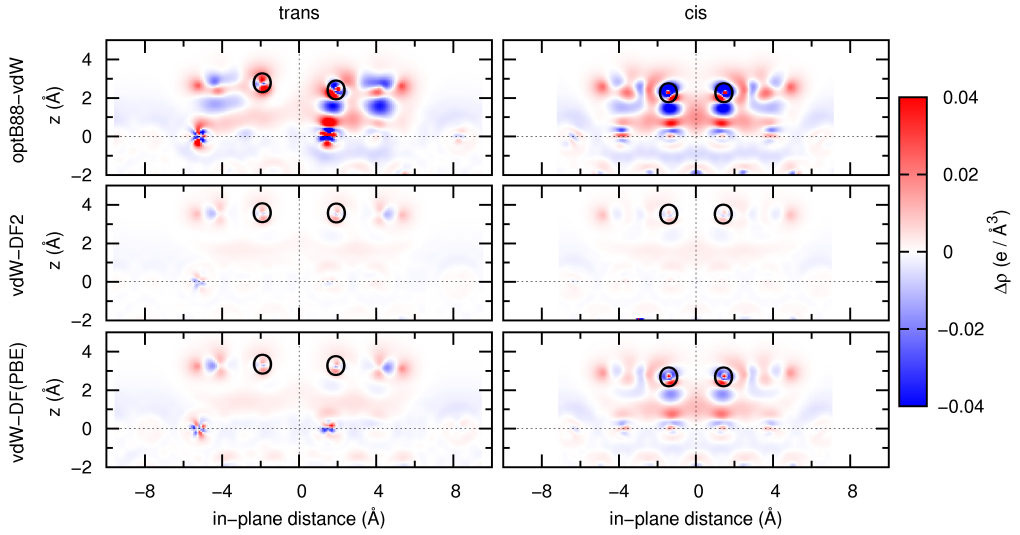

FIGURE 5.9: Charge density difference maps of adsorbed *trans* and *cis*-porphycene for various functionals. The map is drawn at a plane perpendicular to the surface containing the two empty N atoms. Positive (negative) values indicate regions of electron accumulation (depletion) upon adsorption. The horizontal dashed line shows the average z value of the topmost Cu layer and the black circles show the N atom positions.

at the adsorbed configuration geometry. Fig. 5.9 shows two-dimensional cuts of the CDD perpendicular to the surface through the imine N atoms. There it can be distinguished how bonds are formed between these N atoms and some substrate Cu atom, with a quite clear directionality in some of the cases. This happens mainly for optB88-vdW and both imine N atoms of *cis* and also one N in *trans* porphycene, but also for vdW-DF(PBE) and the *cis* isomer. In the other cases the much weaker bonding is manifested as a delocalized and very subtle electron accumulation at the interface. Regarding the relationship between charge transfer and geometry, note that those directional bonds make the half portion of the *cis* molecule containing the imine N atoms lie closer to the surface, while the other half of the molecule lies slightly higher by the influence of vdW forces, which tend to stabilise the molecule farther from the substrate.

In addition, we have determined the charge transfers from a Bader-like atoms-in-molecules charge partitioning analysis [368]. Table 5.3 shows the charge depletion or accumulation ΔQ at the adsorbed molecule with respect to the gas phase. Bear in mind that a Bader analysis of our calculated gas-phase porphycene electron densities underestimates the nominal total charge in the molecule by 0.13 electrons. Thus we can consider this value as an error bar for the ΔQ values of Table 5.3. As expected, vdW-DF2 yields negligible and optB88-vdW yields the largest charge transfers. In the latter case, about 0.6 electrons are donated by the surface to both isomers. The third functional yields a significant donation to the *cis* but not to the *trans* porphycene.

TABLE 5.3: Charges ΔQ in $|e|$ units of adsorbed molecules relative to their gas-phase nominal values calculated from a Bader partitioning scheme of the charge inside the calculation supercell. A negative (positive) sign corresponds to electron transfer from (to) the Cu surface to (from) the molecule.

Functional	*trans*	*cis*
optB88-vdW	-0.550	-0.576
vdW-DF2	0.039	0.037
vdW-DF(PBE)	0.054	-0.243

All these features of the Bader analysis are consistent with the results of the PDOS presented in Fig. 5.8.

Here we note that the porphycene-Cu binding energies do not correlate with the degree of charge transfer. In fact, optB88-vdW stabilizes *cis* more than *trans* on Cu(111), but yields similar $\Delta Q \simeq -0.55|e|$ in both cases. For the medium-binding vdW-DF(PBE), we find negligible ΔQ for *trans* and $\Delta Q \simeq -0.25|e|$ for *cis*, consistent with the LUMO hybridization features observed in the PDOS of Fig. 5.8. Similarly, there is a clear correlation between large ΔQ values and low adsorption heights, but not between large ΔQ and $E_{c-t} > 0$ values. The CDD maps of Fig. 5.9 show that the strongly directional Cu-imine-N bonds are the main contributors to the reported ΔQ values. There, we also observe that in the optB88-vdW case the interaction with Cu causes a significant charge rearrangement within the molecule, not only in the interface region. This extra localized charge redistribution, probably conditioned by the underestimation of the molecule adsorption height, has an important effect on the interaction energetics. It thus appears as one of the main factors responsible for the wrong energetic ordering [*cis* more stable upon adsorption on Cu(111)] using this functional.

5.4.3.1 Interpretation of the STM images

It is clear from Fig. 5.8 that a STM image taken at positive voltages below $\sim 1\,\mathrm{V}$ or even small negative voltages, will map the molecular LUMO. Fig. 5.11 shows the calculated partial charge density (PCD) 2 Å above the adsorbed molecules at the experimental bias voltage $-0.1\,\mathrm{V}$ [43], which can be interpreted as a coarse approximation to simulating the STM images. For a given potential bias V, the PCD is constructed by integration of the electron densities of the KS states lying between the Fermi level energy E_F and $E_F + eV$.

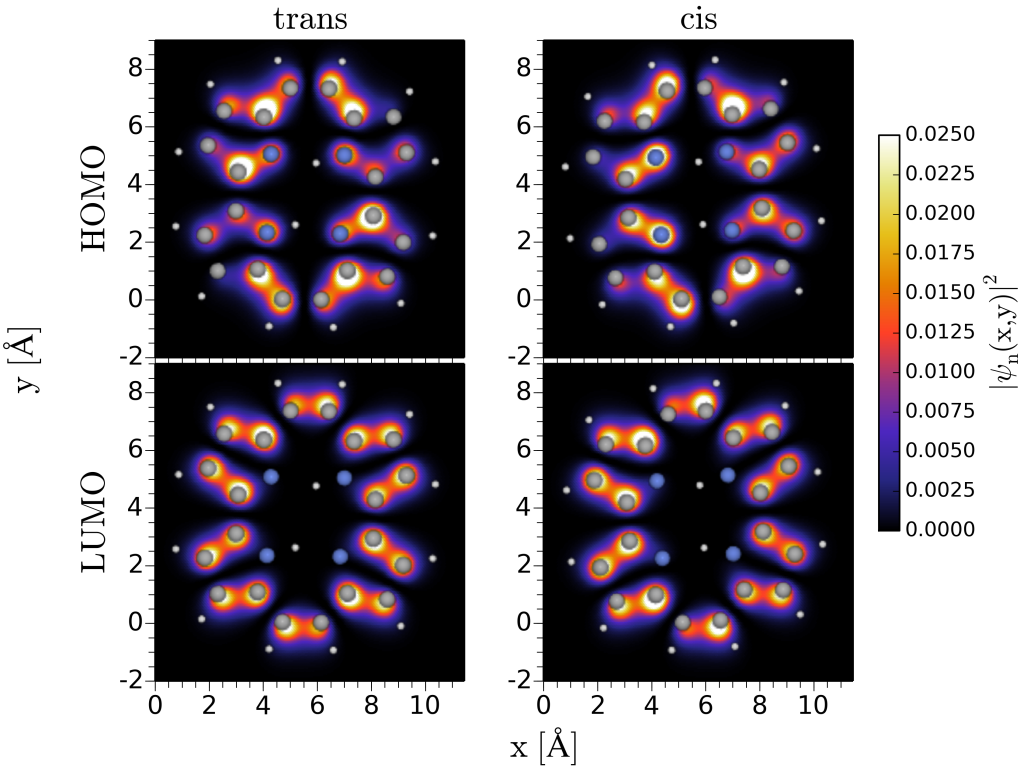

FIGURE 5.10: Electron density associated to the HOMO and LUMO of *trans* and *cis*-porphycene. H, C, and N atoms are shown as white, gray, and blue balls, respectively.

As depicted in Fig. 5.3, the *trans* and *cis* STM experimental images possess distinctive patterns, which enable tautomer recognition. The double-lobed asymmetric elongated image is attributed to *trans*, while the crescent-shaped one to *cis*. This assignment can be made just by consideration of the absence or presence of mirror symmetry (i.e. chiral or achiral character), respectively, of the gas-phase molecules. However, the knowledge of the gas-phase electronic structure alone does not grant the distinction. It is to be expected that either the HOMO or LUMO of the molecule is being imaged in the STM experiment, with some degree of blurriness associated with orbital hybridization at the surface. In Fig. 5.10, both molecular orbitals are found to look very similar for both gas-phase tautomers, since their electronic density is localised at the polyaromatic ring. In the molecular cavity region, where the main difference (the positions of the imine and amine N atoms) between *trans* and *cis* resides, the changes are marginal. Therefore, we conclude that the distinctive features of the STM images must have their origin in the interaction of the HOMO and LUMO with the substrate. This finding already suggests that the very weakly binding vdW-DF2 might not be a suitable functional for modelling porphycene on Cu(111) either, since the molecule retains its gas phase structure and is adsorbed far from the surface ($\sim 3.5\,\text{Å}$) for both the *cis* and *trans* structures. Another important conclusion is that the STM image modulations account for the buckling of the

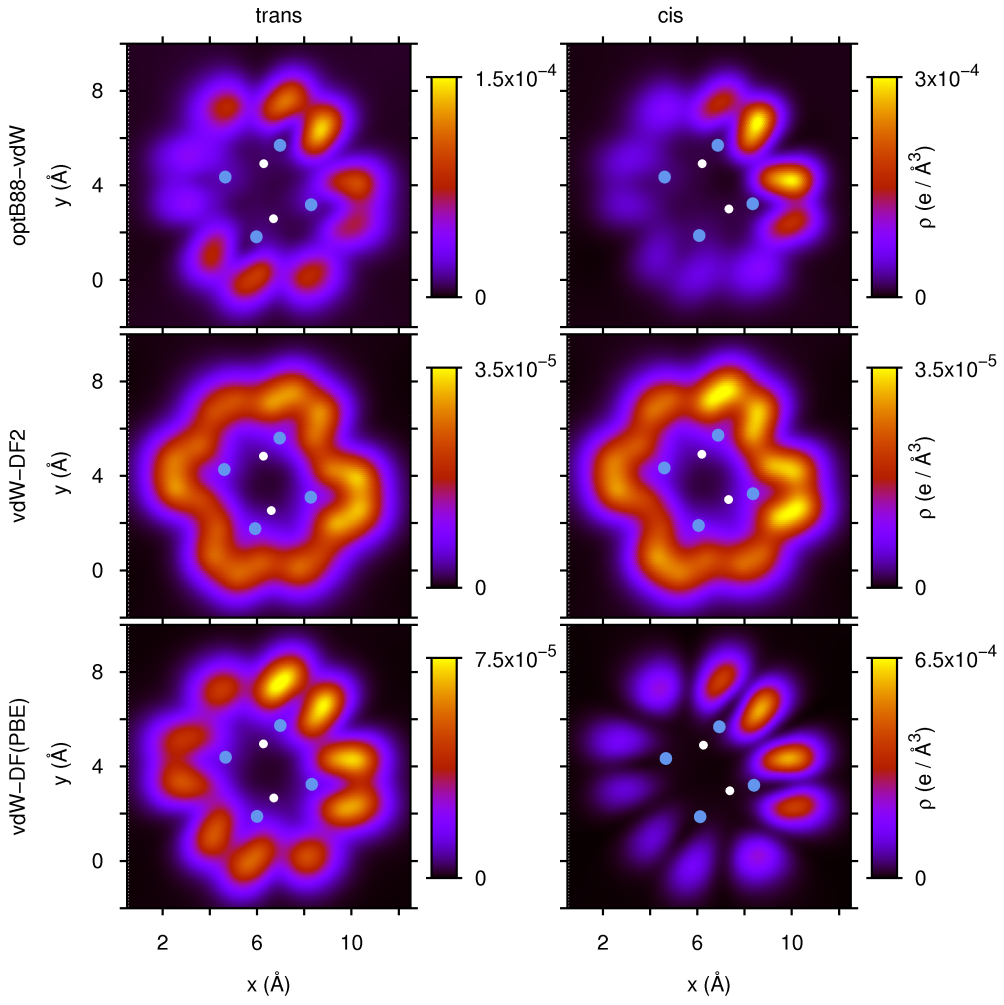

FIGURE 5.11: Partial charge density cut at $z = 2$ Å above the molecule of KS states integrated in an energy window of 0.1 eV below the Fermi level (i.e. the bias voltage used in the images of Ref. [43] for the *trans* and *cis*-porphycene isomers) obtained with three functionals. The (x, y) coordinates of the cavity N and H atoms are indicated by large blue and small white circles, respectively. Note that, here, no attempt was made to enhance the contrast of the PCD images and the STM response is depicted as a linear scale.

polyaromatic ring, which is captured by optB88-vdW and vdW-DF(PBE) only (see bottom right panel of Fig. 5.6).

The PDOS in Fig. 5.8 show that the LUMO is the closest lying orbital above the Fermi level, and that it is strongly hybridized with the surface electron density for *trans* with optB88-vdW, and for *cis* with optB88-vdW and vdW-DF(PBE). In these cases, the hybridized states conform to the observed STM images at a low bias voltage. The interpretation of the crescents of the *cis* images thus appears clearly: the half of the molecule containing the amine N atoms is lifted, while the other one lies closer to the surface. The *trans* case is less clear, though, as none of the performed calculations yield enough hybridization as to bring the imine N atoms closer to the

surface and produce the needed asymmetry in the PCD, with the exception of opB88-vdW. A buckling with the same origin has been reported for H_2-TPP [324], which does not seem to be the case here. The brightest lobes were interpreted in the experimental literature as closely lying to the axis along the molecule diagonal that crosses the amine N atoms, revealing the molecule handedness [43] (see Fig. 5.3). This seems to be a natural interpretation, as the unsaturated N atoms lie closer to the surface when vdW-DF(PBE) and especially optB88-vdW are used. The PCD at $V = -0.1\,\mathrm{V}$ (see Fig. 5.11) for these two functionals shows that there is enough hybridization as to produce the modulation of the LUMO needed to reproduce the asymmetric lobes and the crescent shape characteristic of the *trans* and *cis* tautomers, respectively. Note that the vdW-DF(PBE) seems to slightly underestimate the hybridization, producing just a weak asymmetry. Fig. 5.8 demonstrates the weakness of the surface interaction with both tautomers for vdW-DF2, which is reduced to a pure vdW interaction contribution at long distances $\sim 3.5\,\text{Å}$ with no charge exchange and very little molecular buckling. As expected, the simulated images (Fig. 5.11) are in qualitative disagreement with the experimental ones because the PCD at $V = -0.1\,\mathrm{V}$ does not include any molecular orbital character at all. Therefore, we argue that vdW-DF2 should be disregarded, too. From the buckling calculated with vdW-DF(PBE) and optB88-vdW (see Fig. 5.6), and the experimental images, we may deduce that a buckling of $\sim 0.2\,\text{Å}$ produces a small, yet noticeable, modulation in the STM images, and that bucklings above $0.4\,\text{Å}$ result in very clear contrasts.

5.4.4 Remarks on choosing the appropriate functional

By analysing the electronic structure of the *trans* and *cis* adsorbed configurations for the three selected functionals and interpreting the corresponding STM images we have ruled out the OptB88-vdW and the vdW-DF2 functionals on the basis of wrongly predicting the energetics and the STM images, respectively. The remaining functional, namely vdW-DF(PBE), qualitatively satisfies both of these requirements. Therefore, we consider it appropriate for modelling the *trans* $\rightarrow$ *cis* tautomerization reaction in the porphycene-copper system. Before going into dynamics of this reaction, we summarize some of the electronic structure and geometry details predicted by the above mentioned functionals.

The *cis*$\rightarrow$*trans* process is thermally achieved upon heating the surface up to 30-35 K [43]. This results in all the *cis* molecules being transformed back to the *trans* conformer. The barrier of this activated process is determined to be $42.3 \pm 2.7\,\mathrm{meV}$ [43]. From vdW-DFT (see Fig. 5.6), we obtain the best agreement in this reverse

barrier for vdW-DF(PBE), with 89 meV, whereas the other functionals largely overestimate it. We observe here that the functionals do not just affect the equilibrium configurations energetics but, very importantly, also the transition states.

Interestingly, the barriers for both forward and backward H-transfer processes are higher than the gas-phase ones, i.e. the surface has a stabilizing effect on the tautomers such that no catalysing effect is observed. Intuitively, this makes sense because the N-H$\cdots$N bonds that need to be formed and broken compete with the breaking of the Cu-imine N bonds described above. This seems to be the case of vdW-DF(PBE) and, more clearly, of the optB88-vdW *cis*→*trans* process. Therefore, applying this same argument to the vdW-DF2 case would lead us to expect similar energetics as in the gas phase. However, this is not the case, and indeed we observe that the TS lies ~ 0.1 eV higher than in the gas phase. This unphysical behaviour, in addition to the disagreement with gas-phase MP2 data [363], further dissuades from using vdW-DF2 in this system.

The functional choice also affects the molecule atomic coordinates during H-transfer, as shown in the bottom panels of Fig. 5.6. The competition between hybridization and vdW interaction results in buckling of the molecule, as each of these contributions tends to stabilise adsorbates at different distances from the metal, typically in the ranges of 2.5 and 3.5 Å, respectively. The height-dependent potentials of Fig. 5.7 reflect this, too. Since the three functionals contain similar non-local correlation contributions, they have a similar attractive character at long ranges ($z \geq 4$ Å). The decisive contribution to the binding is made by the exchange part at lower ranges ($z \leq 2.2$ Å), where optB88-vdW is the most repulsive, while vdW-DF2 becomes equally repulsive already at $z \simeq 2.7$ Å. The vdW-DF(PBE) curve, which lies close to the optB88-vdW one at low z, shows that the use of PBE exchange helps suppress the short-range repulsion [80]. It is at the lower range that $V(z)$ of vdW-DF-cx follows closely that of vdW-DF(PBE), while a slightly different behaviour is observed for the *cis* molecule. Finally, note that from the five functionals shown in Fig. 5.7, vdW$^{\text{surf}}$ is clearly the most strongly binding one.

5.5 Tautomerization of porphycene driven by STM-induced potential deformation

So far we have performed an in-depth study of the adiabatic porphycene-copper interaction along the tautomerization path using different vdW functionals to describe the

energetics and the electronic structure. However, that alone cannot explain the irreversibility of the STM- or photo-induced processes. In order to comprehend these processes, dynamic effects (NAC, intramolecular vibrational energy redistribution, etc.) involved in the reaction need to be included. Therefore, using the vdW-DF(PBE), which properly accounts for the requirements set up in the introduction of Sec. 5.4, we construct the deformation potential [Eq. (5.2)] and carry on with the study.

5.5.1 Vibrational properties and nonadiabatic coupling

In Sec. 5.2 we discussed how the intensity of the potential deformation induced by STM excitation [Eq. (5.2)] depends on two main factors: the variation of the NAC strength of the skeletal modes along the reaction path, and the intermode coupling strength. To understand the effect of the latter, Fig. 5.12 shows the vibrational density of states for the *cis* conformer, the TS, and the *trans* conformer (top to bottom panels, respectively). The dashed lines representing the H-transfer mode (i.e., the N-H stretch mode) show the same transition frequency for both conformers, $\sim 350\,\mathrm{meV}$. The higher frequencies at $> 370\,\mathrm{meV}$ correspond to C-H stretch excitation of the outer rings, which are decoupled from the reaction path. In the bias voltage range investigated in the experiment, only the skeletal vibrations can be excited. Interestingly, the DOS of these skeletal modes below 200 meV remains largely unaffected along the reaction path, apart from a shift to higher frequencies ($\sim 230\,\mathrm{meV}$) of the topmost bands at the TS. We can conclude that the potential deformation does not originate from the variation of the vibrational DOS along the tautomerization coordinate. On the other hand, the integrated vibrational DOS projected on the H atom [$\Lambda(\omega_{01})$, red lines in Fig. 5.12] indicates that intermode coupling may be weaker for the *cis* conformer (see Appendix F for more details). This would only amplify the trend stemming from the NAC, as will be shown below.

On the contrary to the vibrational DOS, the electronic DOS varies more significantly along the reaction coordinate. This is illustrated by the behavior of the nonadiabatic damping rates along the adiabatic reaction path, as depicted in Fig. 5.13. The reported lifetimes are calculated as the inverse of the transition rates, Eq. (5.5), for each mode individually. Comparison of the lower (*trans*) and upper (*cis*) panels reveals an important change in the lifetimes of the *trans* ($\sim 5 - 10\,\mathrm{ps}$) and *cis* conformations ($\sim 2 - 5\,\mathrm{ps}$). The origin of this change can be understood from Eq. (5.4). The embedding density n gives a measure of the density of electronic states projected on the adsorbate, which modulates the intensity of the NAC. As already presented in Table 5.2, the porphycene in the *trans* conformation for the vdW-DF(PBE) functional is found to be planar and adsorbed at about 3.5 Å above the surface. The slightly

buckled *cis* conformer binds to the surface via the unsaturated N atoms, at about 2.5 Å. This variation of the adsorbate height along the reaction path (see Fig. 5.6) implies that n increases significantly along the tautomerization coordinate. This, in turn, reduces the zero-bias lifetime of all vibrational modes and the associated STM excitation probabilities. In physical terms, this means that an impinging electron from the STM source resides more briefly on the adsorbate in the *cis* conformation due to its proximity to the surface, and the deformation of the PEC [Eq. (5.2)] is expected to be reduced accordingly.

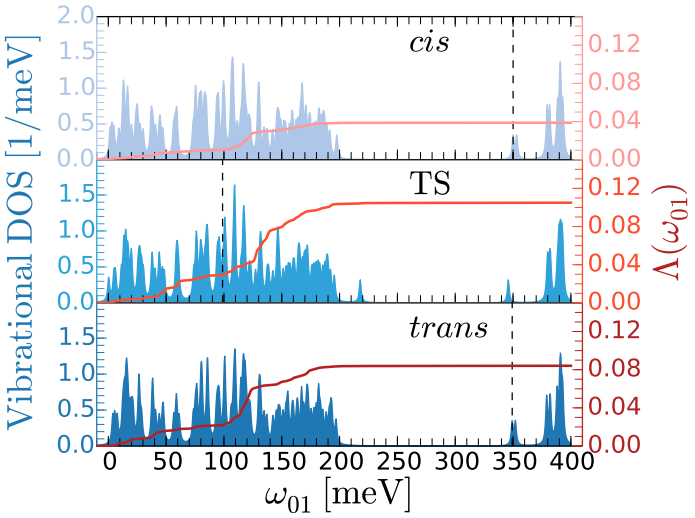

FIGURE 5.12: Vibrational DOS of the porphycene for the three points along the tautomerization coordinate: *cis*, TS, and *trans* configurations. Broadened using a Lorentzian with FWHM=1 meV. The red curves show the integrated vibrational DOS projected on the H atom. The vertical dashed lines represent the frequency of the H-transfer mode.

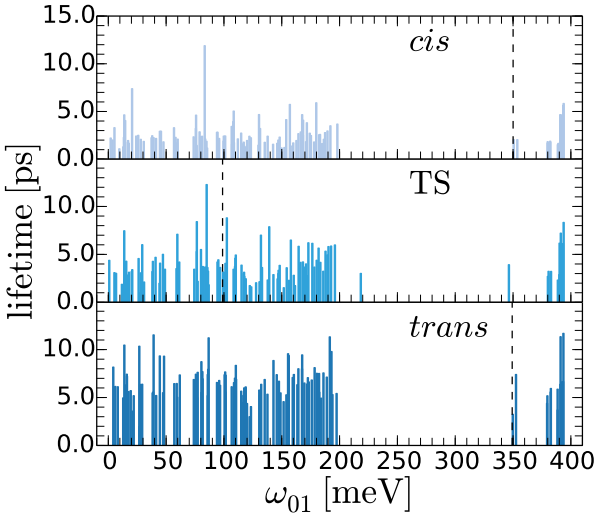

FIGURE 5.13: Harmonic lifetime of all vibrational modes due to *e*-*h* pair coupling at the metal for the three points along the tautomerization coordinate: *cis*, TS, and *trans* configurations. The associated rates are computed using the IAA, see Eq. (5.5). The vertical dashed lines represent the frequency of the H-transfer mode.

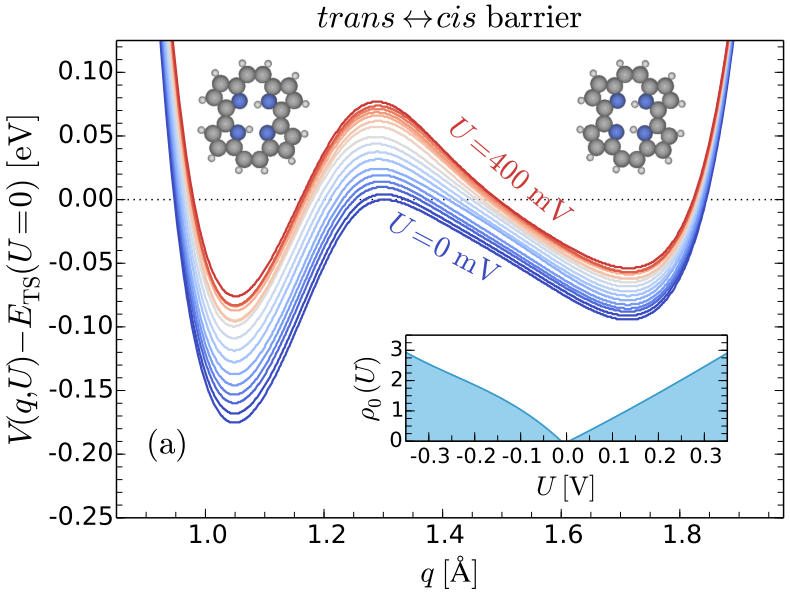

FIGURE 5.14: Potential deformation induced by indirect coupling of the skeletal vibrational modes to *e*-*h* pairs of the metal for increasing STM biases (from 0 mV in blue to 400 mV in red) and fixed STM current intensity $I = 100\,\text{pA}$. Temperature is $T = 5\,\text{K}$. The *trans* configuration (left structure) is seen to be more strongly affected by the presence of the STM than the *cis* conformation (right structure). The inset shows the variation of the projected density of electronic states around the Fermi energy, which affects the efficiency of the NAC.

5.5.2 Potential deformation and population dynamics

The PECs at various biases are shown in Fig. 5.14 for a fixed STM current intensity $I = 100\,\text{pA}$ and temperature $T = 5\,\text{K}$ (as in the experiment [43]). The inset shows $\rho_0(U)$ extracted from DFT calculations, which shows an almost linear dependence at low bias voltages. It can be seen that the STM perturbation generally destabilizes the molecule at the surface. This originates from the quasi-thermal fluctuations induced by excitation of the skeletal modes according to Eq. (5.2). Upon closer inspection, it appears that the *cis* conformer is less destabilized with increasing U compared to the *trans* conformer. This can be rationalized on the basis of the NAC strengths and intramolecular vibrational energy redistribution, as presented in Figs. 5.12 and 5.13. Consequently, the probability of excitation according to Eq. (5.3) is lower and the potential deformation smaller in this region of the PEC. The *trans* conformer is longer-lived and more affected by the bias voltage. Intramolecular vibrational energy redistribution enters the potential deformation via the position-dependence of the harmonic modes in Eq. (5.2). Importantly, the non-uniformity of the potential deformation along the tautomerization coordinate is not sufficient to reverse the energetic ordering of the two potential wells.

The vibrational bound states calculated for PECs at representative bias voltages

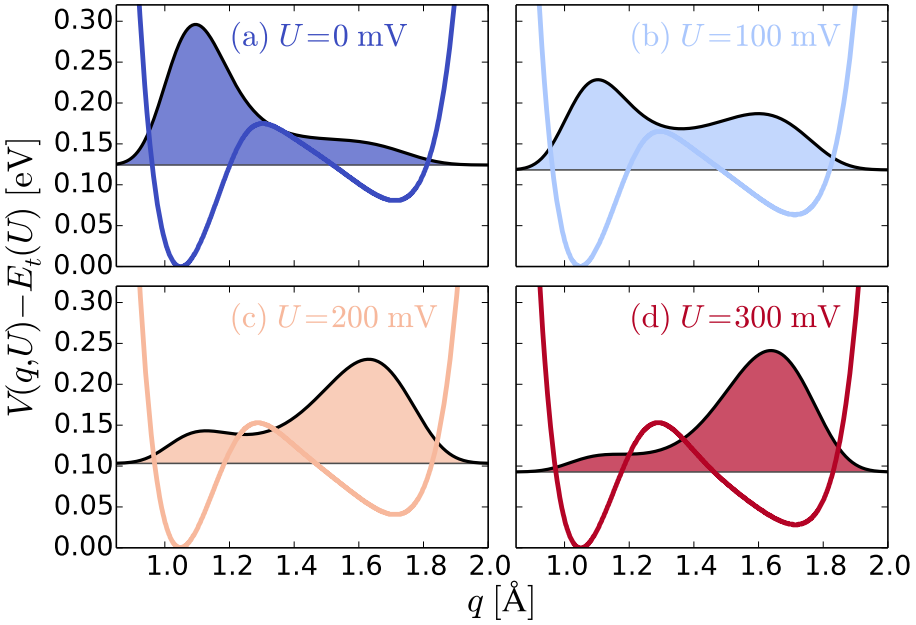

FIGURE 5.15: PECs and vibrational ground state nuclear density (arbitrary units) for (a) $U = 0$ mV, (b) $U = 100$ mV, (c) $U = 200$ mV, and (d) $U = 300$ mV, shifted at the zero-point energy. Despite the small potential deformation, the higher biases are seen to favor the *cis* conformation over the thermodynamically more stable *trans* conformer.

are shown in Fig. 5.15. From the first principles normal mode analysis at 8 discrete points along the reaction path, the mass of the tautomerization mode was found to be that of a H atom, to a good approximation. As it can be seen from Fig. 5.15, the zero-point energy is close to the top of the tautomerization barrier in all PECs, with some degree of delocalization in both the *cis* and *trans* wells. At low biases, the *trans* conformer is favored, in line with the experiment. With increasing bias voltage, the vibrational ground state density (shaded areas) becomes more localized in the *cis* well, with a tipping point at ~ 150 mV. This threshold value is found to be sensitive to the barrier height, the skeletal mode vibrational frequencies, and the NAC rates. To recover the exact tipping point in the simulations, the DFT value of $\rho_0(U)$ was adjusted to $(0.003\,\mathrm{V}^{-1})\,U$.

Figs. 5.16(a)-(b) show the evolution of the nuclear probability density for below- (50 mV) and above-threshold (200 mV) conditions, respectively. The PECs contain the instantaneous reaction of the skeletal vibrational modes to the STM perturbation. The H atom initially found in the *trans* conformation is let to evolve in the perturbed energy landscape from this initial condition. The time-dependent nuclear density is reconstructed as the incoherent sum of localized states $\sum_i P_i(t)\,|\langle q|i\rangle|^2$. Below threshold, the density is seen to remain completely localized in the *trans* well. The quasi-thermal fluctuations induced by the STM are insufficient to trigger the tautomerization reaction. In above-threshold conditions [Fig. 5.16(b)], a smooth transfer

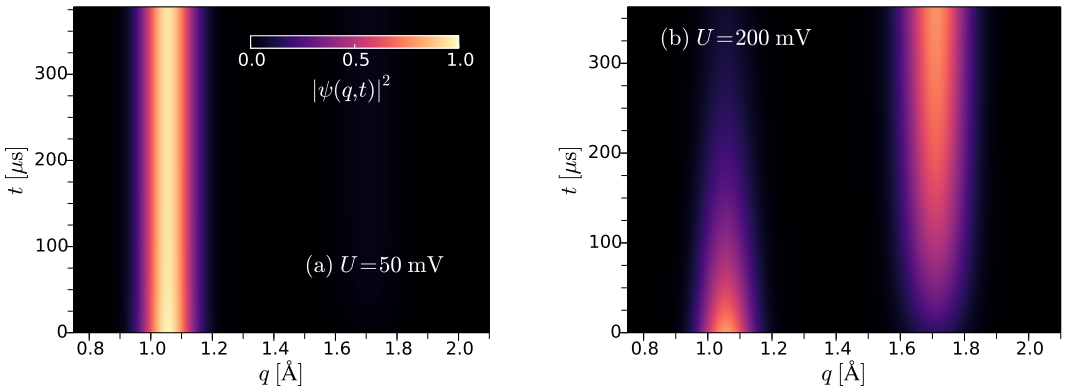

FIGURE 5.16: (a) Below-threshold dynamical evolution of the nuclear density upon application of a $U = 50\,\text{mV}$ bias. The density remains preferentially in the thermodynamically stable *trans* conformation. (b) Above-threshold dynamical evolution of the nuclear density upon application of a $U = 200\,\text{mV}$ bias. The forward tautomerization reaction from the *trans* to the *cis* conformation under the influence of the NAC to the metal is favored.

from the *trans* to the *cis* conformer is seen, with no probability density noticeable in the tunnelling region and without nodal structure building up in either well. This indicates that for such low biases, the tautomerization dynamics is dominated by the direct *trans*→*cis* transfer, mediated by *e-h* pair excitations. This corresponds to the first scenario described in Fig. 5.2, i.e., simultaneous tunnelling and relaxation from the vibrational ground state. In this case, the tautomerization rate is determined by the zero-bias NAC rate, $\gamma_{\text{t}\to\text{c}}$, as described in Eq. (5.4). The latter correlates with the alignment of the fundamental level in the *trans* and *cis* wells, as shown in Fig. 5.17(a). The lifetime broadening (blue circles) is seen to reach a maximum at $U = 100\,\text{mV}$, where the zero-point energies of the *trans* and *cis* conformers are quasi-degenerate (red diamonds). At higher voltages, the levels drift further apart and the rates consequently decrease. It becomes vanishingly small at zero bias, which explains the observed irreversibility of the STM-induced tautomerization reaction: once the transformation occurred, the molecule remains trapped in the *cis* conformation due to inefficient coupling to *e-h* pairs of the metal, as depicted schematically in Fig. 5.2.

Although the NAC rates are larger at $U = 100\,\text{mV}$, the tautomerization efficiency is smaller at below-threshold biases. Fig. 5.17(b) reports the tautomerization time (τ, blue circles) and efficiency (dP_{cis}, red diamonds) at various STM biases. They are obtained by fitting the population of the vibrational ground state of the *cis* isomer to an exponential form, $P_{\text{cis}}(t) = dP_{\text{cis}}\left(1 - e^{-(t-t_0)/\tau}\right)$. All tautomerization times are found to be on the order of microseconds, well below the upper limit inferred from experimental observations. For biases below 350 mV (i.e., the N-H stretch mode), the tautomerization times correlate perfectly with the energy level alignment and the behavior of the NAC rates shown in Fig. 5.17(a). An acceleration of the

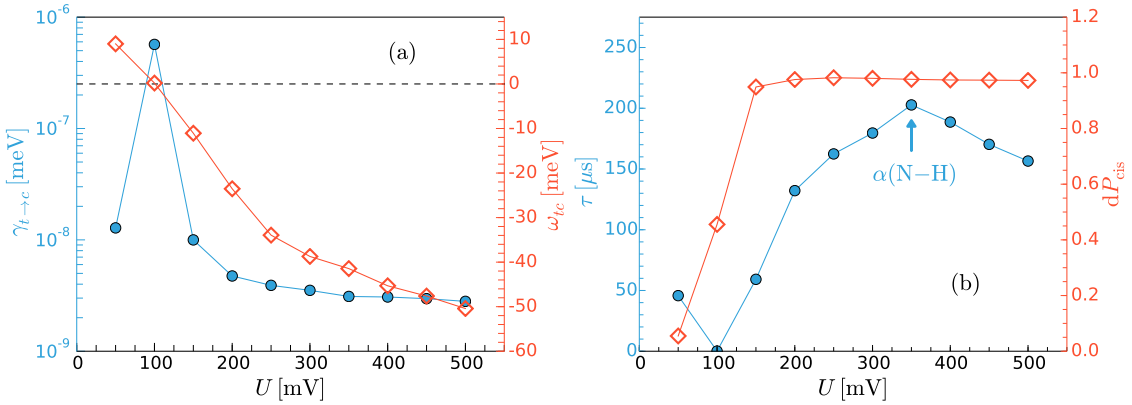

FIGURE 5.17: (a) Zero-bias NAC rate for the *trans*→*cis* ground state to ground state transition (blue circles) and zero-point energy difference (red diamonds) as a function of the bias voltage. (b) Tautomerization time (blue circles) and efficiency (red diamonds) for different bias values. An acceleration is observed for biases above the resonant frequency of the tautomerization mode $\alpha(\mathrm{N}-\mathrm{H})$.

reaction is observed at biases above the resonance energy to directly excite the tautomerization coordinate. This corresponds to the second scenario described in the cartoon, Fig. 5.2: as the tautomerization coordinate becomes directly activated, population is brought up to the first vibrational excited state of the *trans* species, which has a faster tunnelling rate than the local ground state ($\tau_1 < \tau_0$). Consequently, in addition to the simultaneous tunnelling/relaxation mechanism, a sequential channel via the excited state becomes available at higher bias voltages. This latter mechanism becomes more important with increasing biases and accelerates the reaction by inducing larger quasi-thermal fluctuations in the system.

Interestingly, the tautomerization efficiencies and times show different behaviours [see Fig. 5.17(b)]. The former shows that for any above-threshold U value the reaction always takes place, i.e. $dP_{\mathrm{cis}} \simeq 1$, although the latter varies with U. The experiments, however, report that above threshold the tautomerization yields increase with increasing bias. This apparent contradiction can be lifted by considering the following statistical argument. As is seen in our simulations, if a hot electron reaches the molecule, tautomerization will take place according to the potential deformation mechanism described above. Although this accounts for single-molecule tautomerization, the actual observed yield is subject to the availability of hot electrons or holes. The yield is determined experimentally by counting the number of molecules found in the *cis* conformation after application of the STM pulse in a limited area of a few nm^2. Assuming that the hot electrons propagate ballistically as an S-wave through the metal [345], we can estimate the number of electrons N_e impinging on each molecule as a function of time t as $N_e = \frac{It}{e\theta\pi R^2}$, where θ is the coverage and R the mean free path of the hot electrons or holes. Although a precise value of R at bias voltages below 1 V is difficult to calculate, it lies in the order of 1-100 nm and

increases as the bias decreases. Considering the experimental values $I = 100\,\text{pA}$ and $\theta = 0.03 - 0.33\,\text{nm}^{-2}$, too few hot carriers impinge the molecule in the microsecond regime. It is for this reason that the STM pulse needs to be applied, at least, several milliseconds to observe significant yields in the experiment.

5.6 Conclusions

We have studied by DFT the intramolecular H-transfer, known as tautomerization, of the porphycene molecule on Cu(111) induced by inelastic hot electrons. Experimentally, the *trans*→*cis* reaction at low temperature can be *irreversibly* electro-induced using pulses from a STM tip [43] or photo-induced with ultraviolet lasers [330], and the reverse process is thermally activated. The main goal of this chapter was to comprehend the dynamical details of the STM-induced tautomerization reaction and to find a general theoretical framework to successfully account for the multi-dimensional nature of this process. Since the energetics of this type of systems is extremely sensitive to the balance between dispersion forces and exchange contributions, we have also studied the influence of different van der Waals functionals on the DFT description of this system.

We demonstrate in this chapter that a potential energy deformation is the driving mechanism for the STM-induced *trans*→*cis* tautomerization reaction of porphycene on Cu(111). The quasi-thermal excitation of skeletal vibrations by NAC to the metal electrons distorts the potential along the tautomerization coordinate, mediated by intermode coupling. Importantly, all the parameters entering the potential deformation can be computed from first principles. The model explains the experimentally observed stability reversal of the two configurations at a given threshold bias. The tautomerization rates are dominated by the simultaneous tunnelling and relaxation to the *cis* ground state, and dictated by the energetic alignment of the local vibrational ground states. The reaction is found to be complete above a threshold value of the bias voltage. The observed dependency of the tautomerization yield on the applied voltage can be rationalized from geometrical arguments based on the availability of electrons travelling as S-waves in the metallic substrate. The irreversibility of the reaction can be explained as follows on the basis of the present dynamical model. The tautomerization channel is opened by skeletal vibrations excited by NAC to hot electrons impinging from the STM. Hence, the quasi-thermal fluctuations are suppressed at zero-bias and the molecule remains trapped in the nearest local minimum of the potential energy landscape. The reverse *cis*→*trans* reaction becomes possible only once the system is thermally activated, where it can be mediated by random hopping diffusion. Note that, opening up the vibration-phonon coupling channels by

thermal activation of the phonons may lead to larger a potential deformation in Eq. (5.2). This softer potential energy surface sustains more delocalized states, which relax more rapidly and efficiently to the *trans* configuration. This will merely affect the balance between thermal diffusion rates and NAC relaxation but not the general conclusions presented in this work. The model presented here has a general character and could be applied to other similar systems which have already been investigated experimentally, e.g., STM-induced configurational changes in azobenzene derivatives on Au(111) [369] or in diarylethene on Ag(111) [370].

In addition, we show that the interaction between porphycene and Cu(111) is contributed by van der Waals forces, which are responsible for the binding of the outer polyaromatic cycle of the molecule to Cu(111), and by hibridization between the LUMO and the substrate, by which the molecule anchors to individual Cu atoms via the unsaturated N atoms located at the molecule central cavity. In the electronic structure, this is reflected as a partial hybridization of the LUMO with the metallic states at the Fermi level, which produces the characteristic features of each tautomer in the STM images. In our analysis we attribute these features to the molecule buckling, which is enhanced for the lower-lying *cis* tautomer. After analysing various representatives of functional families, we find that a correct DFT description of the subtle balance between those two mechanisms requires a sensible choice of the exchange formulation. On the one hand, optB88-vdW [81] is found to be too attractive because it overestimates LUMO hybridization and predicts that the *cis* conformer is the most stable ($E_{c-t} \simeq -0.15\,\mathrm{eV}$), in disagreement with the experiment. On the other hand, the original vdW-DF2 [353] using rPW86 exchange is too repulsive to cause enough hybridization and, consequently, it cannot account for the experimental STM images. Based on physical arguments on the exchange density enhancement factor, we have proposed a combination of vdW-DF with PBE exchange to find the balance between dispersion interactions and local hybridization of the N-Cu bonds. This intermediate choice makes satisfactory predictions of the thermodynamical stability of *trans*, the *cis*→*trans* barrier, and the main qualitative features of the STM images. Furthermore, the use of this functional is also supported by the good agreement with MP2 literature results for the gas-phase H-transfer energetics, and it reproduces the correct Cu interlayer distance. Thus, we are confident that the present interpretation of the molecule-substrate interaction may be generalized to other polycyclic aromatic molecules where intra-molecular H-transfer is feasible. In these cases the stability of the adsorbate will be dictated by the number of undercoodinated atoms that serve as anchoring points to the metal (N, O, S, or even metal atoms) and by the structure and number of aromatic cycles in the molecule. All in all, the presented detailed functional choice is particularly needed for these type of systems, since the energy landscape features associated to this interaction balance

are very subtle and yet those features are the essential building blocks for studying dynamical effects of the STM- or photo-induced reactions.

Chapter 6

Summary and outlook

The main objective of this Thesis was to elaborate different descriptions of the dynamical coupling of surface electrons with moving adsorbates, i.e., to study the so-called nonadiabatic effects and their role in different surface processes. The dynamical coupling was examined in three scenarios, where we presented our theoretical models and put them into practice. Each of these subjects exemplifies different aspects of the problem and thus requires specific theoretical considerations. All the building blocks needed for this work were extracted from *ab initio* calculations, making the corresponding models quantitatively predictive and applicable to realistic adsorbate-surface systems.

The first class of dynamical processes is the relaxation of hot atoms and molecules on metallic surfaces, namely H, N, and N_2 on Pd(100), Ag(111), and Fe(110), respectively (see Chapter 3). Our goal was to determine the role of *e-h* pair and phonon (i.e., energy transfer to the surface) excitations in the adsorption processes and to establish the correlation between the amount of energy diverted into the *e-h* pair channel and the adsorption energy of the projectile. Apart from analysing the adsorbates energy under the influence of these two dissipation channels, we have also studied their impact on the distances travelled by adsorbates on surfaces. All these pieces of information are of great importance for future considerations on surface reactions, since they predict which are the conditions when the Born-Oppenheimer approximation can provide a satisfactory description and when do we need to go beyond it. In order to determine these conditions we have modified and adapted the *ab initio* molecular dynamics with electronic friction (AIMDEF) methodology, and applied it to study the mentioned three systems. Our results show that the relaxation dynamics of light adsorbates (i.e., H) is governed by the *e-h* pair dissipation channel, while on the other hand, heavy projectiles (i.e., N and N_2) exchange most of their energy with the surface atoms. The simple reasoning behind this behaviour is that the

transfer of energy to the phonon loss channel decreases as the adsorbate-to-surface atom mass ratio becomes smaller. Although the *e-h* pair dissipation channel is secondary for the overall thermalization of heavier species, its role becomes important in the long run, i.e., when the adsorbate reaches the final adsorption well and loses energy until it equilibrates in it. This behaviour correlates with the corresponding adsorption energies, i.e., the species with the higher adsorption energies transfer more energy into the *e-h* pair channel, which is in consistency with experimental findings, although deviations from this behaviour may appear due to the particular details of the surface electron density. In addition, we have performed a systematic analysis of different electron density models in the calculation of the electronic friction coefficient. The AIMDEF together with our most accurate model constitutes a very efficient methodology for studying relaxation processes upon adsorption, desorption, and scattering of atoms and molecules on metal surfaces.

We have treated vibrational relaxation of adsorbates on metallic surfaces in Chapter 4, where we have considered the influence of the electronic damping mechanisms on the phonon linewidth of a vibrating ordered molecular overlayer. Here we have adapted the many-body perturbation theory based in DFT and analysed the nonadiabatic phonon self-energy in the long-wavelength limit. When only the lowest-order phonon self-energy is considered (i.e., first-order in the electron-phonon coupling function) the electrons excited by the studied phonon mode are regarded as noninteracting and the corresponding phonon linewidth formula is analogous to the first-order Fermi's golden rule formula. On the other hand, when higher-order terms are also considered the excited electrons scatter on other phonon modes and the so-called *e-h* self-energy enters the phonon linewidth formula. We have performed a systematic study on the role of these higher-order terms for the prototypical case of the CO stretch mode on the Cu(100) surface. First we have introduced phenomenologically these electron scattering processes (i.e., electron scattering on phonons, as well as on impurities and other electrons) by replacing the actual *e-h* self-energy with a phenomenological parameter. As a result, the higher-order processes improve the first-order Fermi's golden rule result and, therefore, a better agreement with the experimentally measured linewidths is achieved. Next, we have considered the second-order terms of electron-phonon scattering in the intraband phonon self-energy by performing the explicit calculations. These terms account for the electron-mediated coupling of the studied phonon mode with all other phonon modes in the system, which resembles the *e-h* pair dephasing mechanism. By employing this indirect phonon-phonon coupling term, we have shown how the CO frustrated rotation and translation modes couple strongly to the studied long-wavelength stretch mode via *e-h* pairs and contribute significantly to its relaxation. In fact, the order of magnitude of this second-order contribution to the phonon linewidth is of the same order as

the first-order term. Along with the two low-frequency modes, the joint motion of the CO molecule and the surface atoms also influences the CO stretch mode linewidth. Since this indirect coupling mechanism is temperature dependent, it can be used as an alternative explanation for the experimentally observed temperature-dependent linewidth, which was previously attributed in the literature to anharmonic dephasing effects. In addition, we have discussed the deficiencies of the quasi-static limit in our case. Also, we have shown that nonadiabatic effects play an important role in explaining the experimental frequency of the long-wavelength CO stretch mode. In summary, we have performed a rigorous microscopic study of the relaxation processes involved in CO dynamics on Cu(100) and proposed alternative explanations to the experimental observations on the vibrational linewidths. The developed theory is of general character and should be applicable to the study of nonadiabatic phenomena in many other cases as well.

In Chapter 5 we have studied our final example of nonadiabatic effects in adsorbate-surface systems, namely the STM-induced *trans*→*cis* tautomerization reaction (i.e., intramolecular relocation of a H atom) in the porphycene molecule on Cu(111). The backbone of this reaction is the nonadiabatic coupling between the inelastic electron current and the vibrational modes of porphycene. The experiments suggest that the reaction coordinate mode, i.e., the N-H stretch mode, is not triggered directly, but indirectly through intermode coupling with the skeletal vibrational modes of molecule. Therefore, in order to build a successful model to describe the tautomerization reaction, these multi-dimensional dynamical features need to be taken into account. Even further, the corresponding bond breaking of the H atom involves large-amplitude motions and thus anharmonic effects should be also taken into consideration. In this chapter we have constructed a model that is able to capture the main features of the experiment by considering all of the aforesaid dynamical effects in the form of an effective deformation potential term along the reaction coordinate, which lowers the reaction barrier and thus promotes the *trans*→*cis* transition above a certain threshold bias. At that instant, H tunnelling to the *cis* state becomes the dominant process and the molecule is instantaneously relaxed to the local potential energy ground state. Finally, when the porphycene molecule is found in the *cis* configuration and the applied bias is switched off, the fluctuations are suppressed and the molecule remains trapped in that state. Our methodology can be applicable to other similar molecular systems characterized by nonadiabatic effects and a large number of strongly coupled degrees of freedom. Additionally, we have performed a detailed study of the adsorption energetics and the electronic structure of the porphycene-copper system by means of various DFT functionals. Our analysis explains adsorption as the result of a subtle balance between these two mechanisms: the vdW interaction, which is responsible for binding the outer polyaromatic cycle

to the substrate, and the charge transfer between the unsaturated N atoms in the molecule central cavity and the copper surface. Among the many tested functionals, we have found that vdW-DF with PBE exchange does not seem to overestimate any of these two mechanisms over the other. It successfully describes the experimental STM images, measured energy barriers, and, importantly, it predicts *trans* as the thermodynamically stable configuration. These interpretations could be generalized, too, to similar molecule-surface systems and could inspire future functional developments.

Appendix A

Molecular dynamics zones

In usual AIMD (also AIMDEF) simulations, the converged wave functions at each integration step are used to extrapolate the wave functions at the next integration step. This scheme, which certainly facilitates the AIMD calculation, might be problematic when dealing with open-shell atoms or molecules for which the spin state changes with their distance to the surface, more specifically, when it changes from zero to a finite value because the wave functions used in the extrapolation are spin-degenerated. Such is the case of N incident on Ag(111). Figure A.1 shows the spin magnetization of the system as a function of the distance from the surface z, for N

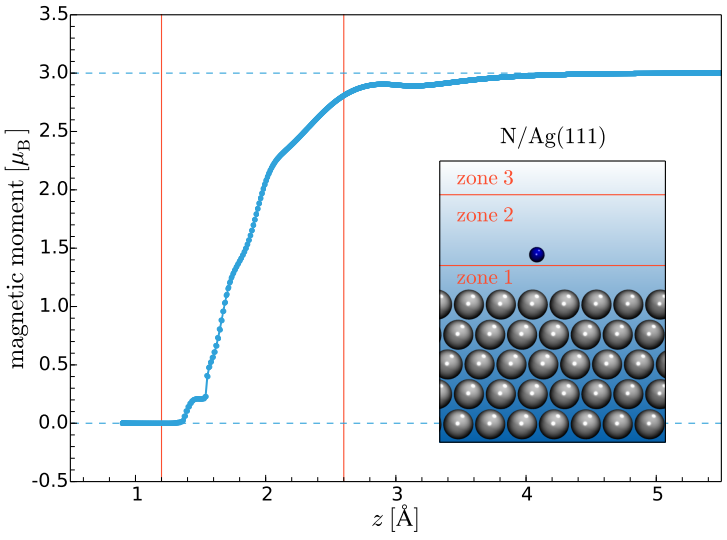

FIGURE A.1: Spin magnetic moment of the system as a function of the distance from the Ag(111) surface z. The vertical red lines represent the AIMD zone boundaries (see text), while the horizontal blue lines represent the magnetic moment of the gas-phase (3 μ_B) and adsorbed (0 μ_B) N atom. Inset: Schematic representation of the three zones used in our AIMD(EF) simulations to properly account for the changing magnetic moment of N above Ag(111).

located above a Ag surface atom. It is zero close to the surface and increases rapidly to the gas-phase value of 3 μ_B far from the surface. Similar variations are obtained for N located at other positions over the Ag(111) surface. The main numerical difficulty consists in converging to the correct non-zero spin-polarized ground state as the N-Ag(111) distance grows. Thus, in order to break the spin-degeneracy of the wave functions during the AIMDEF simulations, we define the following three different zones within the supercell (see inset of Fig. A.1) and adopt a different strategy within each of them,

- zone 1 (z $<$ 1.2 Å), where the N spin is completely quenched. Therefore, as soon as N enters and stays in this zone a standard non-spin polarized AIMD calculation is performed.
- zone 2 (1.2 $<$ z $<$ 2.6 Å), where the spin-polarization varies rapidly with z. In this zone, the mentioned numerical problems in breaking the spin-degeneracy may appear when the N atom enters this zone from the surface (zone 1) with zero spin magnetic moment. In this case, the simulation is stopped at each integration step once the electronic wave functions and the forces on the atoms are converged. For the next integration step, a new calculation is launched from scratch, but using an initial magnetic moment of 3 μ_B for N. There is no need to stop the simulation when N comes from the region z $>$ 2.6 Å.
- zone 3 (z $>$ 2.6 Å), where the spin magnetic moment is that of the gas-phase N. In this zone, a standard spin-polarized AIMD calculation is performed.

Appendix B

JDOS and Lorentzians

We define the complex joint density of states (JDOS) for the $\mathbf{q} \approx 0$ interband parts of functions Eq. (4.4) and Eq. (4.11) using the following function

$$\Lambda_{\varphi}^{\text{inter}}(\mathbf{q} \approx 0, \omega) = \sum_{\mu \neq \mu', \mathbf{k}} \varphi^{-1} \frac{f_{\mu\mathbf{k}} - f_{\mu'\mathbf{k}}}{\omega + \varepsilon_{\mu\mathbf{k}} - \varepsilon_{\mu'\mathbf{k}} + i\Gamma_{\text{inter}}}, \tag{B.1}$$

which for $\varphi = \omega$ is the JDOS related to Eq. (4.4), and for $\varphi = \varepsilon_{\mu'\mathbf{k}} - \varepsilon_{\mu\mathbf{k}} \equiv \Delta\varepsilon$ is the JDOS corresponding to Eq. (4.11). Note that Eqs. (4.4) and (B.1) have a similar functional dependence on ω only if we consider that $\omega_{0\lambda} \to \omega$ in the matrix elements $g_{\lambda}^{\mu\mu'}$ of Eq. (4.4). The imaginary and real parts of these JDOS functions for different damping energies Γ_{inter} and number of Cu layers can qualitatively predict the behaviour of the phonon linewidths and frequency shifts as a function of these parameters. It can also be seen what the difference between the imaginary part of the self-energy with $\varphi = \omega$ and with $\varphi = \varepsilon_{\mu'\mathbf{k}} - \varepsilon_{\mu\mathbf{k}}$ is. In Figs. B.1(a) and B.1(c) we see how the imaginary part of the JDOS obtained for the CO stretch mode increases when increasing the number of Cu layers (compare with Fig. 4.9). The effect of different damping energies Γ_{inter} on the imaginary part of the JDOS is shown in Figs. B.1(b) and B.1(d). The overall difference between the JDOS obtained with $\varphi = \omega$ (left panels in Fig. B.1) and with $\varphi = \varepsilon_{\mu'\mathbf{k}} - \varepsilon_{\mu\mathbf{k}}$ (right panels in Fig. B.1) is that the latter gives smaller values than the former for the same damping energies Γ_{inter}, which is in agreement with the results presented in Fig 4.8. Additionally, we show the results for the real part of JDOS for different number of Cu layers and temperatures in Figs. B.2(a) and B.2(b), respectively. The result for different number of Cu layers is in agreement with the result obtained in Fig. 4.17, where the real part of the interband phonon self-energy does not change drastically with the number of layers.

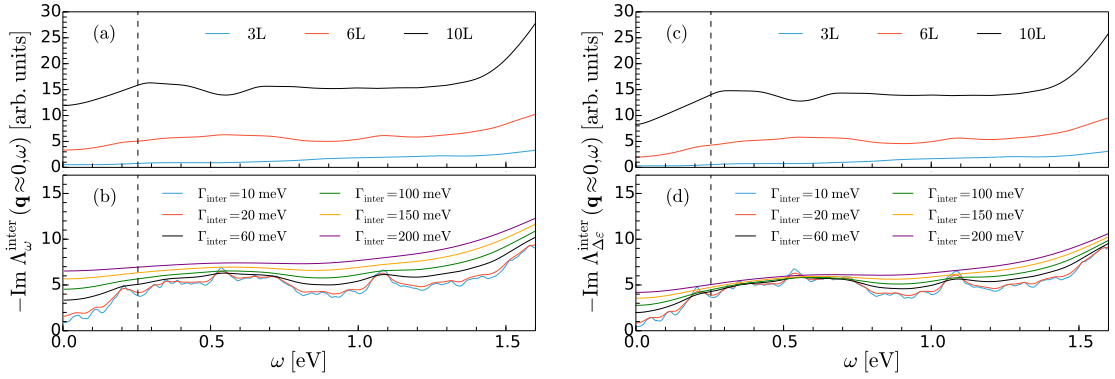

FIGURE B.1: Imaginary part of JDOS Eq. (B.1) with $\varphi = \omega$ as a function of ω for (a) different numbers of Cu layers with $\Gamma_{\text{inter}} = 60$ meV and (b) different damping energies Γ_{inter} with 6 Cu layers. Panels (c) and (d) show the same quantities as (a) and (b), respectively, but with $\varphi = \Delta\varepsilon$. The dashed vertical lines represent the energy of the CO stretch mode.

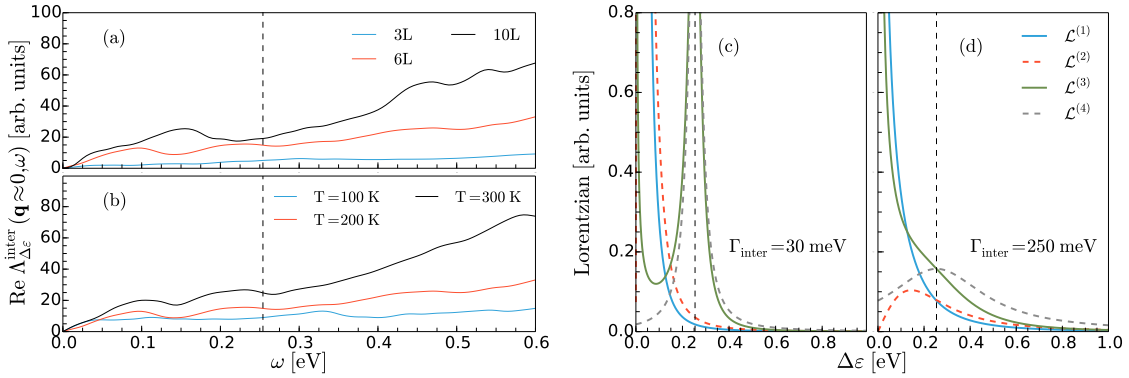

FIGURE B.2: Real part of JDOS Eq. (B.1) as a function of ω for (a) different number of Cu layers with $T = 200$K and (b) different temperatures with 6 Cu layers, where $\varphi = \Delta\varepsilon$. Different types of Lorentzians as a function of excitation energy $\Delta\varepsilon$ for (c) $\Gamma_{\text{inter}} = 30$ meV and (d) $\Gamma_{\text{inter}} = 250$ meV. The dashed vertical lines represent the energy of the CO stretch mode.

The differences and similarities between the methods used in Fig. 4.8 can be further clarified by looking at the corresponding Lorentzians:

- Lorentzian corresponding to Eq. (4.34)

$$\mathcal{L}^{(1)}_{\Gamma_{\text{inter}}}(\Delta\varepsilon) = \frac{1}{|\Delta\varepsilon|}\frac{\Gamma_{\text{inter}}}{\Delta\varepsilon^2 + \Gamma^2_{\text{inter}}}, \tag{B.2}$$

- Lorentzian corresponding to Eq. (4.35)

$$\mathcal{L}^{(2)}_{\Gamma_{\text{inter}}}(\Delta\varepsilon) = \frac{2\Gamma_{\text{inter}}|\Delta\varepsilon|}{\left[\Delta\varepsilon^2 + \Gamma^2_{\text{inter}}\right]^2}, \tag{B.3}$$

- Lorentzian corresponding to the imaginary part of Eq. (4.11)

$$\mathcal{L}^{(3)}_{\Gamma_{\text{inter}}}(\Delta\varepsilon, \omega_{0\lambda}) = \frac{1}{|\Delta\varepsilon|} \frac{\Gamma_{\text{inter}}}{(\omega_{0\lambda} - |\Delta\varepsilon|)^2 + \Gamma^2_{\text{inter}}}, \tag{B.4}$$

- Lorentzian corresponding to the imaginary part of Eq. (4.4)

$$\mathcal{L}^{(4)}_{\Gamma_{\text{inter}}}(\Delta\varepsilon, \omega_{0\lambda}) = \frac{1}{\omega_{0\lambda}} \frac{\Gamma_{\text{inter}}}{(\omega_{0\lambda} - |\Delta\varepsilon|)^2 + \Gamma^2_{\text{inter}}}. \tag{B.5}$$

Here we consider the energy difference $\Delta\varepsilon$ and damping energy Γ_{inter} as free parameters, while the phonon frequency $\omega_{0\lambda}$ is the one for the CO stretch mode. It can be seen that $\mathcal{L}^{(1)}_{\Gamma_{\text{inter}}} \approx \mathcal{L}^{(2)}_{\Gamma_{\text{inter}}}$ and $\mathcal{L}^{(3)}_{\Gamma_{\text{inter}}} \approx \mathcal{L}^{(4)}_{\Gamma_{\text{inter}}}$ for small values of Γ_{inter} [Fig. B.2(c)], while $\mathcal{L}^{(1)}_{\Gamma_{\text{inter}}} \approx \mathcal{L}^{(3)}_{\Gamma_{\text{inter}}}$ and $\mathcal{L}^{(2)}_{\Gamma_{\text{inter}}} \approx \mathcal{L}^{(4)}_{\Gamma_{\text{inter}}}$ for large values of Γ_{inter} [Fig. B.2(d)]. The similar form of the Lorentzians $\mathcal{L}^{(2)}_{\Gamma_{\text{inter}}}$ and $\mathcal{L}^{(4)}_{\Gamma_{\text{inter}}}$ for large Γ_{inter} is accidental and for a different value of $\omega_{0\lambda}$ they would be different. For values $\Gamma_{\text{inter}} < 150$ meV the difference between $\mathcal{L}^{(1,2)}_{\Gamma_{\text{inter}}}$ (quasi-static limits) and $\mathcal{L}^{(3,4)}_{\Gamma_{\text{inter}}}$ is very pronounced (in the same way there is a difference between the different $\gamma^{\text{inter}}_{0\lambda}$ curves for small Γ_{inter} in Fig. 4.8).

Appendix C

Possible RTA form of $\widehat{\pi}^0_\lambda$

Since the usual starting point of the contemporary nonadiabatic calculations is the phonon self-energy with adiabatic phonon frequency and finite numerical broadening parameter $\eta > 0$, it would be useful to have the RTA form of $\widehat{\pi}^0_\lambda$ obtained with Eq. (4.11) where its imaginary part is equal to the imaginary part of Eq. (4.4) in RTA, $\mathrm{Im}\widehat{\pi}^0_\lambda(\omega) = \mathrm{Im}\pi^0_\lambda(\omega)$. Since the direct diagrammatic perturbation expansion of $\widehat{\pi}^0_\lambda$ has not been developed to our knowledge, we take a different approach here. First we account for all the relevant electron scattering processes (at least formally) in the phonon self-energy $\Pi_\lambda(\omega)$ and then we subtract the adiabatic term in the clean noninteracting limit $\pi^0_\lambda(0)$. In that way, we avoid the direct perturbation expansion of $\widehat{\pi}^0_\lambda$ by constructing $\widehat{\Pi}_\lambda$ *a posteriori*. In Matsubara notation this reads

$$\begin{aligned}\widehat{\Pi}_\lambda(\mathbf{q}, i\nu_n) &= \Pi_\lambda(\mathbf{q}, i\nu_n) - \pi^0_\lambda(\mathbf{q}, 0) \\ &= \sum_{\mu\mu'\mathbf{k}\sigma} \frac{1}{\beta} \sum_{i\omega_n} \left[g^{\mu\mu'}_\lambda(\mathbf{k}, \mathbf{q})\right]^* \widetilde{g}^{\mu\mu'}_\lambda(\mathbf{k}, \mathbf{q}) \frac{G_\mu(\mathbf{k}) - G_{\mu'}(\mathbf{k}+\mathbf{q})}{i\nu_n + \varepsilon_{\mu\mathbf{k}} - \varepsilon_{\mu'\mathbf{k}+\mathbf{q}} + \Delta\Sigma_{\mu\mu'}(\mathbf{k}, \mathbf{q})} \\ &\quad - \sum_{\mu\mu'\mathbf{k}\sigma} \frac{1}{\beta} \sum_{i\omega_n} \left|g^{\mu\mu'}_\lambda(\mathbf{k}, \mathbf{q})\right|^2 \frac{G^0_\mu(\mathbf{k}) - G^0_{\mu'}(\mathbf{k}+\mathbf{q})}{\varepsilon_{\mu\mathbf{k}} - \varepsilon_{\mu'\mathbf{k}+\mathbf{q}}}\end{aligned} \tag{C.1}$$

where the dependence on $i\omega_n$ and $i\nu_n$ is assumed in $\widetilde{g}_\lambda$, G and $\Delta\Sigma$. In the simplest RTA form (as described in Sec. 4.2.2), Eq. (C.1) can be expressed as

$$\widehat{\pi}^{0,\mathrm{RTA}}_\lambda(\mathbf{q}, \omega) = \sum_{\mu\mu'\mathbf{k}\sigma} \left|g^{\mu\mu'}_\lambda(\mathbf{k}, \mathbf{q})\right|^2 \frac{f_{\mu\mathbf{k}} - f_{\mu'\mathbf{k}+\mathbf{q}}}{\varepsilon_{\mu\mathbf{k}} - \varepsilon_{\mu'\mathbf{k}+\mathbf{q}}} \frac{-(\omega + i\Gamma)}{\omega + \varepsilon_{\mu\mathbf{k}} - \varepsilon_{\mu'\mathbf{k}+\mathbf{q}} + i\Gamma}, \tag{C.2}$$

where the corresponding imaginary and real parts are

$$\mathrm{Im}\widehat{\pi}^{0,\mathrm{RTA}}_\lambda(\mathbf{q},\omega) = \sum_{\mu\mu'\mathbf{k}\sigma} \left|g^{\mu\mu'}_\lambda(\mathbf{k},\mathbf{q})\right|^2 (f_{\mu\mathbf{k}} - f_{\mu'\mathbf{k}+\mathbf{q}}) \frac{-\Gamma}{(\omega + \varepsilon_{\mu\mathbf{k}} - \varepsilon_{\mu'\mathbf{k}+\mathbf{q}})^2 + \Gamma^2} \tag{C.3}$$

and

$$\mathrm{Re}\widehat{\pi}^{0,\mathrm{RTA}}_\lambda(\mathbf{q},\omega) = -\sum_{\mu\mu'\mathbf{k}\sigma} \left|g^{\mu\mu'}_\lambda(\mathbf{k},\mathbf{q})\right|^2 \frac{f_{\mu\mathbf{k}} - f_{\mu'\mathbf{k}+\mathbf{q}}}{\varepsilon_{\mu\mathbf{k}} - \varepsilon_{\mu'\mathbf{k}+\mathbf{q}}} \frac{\omega(\omega + \varepsilon_{\mu\mathbf{k}} - \varepsilon_{\mu'\mathbf{k}+\mathbf{q}}) - \Gamma^2}{(\omega + \varepsilon_{\mu\mathbf{k}} - \varepsilon_{\mu'\mathbf{k}+\mathbf{q}})^2 + \Gamma^2}. \tag{C.4}$$

We can see that the imaginary part of (C.2) gives the same result as the RTA form of $\mathrm{Im}\pi^0_\lambda(\omega)$, while the real part gives directly the nonadiabatic correction to the adiabatic phonon frequency. The superscript RTA is used here to distinguish Eq. (C.2) from Eq. (4.17).

Appendix D

Equation of motion for the two-particle propagator

The analytically continued equation for the exact phonon self-energy [Eq. (2.91)] can be expressed explicitly using the two-particle propagator $\mathcal{G}_{\mu\mu'}$ in the following way

$$\Pi_\lambda(\mathbf{q},\omega) = \sum_{\mu\mu'\mathbf{k}\sigma} \left[g_\lambda^{\mu\mu'}(\mathbf{k},\mathbf{q})\right]^* g_\lambda^{\mu\mu'}(\mathbf{k}_1,\mathbf{q})\mathcal{G}_{\mu\mu'}(\mathbf{k},\mathbf{k}_+,\mathbf{k}_1,\mathbf{k}_{1+},\omega), \tag{D.1}$$

where $\mathbf{k}_+$ and $\mathbf{k}_{1+}$ stand for $\mathbf{k}+\mathbf{q}$ and $\mathbf{k}_1+\mathbf{q}$, respectively. Here we gather all the relevant vertex correction contributions into $\mathcal{G}_{\mu\mu'}$, while in Eq. (2.91) they are in one of the vertex functions. Within the usual equation of motion approach for the propagators, it is custom to start with the time dependent form of $\mathcal{G}_{\mu\mu'}$

$$\begin{aligned}\mathcal{G}_{\mu\mu'}(\mathbf{k},\mathbf{k}_+,\mathbf{k}_1,\mathbf{k}_{1+},t) &= -i\theta(t)\left\langle\left[A_{\mathbf{kq}\sigma}^{\mu\mu'}(t), B_{\mathbf{k}_1\mathbf{q}\sigma}^{\mu\mu'}(0)\right]\right\rangle \\ &= \int_{-\infty}^{\infty}\frac{d\omega}{2\pi}e^{i\omega t-\eta t}\mathcal{G}_{\mu\mu'}(\mathbf{k},\mathbf{k}_+,\mathbf{k}_1,\mathbf{k}_{1+},\omega),\end{aligned} \tag{D.2}$$

where the Heisenberg operators are defined as

$$A_{\mathbf{kq}\sigma}^{\mu\mu'}(t) = c_{\mu\mathbf{k}\sigma}^\dagger(t)c_{\mu'\mathbf{k}+\mathbf{q}\sigma}(t) \tag{D.3}$$

and

$$B_{\mathbf{k}_1\mathbf{q}\sigma}^{\mu\mu'}(0) = c_{\mu'\mathbf{k}_1\sigma}^\dagger(0)c_{\mu\mathbf{k}_1+\mathbf{q}\sigma}(0), \tag{D.4}$$

with $c_{\mu\mathbf{k}\sigma}^\dagger(t)$ and $c_{\mu\mathbf{k}\sigma}(t)$ being the electron creation and annihilation operators, respectively. In our present analysis for an electron-phonon system with impurities,

the Hamiltonian can be written as

$$H = H_e + H_p + H_{ep} + H_{\text{imp}}, \tag{D.5}$$

where H_e and H_p are the usual adiabatic electron and phonon Hamiltonians, H_{ep} is the electron-phonon coupling given by Eq. (2.77), and

$$H_{\text{imp}} = \sum_{\mu\mathbf{k}\mathbf{k}_1\sigma} v_{\text{imp}}(\mathbf{k}-\mathbf{k}_1) c^\dagger_{\mu\mathbf{k}\sigma} c_{\mu\mathbf{k}_1\sigma} \tag{D.6}$$

represents the quasi-elastic single-electron scattering processes on the impurities, which are restricted to the intraband contributions only. We can write now the equation of motion as [10, 125]

$$\begin{aligned} &i\frac{\partial}{\partial t}\mathcal{G}_{\mu\mu'}(\mathbf{k},\mathbf{k}_+,\mathbf{k}_1,\mathbf{k}_{1+},t) = \delta(t)\delta_{\mathbf{k},\mathbf{k}_1}\left(f_{\mu\mathbf{k}} - f_{\mu'\mathbf{k}+\mathbf{q}}\right) \\ &-\left(\varepsilon_{\mu\mathbf{k}} - \varepsilon_{\mu'\mathbf{k}+\mathbf{q}}\right)\mathcal{G}_{\mu\mu'}(\mathbf{k},\mathbf{k}_+,\mathbf{k}_1,\mathbf{k}_{1+},t) - i\theta(t)\left\langle\left[\left[A^{\mu\mu'}_{\mathbf{k}\mathbf{q}\sigma}(t),H'\right],B^{\mu\mu'}_{\mathbf{k}_1\mathbf{q}\sigma}(0)\right]\right\rangle, \end{aligned} \tag{D.7}$$

where $H' = H_{ep} + H_{\text{imp}}$. In the present work we are mostly interested in the long-wavelength part of the phonon self-energy, thus $\mathbf{q} = 0$ should be used throughout in Eq. (D.7). Furthermore, we restrict our consideration to the intraband transitions ($\mu = \mu'$) for which the first and second terms are zero. After performing the Fourier transform of Eq. (D.7) we get

$$\begin{aligned} \omega\mathcal{G}_{\mu\mu}(\mathbf{k},\mathbf{k},\mathbf{k}_1,\mathbf{k}_1,\omega) &= -i\int_{-\infty}^{\infty} dt e^{-i\omega t}\theta(t)\left\langle\left[\left[A^{\mu\mu}_{\mathbf{k}\sigma}(t),H'\right],B^{\mu\mu}_{\mathbf{k}_1\sigma}(0)\right]\right\rangle \\ &\equiv \left\langle\left\langle\left[A^{\mu\mu}_{\mathbf{k}\sigma},H'\right];B^{\mu\mu}_{\mathbf{k}_1\sigma}\right\rangle\right\rangle_\omega. \end{aligned} \tag{D.8}$$

The next step is to use the equation of motion Eq. (D.7) but now for the propagator at the right hand side of Eq. (D.8). By doing this we can express Eq. (D.8) as

$$\begin{aligned} \omega\mathcal{G}_{\mu\mu}(\mathbf{k},\mathbf{k},\mathbf{k}_1,\mathbf{k}_1,\omega) &= \frac{1}{\omega}\left\langle\left\langle\left[A^{\mu\mu}_{\mathbf{k}\sigma},H'\right];B^{\mu\mu}_{\mathbf{k}_1\sigma}\right\rangle\right\rangle \\ &\quad -\frac{1}{\omega}\left\langle\left\langle\left[A^{\mu\mu}_{\mathbf{k}\sigma},H'\right];\left[B^{\mu\mu}_{\mathbf{k}_1\sigma},H'\right]\right\rangle\right\rangle_\omega, \end{aligned} \tag{D.9}$$

where the second term on the right hand side is the propagator part of the force-force correlation function [10, 129, 276],

$$\Phi_{\mu\mu}(\mathbf{k},\mathbf{k},\mathbf{k}_1,\mathbf{k}_1,\omega) = \left\langle\left\langle [A^{\mu\mu}_{\mathbf{k}\sigma}, H'] \,;\, \left[B^{\mu\mu}_{\mathbf{k}_1\sigma}, H'\right]\right\rangle\right\rangle_{\omega} \tag{D.10}$$

By taking the formal limit $\omega = 0$ we can express the two-particle propagator solely through the force-force correlation function

$$\mathcal{G}_{\mu\mu}(\mathbf{k},\mathbf{k},\mathbf{k}_1,\mathbf{k}_1,\omega) = -\frac{1}{\omega^2}\left[\Phi_{\mu\mu}(\mathbf{k},\mathbf{k},\mathbf{k}_1,\mathbf{k}_1,\omega) - \Phi_{\mu\mu}(\mathbf{k},\mathbf{k},\mathbf{k}_1,\mathbf{k}_1,0)\right]. \tag{D.11}$$

Finally, if we include Eq. (D.11) into Eq. (D.1) we get the force-force correlation function approach for obtaining the $\mathbf{q} \approx 0$ intraband phonon self-energy. The final equation is expressed in Eq. (4.37) using the Matsubara notation.

Appendix E

Potential energy fitting and localization procedures

The potential energy curves along the adiabatic reaction path are found to be accurately represented using one Morse function for each of the NH bonds in either the *cis* and *trans* conformations, smoothly connected by a sigmoid function centred at the transition state

$$\begin{aligned} V(q,U) &= D_{\mathrm{t}}\Big(1-e^{-a_{\mathrm{t}}(q-q_{\mathrm{t}})}\Big)^2\big(1-S(q)\big) + D_{\mathrm{c}}\Big(1-e^{-a_{\mathrm{c}}(q-q_{\mathrm{c}})}\Big)^2 S(q) \\ S(q) &= \Big(1+e^{-b_{\mathrm{TST}}(q-q_{\mathrm{TST}})}\Big)^{-1} \end{aligned} \tag{E.1}$$

For each potential bias, the parameters $\left\{D_{\{\mathrm{t,c}\}}, a_{\{\mathrm{t,c}\}}, b_{\mathrm{TST}}\right\}$ are fitted using the Levenberg-Marquardt algorithm as implemented in Gnuplot [371]. The remaining parameters are obtained from DFT analysis of the stationary points and kept frozen during the optimization.

The vibrational bound states of the reaction path Hamiltonian are first calculated using a basis of 400 discrete variable representation functions on the range $q \in [0.75, 2.1]$Å, where the kinetic part is approximated using the discrete variable representation form [372]. The eigenfunctions are then used to construct a matrix representation of approximate spatial projectors [373]. For this purpose, we use Gauss functions centered at the *trans* and *cis* conformers

$$G_{\{\mathrm{t,c}\}} = A_{\{\mathrm{t,c}\}} e^{-(q-q_{\{\mathrm{t,c}\}})^2/2\sigma^2_{\{\mathrm{t,c}\}}} \tag{E.2}$$

The parameters $\left\{A_{\{\mathrm{t,c}\}}, q_{\{\mathrm{t,c}\}}, \sigma_{\{\mathrm{t,c}\}}\right\}$ are defined from the ground state of the two Morse potentials used to fit the PEC. An appropriate localization operator is defined as $\hat{L} = G_{\mathrm{t}} - G_{\mathrm{c}}$, which yields a continuous spectrum between $[-1, 1]$ for functions

belonging to the *cis* and *trans* isomers, respectively. The individual matrix elements of the localization operator, $L_{IJ} = \langle I|G_{\mathrm{t}} - G_{\mathrm{c}}|J\rangle$, are weighted according to the inverse of their energy difference to ensure that the maximally localized functions retain their physical meaning. The width of the energy window is chosen such that the fundamental frequency in the *trans* well at zero-bias equals that of the harmonic analysis obtained from reference VASP calculations. Diagonalization of the matrix representation of the localization operator

$$\mathbf{L}\mathbf{U} = \mathbf{U}\lambda \tag{E.3}$$

yields a unitary transformation matrix $\mathbf{U}$, which is used to localize the vibrational eigenvectors according to

$$|i\rangle = \mathbf{U}^{\dagger}|I\rangle \tag{E.4}$$

The notations $|I\rangle$ and $|i\rangle$ are used here to differentiate between delocalized and localized states, respectively. The localized eigenfunctions $|i\rangle$ are used to compute the transition rates in Eq. (5.6) according to Eq. (5.3).

Appendix F

Vibrational projected density of states

In order to understand qualitatively the degree of coupling between the N-H stretch mode and all other modes within the porphycene molecule, we define the vibrational density of states projected on the H atom of the porphycene in the following way

$$\mathrm{VPDOS}(\omega) = \sum_{\alpha \neq \alpha'} \left| \sum_{\nu,k} e^{\nu,k}_{\alpha'}(q) P^{\nu,k}_{\mathrm{H}} e^{\nu,k}_{\alpha}(q) \right|^2 \delta(\omega - \omega^{(\alpha)}_{01}(q)), \tag{F.1}$$

where k runs over the cartesian coordinates, ν runs over all the atoms in molecule, α' denotes the N-H stretch mode, q is the reaction coordinate, $\hat{e}_\alpha$ are the eigenvectors of the normal mode α, and $\omega^{(\alpha)}_{01}$ are the associated frequencies. The latter two quantities are calculated, by means of DFT, at 3 points along the reaction path, namely the *trans*, transition state (TS), and *cis* configurations. The projector $P^{\nu,k}_{\mathrm{H}}$ is one when ν is equal to the H atom associated to the reaction mode, and zero otherwise.

To estimate the intermode coupling in the porphycene molecule for the given income energy ω, we integrate the PDOS as follows

$$\Lambda(\omega) = \int_0^\omega d\Omega \ \mathrm{PDOS}(\Omega). \tag{F.2}$$

In the case of an STM-induced reaction the upper integration limit is the applied bias voltage, i.e. $\omega = eU$, and the corresponding Λ is a qualitative measure of the intermode coupling.

In Fig. F.1 we show Eqs. (F.1) and (F.2) as a function of ω_{01} calculated at the *cis*, TS, and *trans* configurations. The obtained trend indicates that the intermode

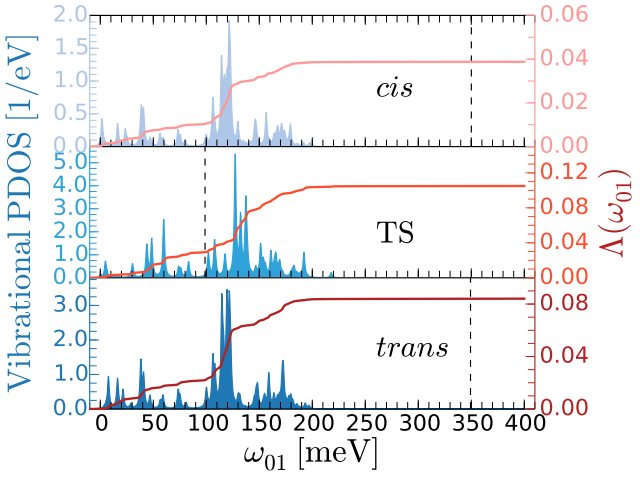

FIGURE F.1: Vibrational density of states projected on the H atom of the porphycene molecule for three points along the tautomerization coordinate: *cis*, TS, and *trans* configurations. The red curves show the corresponding integrated values. The vertical dashed lines represent the frequency of the H transfer mode.

coupling for the *cis* configuration is weaker than for the other two. A very similar trend is observed for the non-adiabatic vibrational lifetimes [see Fig. 5.12(b)].

Resumen

Tal y como abiertamente manifiesta su título, esta Tesis discute los aspectos fundamentales de la interacción entre partículas en movimiento (átomos y moléculas) y superficies metálicas, y proporciona un contribución teórica a este problema. Los esfuerzos hasta la fecha de otros autores por entender la naturaleza de los procesos subyacentes en esta interacción –el acoplamiento electrón-ion–, han dado lugar a un gran número de teorías y conceptos relevantes. A pesar de que estos trabajos se inciaron hace más de un siglo, vinculados al surgimiento de mecánica cuántica, todavía existen lagunas en la descripción de la interacción electrón-ion. Una de las razones es su carácter de muchos cuerpos, que ha empujado en el pasado a los investigadores a desarrollar teorías perturbativas y a aplicar diversas aproximaciones. Hoy en día los investigadores tenemos, afortunadamente, accesso a grandes recursos computacionales que nos permiten superar algunos obstáculos prácticos en estas líneas de investigación. La experimentación en este campo también ha experimentado avances que permiten extraer información muy precisa. Por ello, hemos tratado de entender dichos avances y utilizar los resultados experimentales para valorar la validez y la aplicabilidad de las consideraciones teóricas presentadas en esta Tesis.

Probablemente, la contribución estática a la interacción electrón-ion es la más conocida. Ésta se origina cuando los electrones siguen instantáneamente el movimiento de los iones (adiabaticidad) [1]. Puesto que su cálculo requiere menos recursos computacionales que la contribución dinámica, muchas investigaciones se fundamentan en ella (ver Capítulo 2). En realidad, en muchas ocasiones esta contribución adiabática, junto a aproximaciones adecuadas de la interacción electrón-electrón, basta para explicar las propiedades del estado fundamental de los sistemas. No obstante, algunos aspectos de la interacción electrón-ion, como los mecanismos de amortiguamiento (*damping*) de un ion en movimiento, se omiten al emplear la aproximación estática. Por ello es necesario añadir la contribución dinámica o no adiabática. Dicha contribución articula la presente Tesis, sirviendo como nexo entre los temas tratados en los distintos capítulos.

Históricamente, el estudio de la interacción electrón-ion se asoció a sistemas

periódicos extendidos, en los que el problema de los electrones interactuando con ondas de distorsiones elásticas de la red (fonones) fue abordado por primera vez [2–7]. En estos trabajos se reflejaba la ambición de los autores por construir una teoría general de transporte de electrones en un potencial iónico periódico. En otras palabras, trataban de describir el comportamiento dinámico de los electrones de un sistema metálico incluyendo una probabilidad de intercambio de energía y momento con los fonones. Estos trabajos desembocaron en el desarrollo de ideas innovadoras y teorías que explicaban observaciones experimentales sobre superconductividad mediada por fonones, dependencia en la temperatura de la resistividad absorción óptica, etc. [8]. Estos fenómenos y sus teorías correspondientes enfatizan la "cara electrónica" de la interacción electrón-fonón. Sin embargo, el foco de esta Tesis es el otro aspecto: la influencia de la interacción electrón-fonón en los fonones. Por suerte, la teoría perturbativa desarrollada en el contexto del transporte electrónico [7, 9, 10] puede ser igualmente aplicada al estudio de los efectos no adiabáticos en fonones [11, 12]. De hecho, consigue explicar con éxito experimentos de difracción de helio [13, 14] y espectroscopía Raman infrarroja [15, 16]. Otro ejemplo interesante es la teoría acuñada para explicar la pérdida de energía durante la penetración de iones en metales [17, 18], por ejemplo cuando un átomo de hidrógeno colisiona con la pared interna de un reactor termonuclear [19]. Las ecuaciones de *stopping power* adoptadas ahí habían sido desarrolladas inicialmente en el contexto de la teoría de respuesta lineal (y posteriormente no lineal) para una impureza en movimiento en un gas de electrones. Es remarcable que estas ecuaciones guardan similitudes con los *damping rates* obtenidos mediante teoría de transporte[1].

Hasta cierto punto, las metodologías desarrolladas en esta Tesis importan algunas de esas ideas previas para explicar problemas particulares de interacción de átomos y moléculas con superficies metálicas. Este es un campo de investigación activo debido a su relación con diversos procesos industriales, por ejemplo, la catálisis heterogénea, donde la presencia de la superficie puede disminuir la barrera de energía de las reacciones químicas. El intercambio de energía entre el adsorbato en movimiento y los electrones de la superficie es un factor decisivo en algunas reacciones. Las primeras evidencias experimentales relacionadas se encuentran en las medidas de vidas medias (*lifetimes*) de la excitación vibracional de moléculas adsorbidas en metales, obtenidas mediante espectroscopía de absorción infrarroja (IRAS) o técnicas *pump-probe* [16, 20–22]. Estos estudios muestran que la vida media de un modo vibracional de alta frecuencia del adsorbato sobre un metal es menor que cuando se encuentra depositado sobre un aislante. Otros experimentos de adsorción y dispersión en superficies reportan evidencias similares de fenónomenos no adiabáticos

[1]Esta similitud, junto a la analogía entre los *damping rates* para fonones y los obtenidos en teoría de transporte es reminiscente de la tercera ley de Newton.

[23–27]. En estos ejemplos puede observarse también el proceso inverso, es decir, la interacción electrón-ion puede inducir una vibración, e incluso provocar la ruptura de enlaces moleculares. Este tipo de manipulación puede conseguirse mediante, por ejemplo, microscopía de efecto túnel (STM) y pulsos de luz láser [28–32]. Todavía quedan puntos en este ámbito que requieren clarificación teórica, y esta Tesis trata de darla.

Nuestra contribución a la literatura comienza en el Capítulo 3, donde estudiamos la dinámica de adsorción de H, N, y N_2 hipertérmicos sobre superficies de Pd(100), Ag(111), y Fe(110), respectivamente. En particular, estudiamos los dos mecanismos responsables de la pérdida de energía durante estos procesos: el movimiento de átomos de la superficie y la excitación de pares electrón-hueco de baja energía, es decir, efectos no adiabáticos. El objetivo principal es entender el paper de cada unos de estos mecanismos en tres escenarios diferentes, bien ejemplificados por estos sistemas, complementando los hallazgos experimentales existentes. Entre ellos, las Refs. [25, 26] son specialmente interesantes, ya que observan que la intensidad de corriente generada durante la adsorción de varias especies sobre metales escala con la energía de adsorción. Aquí empleamos como herramienta teórica la dinámica molecular *ab initio* con fricción electrónica (AIMDEF) [33], donde las fuerzas ejercidas sobre los átomos se calculan en cada paso de la simulación mediante teoría del funcional de la densidad (DFT), mientras que un término de fricción da cuenta de las excitaciones electrónicas. El coeficiente de fricción necesario se calcula a partir de la expresión de *stopping power* dentro de la teoría de respuesta no lineal anteriormente mencionada para una impureza en movimiento dentro de un gas de electrones libres (FEG). Así, el coeficiente de fricción varía con la densidad del FEG, y en AIMDEF es reemplazado por la densidad de carga en la posición de la impureza obtenida por DFT [34]. En el primer trabajo con AIMDEF, donde se observa que el mecanismo de excitación de pares electrón-hueco domina la pérdida de energía de átomos de H hipertérmicos sobre Pd(100), la densidad de carga se determina a partir de un cálculo para la superficie de Pd(100) rígida [33]. Esta aproximación puede dar lugar a errores cuando proyectiles más pesados, como N y N_2, inciden en la superficie, ya que producen distorsiones mucho mayores de la red. Por ello, aquí proponemos y exploramos sistemáticamente otros modelos para la densidad de carga que dan cuenta del efecto del desplazamiento de los átomos de la superficie. El modelo más robusto, que se basa en una partición de carga de tipo Hirshfeld, convierte a AIMDEF en una herramienta teórica eficiente que trata los dos canales de pérdida por igual, y puede ser empleada en el estudio de gran variedad de sistemas.

En el Capítulo 4 exploramos los efectos que la relajación electrónica tiene sobre la vibración de moléculas adsorbidas. Al contrario que en el Capítulo 3, donde investigamos adsorbatos aislados, aquí estudiamos el movimiento colectivo de una capa

extendida y ordenada de moléculas, por lo que la interacción general electrón-ion se manifiesta como interacción electrón-fonón. En este capítulo empleamos la teoría de perturbaciones de muchos cuerpos basada en DFT. Los fundamentos de esta teoría, como explicamos más arriba, se establecieron hace muchas décadas, pero siguen vigentes hoy en día y proporcionan predicciones cuantitativas útiles cuando se combinan con cálculos DFT. Para comenzar, nosotros utilizamos estas teorías en primer orden de aproximación, es decir, la fórmula que obtenemos para el *damping* del fonón de nuestro interés es cuadrático en el término de acoplamiento electrón-fonón [36–40]. Encontramos que es necesario incluir efectos de orden más alto (procesos de relajación electrónica), ya que la fórmula de primer orden no explica satisfactoriamente las vidas medias experimentales para fonones de alta frecuencia de la capa molecular. Cabe mencionar que los primeros cálculos reportados de vidas medias para moléculas diatómicas sobre metales parecían estar en buen acuerdo con los experimentos, a pesar de emplear fórmulas de primer orden [36, 37]. Sin embargo, simulaciones más precisas basadas en DFT muestran discrepancias y apuntan a que otras contribuciones deben ser incluidas [40]. Para incorporar los procesos de relajación electrónica, primero hacemos un tratamiento fenomenológico consistente en introducir un parámetro en la expresión de la vida media que dé cuenta de esos procesos. Además, calculamos explícitamente el término de segundo orden [9, 11, 41], donde el fonón estudiado excita electrones, los cuales posteriormente son inelásticamente dispersados por otros fonones o por impurezas. El primero de estos procesos de dispersión corresponde al acoplamiento indirecto fonón-fonón mediado por excitaciones electrónicas, que debe ser distinguido de los procesos anarmónicos usuales. Este proceso indirecto introduce una dependencia de la temperatura en la fórmula de la vida media, por lo que puede resultar importante a la hora de explicar algunas observaciones experimentales[42]. Nuestro caso de estudio es CO sobre Cu(100). Esta elección de sistema está en parte motivada por la cantidad de información existente sobre él [16, 20–22]. El consenso general establece que la vida media es de alrededor de 2 ps, unas cinco veces menor que el obtenido en simulaciones basadas en DFT [40]. Uno de los experimentos incluso encuentra una pequeña dependencia en la temperatura [22] que puede provenir de acoplamientos anarmónicos directos o acoplamientos fonón-fonón indirectos mediados por excitaciones electrónicas. Estos y otros detalles relevantes de la interacción electrón-fonón en sistemas adsorbato-superficie se discuten en el Capítulo 4.

Finalmente, en el Capítulo 5 examinamos la manipulación de una molécula aislada sobre un metal mediante corrientes inelásticas inducidas por STM [30], que constuyen otra interesante manifestación de la interacción dinámica electrón-ion. Desde los primeros experimentos en los que se consiguió disociar [28] y rotar [29] moléculas individualmente, se han intentado inducir otras reacciones de forma similar. Uno de dichos ejemplos, que ofrece amplias perspectivas de aplicación tecnológica,

es la reacción de tautomerización o transferencia intramolecular de un átomo de hidrógeno [43–46]. Esta recolocación atómica puede alterar significativamente las propiedades de la molécula, modificando por ejemplo su conductividad. Esta característica puede ser explotada en los nanodispositivos electrónicos conocidos como "interruptores moleculares" [47]. El caso particular que estudiamos en esta Tesis es la recientemente conseguida tautomerización *trans* $\leftrightarrow$ *cis* de porphyceno adsorbido sobre Cu(111) [43]. Se piensa que el mecanismo que activa esta reacción es el acoplamiento no adiabático entre los electrones inelásticos inyectados por STM y los modos vibracionales de la molécula de porphyceno. Además, dado que la energía del modo asociado a la reacción (elongación del enlace interno N-H) es casi el doble que el voltaje umbral necesario para que se dé la reacción, cabe esperar que la excitación de los otros modos vibracionales del esqueleto de la molécula participen indirectamente en la activación de la reacción. Esto es, el acoplamiento entre modos tiene un papel decisivo. Por un lado, la mayor parte de modelos presentados en la literatura para describir este tipo de reacciones se fundamentan en la aproximación armónica [48, 49] y por tanto no son aplicables a nuestro caso, donde la reacción de transferencia del H implica grandes desplazamientos atómicos. Por otro lado, las teorías anarmónicas de la literatura no sirven para abordar de manera eficiente el caso del porphyceno [50, 51], ya que son muchos los grados de libertad moleculares implicados en la reacción. Por tanto, nuestro principal objetivo es introducir un modelo teórico que resuelva esas limitaciones manteniendo a la vez un coste computacional reducido. En dicho modelo incorporamos efectivamente el acoplamiento electrón-vibración y la transferencia energética inter-modos a través de una deformación de la energía potencial a lo largo de la coordenada de reacción. De esta manera, la compleja reacción de tautomerización se mapea efectivamente en un problema unidimensional más sencillo. Todos los ingredientes de nuestro modelo, como el análisis de modos vibracionales, las densidades de carga y las barreras de reacción, se calculan mediante DFT. Dado el carácter van der Waals (vdW) de la interacción porphyceno-cobre, es necesario elegir un funcional para estos cálculos que la describa correctamente [52]. Por ello, realizamos un análisis adicional para determinar al detalle la energética de la adsorción y la estructura electrónica de la interfase, y cómo estas propiedades dependen del funcional utilizado en el cálculo.

List of publications

Publications discussed in this Thesis:

- *Ab initio molecular dynamics with simultaneous electron and phonon excitations: Application to the relaxation of hot atoms and molecules on metal surfaces*. D. Novko, M. Blanco-Rey, J. I. Juaristi, and M. Alducin. Phys. Rev. B **92**, 201411(R) (2015).

- *Surface electron density models for accurate ab initio molecular dynamics with electronic friction*. D. Novko, M. Blanco-Rey, M. Alducin, and J. I. Juaristi. Phys. Rev. B **93**, 245435 (2016).

- *Energy loss in gas-surface dynamics: Electron-hole pair and phonon excitation upon adsorbate relaxation*. D. Novko, M. Blanco-Rey, J. Juaristi, and M. Alducin. Nucl. Instrum. Methods Phys. Res., Sect. B **382**, 26 (2016).

- *Effects of electronic relaxation processes on vibrational linewidths of adsorbates on surfaces: The case of CO/Cu(100)*. D. Novko, M. Alducin, M. Blanco-Rey, and J. I. Juaristi. Phys. Rev. B **94**, 224306 (2016).

- *On the tautomerisation of porphycene on copper (111): Finding the subtle balance between van der Waals interactions and hybridisation*. D. Novko, J. C. Tremblay, and M. Blanco-Rey. J. Chem. Phys. **145**, 244701 (2016).

- *Intermode coupling drives the irreversible tautomerization in porphycene on copper(111) induced by scanning tunnelling microscopy*. D. Novko, M. Blanco-Rey, and J. C. Tremblay. submitted (2017).

Other publications:

- *Two-dimensional and π plasmon spectra in pristine and doped graphene*. V. Despoja, D. Novko, K. Dekanić, M. Šunjić, and L. Marušić. Phys. Rev. B **87**, 075447 (2013).

- *Changing character of electronic transitions in graphene: From single-particle excitations to plasmons*. D. Novko, V. Despoja, and M. Šunjić. Phys. Rev. B **91**, 195407 (2015).
- *Optical absorption and conductivity in quasi-two-dimensional crystals from first principles: Application to graphene*. D. Novko, M. Šunjić, and V. Despoja. Phys. Rev. B **93**, 125413 (2016).

Bibliography

[1] M. Born and R. Oppenheimer. Zur Quantentheorie der Molekeln. *Ann. Phys.*, 389:457, 1927. (Cited on pages 1, 10, and 181).

[2] F. Bloch. Über die Quantenmechanik der Elektronen in Kristallgittern. *Z. Phys.*, 52:555, 1929. (Cited on pages 2, 19, and 182).

[3] A. B. Migdal. Application of Quantum Field Theory Methods to the Many Body Problem. *JETP*, 7:996, 1958. (Cited on pages 2, 38, and 182).

[4] V. M. Galitskii and A. B. Migdal. Interaction between Electrons and Lattice Vibrations in a Normal Metal. *JETP*, 7:96, 1958. (Cited on pages 2 and 182).

[5] G. Baym. Field-theoretic approach to the properties of the solid state. *Ann. Phys.*, 14:1, 1961. (Cited on pages 2 and 182).

[6] S. Engelsberg and J. R. Schrieffer. Coupled Electron-Phonon System. *Phys. Rev.*, 131:993, 1963. (Cited on pages 2, 32, 36, 82, 87, and 182).

[7] T. Holstein. Theory of transport phenomena in an electron-phonon gas. *Ann. Phys.*, 29:410, 1964. (Cited on pages 2, 104, and 182).

[8] F. Giustino. Electron-phonon interactions from first principles. *arXiv:1603.06965*, 2016. (Cited on pages 2, 32, 36, 37, 38, 39, 40, 41, 87, 89, 95, 106, and 182).

[9] P. B. Allen. Electron-Phonon Effects in the Infrared Properties of Metals. *Phys. Rev. B*, 3:305, 1971. (Cited on pages 2, 5, 41, 83, 90, 98, 101, 104, 182, and 184).

[10] W. Götze and P. Wölfle. Homogeneous Dynamical Conductivity of Simple Metals. *Phys. Rev. B*, 6:1226, 1972. (Cited on pages 2, 83, 99, 104, 174, and 182).

[11] F. Marsiglio, R. Akis, and J. P. Carbotte. Phonon self-energy effects due to superconductivity: A real-axis formulation. *Phys. Rev. B*, 45:9865, 1992. (Cited on pages 2, 5, 82, 83, 100, 113, 117, 182, and 184).

[12] E.G Maksimov and S.V Shulga. Nonadiabatic effects in optical phonon self-energy. *Solid State Commun.*, 97:553, 1996. (Cited on pages 2, 36, 82, 83, 98, 100, 113, 117, 124, and 182).

[13] G. Benedek and J. P. Toennies. Helium atom scattering spectroscopy of surface phonons: genesis and achievements. *Surf. Sci.*, 299300:587, 1994. (Cited on pages 2 and 182).

[14] G. Benedek, M. Bernasconi, K.-P. Bohnen, D. Campi, E. V. Chulkov, P. M. Echenique, R. Heid, I. Yu. Sklyadneva, and J. P. Toennies. Unveiling mode-selected electron-phonon interactions in metal films by helium atom scattering. *Phys. Chem. Chem. Phys.*, 16:7159, 2014. (Cited on pages 2 and 182).

[15] J. A. Creighton. *Raman Spectroscopy of Adsorbates at Metal Surfaces*, page 145. Springer Berlin Heidelberg, Berlin, Heidelberg, 1980. (Cited on pages 2 and 182).

[16] H. Ueba. Vibrational relaxation and pump-probe spectroscopies of adsorbates on solid surfaces. *Prog. Surf. Sci.*, 55:115, 1997. (Cited on pages 2, 3, 5, 82, 84, 108, 110, 118, 119, 120, 121, 122, 182, and 184).

[17] T. L. Ferrell and R. H. Ritchie. Energy losses by slow ions and atoms to electronic excitation in solids. *Phys. Rev. B*, 16:115, 1977. (Cited on pages 2, 26, 29, 30, 31, and 182).

[18] P M Echenique, R M Nieminen, and R H Ritchie. Density functional calculation of stopping power of an electron gas for slow ions. *Solid State Commun.*, 37:779, 1981. (Cited on pages 2, 26, 31, 53, and 182).

[19] J.T. Hogan and J.F. Clarke. Fluxes of charged and neutral particles from tokamaks. *J. Nucl. Mater.*, 53:1, 1974. (Cited on pages 2 and 182).

[20] R. Ryberg. Vibrational line shape of chemisorbed CO. *Phys. Rev. B*, 32:2671, 1985. (Cited on pages 3, 5, 84, 85, 107, 110, 116, 119, 126, 182, and 184).

[21] M. Morin, N. J. Levinos, and A. L. Harris. Vibrational energy transfer of CO/Cu(100): Nonadiabatic vibration/electron coupling. *J. Chem. Phys.*, 96: 3950, 1992. (Cited on pages 3, 5, 82, 85, 107, 110, 119, 120, 182, and 184).

[22] T. A. Germer, J. C. Stephenson, E. J. Heilweil, and R. R. Cavanagh. Picosecond timeresolved adsorbate response to substrate heating: Spectroscopy and dynamics of CO/Cu(100). *J. Chem. Phys.*, 101:1704, 1994. (Cited on pages 3, 5, 85, 110, 115, 118, 182, and 184).

[23] C. T. Rettner, F. Fabre, J. Kimman, and D. J. Auerbach. Observation of Direct Vibrational Excitation in Gas-Surface Collisions: NO on Ag(111). *Phys. Rev. Lett.*, 55:1904, 1985. (Cited on pages 3 and 183).

[24] Y. Huang, C. T. Rettner, D. J. Auerbach, and A. M. Wodtke. Vibrational Promotion of Electron Transfer. *Science*, 290:111, 2000. (Cited on pages 3, 82, and 183).

[25] H. Nienhaus, H.S. Bergh, B. Gergen, A. Majumdar, W.H. Weinberg, and E.W. McFarland. Direct detection of electronhole pairs generated by chemical reactions on metal surfaces. *Surf. Sci.*, 445:335, 2000. (Cited on pages 3, 82, and 183).

[26] B Gergen, H Nienhaus, W H Weinberg, and E W McFarland. Chemically Induced Electronic Excitations at Metal Surfaces. *Science*, 294:2521, 2001. (Cited on pages 3, 47, 48, 49, 73, 82, and 183).

[27] J. D. White, J. Chen, D. Matsiev, D. J. Auerbach, and A. M. Wodtke. Conversion of large-amplitude vibration to electron excitation at a metal surface. *Nature*, 433:503, 2005. (Cited on pages 3, 82, and 183).

[28] B. C. Stipe, M. A. Rezaei, W. Ho, S. Gao, M. Persson, and B. I. Lundqvist. Single-Molecule Dissociation by Tunneling Electrons. *Phys. Rev. Lett.*, 78: 4410, 1997. (Cited on pages 3, 6, 49, 127, 128, 183, and 184).

[29] B. C. Stipe, M. A. Rezaei, and W. Ho. Coupling of Vibrational Excitation to the Rotational Motion of a Single Adsorbed Molecule. *Phys. Rev. Lett.*, 81: 1263, 1998. (Cited on pages 3, 6, 127, 128, 183, and 184).

[30] N Lorente, R Rurali, and H Tang. Single-molecule manipulation and chemistry with the STM. *J. Phys.: Condens. Matter*, 17:S1049, 2005. (Cited on pages 3, 5, 127, 183, and 184).

[31] H. Guo, P. Saalfrank, and T. Seideman. Theory of photoinduced surface reactions of admolecules. *Prog. Surf. Sci.*, 62:239, 1999. (Cited on pages 3, 127, 128, and 183).

[32] W. R. Browne and B. L. Feringa. Light Switching of Molecules on Surfaces. *Annu. Rev. Phys. Chem.*, 60:407, 2009. (Cited on pages 3, 127, 128, and 183).

[33] M Blanco-Rey, J I Juaristi, R Díez Muiño, H F Busnengo, G J Kroes, and M Alducin. Electronic Friction Dominates Hydrogen Hot-Atom Relaxation on Pd(100). *Phys. Rev. Lett.*, 112:103203, 2014. (Cited on pages 4, 31, 47, 48, 49, 50, 51, 53, 54, 55, 70, 74, 76, 82, and 183).

[34] J I Juaristi, M Alducin, R Díez Muiño, H F Busnengo, and A Salin. Role of Electron-Hole Pair Excitations in the Dissociative Adsorption of Diatomic Molecules on Metal Surfaces. *Phys. Rev. Lett.*, 100:116102, 2008. (Cited on pages 4, 31, 48, 49, 53, 82, and 183).

[35] F L Hirshfeld. Bonded-atom fragments for describing molecular charge densities. *Theoret. Chim. Acta*, 44:129, 1977. (Cited on pages 4 and 55).

[36] B.N.J. Persson and M. Persson. Vibrational lifetime for CO adsorbed on Cu(100). *Solid State Commun.*, 36:175, 1980. (Cited on pages 5, 82, 85, and 184).

[37] B Hellsing and M Persson. Electronic Damping of Atomic and Molecular Vibrations at Metal Surfaces. *Phys. Scr.*, 29:360, 1984. (Cited on pages 5, 26, 31, 54, 82, 85, 97, 133, and 184).

[38] V. Krishna and J. C. Tully. Vibrational lifetimes of molecular adsorbates on metal surfaces. *J. Chem. Phys.*, 125:054706, 2006. (Cited on pages 5, 82, 83, 85, 97, and 184).

[39] M. Forsblom and M. Persson. Vibrational lifetimes of cyanide and carbon monoxide on noble and transition metal surfaces. *J. Chem. Phys.*, 127, 2007. (Cited on pages 5, 82, 83, 85, 97, and 184).

[40] R. J. Maurer, M. Askerka, V. S. Batista, and J. C. Tully. *ab initio* tensorial electronic friction for molecules on metal surfaces: nonadiabatic vibrational relaxation. *Phys. Rev. B*, 94:115432, 2016. (Cited on pages 5, 82, 85, and 184).

[41] I. Kupčić. General theory of intraband relaxation processes in heavily doped graphene. *Phys. Rev. B*, 91:205428, 2015. (Cited on pages 5, 83, 84, 87, 90, 101, 104, and 184).

[42] E. Cappelluti. Electron-phonon effects on the Raman spectrum in MgB_2. *Phys. Rev. B*, 73:140505, 2006. (Cited on pages 5, 83, 100, 113, 117, 124, and 184).

[43] J N Ladenthin, L Grill, S Gawinkowski, S Liu, J Waluk, and T Kumagai. Hot Carrier-Induced Tautomerization within a Single Porphycene Molecule on Cu(111). *ACS Nano*, 9:7287, 2015. (Cited on pages 6, 128, 129, 132, 134, 136, 137, 139, 146, 148, 149, 153, 157, and 185).

[44] T Kumagai, F Hanke, S Gawinkowski, J Sharp, K Kotsis, J Waluk, M Persson, and L Grill. Thermally and Vibrationally Induced Tautomerization of Single Porphycene Molecules on a Cu(110) Surface. *Phys. Rev. Lett.*, 111:246101, 2013. (Cited on pages 6, 128, 129, and 185).

[45] T Kumagai, F Hanke, S Gawinkowski, J Sharp, K Kotsis, J Waluk, M Persson, and L Grill. Controlling intramolecular hydrogen transfer in a porphycene molecule with single atoms or molecules located nearby. *Nat. Chem.*, 6:41, 2014. (Cited on pages 6, 128, 138, and 185).

[46] J N Ladenthin, T Frederiksen, M Persson, J C Sharp, S Gawinkowski, J Waluk, and T Kumagai. Force-induced tautomerization in a single molecule. *Nat. Chem.*, 8:935, 2016. (Cited on pages 6, 128, and 185).

[47] L Antonov, editor. *Tautomerism: Methods and Theories*. Wiley-VCH Verlag GmbH & Co. KGaA, 2013. (Cited on pages 6, 128, and 185).

[48] S. Gao, M. Persson, and B. I. Lundqvist. Theory of atom transfer with a scanning tunneling microscope. *Phys. Rev. B*, 55:4825, 1997. (Cited on pages 6, 128, and 185).

[49] N. Lorente and M. Persson. Theoretical aspects of tunneling-current-induced bond excitation and breaking at surfaces. *Faraday Discuss.*, 117:277, 2000. (Cited on pages 6, 82, 83, 85, 97, 107, 128, and 185).

[50] B. N. J. Persson and H. Ueba. Theory of inelastic tunneling induced motion of adsorbates on metal surfaces. *Surf. Sci.*, 502503:18, 2002. (Cited on pages 7, 83, 100, 104, 124, 128, and 185).

[51] J. C. Tremblay. A unifying model for non-adiabatic coupling at metallic surfaces beyond the local harmonic approximation: From vibrational relaxation to scanning tunneling microscopy. *J. Chem. Phys.*, 138:244106, 2013. (Cited on pages 7, 46, 82, 128, 133, and 185).

[52] J. Klimeś and A. Michaelides. Perspective: Advances and challenges in treating van der Waals dispersion forces in density functional theory. *J. Chem. Phys.*, 137:120901, 2012. (Cited on pages 7, 18, 19, 130, and 185).

[53] E. Schrödinger. Quantisierung als Eigenwertproblem. *Ann. Phys.*, 384:361, 1926. (Cited on page 9).

[54] E. G. Brovman and Yu. Kagan. The phonon spectrum of metals. *JETP*, 25: 365, 1967. (Cited on pages 11, 37, 89, and 122).

[55] B. T. Geilikman. The adiabatic approximation and Fröhlich model in the theory of metals. *J. Low Temp. Phys.*, 4:189, 1971. (Cited on pages 11, 37, and 89).

[56] G. Grimvall. *The Electron-Phonon Interaction in Metals*. North-Holland, Amsterdam, New York, Oxford, 1981. (Cited on pages 11, 32, 36, 37, 89, and 95).

[57] P. Hohenberg and W. Kohn. Inhomogeneous Electron Gas. *Phys. Rev.*, 136: B864, 1964. (Cited on pages 12 and 14).

[58] W. Kohn. Nobel Lecture: Electronic structure of matter¯wave functions and density functionals. *Rev. Mod. Phys.*, 71:1253, 1999. (Cited on pages 12, 14, 16, and 17).

[59] J. C. Slater. Note on Hartree's Method. *Phys. Rev.*, 35:210, 1930. (Cited on page 12).

[60] L. H. Thomas. The calculation of atomic fields. *Mathematical Proceedings of the Cambridge Philosophical Society*, 23:542, 1927. (Cited on page 14).

[61] E. Fermi. Un metodo statistico per la determinazione di alcune priopriet dellatomo. *Rend. Accad. Naz. Lincei*, 6:602, 1927. (Cited on page 14).

[62] M. Levy. Electron densities in search of Hamiltonians. *Phys. Rev. A*, 26:1200, 1982. (Cited on page 14).

[63] W. Kohn and L. J. Sham. Self-Consistent Equations Including Exchange and Correlation Effects. *Phys. Rev.*, 140:A1133, 1965. (Cited on pages 14, 16, and 17).

[64] P. A. M. Dirac. Note on Exchange Phenomena in the Thomas Atom. *Mathematical Proceedings of the Cambridge Philosophical Society*, 26:376, 1930. (Cited on page 16).

[65] D. M. Ceperley and B. J. Alder. Ground State of the Electron Gas by a Stochastic Method. *Phys. Rev. Lett.*, 45:566, 1980. (Cited on page 16).

[66] J. P. Perdew and A. Zunger. Self-interaction correction to density-functional approximations for many-electron systems. *Phys. Rev. B*, 23:5048, 1981. (Cited on pages 16 and 106).

[67] D. C. Langreth and M. J. Mehl. Beyond the local-density approximation in calculations of ground-state electronic properties. *Phys. Rev. B*, 28:1809, 1983. (Cited on page 17).

[68] A. D. Becke. Density-functional exchange-energy approximation with correct asymptotic behavior. *Phys. Rev. A*, 38:3098, 1988. (Cited on pages 17 and 142).

[69] J P Perdew and Y Wang. Accurate and simple density functional for the electronic exchange energy: Generalized gradient approximation. *Phys. Rev. B*, 33:8800(R), 1986. (Cited on pages 17 and 141).

[70] J P Perdew, J A Chevary, S H Vosko, K A Jackson, M R Pederson, D J Singh, and C Fiolhais. Atoms, molecules, solids, and surfaces: Applications of the generalized gradient approximation for exchange and correlation. *Phys. Rev. B*, 46:6671, 1992. (Cited on pages 17 and 50).

[71] J. P. Perdew, K. Burke, and M. Ernzerhof. Generalized Gradient Approximation Made Simple. *Phys. Rev. Lett.*, 77:3865, 1996. (Cited on pages 17 and 106).

[72] E H Lieb and S Oxford. Improved lower bound on the indirect Coulomb energy. *Int. J. Quantum Chem.*, 19:427, 1981. (Cited on pages 17 and 142).

[73] Y. Zhang and W. Yang. Comment on "Generalized Gradient Approximation Made Simple". *Phys. Rev. Lett.*, 80:890, 1998. (Cited on pages 17 and 106).

[74] B Hammer, L B Hansen, and J K Nørskov. Improved adsorption energetics within density-functional theory using revised Perdew-Burke-Ernzerhof functionals. *Phys. Rev. B*, 59:7413, 1999. (Cited on pages 17, 50, and 142).

[75] H. Rydberg, B. I. Lundqvist, D. C. Langreth, and M. Dion. Tractable nonlocal correlation density functionals for flat surfaces and slabs. *Phys. Rev. B*, 62:6997, 2000. (Cited on page 18).

[76] M. Dion, H. Rydberg, E. Schröder, D. C. Langreth, and B. I. Lundqvist. Van der Waals Density Functional for General Geometries. *Phys. Rev. Lett.*, 92: 246401, 2004. (Cited on pages 18, 123, and 135).

[77] D. C. Langreth, M. Dion, H. Rydberg, E. Schrder, P. Hyldgaard, and B. I. Lundqvist. Van der Waals density functional theory with applications. *Int. J. Quantum Chem.*, 101:599, 2005. (Cited on page 18).

[78] K Berland, V R Cooper, K Lee, E Schröder, T Thonhauser, P Hyldgaard, and B I Lundqvist. van der Waals forces in density functional theory: a review of the vdW-DF method. *Rep. Prog. Phys.*, 78:066501, 2015. (Cited on pages 18, 135, and 142).

[79] G. Román-Pérez and J. M. Soler. Efficient Implementation of a van der Waals Density Functional: Application to Double-Wall Carbon Nanotubes. *Phys. Rev. Lett.*, 103:096102, 2009. (Cited on page 18).

[80] A. Gulans, M. J. Puska, and R. M. Nieminen. Linear-scaling self-consistent implementation of the van der Waals density functional. *Phys. Rev. B*, 79: 201105, 2009. (Cited on pages 18, 123, 135, and 150).

[81] J. Klimeš, D. R. Bowler, and A. Michaelides. Chemical accuracy for the van der Waals density functional. *J. Phys.: Condens. Matter*, 22:022201, 2010. (Cited on pages 18, 135, and 158).

[82] J Klimeš, D R Bowler, and A Michaelides. Van der Waals density functionals applied to solids. *Phys. Rev. B*, 83:195131, 2011. (Cited on pages 18, 135, and 142).

[83] K Berland and P Hyldgaard. Exchange functional that tests the robustness of the plasmon description of the van der Waals density functional. *Phys. Rev. B*, 89:035412, 2014. (Cited on pages 18 and 135).

[84] I Hamada. van der Waals density functional made accurate. *Phys. Rev. B*, 89: 121103(R), 2014. (Cited on pages 18 and 135).

[85] P Jurečka, J Šponer, J Černy, and P Hobza. Benchmark database of accurate (MP2 and CCSD(T) complete basis set limit) interaction energies of small model complexes, DNA base pairs, and amino acid pairs. *Phys. Chem. Chem. Phys.*, 8:1985, 2006. (Cited on pages 18, 135, and 142).

[86] S. Grimme. Semiempirical GGA-type density functional constructed with a long-range dispersion correction. *J. Comput. Chem.*, 27:1787, 2006. (Cited on page 18).

[87] A. Tkatchenko and M. Scheffler. Accurate Molecular Van Der Waals Interactions from Ground-State Electron Density and Free-Atom Reference Data. *Phys. Rev. Lett.*, 102:073005, 2009. (Cited on pages 19 and 135).

[88] S. Grimme, J. Antony, S. Ehrlich, and H. Krieg. A consistent and accurate ab initio parametrization of density functional dispersion correction (DFT-D) for the 94 elements H-Pu. *J. Chem. Phys.*, 132:154104, 2010. (Cited on pages 19 and 135).

[89] V. G. Ruiz, W. Liu, E. Zojer, M. Scheffler, and A. Tkatchenko. Density-Functional Theory with Screened van der Waals Interactions for the Modeling of Hybrid Inorganic-Organic Systems. *Phys. Rev. Lett.*, 108:146103, 2012. (Cited on pages 19 and 135).

[90] A. Tkatchenko, R. A. DiStasio, R. Car, and M. Scheffler. Accurate and Efficient Method for Many-Body van der Waals Interactions. *Phys. Rev. Lett.*, 108:236402, 2012. (Cited on pages 19 and 135).

[91] S. Grimme, S. Ehrlich, and L. Goerigk. Effect of the damping function in dispersion corrected density functional theory. *J. Comput. Chem.*, 32:1456, 2011. (Cited on page 19).

[92] W Liu, F Maass, M Willenbockel, C Bronner, M Schulze, S Soubatch, F S Tautz, P Tegeder, and A Tkatchenko. Quantitative Prediction of Molecular Adsorption: Structure and Binding of Benzene on Coinage Metals. *Phys. Rev. Lett.*, 115:036104, 2015. (Cited on pages 19 and 144).

[93] R J Maurer, V G Ruiz, and A Tkatchenko. Many-body dispersion effects in the binding of adsorbates on metal surfaces. *J. Chem. Phys.*, 143:102808, 2015. (Cited on pages 19 and 135).

[94] R J Maurer, W Liu, I Poltavsky, T Stecher, H Oberhofer, K Reuter, and A Tkatchenko. Thermal and Electronic Fluctuations of Flexible Adsorbed Molecules: Azobenzene on Ag(111). *Phys. Rev. Lett.*, 116:146101, 2016. (Cited on page 19).

[95] M. C. Payne, M. P. Teter, D. C. Allan, T. A. Arias, and J. D. Joannopoulos. Iterative minimization techniques for *ab initio* total-energy calculations: molecular dynamics and conjugate gradients. *Rev. Mod. Phys.*, 64:1045, 1992. (Cited on pages 20, 21, and 22).

[96] R. M. Martin. *Electronic Structure: Basic theory and practical methods*. Cambridge University Press, Cambridge, 2011. (Cited on page 20).

[97] D. R. Hamann, M. Schlüter, and C. Chiang. Norm-Conserving Pseudopotentials. *Phys. Rev. Lett.*, 43:1494, 1979. (Cited on page 21).

[98] N. Troullier and José Luís Martins. Efficient pseudopotentials for plane-wave calculations. *Phys. Rev. B*, 43:1993, 1991. (Cited on page 21).

[99] D. Vanderbilt. Soft self-consistent pseudopotentials in a generalized eigenvalue formalism. *Phys. Rev. B*, 41:7892, 1990. (Cited on page 21).

[100] P. E. Blöchl. Projector augmented-wave method. *Phys. Rev. B*, 50:17953, 1994. (Cited on page 21).

[101] S. G. Louie, S. Froyen, and M. L. Cohen. Nonlinear ionic pseudopotentials in spin-density-functional calculations. *Phys. Rev. B*, 26:1738, 1982. (Cited on page 21).

[102] N. W. Ashcroft and N. D. Mermin. *Solid State Physics*. Brooks Cole, 1976. (Cited on pages 22, 112, and 115).

[103] H J Monkhorst and J D Pack. Special points for Brillouin-zone integrations. *Phys. Rev. B*, 13:5188, 1976. (Cited on pages 22, 51, 106, and 135).

[104] G. Kresse and J. Furthmüller. Efficient iterative schemes for *ab initio* total-energy calculations using a plane-wave basis set. *Phys. Rev. B*, 54:11169, 1996. (Cited on pages 23 and 135).

[105] P. Giannozzi, S. Baroni, N. Bonini, M. Calandra, R. Car, C. Cavazzoni, D. Ceresoli, G. L Chiarotti, M. Cococcioni, I. Dabo, and *et al.* QUANTUM ESPRESSO: a modular and open-source software project for quantum simulations of materials. *J. Phys.: Condens. Matter*, 21:395502, 2009. (Cited on pages 23 and 106).

[106] A. Groß. Quantum effects in the dissociative adsorption of hydrogen. *J. Chem. Phys.*, 110:8696, 1999. (Cited on page 23).

[107] A Groß. Ab initio Molecular Dynamics Study of Hot Atom Dynamics after Dissociative Adsorption of H_2 on Pd(100). *Phys. Rev. Lett.*, 103:246101, 2009. (Cited on pages 23, 47, and 48).

[108] A Lozano, A Groß, and H F Busnengo. Adsorption dynamics of H_2 on Pd(100) from first principles. *Phys. Chem. Chem. Phys.*, 11:5814, 2009. (Cited on pages 23 and 51).

[109] H.F. Busnengo, E. Pijper, M.F. Somers, G.J. Kroes, A. Salin, R.A. Olsen, D. Lemoine, and W. Dong. Six-dimensional quantum and classical dynamics study of H_2(=0,J=0) scattering from Pd(1 1 1). *Chem. Phys. Lett.*, 356:515, 2002. (Cited on page 23).

[110] P. Ehrenfest. Bemerkung über die angenäherte Gültigkeit der klassischen Mechanik innerhalb der Quantenmechanik. *Z. Phys.*, 45:455, 1927. (Cited on page 23).

[111] H. Hellmann. Zur Rolle der kinetischen Elektronenenergie für die zwischenatomaren Kräfte. *Z. Phys.*, 85:180, 1933. (Cited on page 24).

[112] R. P. Feynman. Forces in Molecules. *Phys. Rev.*, 56:340, 1939. (Cited on page 24).

[113] R. Kubo. The fluctuation-dissipation theorem. *Rep. Prog. Phys.*, 29:255, 1966. (Cited on pages 25 and 27).

[114] A. Schmid. On a quasiclassical Langevin equation. *J. Low Temp. Phys.*, 49: 609, 1982. (Cited on page 25).

[115] S. Nosé. A unified formulation of the constant temperature molecular dynamics methods. *J. Chem. Phys.*, 81:511, 1984. (Cited on page 25).

[116] W. G. Hoover. Canonical dynamics: Equilibrium phase-space distributions. *Phys. Rev. A*, 31:1695, 1985. (Cited on page 25).

[117] G Kresse and J Hafner. Ab initio molecular dynamics for liquid metals. *Phys. Rev. B*, 47:558, 1993. (Cited on pages 25 and 55).

[118] E. G. d'Agliano, P. Kumar, W. Schaich, and H. Suhl. Brownian motion model of the interactions between chemical species and metallic electrons: Bootstrap derivation and parameter evaluation. *Phys. Rev. B*, 11:2122, 1975. (Cited on pages 26, 29, and 31).

[119] M. Head-Gordon and J. C. Tully. Molecular dynamics with electronic frictions. *J. Chem. Phys.*, 103:10137, 1995. (Cited on pages 26, 47, and 53).

[120] M. Persson and B. Hellsing. Electronic Damping of Adsorbate Vibrations on Metal Surfaces. *Phys. Rev. Lett.*, 49:662, 1982. (Cited on page 26).

[121] P M Echenique, R M Nieminen, J C Ashley, and R H Ritchie. Nonlinear stopping power of an electron gas for slow ions. *Phys. Rev. A*, 33:897, 1986. (Cited on pages 26, 31, 53, and 74).

[122] C. C. Sung and R. H. Ritchie. Z_1^3 dependence of the energy loss of an ion passing through an electron gas. *Phys. Rev. A*, 28:674, 1983. (Cited on pages 26, 29, and 30).

[123] H. Ishida. Theory of the direct and indirect forces for a single impurity atom in the electron gas. *Phys. Rev. B*, 51:10345, 1995. (Cited on pages 26 and 28).

[124] J. R. Trail, D. M. Bird, M. Persson, and S. Holloway. Electron–hole pair creation by atoms incident on a metal surface. *J. Chem. Phys.*, 119:4539, 2003. (Cited on pages 26 and 53).

[125] R. Kubo, M. Toda, and N. Hashitsume. *Statistical Physics II: Nonequilibrium Statistical Mechanics*. Springer-Verlag, Berlin, 1991. (Cited on pages 27 and 174).

[126] D. Pines and P. Noziéres. *The Theory of Quantum Liquids I*. Westview Press, 1999. (Cited on pages 28, 88, and 94).

[127] Blandin, A., Nourtier, A., and Hone, D.W. Localized time-dependent perturbations in metals : formalism and simple examples. *J. Phys. France*, 37:369, 1976. (Cited on page 29).

[128] W. H. Butler, F. J. Pinski, and P. B. Allen. Phonon linewidths and electron-phonon interaction in Nb. *Phys. Rev. B*, 19:3708, 1979. (Cited on page 29).

[129] G. D. Mahan. *Many-Particle Physics*. Plenum, New York, 3rd ed. edition, 2000. (Cited on pages 30, 31, 38, 39, 40, 41, 83, 90, 97, 99, 100, 102, and 174).

[130] K. Schönhammer. Nonlinear friction in a homogenous electron gas: Exact results. *Phys. Rev. B*, 37:7735, 1988. (Cited on page 31).

[131] L. Bönig and K. Schönhammer. Time-dependent local perturbation in a free-electron gas: Exact results. *Phys. Rev. B*, 39:7413, 1989. (Cited on page 31).

[132] J. I. Juaristi, A. Arnau, P. M. Echenique, C. Auth, and H. Winter. Charge State Dependence of the Energy Loss of Slow Ions in Metals. *Phys. Rev. Lett.*, 82:1048, 1999. (Cited on pages 31 and 53).

[133] H. Winter, J. I. Juaristi, I. Nagy, A. Arnau, and P. M. Echenique. Energy loss of slow ions in a nonuniform electron gas. *Phys. Rev. B*, 67:245401, 2003. (Cited on pages 31, 53, and 74).

[134] A Salin, A Arnau, P M Echenique, and E Zaremba. Dynamic nonlinear screening of slow ions in an electron gas. *Phys. Rev. B*, 59:2537, 1999. doi: 10.1103/PhysRevB.59.2537. (Cited on page 31).

[135] S. Baroni, S. de Gironcoli, A. Dal Corso, and P. Giannozzi. Phonons and related crystal properties from density-functional perturbation theory. *Rev. Mod. Phys.*, 73:515, 2001. (Cited on pages 32, 33, 34, 35, 36, 41, 82, and 106).

[136] M. Calandra, G. Profeta, and F. Mauri. Adiabatic and nonadiabatic phonon dispersion in a Wannier function approach. *Phys. Rev. B*, 82:165111, 2010. (Cited on pages 33, 34, 89, and 106).

[137] R. M. Pick, M. H. Cohen, and R. M. Martin. Microscopic Theory of Force Constants in the Adiabatic Approximation. *Phys. Rev. B*, 1:910, 1970. (Cited on page 34).

[138] E G Maksimov and A E Karakozov. On nonadiabatic effects in phonon spectra of metals. *Phys. Usp.*, 51:535, 2008. (Cited on pages 34, 36, 82, and 91).

[139] S. Baroni, P. Giannozzi, and A. Testa. Green's-function approach to linear response in solids. *Phys. Rev. Lett.*, 58:1861, 1987. (Cited on page 34).

[140] R. M. Sternheimer. Electronic Polarizabilities of Ions from the Hartree-Fock Wave Functions. *Phys. Rev.*, 96:951, 1954. (Cited on page 35).

[141] G. D. Mahan. Modified Sternheimer equation for polarizability. *Phys. Rev. A*, 22:1780, 1980. (Cited on page 35).

[142] I. P. Ipatova and A. V. Subashiev. Long-wave optical-phonon spectrum in metals and heavily doped semiconductors. *JETP*, 39:349, 1974. (Cited on pages 36, 82, 88, 89, 93, 95, and 122).

[143] M. Born and V. Fock. Beweis des Adiabatensatzes. *Z. Phys.*, 51:165, 1928. (Cited on page 37).

[144] A. A. Abrikosov, L. P. Gorkov, and I. E. Dzyaloshinski. *Methods of Quantum Field Theory in Statistical Physics*. Dover, New York, 1975. (Cited on page 38).

[145] P. B. Allen and R. Silberglitt. Some effects of phonon dynamics on electron lifetime, mass renormalization, and superconducting transition temperature. *Phys. Rev. B*, 9:4733, 1974. (Cited on pages 41, 102, and 103).

[146] Lon van Hove. Quantum-mechanical perturbations giving rise to a statistical transport equation. *Physica*, 21:517, 1954. (Cited on pages 42 and 43).

[147] W. Kohn and J. M. Luttinger. Quantum Theory of Electrical Transport Phenomena. *Phys. Rev.*, 108:590, 1957. (Cited on pages 42 and 43).

[148] G. Lindblad. On the generators of quantum dynamical semigroups. *Commun. Math. Phys.*, 48:119, 1976. (Cited on page 42).

[149] V. Gorini and A. Kossakowski. Nlevel system in contact with a singular reservoir. *J. Math. Phys.*, 17:1298, 1976. (Cited on page 42).

[150] V. Gorini, A. Kossakowski, and E. C. G. Sudarshan. Completely positive dynamical semigroups of Nlevel systems. *J. Math. Phys.*, 17:821, 1976. (Cited on page 42).

[151] M. V. Fischetti. Theory of electron transport in small semiconductor devices using the Pauli master equation. *J. Appl. Phys.*, 83:270, 1998. (Cited on pages 42 and 43).

[152] J. C. Tremblay, T. Klamroth, and P. Saalfrank. Time-dependent configuration-interaction calculations of laser-driven dynamics in presence of dissipation. *J. Chem. Phys.*, 129:084302, 2008. (Cited on page 42).

[153] S. Beyvers, Y. Ohtsuki, and P. Saalfrank. Optimal control in a dissipative system: Vibrational excitation of COCu(100) by IR pulses. *J. Chem. Phys.*, 124:234706, 2006. (Cited on page 42).

[154] J. C. Tremblay, S. Monturet, and P. Saalfrank. Electronic damping of anharmonic adsorbate vibrations at metallic surfaces. *Phys. Rev. B*, 81: 125408, 2010. (Cited on pages 42, 43, 82, 83, 128, and 133).

[155] J. C. Tremblay and P. Saalfrank. Selective subsurface absorption of hydrogen in palladium using laser distillation. *J. Chem. Phys.*, 131:084716, 2009. (Cited on pages 42 and 128).

[156] J C Tremblay and M Blanco-Rey. Manipulating interfacial hydrogens at palladium via STM. *Phys. Chem. Chem. Phys.*, 17:13973, 2015. (Cited on pages 42, 130, and 133).

[157] A. Groß. Reactions at surfaces studied by ab initio dynamics calculations. *Surf. Sci. Rep.*, 32:291, 1998. (Cited on page 47).

[158] G. J. Kroes and C. Díaz. Quantum and classical dynamics of reactive scattering of H_2 from metal surfaces. *Chem. Soc. Rev.*, page 3658, 2016. (Cited on page 47).

[159] G. J. Kroes, E. Pijper, and A. Salin. Dissociative chemisorption of H_2 on the Cu(110) surface: A quantum and quasiclassical dynamical study. *J. Chem. Phys.*, 127:164722, 2007. (Cited on page 47).

[160] C. Díaz, E. Pijper, R. A. Olsen, H. F. Busnengo, D. J. Auerbach, and G. J. Kroes. Chemically Accurate Simulation of a Prototypical Surface Reaction: H_2 Dissociation on Cu(111). *Science*, 326:832, 2009. (Cited on page 47).

[161] C. Díaz, R. A. Olsen, D. J. Auerbach, and G. J. Kroes. Six-dimensional dynamics study of reactive and non reactive scattering of H_2 from Cu(111) using a chemically accurate potential energy surface. *Phys. Chem. Chem. Phys.*, 12:6499, 2010. (Cited on page 47).

[162] M. Alducin, R. Díez Muiño, H. F. Busnengo, and A. Salin. Why N_2 Molecules with Thermal Energy Abundantly Dissociate on W(100) and Not on W(110). *Phys. Rev. Lett.*, 97:056102, 2006. (Cited on page 47).

[163] C. Díaz, J. K. Vincent, G. P. Krishnamohan, R. A. Olsen, G. J. Kroes, K. Honkala, and J. K. Nørskov. Multidimensional Effects on Dissociation of N_2 on Ru(0001). *Phys. Rev. Lett.*, 96:096102, 2006. (Cited on page 47).

[164] I. Goikoetxea, J. I. Juaristi, R. Díez Muiño, and M. Alducin. Surface Strain Improves Molecular Adsorption but Hampers Dissociation for N_2 on the Fe/W(110) Surface. *Phys. Rev. Lett.*, 113:066103, 2014. (Cited on pages 47, 48, 72, and 78).

[165] M. Alducin, H. F. Busnengo, and R. Díez Muiño. Dissociative dynamics of spin-triplet and spin-singlet O_2 on Ag(100). *J. Chem. Phys.*, 129:224702, 2008. (Cited on page 47).

[166] I. Goikoetxea, J. Beltrán, J. Meyer, J. I. Juaristi, M. Alducin, and K. Reuter. Non-adiabatic effects during the dissociative adsorption of O_2 at Ag(111)? A first-principles divide and conquer study. *New J. Phys.*, 14:013050, 2012. (Cited on page 47).

[167] I. Lončarić, M. Alducin, and J. I. Juaristi. Dissociative dynamics of O_2 on Ag(110). *Phys. Chem. Chem. Phys.*, 17:9436, 2015. (Cited on page 47).

[168] P. M. Hundt, B. Jiang, M. E. van Reijzen, H. Guo, and R. D. Beck. Vibrationally Promoted Dissociation of Water on Ni(111). *Science*, 344:504, 2014. (Cited on page 47).

[169] B. Jiang and H. Guo. Dynamics of Water Dissociative Chemisorption on Ni(111): Effects of Impact Sites and Incident Angles. *Phys. Rev. Lett.*, 114: 166101, 2015. (Cited on page 47).

[170] B. Jiang, M. Alducin, and H. Guo. Electron-Hole Pair Effects in Polyatomic Dissociative Chemisorption: Water on Ni(111). *J. Phys. Chem. Lett.*, 7:327, 2016. (Cited on pages 47 and 53).

[171] B. Jiang and H. Guo. Communication: Enhanced dissociative chemisorption of CO_2 via vibrational excitation. *J. Chem. Phys.*, 144:091101, 2016. (Cited on page 47).

[172] X. J. Shen, A. Lozano, W. Dong, H. F. Busnengo, and X. H. Yan. Towards Bond Selective Chemistry from First Principles: Methane on Metal Surfaces. *Phys. Rev. Lett.*, 112:046101, 2014. (Cited on page 47).

[173] V. Moron, P. Gamallo, L. Martin-Gondre, C. Crespos, P. Larrégaray, and R. Sayos. Recombination and chemical energy accommodation coefficients from chemical dynamics simulations: O/O_2 mixtures reacting over a β-cristobalite (001) surface. *Phys. Chem. Chem. Phys.*, 13:17494, 2011. (Cited on page 47).

[174] M Blanco-Rey, E Díaz, G A Bocan, R Díez Muiño, M Alducin, and J I Juaristi. Efficient N_2 Formation on Ag(111) by Eley-Rideal Recombination of Hyperthermal Atoms. *J. Phys. Chem. Lett.*, 4:3704, 2013. (Cited on pages 47 and 48).

[175] R. Pétuya, P. Larrégaray, C. Crespos, H. F. Busnengo, and A. E. Martínez. Dynamics of H_2 Eley-Rideal abstraction from W(110): Sensitivity to the representation of the molecule-surface potential. *J. Chem. Phys.*, 141:024701, 2014. (Cited on page 47).

[176] R. Pétuya, P. Larrégaray, C. Crespos, P. Aurel, H. F. Busnengo, and A. E. Martínez. Scattering of Atomic Hydrogen Off a H-Covered W(110) Surface: Hot-Atom versus Eley-Rideal Abstraction Dynamics. *J. Phys. Chem. C*, 119: 3171, 2015. (Cited on page 47).

[177] R. Pétuya, M. A. Nosir, C. Crespos, R. Díez Muiño, and P. Larrégaray. Isotope Effects in Eley-Rideal and Hot-Atom Abstraction Dynamics of Hydrogen from Tungsten (100) and (110) Surfaces. *J. Phys. Chem. C*, 119: 15325, 2015. (Cited on page 47).

[178] D. Farías, C. Díaz, P. Rivière, H. F. Busnengo, P. Nieto, M. F. Somers, G. J. Kroes, A. Salin, and F. Martín. In-Plane and Out-of-Plane Diffraction of H_2 from Metal Surfaces. *Phys. Rev. Lett.*, 93:246104, 2004. (Cited on page 47).

[179] D. Barredo, G. Laurent, C. Díaz, P. Nieto, H. F. Busnengo, A. Salin, D. Farías, and F. Martín. Experimental evidence of dynamic trapping in the scattering of H_2 from Pd(110). *J. Chem. Phys.*, 125:051101, 2006. (Cited on page 47).

[180] M. del Cueto, A. S. Muzas, G. Füchsel, F. Gatti, F. Martín, and C. Díaz. Role of van der Waals forces in the diffraction of noble gases from metal surfaces. *Phys. Rev. B*, 93:060301, 2016. (Cited on page 47).

[181] H. F. Busnengo, E. Pijper, G. J. Kroes, and A. Salin. Rotational effects in dissociation of H_2 on Pd(111): Quantum and classical study. *J. Chem. Phys.*, 119:12553, 2003. (Cited on page 47).

[182] C. Díaz, J. K. Vincent, G. P. Krishnamohan, R. A. Olsen, G. J. Kroes, K. Honkala, and J. K. Nørskov. Reactive and nonreactive scattering of N_2 from Ru(0001): A six-dimensional adiabatic study. *J. Chem. Phys.*, 125: 114706, 2006. (Cited on page 47).

[183] K. R Geethalakshmi, J. I Juaristi, R. Díez Muiño, and M. Alducin. Non-reactive scattering of N_2 from the W(110) surface studied with differ ent exchange-correlation functionals. *Phys. Chem. Chem. Phys.*, 13:4357, 2011. (Cited on page 47).

[184] A. S. Muzas, J. I. Juaristi, M. Alducin, R. Díez Muiño, G. J. Kroes, and C. Díaz. Vibrational deexcitation and rotational excitation of H_2 and D_2 scattered from Cu(111): Adiabatic versus non-adiabatic dynamics. *J. Chem. Phys.*, 137:064707, 2012. (Cited on pages 47 and 53).

[185] M Blanco-Rey, L Martin-Gondre, R Díez Muiño, M Alducin, and J I Juaristi. Dynamics of Nitrogen Scattering off N-Covered Ag(111). *J. Phys. Chem. C*, 116:21903, 2012. (Cited on page 47).

[186] L Martin-Gondre, G A Bocan, M Blanco-Rey, M Alducin, J I Juaristi, and R Díez Muiño. Scattering of Nitrogen Atoms off Ag(111) Surfaces: A Theoretical Study. *J. Phys. Chem. C*, 117:9779, 2013. (Cited on pages 47 and 62).

[187] R. Pétuya, P.-A. Plötz, C. Crespos, and P. Larrégaray. Revisiting the Nonreactive Scattering of N_2 off W(100): On the Influence of the Scattering Azimuth on In-Plane Angular Distributions. *J. Phys. Chem. C*, 118:21904, 2014. (Cited on pages 47 and 48).

[188] I. Goikoetxea, J. Meyer, J. I. Juaristi, M. Alducin, and K. Reuter. Role of Physisorption States in Molecular Scattering: A Semilocal Density-Functional Theory Study on O_2/Ag(111). *Phys. Rev. Lett.*, 112:156101, 2014. (Cited on pages 47 and 48).

[189] G. Armand and J. R. Manson. Inelastic Low-Energy Atom-Surface Scattering. *Phys. Rev. Lett.*, 53:1112, 1984. (Cited on page 47).

[190] Y. Li and G. Wahnström. Nonadiabatic effects in hydrogen diffusion in metals. *Phys. Rev. Lett.*, 68:3444, 1992. (Cited on page 47).

[191] H Nienhaus. Electronic excitations by chemical reactions on metal surfaces. *Surf. Sci. Rep.*, 45:1, 2002. (Cited on pages 47, 48, 49, and 82).

[192] J. R. Trail, M. C. Graham, D. M. Bird, M. Persson, and S. Holloway. Energy Loss of Atoms at Metal Surfaces due to Electron-Hole Pair Excitations: First-Principles Theory of "Chemicurrents". *Phys. Rev. Lett.*, 88:166802, 2002. (Cited on page 47).

[193] A. C. Luntz and M. Persson. How adiabatic is activated adsorption/associative desorption? *J. Chem. Phys.*, 123:074704, 2005. (Cited on pages 47 and 53).

[194] M. Lindenblatt and E. Pehlke. Ab initio Simulation of the Spin Transition during Chemisorption: H/Al(111). *Phys. Rev. Lett.*, 97:216101, 2006. (Cited on page 47).

[195] M. Timmer and P. Kratzer. Electron-hole spectra created by adsorption on metals from density functional theory. *Phys. Rev. B*, 79:165407, 2009. (Cited on page 47).

[196] G. Füchsel, T. Klamroth, S. Monturet, and P. Saalfrank. Dissipative dynamics within the electronic friction approach: the femtosecond laser desorption of H_2/D_2 from Ru(0001). *Phys. Chem. Chem. Phys.*, 13:8659, 2011. (Cited on pages 47, 48, and 53).

[197] J. Meyer and K. Reuter. Electron-hole pairs during the adsorption dynamics of O_2 on Pd(100): Exciting or not? *New J. Phys.*, 13:085010, 2011. (Cited on page 47).

[198] L. Martin-Gondre, M. Alducin, G. A. Bocan, R. Díez Muiño, and J. I. Juaristi. Competition between Electron and Phonon Excitations in the Scattering of Nitrogen Atoms and Molecules off Tungsten and Silver Metal Surfaces. *Phys. Rev. Lett.*, 108:096101, 2012. (Cited on pages 47, 48, 53, and 82).

[199] S M Janke, M Pavanello, G J Kroes, D J Auerbach, A M Wodtke, and A Kandratsenka. Toward Detection of Electron-Hole Pair Excitation in H-atom Collisions with Au(111): Adiabatic Molecular Dynamics with a Semi-Empirical Full-Dimensional Potential Energy Surface. *Z. Phys. Chem.*, 227:1467, 2013. (Cited on page 47).

[200] M Pavanello, D J Auerbach, A M Wodtke, M Blanco-Rey, M Alducin, and G J Kroes. Adiabatic Energy Loss in Hyperthermal H Atom Collisions with Cu and Au: A Basis for Testing the Importance of Nonadiabatic Energy Loss. *J. Phys. Chem. Lett.*, 4:3735, 2013. (Cited on pages 47, 48, and 53).

[201] J. Meyer and Karsten Reuter. Modeling Heat Dissipation at the Nanoscale: An Embedding Approach for Chemical Reaction Dynamics on Metal Surfaces. *Angew. Chem. Int. Ed.*, 53:4721, 2014. (Cited on pages 47 and 48).

[202] J T Kindt, J C Tully, M Head-Gordon, and M A Gomez. Electron-hole pair contributions to scattering, sticking, and surface diffusion: CO on Cu(100). *J. Chem. Phys.*, 109:3629, 1998. (Cited on page 47).

[203] J.V. Barth. Transport of adsorbates at metal surfaces: from thermal migration to hot precursors. *Surf. Sci. Rep.*, 40:75, 2000. (Cited on page 47).

[204] H. Hedgeland, P. Fouquet, A. P. Jardine, G. Alexandrowicz, W. Allison, and J. Ellis. Measurement of single-molecule frictional dissipation in a prototypical nanoscale system. *Nat. Phys.*, 5:561, 2009. (Cited on page 47).

[205] K. R. Harikumar, J. C. Polanyi, A. Zabet-Khosousi, P. Czekala, H. Lin, and W. A. Hofer. Directed long-range molecular migration energized by surface reaction. *Nat. Chem.*, 3:400, 2011. (Cited on page 47).

[206] B. Schindler, D. Diesing, and E. Hasselbrink. Electronic excitations induced by hydrogen surface chemical reactions on gold. *J. Chem. Phys.*, 134:034705, 2011. (Cited on page 47).

[207] E. Quintas-Sánchez, C. Crespos, P. Larrégaray, J. C. Rayez, L. Martin-Gondre, and J. Rubayo-Soneira. Surface Temperature Effects on the Dynamics of N_2 Eley-Rideal Recombination on W(100). *J. Chem. Phys.*, 138:024706, 2013. (Cited on pages 47 and 48).

[208] J. A. Prybyla, T. F. Heinz, J. A. Misewich, M. M. T. Loy, and J. H. Glownia. Desorption induced by femtosecond laser pulses. *Phys. Rev. Lett.*, 64:1537, 1990. (Cited on page 48).

[209] F. Budde, T. F. Heinz, M. M. T. Loy, J. A. Misewich, F. de Rougemont, and H. Zacharias. Femtosecond time-resolved measurement of desorption. *Phys. Rev. Lett.*, 66:3024, 1991. (Cited on page 48).

[210] M. Bonn, S. Funk, Ch. Hess, D. N. Denzler, C. Stampfl, M. Scheffler, M. Wolf, and G. Ertl. Phonon- Versus Electron-Mediated Desorption and Oxidation of CO on Ru(0001). *Science*, 285:1042, 1999. (Cited on page 48).

[211] D. N. Denzler, C. Frischkorn, C. Hess, M. Wolf, and G. Ertl. Electronic Excitation and Dynamic Promotion of a Surface Reaction. *Phys. Rev. Lett.*, 91:226102, 2003. (Cited on page 48).

[212] M. Dell'Angela, T. Anniyev, M. Beye, R. Coffee, A. Füsch, J. Gladh, T. Katayama, S. Kaya, O. Krupin, J. LaRue, A. Møgelhøj, D. Nordlund, J. K. Nørskov, H. Öberg, H. Ogasawara, H. Öström, L. G. M. Pettersson, W. F. Schlotter, J. A. Sellberg, F. Sorgenfrei, J. J. Turner, M. Wolf, W. Wurth, and A. Nilsson. Real-Time Observation of Surface Bond Breaking with an X-ray Laser. *Science*, 339:1302, 2013. (Cited on page 48).

[213] H. Öström, H. Öberg, H. Xin, J. LaRue, M. Beye, M. Dell'Angela, J. Gladh, M. L. Ng, J. A. Sellberg, S. Kaya, G. Mercurio, D. Nordlund, M. Hantschmann, F. Hieke, D. Kühn, W. F. Schlotter, G. L. Dakovski, J. J. Turner, M. P. Minitti, A. Mitra, S. P. Moeller, A. Föhlisch, M. Wolf, W. Wurth, M. Persson, J. K. Nørskov, F. Abild-Pedersen, H. Ogasawara, L. G. M. Pettersson, and A. Nilsson. Probing the transition state region in catalytic CO oxidation on Ru. *Science*, 347:978, 2015. (Cited on page 48).

[214] J. A. Misewich, T. F. Heinz, and D. M. Newns. Desorption induced by multiple electronic transitions. *Phys. Rev. Lett.*, 68:3737, 1992. (Cited on page 48).

[215] C. Springer, M. Head-Gordon, and J. C. Tully. Simulations of femtosecond laser-induced desorption of CO from Cu(100). *Surf. Sci.*, 320:L57, 1994. (Cited on page 48).

[216] M. Brandbyge, P. Hedegård, T. F. Heinz, J. A. Misewich, and D. M. Newns. Electronically driven adsorbate excitation mechanism in femtosecond-pulse laser desorption. *Phys. Rev. B*, 52:6042, 1995. (Cited on page 48).

[217] H. Guo, P. Saalfrank, and T. Seideman. Theory of photoinduced surface reactions of admolecules. *Prog. Surf. Sci.*, 62:239, 1999. (Cited on page 48).

[218] P. Saalfrank. Quantum Dynamical Approach to Ultrafast Molecular Desorption from Surfaces. *Chem. Rev.*, 106:4116, 2006. (Cited on pages 48, 127, and 128).

[219] I. Lončarić, M. Alducin, P. Saalfrank, and J. I. Juaristi. Femtosecond-laser-driven molecular dynamics on surfaces: Photodesorption of molecular oxygen from Ag(110). *Phys. Rev. B*, 93:014301, 2016. (Cited on pages 48, 53, and 82).

[220] H F Busnengo, M A di Césare, W Dong, and A Salin. Surface temperature effects in dynamic trapping mediated adsorption of light molecules on metal surfaces: H_2 on Pd(111) and Pd(110). *Phys. Rev. B*, 72:125411, 2005. (Cited on pages 48 and 60).

[221] L Martin-Gondre, G A Bocan, M Alducin, J I Juaristi, and R Díez Muiño. Energy dissipation channels in the adsorption of N on Ag(111). *Comp. Theo. Chem.*, 990:126, 2012. (Cited on pages 48, 50, 53, 60, 72, and 76).

[222] I Goikoetxea, M Alducin, R Díez Muiño, and J I Juaristi. Dissociative and non-dissociative adsorption dynamics of N_2 on Fe(110). *Phys. Chem. Chem. Phys*, 14:7471, 2012. (Cited on pages 48, 50, 61, 62, 72, and 78).

[223] I. Goikoetxea, M. Alducin, R. Díez Muiño, and J. I. Juaristi. The dynamics of adsorption and dissociation of N_2 in a monolayer of iron on W(110). *Phys. Chem. Chem. Phys.*, 17:19432, 2015. (Cited on page 48).

[224] S A Adelman and J D Doll. Generalized Langevin theory for gas/solid processes: Dynamical solid models. *J. Chem. Phys.*, 64:2375, 1976. (Cited on pages 48 and 60).

[225] S A Adelman. Generalized Langevin theory for manybody problems in chemical dynamics: General formulation and the equivalent harmonic chain representation. *J. Chem. Phys.*, 71:4471, 1979. (Cited on pages 48 and 60).

[226] John C. Tully. Dynamics of gas-surface interactions: 3D generalized Langevin model applied to fcc and bcc surfaces. *J. Chem. Phys.*, 73:1975, 1980. (Cited on pages 48 and 60).

[227] A. Groß, M. Bockstedte, and M. Scheffler. Ab initio Molecular Dynamics Study of the Desorption of D_2 from Si(100). *Phys. Rev. Lett.*, 79:701, 1997. (Cited on page 48).

[228] A. Groß and A. Dianat. Hydrogen Dissociation Dynamics on Precovered Pd Surfaces: Langmuir is Still Right. *Phys. Rev. Lett.*, 98:206107, 2007. (Cited on page 48).

[229] A. Groß. Ab initio molecular dynamics simulations of the adsorption of H_2 on palladium surfaces. *Chem. Phys. Chem.*, 11:1374, 2010. (Cited on page 48).

[230] A. Lozano, A. Groß, and H. F. Busnengo. Molecular dynamics study of H_2 dissociation on H-covered Pd(100). *Phys. Rev. B*, 81:121402, 2010. (Cited on pages 48 and 51).

[231] F. Nattino, C. Díaz, B. Jackson, and G. J. Kroes. Effect of Surface Motion on the Rotational Quadrupole Alignment Parameter of D_2 Reacting on Cu(111). *Phys. Rev. Lett.*, 108:236104, 2012. (Cited on page 48).

[232] F. Nattino, H. Ueta, H. Chadwick, M. E. van Reijzen, R. D. Beck, B. Jackson, M. C. van Hemert, and G. J. Kroes. Ab Initio Molecular Dynamics Calculations versus Quantum-State-Resolved Experiments on CHD_3 + Pt(111): New Insights into a Prototypical Gas-Surface Reaction. *J. Phys. Chem. Lett.*, 5:1294, 2014. (Cited on page 48).

[233] J. R. Manson. Inelastic scattering from surfaces. *Phys. Rev. B*, 43:6924, 1991. (Cited on page 48).

[234] H. Ambaye and J. R. Manson. Translational to rotational energy transfer in molecule-surface collisions. *J. Chem. Phys.*, 125:084717, 2006. (Cited on page 48).

[235] W. W. Hayes and J. R. Manson. Argon scattering from Ru(0001): Calculations and comparison with experiment. *Phys. Rev. B*, 75:113408, 2007. (Cited on page 48).

[236] J. R. Hahn and W. Ho. Orbital specific chemistry: Controlling the pathway in single-molecule dissociation. *J. Chem. Phys.*, 122:244704, 2005. (Cited on page 49).

[237] P E Blöchl. Projector augmented-wave method. *Phys. Rev. B*, 50:17953, 1994. (Cited on pages 50 and 135).

[238] D Beeman. Some multistep methods for use in molecular dynamics calculations. *J. Comput. Phys.*, 20:130, 1976. (Cited on page 51).

[239] I Goikoetxea, J I Juaristi, M Alducin, and R. Díez Muiño. Dissipative effects in the dynamics of N_2 on tungsten surfaces. *J. Phys.: Condens. Matter*, 21: 264007, 2009. (Cited on page 53).

[240] J. C. Tremblay, S. Monturet, and P. Saalfrank. Electronic damping of anharmonic adsorbate vibrations at metallic surfaces. *Phys. Rev. B*, 81: 125408, 2010. (Cited on page 53).

[241] P. Saalfrank, J. I. Juaristi, M. Alducin, M. Blanco-Rey, and R. Díez Muiño. Vibrational lifetimes of hydrogen on lead films: An ab initio molecular dynamics with electronic friction (AIMDEF) study. *J. Chem. Phys.*, 141: 234702, 2014. (Cited on pages 53, 54, and 82).

[242] O. Galparsoro, R. Pétuya, J. I. Juaristi, C. Crespos, M. Alducin, and P. Larregaray. Energy Dissipation to Tungsten Surfaces upon Eley-Rideal Recombination of N_2 and H_2. *J. Phys. Chem. C*, 119:15434, 2015. (Cited on pages 53 and 82).

[243] D. Novko, M. Blanco-Rey, J. I. Juaristi, and M. Alducin. *ab initio* molecular dynamics with simultaneous electron and phonon excitations: application to the relaxation of hot atoms and molecules on metal surfaces. *Phys. Rev. B*, 92:201411, 2015. (Cited on pages 53, 55, and 60).

[244] S. M. Janke, D. J. Auerbach, A. M. Wodtke, and A. Kandratsenka. An accurate full-dimensional potential energy surface for H/Au(111): Importance of nonadiabatic electronic excitation in energy transfer and adsorption. *J. Chem. Phys.*, 143:124708, 2015. (Cited on page 53).

[245] D. Novko, M. Blanco-Rey, J. I. Juaristi, and M. Alducin. Energy loss in gas-surface dynamics: Electron-hole pair and phonon excitation upon adsorbate relaxation. *Nucl. Instrum. Methods Phys. Res., Sect. B*, 382:26, 2016. (Cited on page 53).

[246] O. Bünermann, H. Jiang, Y. Dorenkamp, A. Kandratsenka, S. M. Janke, D. J. Auerbach, and A. M. Wodtke. Electron-hole pair excitation determines the mechanism of hydrogen atom adsorption. *Science*, 350:1346, 2015. (Cited on page 53).

[247] R. Díez Muiño and A. Salin. Self-consistent screening of diatomic molecules in an electron gas. *Phys. Rev. B*, 60:2074, 1999. (Cited on page 53).

[248] S. P. Rittmeyer, J. Meyer, J. I. Juaristi, and K. Reuter. Electronic Friction-Based Vibrational Lifetimes of Molecular Adsorbates: Beyond the Independent-Atom Approximation. *Phys. Rev. Lett.*, 115:046102, 2015. (Cited on pages 54, 55, 82, and 85).

[249] M. Askerka, R. J. Maurer, V. S. Batista, and J. C. Tully. Role of Tensorial Electronic Friction in Energy Transfer at Metal Surfaces. *Phys. Rev. Lett.*, 116:217601, 2016. (Cited on pages 54, 82, 83, 112, and 125).

[250] B. Baule. Theoretische Behandlung der Erscheinungen in verdnnten Gasen. *Ann. Phys.*, 44:145, 1914. (Cited on page 62).

[251] A. Groß. *Theoretical Surface Science*. Springer, Berlin, 2003. (Cited on page 62).

[252] M. J. Puska and R. M. Nieminen. Atoms embedded in an electron gas: Phase shifts and cross sections. *Phys. Rev. B*, 27:6121, 1983. (Cited on page 74).

[253] Zhibin Lin, Leonid V. Zhigilei, and Vittorio Celli. Electron-phonon coupling and electron heat capacity of metals under conditions of strong electron-phonon nonequilibrium. *Phys. Rev. B*, 77:075133, 2008. (Cited on page 75).

[254] R. C. Millikan. Vibrational Fluorescence of Carbon Monoxide. *J. Chem. Phys.*, 38:2855, 1963. (Cited on page 82).

[255] J. D. Beckerle, M. P. Casassa, R. R. Cavanagh, E. J. Heilweil, and J. C. Stephenson. Ultrafast infrared response of adsorbates on metal surfaces: Vibrational lifetime of CO/Pt(111). *Phys. Rev. Lett.*, 64:2090, 1990. (Cited on page 82).

[256] T. T. Rantala and A. Rosén. Electronic damping of adsorbate motion: CO vibration on the Cu(100) surface. *Phys. Rev. B*, 34:837, 1986. (Cited on pages 82 and 85).

[257] J.R. Trail, M.C. Graham, and D.M. Bird. Electronic damping of molecular motion at metal surfaces. *Comput. Phys. Commun.*, 137:163, 2001. (Cited on pages 82, 83, 96, and 111).

[258] S. Monturet and P. Saalfrank. Role of electronic friction during the scattering of vibrationally excited nitric oxide molecules from Au(111). *Phys. Rev. B*, 82:075404, 2010. (Cited on page 82).

[259] P. N. Keating. Dielectric Screening and the Phonon Spectra of Metallic and Nonmetallic Crystals. *Phys. Rev.*, 175:1171, 1968. (Cited on pages 82 and 87).

[260] Ž. Crljen and D. C. Langreth. Asymmetric line shapes and the electron-hole pair mechanism for adsorbed molecules on surfaces. *Phys. Rev. B*, 35:4224, 1987. (Cited on page 83).

[261] J. W. Quilty, S. Lee, A. Yamamoto, and S. Tajima. Superconducting Gap in MgB_2: Electronic Raman Scattering Measurements of Single Crystals. *Phys. Rev. Lett.*, 88:087001, 2002. (Cited on page 83).

[262] J. Hlinka, I. Gregora, J. Pokorny, C. Hérold, N. Emery, J. F. Marêché, and P. Lagrange. Lattice dynamics of CaC_6 by Raman spectroscopy. *Phys. Rev. B*, 76:144512, 2007. (Cited on page 83).

[263] C. A. Howard, M. P. M. Dean, and F. Withers. Phonons in potassium-doped graphene: The effects of electron-phonon interactions, dimensionality, and adatom ordering. *Phys. Rev. B*, 84:241404, 2011. (Cited on page 83).

[264] G. Froehlicher and S. Berciaud. Raman spectroscopy of electrochemically gated graphene transistors: Geometrical capacitance, electron-phonon, electron-electron, and electron-defect scattering. *Phys. Rev. B*, 91:205413, 2015. (Cited on page 83).

[265] A. M. Saitta, M. Lazzeri, M. Calandra, and F. Mauri. Giant Nonadiabatic Effects in Layer Metals: Raman Spectra of Intercalated Graphite Explained. *Phys. Rev. Lett.*, 100:226401, 2008. (Cited on pages 83, 90, and 122).

[266] V. L. Aksenov and V. V. Kabanov. Electron-phonon interaction and Raman linewidth in superconducting fullerides. *Phys. Rev. B*, 57:608, 1998. (Cited on pages 83 and 98).

[267] M. Calandra and F. Mauri. Electron-phonon coupling and phonon self-energy in MgB_2: Interpretation of MgB_2 Raman spectra. *Phys. Rev. B*, 71:064501, 2005. (Cited on pages 83, 88, 96, 97, and 125).

[268] J. Ruvalds and A. Virosztek. Optical properties and Fermi-surface nesting in superconducting oxides. *Phys. Rev. B*, 43:5498, 1991. (Cited on page 83).

[269] P. B. Allen. Electron self-energy and generalized Drude formula for infrared conductivity of metals. *Phys. Rev. B*, 92:054305, 2015. (Cited on pages 83 and 102).

[270] D. Novko, M. Šunjić, and V. Despoja. Optical absorption and conductivity in quasi-two-dimensional crystals from first principles: Application to graphene. *Phys. Rev. B*, 93:125413, 2016. (Cited on pages 83, 84, 87, 91, and 112).

[271] A. Zawadowski and M. Cardona. Theory of Raman scattering on normal metals with impurities. *Phys. Rev. B*, 42:10732, 1990. (Cited on page 83).

[272] V. N. Kostur. Electron Raman scattering in metals with strong electron-phonon coupling. *Z. Phys. B*, 89:149, 1992. (Cited on pages 83, 100, and 113).

[273] A. Virosztek and J. Ruvalds. Raman spectrum of superconducting oxides. *Phys. Rev. B*, 45:347, 1992. (Cited on pages 83 and 98).

[274] L.A. Falkovsky. Inelastic electronic light scattering in superconducting and normal metals with impurities. *JETP*, 76:331, 1993. (Cited on pages 83 and 98).

[275] I. Kupčić and S. Barišić. Electronic Raman scattering in a multiband model for cuprate superconductors. *Phys. Rev. B*, 75:094508, 2007. (Cited on pages 83, 84, 91, 93, and 98).

[276] I. Kupčić. Incoherent optical conductivity and breakdown of the generalized Drude formula in quasi-one-dimensional bad metallic systems. *Phys. Rev. B*, 79:235104, 2009. (Cited on pages 83, 84, 91, 98, 99, 123, and 174).

[277] B. Chakraborty and P. B. Allen. Solids with thermal or static disorder. II. Optical properties. *Phys. Rev. B*, 18:5225, 1978. (Cited on page 83).

[278] Yu. S. Ponosov and S. V. Streltsov. Measurements of Raman scattering by electrons in metals: The effects of electron-phonon coupling. *Phys. Rev. B*, 86:045138, 2012. (Cited on pages 83 and 100).

[279] E. Cappelluti and L. Pietronero. Small Fermi energy, strong electron-phonon effects and anharmonicity in MgB_2. *Phys. C*, 460462, Part 1:70, 2007. (Cited on pages 83, 100, 104, and 124).

[280] H. Morawitz. Electron-hole pair dephasing of adsorbate vibrations. *Phys. Rev. Lett.*, 58:2778, 1987. (Cited on pages 83, 100, 118, and 124).

[281] E. Riccardi, M.-A. Méasson, M. Cazayous, A. Sacuto, and Y. Gallais. Gate-Dependent Electronic Raman Scattering in Graphene. *Phys. Rev. Lett.*, 116:066805, 2016. (Cited on page 84).

[282] B N J Persson. Vibrational energy and phase relaxation at surfaces. *J. Phys. C*, 17:4741, 1984. (Cited on pages 84, 85, 119, and 120).

[283] D. J. Diestler and A. H. Zewail. Vibronic dephasing of anharmonic molecules. II. Impurity molecules isolated in low-temperature matrices. *J. Chem. Phys.*, 71:3113, 1979. (Cited on page 84).

[284] D. J. Diestler and A. H. Zewail. Vibronic dephasing of anharmonic molecules. I. Theory and its application to the separability of intra- and inter-molecular processes. *J. Chem. Phys.*, 71:3103, 1979. (Cited on page 84).

[285] Yu. Kagan and A. P. Zhernov. Contribution to the Theory of Electric Conductivity of Metals with Nonmagnetic Impurities. *JETP*, 23:737, 1966. (Cited on pages 84 and 120).

[286] V. Despoja, D. Novko, K. Dekanić, M. Šunjić, and L. Marušić. Two-dimensional and π plasmon spectra in pristine and doped graphene. *Phys. Rev. B*, 87:075447, 2013. (Cited on page 87).

[287] D. Novko, V. Despoja, and M. Šunjić. Changing character of electronic transitions in graphene: From single-particle excitations to plasmons. *Phys. Rev. B*, 91:195407, 2015. (Cited on page 87).

[288] T. Ando. Magnetic Oscillation of Optical Phonon in Graphene. *J. Phys. Soc. Jpn.*, 76:024712, 2007. (Cited on page 89).

[289] J. Dietel and H. Kleinert. Optical phonon lineshapes and transport in metallic carbon nanotubes under high bias voltage. *Phys. Rev. B*, 82:195437, 2010. (Cited on page 89).

[290] P. Zhang, S. G. Louie, and M. L. Cohen. Nonlocal Screening, Electron-Phonon Coupling, and Phonon Renormalization in Metals. *Phys. Rev. Lett.*, 94:225502, 2005. (Cited on page 90).

[291] S. Huotari, J. A. Soininen, T. Pylkkänen, K. Hämäläinen, A. Issolah, A. Titov, J. McMinis, J. Kim, K. Esler, D. M. Ceperley, M. Holzmann, and V. Olevano. Momentum Distribution and Renormalization Factor in Sodium and the Electron Gas. *Phys. Rev. Lett.*, 105:086403, 2010. (Cited on page 93).

[292] P. B. Allen. Neutron Spectroscopy of Superconductors. *Phys. Rev. B*, 6:2577, 1972. (Cited on pages 96 and 103).

[293] R. Bauer, A. Schmid, P. Pavone, and D. Strauch. Electron-phonon coupling in the metallic elements Al, Au, Na, and Nb: A first-principles study. *Phys. Rev. B*, 57:11276, 1998. (Cited on page 102).

[294] T. Komeda, Y. Kim, Maki Kawai, B. N. J. Persson, and H. Ueba. Lateral Hopping of Molecules Induced by Excitation of Internal Vibration Mode. *Science*, 295:2055, 2002. (Cited on pages 104 and 128).

[295] F. Marsiglio and J. P. Carbotte. *Electron-Phonon Superconductivity*, page 73. Springer Berlin Heidelberg, Berlin, Heidelberg, 2008. (Cited on pages 104 and 117).

[296] Z. Wu and R. E. Cohen. More accurate generalized gradient approximation for solids. *Phys. Rev. B*, 73:235116, 2006. (Cited on page 106).

[297] S. Andersson and J. B. Pendry. Structure of CO Adsorbed on Cu(100) and Ni(100). *Phys. Rev. Lett.*, 43:363, 1979. (Cited on page 107).

[298] G. Teobaldi, M. Peñalba, A. Arnau, N. Lorente, and W. A. Hofer. Including the probe tip in theoretical models of inelastic scanning tunneling spectroscopy: CO on Cu(100). *Phys. Rev. B*, 76:235407, 2007. (Cited on page 107).

[299] I. Kupčić. Damping effects in doped graphene: The relaxation-time approximation. *Phys. Rev. B*, 90:205426, 2014. (Cited on page 112).

[300] G. Nilsson and S. Rolandson. Lattice Dynamics of Copper at 80 K. *Phys. Rev. B*, 7:2393, 1973. (Cited on page 116).

[301] C. J. Hirschmugl, G. P. Williams, F. M. Hoffmann, and Y. J. Chabal. Adsorbate-substrate resonant interactions observed for CO on Cu(100) in the far infrared. *Phys. Rev. Lett.*, 65:480, 1990. (Cited on page 116).

[302] A. P. Graham. The low energy dynamics of adsorbates on metal surfaces investigated with helium atom scattering. *Surf. Sci. Rep.*, 49:115, 2003. (Cited on page 116).

[303] B. N. J. Persson and R. Ryberg. Vibrational line shapes of low-frequency adsorbate modes: CO on Pt(111). *Phys. Rev. B*, 40:10273, 1989. (Cited on pages 118 and 126).

[304] J. P. Carbotte, E. Schachinger, and J. Hwang. Boson structures in the relation between optical conductivity and quasiparticle dynamics. *Phys. Rev. B*, 71:054506, 2005. (Cited on page 121).

[305] T. Thonhauser, V. R. Cooper, S. Li, A. Puzder, P. Hyldgaard, and D. C. Langreth. Van der Waals density functional: Self-consistent potential and the nature of the van der Waals bond. *Phys. Rev. B*, 76:125112, 2007. (Cited on pages 123 and 135).

[306] R. Sabatini, T. Gorni, and S. de Gironcoli. Nonlocal van der Waals density functional made simple and efficient. *Phys. Rev. B*, 87:041108, 2013. (Cited on page 123).

[307] B. N. J. Persson, F. M. Hoffmann, and R. Ryberg. Influence of exciton motion on the shape of optical absorption lines: Applications to vibrations at surfaces. *Phys. Rev. B*, 34:2266, 1986. (Cited on page 126).

[308] K. Stokbro, C. Thirstrup, M. Sakurai, U. Quaade, Ben Yu-Kuang Hu, F. Perez-Murano, and F. Grey. STM-Induced Hydrogen Desorption via a Hole Resonance. *Phys. Rev. Lett.*, 80:2618, 1998. (Cited on pages 127 and 128).

[309] L. Bartels, G. Meyer, K.-H. Rieder, D. Velic, E. Knoesel, A. Hotzel, M. Wolf, and G. Ertl. Dynamics of Electron-Induced Manipulation of Individual CO Molecules on Cu(111). *Phys. Rev. Lett.*, 80:2004, 1998. (Cited on page 127).

[310] L. J. Lauhon and W. Ho. Control and Characterization of a Multistep Unimolecular Reaction. *Phys. Rev. Lett.*, 84:1527, 2000. (Cited on page 128).

[311] M. J. Comstock, N. Levy, A. Kirakosian, J. Cho, F. Lauterwasser, J. H. Harvey, D. A. Strubbe, J. M. J. Fréchet, D. Trauner, S. G. Louie, and M. F. Crommie. Reversible Photomechanical Switching of Individual Engineered Molecules at a Metallic Surface. *Phys. Rev. Lett.*, 99:038301, 2007. (Cited on page 128).

[312] M. Alemani, M. V. Peters, S. Hecht, K. H. Rieder, F. Moresco, and L. Grill. Electric Field-Induced Isomerization of Azobenzene by STM. *J. Am. Chem. Soc.*, 128:14446, 2006. (Cited on pages 128 and 132).

[313] P. Liljeroth, J. Repp, and G. Meyer. Current-Induced Hydrogen Tautomerization and Conductance Switching of Naphthalocyanine Molecules. *Science*, 317:1203, 2007. (Cited on page 128).

[314] C Caroli, R Combescot, P Nozieres, and D Saint-James. A direct calculation of the tunnelling current: IV. Electron-phonon interaction effects. *J. Phys. C: Solid State Phys.*, 5:21, 1972. (Cited on page 128).

[315] Shiwu Gao, Mats Persson, and B.I. Lundqvist. Atomic switch proves importance of electron-hole pair mechanism in processes on metal surfaces. *Solid State Commun.*, 84:271, 1992. (Cited on page 128).

[316] H. Ueba, T. Mii, N. Lorente, and B. N. J. Persson. Adsorbate motions induced by inelastic-tunneling current: Theoretical scenarios of two-electron processes. *J. Chem. Phys.*, 123:084707, 2005. (Cited on page 128).

[317] T. Kumagai, A. Shiotari, H. Okuyama, S. Hatta, T. Aruga, I. Hamada, T. Frederiksen, and H. Ueba. H-atom relay reactions in real space. *Nat. Mater.*, 11:167, 2012. (Cited on page 128).

[318] H. Ueba. Analysis of lateral hopping of a single CO molecule on Pd(110). *Phys. Rev. B*, 86:035440, 2012. (Cited on page 128).

[319] T. Frederiksen, M. Paulsson, and H. Ueba. Theory of action spectroscopy for single-molecule reactions induced by vibrational excitations with STM. *Phys. Rev. B*, 89:035427, 2014. (Cited on pages 128 and 133).

[320] A Lapworth and A C Osborn Hann. CXLVIII.-Optically active esters of [small beta]-ketonic and [small beta]-aldehydic acids. Part II. Menthyl acetoacetate. *J. Chem. Soc., Trans.*, 81:1508, 1902. (Cited on page 128).

[321] A Sperl, J Kröger, and R Berndt. Controlled Metalation of a Single Adsorbed Phthalocyanine. *Angew. Chem. Int. Ed.*, 50:5294, 2011. (Cited on page 128).

[322] J Prasongkit, A Grigoriev, R Ahuja, and G Wendin. Interference effects in phtalocyanine controlled by H-H tautomerization: Potential two-terminal unimolecular electronic switch. *Phys. Rev. B*, 84:165437, 2011. (Cited on page 128).

[323] W Auwärter, K Seufert, D Ecija, S Vijayaraghavan, S Joshi, F Klappenberger, N Samudrala, and J V Barth. A surface-anchored molecular four-level conductance switch based on single proton transfer. *Nat. Nanotech.*, 7:41, 2012. (Cited on page 128).

[324] G Bussetti, M Campione, M Riva, A Picone, L Raimondo, L Ferraro, C Hogan, M Palummo, A Brambilla, M Finazzi, L Duò, A Sassella, and F Ciccacci. Stable Alignment of Tautomers at Room Temperature in Porphyrin 2D Layers. *Adv. Funct. Mater.*, 24:958, 2014. (Cited on pages 128 and 149).

[325] G J Simpson, S W L Hogan, M Caffio, C J Adams, H Früchtl, Tanja van Mourik, and R Schaub. New Class of Metal Bound Molecular Switches Involving H-Tautomerism. *Nano Lett.*, 14:634, 2014. (Cited on page 128).

[326] H H Kong, Q Sun, L K Wang, Q G Tan, C Zhang, K Sheng, and W Xu. Atomic-Scale Investigation on the Facilitation and Inhibition of Guanine Tautomerization at Au(111) Surface. *ACS Nano*, 8:1804, 2014. (Cited on page 128).

[327] C Zhang, L Xie, L K Wang, H H Kong, Q G Tan, and W Xu. Atomic-Scale Insight into Tautomeric Recognition, Separation, and Interconversion of Guanine Molecular Networks on Au(111). *J. Am. Chem. Soc*, 137:11795, 2015. (Cited on page 128).

[328] S A Tawfik, X Y Cui, S P Ringer, and C Stampfl. High On/Off Conductance Switching Ratio via H-Tautomerization in Quinone. *J. Chem. Theory Comput.*, 11:4154, 2005. (Cited on page 128).

[329] V D Pham, V Repain, C Chacon, A Bellec, Y Girard, S Rousset, A Smogunov, Y J Dappe, and J Lagoute. Control of MoleculeMetal Interaction by Hydrogen Manipulation in an Organic Molecule. *J. Chem. Phys. Lett.*, 7:1416, 2016. (Cited on page 128).

[330] H Böckmann, S Liu, J Mielke, J Waluk, L Grill, M Wolf, and T Kumagai. Direct Observation of Photoinduced Tautomerization in Single Molecules at a Metal Surface. *Nano Lett.*, 16:1034, 2016. (Cited on pages 128 and 157).

[331] S. Gawinkowski, L. Walewski, A. Vdovin, A. Slenczka, S. Rols, M. R. Johnson, B. Lesyng, and J. Waluk. Vibrations and hydrogen bonding in porphycene. *Phys. Chem. Chem. Phys.*, 14:5489, 2012. (Cited on page 129).

[332] M F Shibl, M Tachikawa, and O Kühn. The geometric (H/D) isotope effect in porphycene: grid-based Born-Oppenheimer vibrational wavefunctions vs. multi-component molecular orbital theory. *Phys. Chem. Chem. Phys.*, 7:1368, 2005. (Cited on page 129).

[333] M F Shibl, M Pietrzak, H H Limbach, and O Kühn. Geometric H/D Isotope Effects and Cooperativity of the Hydrogen Bonds in Porphycene. *ChemPhysChem*, 8:315, 2007. (Cited on page 129).

[334] E C H Sykes, L C Fernandez-Torres, S U Nanayakkara, B A Mantooth, R M Nevin, and P S Weiss. Observation and manipulation of subsurface hydride in Pd111 and its effect on surface chemical, physical, and electronic properties. *Proc. Natl. Acad. Sci.*, 102:17907, 2005. (Cited on page 130).

[335] T Mitsui, E Fomin, D F Ogletree, M Salmeron, A U Nilekar, and M Mavrikakis. Manipulation and Patterning of the Surface Hydrogen Concentration on Pd(111) by Electric Fields. *Angew. Chem. Int. Ed.*, 46: 5757, 2007. (Cited on page 130).

[336] T Bucko, J Hafner, S Lebegue, and J G Angyan. Improved Description of the Structure of Molecular and Layered Crystals: Ab Initio DFT Calculations with van der Waals Corrections. *J. Phys. Chem. A*, 114:11814, 2010. (Cited on page 130).

[337] P Santra, J Klimeš, D Alfe, A Tkatchenko, B Slater, A Michaelides, R Car, and M Scheffler. Hydrogen Bonds and van der Waals Forces in Ice at Ambient and High Pressures. *Phys. Rev. Lett.*, 107:185701, 2011. (Cited on page 130).

[338] T Bjorkman, A Gulans, A V Krasheninnikov, and R M Nieminen. van der Waals Bonding in Layered Compounds from Advanced Density-Functional First-Principles Calculations. *Phys. Rev. Lett.*, 108:235502, 2012. (Cited on page 130).

[339] J Carrasco, W Liu, A Michaelides, and A Tkatchenko. Insight into the description of van der Waals forces for benzene adsorption on transition metal (111) surfaces. *J. Chem. Phys.*, 140:084704, 2014. (Cited on page 130).

[340] Y. L. Huang, E. Wruss, D. A. Egger, S. Kera, N. Ueno, W. A. Saidi, T. Bucko, A. T. S. Wee, and E. Zojer. Understanding the Adsorption of CuPc and ZnPc on Noble Metal Surfaces by Combining Quantum-Mechanical Modelling and Photoelectron Spectroscopy. *Molecules*, 19:2969, 2014. (Cited on page 130).

[341] W Liu, A Tkatchenko, and M Scheffler. Modeling Adsorption and Reactions of Organic Molecules at Metal Surfaces. *Acc. Chem. Res.*, 47:3369, 2014. (Cited on page 130).

[342] R J Maurer, V G Ruiz, J Camarillo-Cisneros, W Liu, N Ferri, K Reuter, and A Tkatchenko. Adsorption structures and energetics of molecules on metal surfaces: Bridging experiment and theory. *Prog. Surf. Sci.*, 91:72, 2016. (Cited on page 130).

[343] L Martin-Gondre, J I Juaristi, M Blanco-Rey, R Díez Muiño, and M Alducin. Influence of the van der Waals interaction in the dissociation dynamics of N_2 on W(110) from first principles. *J. Chem. Phys.*, 142:074704, 2015. doi: 10.1063/1.4908060. (Cited on page 130).

[344] M Wijzenbroek, D M Klein, B Smits, M Somers, and G J Kroes. Performance of a Non-Local van der Waals Density Functional on the Dissociation of H_2 on Metal Surfaces. *J. Phys. Chem. A*, 119:12146, 2015. doi: 10.1021/acs.jpca.5b06008. (Cited on page 130).

[345] M. Blanco-Rey, M. Alducin, J. I. Juaristi, and P. L. de Andres. Diffusion of Hydrogen in Pd Assisted by Inelastic Ballistic Hot Electrons. *Phys. Rev. Lett.*, 108:115902, 2012. (Cited on pages 131, 133, and 156).

[346] K. Liu and S. Gao. Excitation of Frustrated Translation and Nonadiabatic Adatom Hopping Induced by Inelastic Tunneling. *Phys. Rev. Lett.*, 95:226102, 2005. (Cited on pages 132 and 134).

[347] P. Saalfrank. Manipulation of adsorbates with electric fields. *J. Chem. Phys.*, 113:3780, 2000. (Cited on page 132).

[348] M. Blanco-Rey and J. C. Tremblay. Diffusion of hydrogen interstitials in the near-surface region of Pd(111) under the influence of surface coverage and external static electric fields. *J. Chem. Phys.*, 142:154704, 2015. (Cited on page 132).

[349] M. Alemani, S. Selvanathan, F. Ample, M. V. Peters, K. H. Rieder, F. Moresco, C. Joachim, S. Hecht, and L. Grill. Adsorption and Switching Properties of Azobenzene Derivatives on Different Noble Metal Surfaces: Au(111), Cu(111), and Au(100). *J. Phys. Chem. C*, 112:10509, 2008. (Cited on page 132).

[350] G. Füchsel, T. Klamroth, J. Dokić, and P. Saalfrank. On the Electronic Structure of Neutral and Ionic Azobenzenes and Their Possible Role as Surface Mounted Molecular Switches. *J. Phys. Chem. B*, 110:16337, 2006. (Cited on page 132).

[351] S. G. Tikhodeev and H. Ueba. Relation between inelastic electron tunneling and vibrational excitation of single adsorbates on metal surfaces. *Phys. Rev. B*, 70:125414, 2004. (Cited on page 133).

[352] K. Zenichowski, T. Klamroth, and P. Saalfrank. Open-system density matrix description of an STM-driven atomic switch: H on Si(100). *Appl. Phys. A*, 93: 319, 2008. (Cited on page 134).

[353] K Lee, E D Murray, L Kong, B I Lundqvist, and D C Langreth. Higher-accuracy van der Waals density functional. *Phys. Rev. B*, 82:081101, 2010. (Cited on pages 135 and 158).

[354] G Román-Pérez and J M Soler. Efficient Implementation of a van der Waals Density Functional: Application to Double-Wall Carbon Nanotubes. *Phys. Rev. Lett*, 103:096102, 2009. (Cited on page 135).

[355] A Ambrosetti, A M Reilly, R A DiStasio Jr., and A Tkatchenko. Long-range correlation energy calculated from coupled atomic response functions. *J. Chem. Phys.*, 140:18A508, 2014. (Cited on page 135).

[356] S R Bahn and K W Jacobsen. An Object-Oriented Scripting Interface to a Legacy Electronic Structure Code. *Comput. Sci. Eng.*, 4:56, 2002. (Cited on page 136).

[357] E Bitzek, P Koskinen, F Gähler, M Moseler, and P Gumbsch. Structural Relaxation Made Simple. *Phys. Rev. Lett.*, 97:170201, 2006. (Cited on page 136).

[358] C Lee and W Yang ans R G Parr. Development of the Colle-Salvetti correlation-energy formula into a functional of the electron density. *Phys. Rev. B*, 37:758, 1988. (Cited on page 137).

[359] A D Becke. Density-functional thermochemistry. III. The role of exact exchange. *J. Chem. Phys.*, 98:5648, 1993. (Cited on page 137).

[360] C Møller and M S Plesset. Note on an Approximation Treatment for Many-Electron Systems. *Phys. Rev. B*, 46:618, 1934. (Cited on page 137).

[361] M Head-Gordon, J A Pople, and M J Frisch. MP2 energy evaluation by direct methods. *Chem. Phys. Lett.*, 153:503, 1988. (Cited on page 137).

[362] P M Kozlowski, M Z Zgierski, and J Baker. The inner-hydrogen migration and ground-state structure of porphycene. *J. Chem. Phys.*, 109:5905, 1998. (Cited on pages 137 and 138).

[363] Z Smedarchina, M F Shibl, O Kühn, and A Fernández-Ramos. The tautomerization dynamics of porphycene and its isotopomers Concerted versus stepwise mechanisms. *Chem. Phys. Lett.*, 436:314, 2007. (Cited on pages 137, 138, and 150).

[364] E D Murray, K Lee, and D C Langreth. Investigation of Exchange Energy Density Functional Accuracy for Interacting Molecules. *J. Chem. Theory Comput.*, 5:2754, 2009. (Cited on pages 141 and 142).

[365] A D Becke. On the large-gradient behavior of the density functional exchange energy. *J. Chem. Phys.*, 85:7184, 1986. (Cited on page 142).

[366] A D Becke. Density functional calculations of molecular bond energies. *J. Chem. Phys.*, 84:4524, 1986. (Cited on page 142).

[367] J Waluk, M Müller, P Swiderek, M Köcher, E Vogel, G Hohlneicher, and J Michl. Electronic states of porphycenes. *J. Am. Chem. Soc.*, 113:5511, 1991. (Cited on page 144).

[368] R F W Bader, editor. *Atoms in Molecules: A Quantum Theory*. Oxford University Press, Oxford, U.K., 1990. (Cited on page 145).

[369] N. Henningsen, K. J. Franke, I. F. Torrente, G. Schulze, B. Priewisch, K. Rück-Braun, J. Dokic, T. Klamroth, P. Saalfrank, and J. I. Pascual. Inducing the Rotation of a Single Phenyl Ring with Tunneling Electrons. *J. Phys. Chem. C*, 111:14843, 2007. (Cited on page 158).

[370] J. Wirth, N. Hatter, R. Drost, T. R. Umbach, S. Barja, M. Zastrow, K. Rck-Braun, J. I. Pascual, P. Saalfrank, and K. J. Franke. Diarylethene Molecules on a Ag(111) Surface: Stability and Electron-Induced Switching. *J. Phys. Chem. C*, 119:4874, 2015. (Cited on page 158).

[371] T. Williams, C. Kelley, and many others. Gnuplot 4.6: an interactive plotting program. (Cited on page 177).

[372] J. C. Light and T. Carrington. *Discrete-Variable Representations and their Utilization*, page 263. John Wiley and Sons, Inc., 2007. (Cited on page 177).

[373] J. C. Tremblay, G. Füchsel, and P. Saalfrank. Excitation, relaxation, and quantum diffusion of CO on copper. *Phys. Rev. B*, 86:045438, 2012. (Cited on page 177).

Acknowledgements

The work I present in this Thesis started more than three years ago and the feeling I had back then is somehow resembling the one I have at this stage of my life: "I know so little...". I guess the beginnings and the ends are very similar in this respect and it always seems to us that nothing much has changed. Fortunately, feelings are feelings, and accomplished work and people who helped along the way are real proof that much has been done and learned. Actually, once I was told that people without work or work without people does not work. Therefore, whenever I look at this Thesis and think about all the people who supported me and my work, the aforesaid feeling dissolves and the superior one appears: "I am so grateful...".

First and foremost, I would like to express my sincere gratitude to my supervisor María Blanco Rey, for giving me the opportunity to be part of this unique scientific atmosphere and for always supporting my ideas and work. I cannot thank you enough for your patience and free time whenever I needed help or some guidance. I am also very thankful for your tolerance and endurance while you were reading and correcting my drafts. This and your instructions improve my scientific writing skills. You should know that without your continuous support and optimism, this Thesis and the corresponding work would look like a collection of child's drawings pinned to a refrigerator.

Also, I am very grateful to Maite and Iñaki. I really enjoyed our long-lasting (and sometimes "ever-lasting") conversations of the scientific problems we had. I really admire the patience and stoicism you two and María showed whenever I expressed my stubbornness and non-political stance. Our discussions shaped and improved my way of thinking and attitude towards scientific problems. Friendly and vivid atmosphere, which you always were able to create, helped me a lot during my stay here. I should also add that I will very much miss your Christmas turones. Ups! I mean, my family will miss them.

I would also like to thank Jean Christophe Tremblay, for our nice collaboration and for all the great work we did together. I enjoyed very much my stay in your group

and I will never forget our "daily oscillations" in our working progress. I admire your constant optimism that successfully elevated us from "the deeps of this oscillations". I appreciate your support during my stay in Berlin and I really hope to be part of another barbecue party at some point in the future (we should not settle with the current number of parties, right?).

I also owe a lot of intellectual debts to Vito Despoja and Ivan Kupčić and I really hope that you are looking forward to my new doses of curiosity and scientific questions in the future... I am!

I would also like to acknowledge my current institute Donostia International Physics Center (DIPC) and all the people working in the administration and computing center service. My special thanks goes to the latter, since most of my computational work was done on the DIPC supercomputers.

Further, I would like to thank a group of people, which is sometimes called the "Donostia family". Although I am sincerely thankful to all members of this community, I will mention a few: Ivor, thank you for 42 kg of fish. Berni, thank you for your sober thoughts. Francesco, thank you for figs. Moritz, thank you for complaining. Tomáš, thank you for being Basque. Nieves, thank you for filters. Mathias, thank you for your theistic intuition. Pedro, thank you for your green band. Aupi! Miguel. Oihana, thank you for bla bla. Fede, thank you for your Italian accent...

And a very very special gratitude goes to my family in Croatia... what would I call a true family. Ovdje nema govora o najvećim ili najmanjim zahvalama. U suportnosti s mojim računima, ovdje je sve s onu stranu mjerljivosti. Ali s nekim se mora početi. Nemjerljivo se zahvaljujem Martini, koja je uvijek bila tu za mene, kolko god je mogla. Ona možda najviše zna kakve su ovo zanimljive godine bile (zapravo, ona i još jedno "mnoštvo"; sad se to "mnoštvo" smije). Jedno isto tako veliko nemjerljivo hvala ide mojim roditeljima i mojoj braći, Denisu i Tončeku. Vi ste me "podigli" i napravili iz mene osobu. Zapravo ovo posljednje je još u tijeku. Hvala nemjerljivo puno i mojoj baki koja uvijek pazi da li se dobro hranim. Puno nemjerljivih hvala i mojim frendovima (Pinki, Zlac, Marac, Srdjo, Alek,...), koji su se uvijek teška srca izdvojili iz svoje rutine i uljepšali mi praznike. Možda vam nije na prvo očito, al svi vi ste nemjerljivo pomogli u izradi ovog rada.